## RESEARCH ARTICLE

# Properties of graphene: a theoretical perspective

D.S.L. Abergel[a], V. Apalkov[b], J. Berashevich[a], K. Ziegler[c] and Tapash Chakraborty[a]*

*[a]Department of Physics and Astronomy, University of Manitoba, Winnipeg, MB R3T 2N2, Canada; [b]Department of Physics and Astronomy, Georgia State University, Atlanta, GA 30303, USA; [c]Institut für Physik, Universität Augsburg, D-86135 Augsburg, Germany*

The electronic properties of graphene, a two-dimensional crystal of carbon atoms, are exceptionally novel. For instance, the low-energy quasiparticles in graphene behave as massless chiral Dirac fermions which has led to the experimental observation of many interesting effects similar to those predicted in the relativistic regime. Graphene also has immense potential to be a key ingredient of new devices, such as single molecule gas sensors, ballistic transistors and spintronic devices. Bilayer graphene, which consists of two stacked monolayers and where the quasiparticles are massive chiral fermions, has a quadratic low-energy band structure which generates very different scattering properties from those of the monolayer. It also presents the unique property that a tunable band gap can be opened and controlled easily by a top gate. These properties have made bilayer graphene a subject of intense interest. In this review, we provide an in-depth description of the physics of monolayer and bilayer graphene from a theorist's perspective. We discuss the physical properties of graphene in an external magnetic field, reflecting the chiral nature of the quasiparticles near the Dirac point with a Landau level at zero energy. We address the unique integer quantum Hall effects, the role of electron correlations, and the recent observation of the fractional quantum Hall effect in the monolayer graphene. The quantum Hall effect in bilayer graphene is fundamentally different from that of a monolayer, reflecting the unique band structure of this system. The theory of transport in the absence of an external magnetic field is discussed in detail, along with the role of disorder studied in various theoretical models. Recent experminental observations of a metal–insulator transition in hydrogenated graphene is discussed in terms of a self-consistent theory and compared with related numerical simulations. We highlight the differences and similarities between monolayer and bilayer graphene, and focus on thermodynamic properties such as the compressibility, the plasmon spectra, the weak localization correction, quantum Hall effect and optical properties. Confinement of electrons in graphene is non-trivial due to Klein tunnelling. We review various theoretical and experimental studies of quantum confined structures made from graphene. The band structure of graphene nanoribbons and the role of the sublattice symmetry, edge geometry and the size of the nanoribbon on the electronic and magnetic properties are very active areas of research, and a detailed

---

*Corresponding author. Email: tapash@physics.umanitoba.ca

review of these topics is presented. Also, the effects of substrate interactions, adsorbed atoms, lattice defects and doping on the band structure of finite-sized graphene systems are discussed. We also include a brief description of graphane – gapped material obtained from graphene by attaching hydrogen atoms to each carbon atom in the lattice.

**Keywords:** monolayer graphene; bilayer graphene; Dirac fermions; quantum Hall effect; electron-electron interaction; plasmon dispersion; zero-field transport; metal-insulator transition; quantum dots; graphene nanoribbons; edge-states; graphane

## Contents

## 1. Introduction

Everything about graphite involves a mix of the very old and very young. Known to man since ancient times (*ca* 1500CE), graphite is as ubiquitous as the *lead* in a pencil, and yet the subject of our current review, graphene, being a single atomic layer of graphite, was isolated only in 2004! That discovery marked the beginning of the academic equivalent of a gold rush which has become a major topic of research for the condensed matter and materials physics community, along with chemists, electrical engineers and device specialists. Several thousand papers have been written in the past couple of years that have attempted to explain every aspect of the electronic properties of graphene. There are review articles, long and short (see, e.g. [1–5]), special journal issues [6] and popular magazine articles (see, e.g. [7]). This development at 'Mozartian speed' is primarily due to the fact that a two-dimensional system of electrons in graphene behaves rather uniquely as compared to its counterpart in semiconductor systems. In fact, many of the fundamental properties of graphene that were crucial for the present developments were already reported in the early part of the past century, merely waiting to be confirmed experimentally until now.

In graphene, one finds a new class of low-dimensional system, only one atom thick, with vast potential for applications in future nanotechnology. Our review is organized as follows. In this section, we introduce graphene by describing its crystal structure, and discussing its band structure via the frequently-used tight-binding model. We also discuss the low-energy properties of this material, and in particular we focus on the linear (Dirac-like) nature of the energy dispersion near the edges of the Brillouin zone, and on the chiral nature of the low-energy electrons. We also briefly discuss fabrication techniques for graphene, and whet the appetite for study of this material by describing some of the devices utilizing the unique properties of graphene which have already been created in the laboratory.

Section 2 deals with the quantum Hall effect, i.e. quantization of Hall conductance as a function of the magnetic field or the electron density, that was initially discovered in conventional non-relativistic two-dimensional electron systems. The effect is a direct manifestation of the Landau quantization of electron dynamics. An electron system in graphene, being a two-dimensional system, also shows Landau quantization of electron motion and the corresponding quantum Hall effect, which has been observed experimentally. The relativistic massless nature of the energy dispersion law in graphene results in striking differences between the quantum Hall effect observed in graphene and in conventional two-dimensional systems. In graphene, the quantum Hall effect can be observed even at room temperature, while in non-relativistic systems it is observable only at low temperatures. The quantized Hall effect in graphene occurs not at integer values as in the conventional Hall effect, but at half-integer values. Such anomalous behavior of the quantum Hall effect is due to massless relativistic nature of the charge carrier dispersion and the electron–hole symmetry of the system. In addition to anomalous half-integer values of the Hall conductance, a rich structure of Hall plateaus has been observed experimentally. This structure is associated with the lifting of valley and spin degeneracy of the Landau levels. Different many-body mechanisms of lifting of the degeneracy of the Landau levels have been proposed in the literature. These mechanisms are reviewed in detail. The specific features of the many-particle excitations of the quantum Hall states, the fractional quantum Hall effect in graphene and the unique structure of the quantum Hall state edge states are also discussed in this article.

In Section 3, we discuss specific aspects of bilayer graphene, and try to highlight the similarities and differences between this and the monolayer material. We introduce experimental techniques for distinguishing the number of layers in a graphene flake. We present the tight-binding formalism in order to derive the quadratic low-energy spectrum, and to discuss the influence of trigonal warping and the formation of a band gap. We describe the quantum Hall effect and the formation of the zero-energy level with doubled degeneracy, which is unique to this system. The interactions between electrons are fascinating in this material, and several properties are distinct from both the monolayer and traditional two-dimensional electron systems, and we describe the formation of spin-polarized and other ordered states. The interactions between electrons and phonons are also important (e.g. in the context of Raman scattering experiments), so we briefly describe the phonon anomalies and the electron–phonon interaction. Lastly, we review some of the proposals for devices which utilize bilayer graphene in their design.

Electronic properties that are intimately related to electron–electron interactions, namely, the compressibility and plasmon dispersion in a two-dimensional electron gas shows unique behavior in graphene. The compressibility of a two-dimensional electron gas is an important physical quantity which can be deduced from the ground state energy. It provides important information about the electron correlations, the chemical potential, the stability of the system, and so on. In Section 4, we discuss the unique behavior of the electron compressibility in monolayer and bilayer graphene. In that section, we also describe the excitation spectra of graphene in the presence of the spin–orbit interaction (SOI) within the random-phase approximation (RPA). The SOI opens a gap between the valence and conduction bands and between the intraband and inter-band electron–hole excitation continuum (EHC) of the semimetal Dirac system. As a result, one sees a dramatic change in the long-wavelength dielectric function of the system. An undamped plasmon mode appears in the EHC gap reflecting the interplay between the intraband and interband electron correlations. In undoped bilayer graphene, the static screening effect is anisotropic and much stronger than that in monolayer graphene. The dynamic screening shows the properties of a Dirac gas in the low-frequency limit and of Fermi gas in the high-frequency limit. A similar transition from the Dirac gas to the Fermi gas is also observed in the plasmon spectrum. In doped bilayer graphene, the plasmon spectrum is quite similar to that of Fermi gas for momentum less than half the Fermi momentum while becoming softer at higher momentum. We close this section with a discussion of the properties of graphene in a strong external electromagnetic field (EMF). The possibility of inducing valley-polarized currents by irradiating gapped bilayer graphene is described.

In Section 5, we review the transport behavior of monolayer and bilayer graphene in the absence of an external magnetic field, focusing on properties in the vicinity of the charge neutrality points. Beginning with the classical Boltzmann approach, we compare the latter with the more general linear-response (Kubo) approach. The effect of electron–electron and electron–phonon interactions as well as the effect of different types of disorder are discussed. Of all these effects, disorder seems to be the most important. We present and compare several schemes of approximation: perturbation theory, self-consistent and saddle-point approximations and numerical simulations. Finally, the properties of a random gap and a related metal–insulator transition are investigated.

Quantum dots (QDs) or *artificial atoms* [8,9] are crucial building blocks in many nanoscale semiconductor applications. Their unique properties, such as superior transport and tunable optical spectra, originate from their zero dimensionality, which results in discrete energy spectra and sharp density of states. In conventional ‘non-relativistic’ semiconductor systems, the natural way to realize nanoscale QDs is through a confinement potential or as nanoscale islands of semiconductor material. In both cases the QDs have discrete energy spectra and electrons are localized within the QD regions. In graphene, the massless relativistic nature of the dispersion law results in unique properties of graphene QDs. That is, the above two approaches of the realization of QDs have very different outcomes in graphene. While the QDs as isolated islands of graphene have been successfully realized experimentally and have all the properties of zero-dimensional systems with discrete energy spectra, the conventional QDs realized through the confinement potential do not exist in graphene. This is due to Klein’s tunnelling, which provides an efficient escape channel from a confinement potential of any strength. Therefore electrons in graphene cannot be localized by a confinement potential. Different approaches have been proposed to overcome this problem: generation of an electron effective mass through interaction with a substrate, introducing a confinement potential in a double-layer system, in which electrons have non-zero mass under applied gate voltage, or considering special types of confinement potentials, e.g. smooth cylindrically symmetric potentials, for which not the problem of localization but the problem of efficient electron trapping is discussed. In Section 6, we review different approaches to overcome the Klein’s tunnelling and realize graphene QDs through a confinement potential. Even for QDs realized as islands of materials, the graphene islands show some unique properties. Although the main manifestations of a two-dimensional quantization, such as the Coulomb blockade and discrete energy spectra, are observed in experiments, the graphene nanoscale islands show specific features. Such features are degenerate zero-energy edge states with unique magnetic properties, specific energy level statistics related to the Dirac billiard and so on. These special properties of nanoscale graphene islands are also discussed. Finally, we also present a brief review of QDs in bilayer graphene.

In Section 7, we review the band structure of graphene nanoribbons which is known to be modified by the presence of edges where the alteration of the $sp^2$ network due to the mixture of the sp and $sp^2$ hybridization occurs. The nature of the zigzag edges impose localization of the electron density with the maximum at the border carbon atoms leading to the formation of flat conduction and valence bands near the Fermi level when the wave vector, $k \geq 2\pi/3$. The localized states are spin-polarized and in the case of ordering of the electron spin along the zigzag edges, graphene can be established in ferromagnetic or antiferromagnetic phases. The antiferromagnetic spin ordering of the localized states at the opposite zigzag edges breaks the sublattice symmetry of graphene that changes its band structure and opens a gap. Because the energetics, localization and spin ordering of the edge states can be modified by the size of graphene nanoribbon, edge geometry, orbital hybridization at the edges and an external electric field, their influence on the electronic and magnetic properties of graphene are discussed. Finally, we turn to finite-sized bilayer graphene systems, e.g. nanoribbons, and describe how the confinement and edge structures affect the properties of this system.

Graphene in the real world would interact with a substrate and the surrounding environment. If these interactions cause an imbalance of the charge or spin distribution between graphene sublattices or modify the graphene lattice, the sublattice or lattice symmetry of graphene will be broken, resulting in a change of the electronic and magnetic properties of the graphene. The edges of graphene are chemically active and prone to structural modifications and interactions with gas dissolved in the environment, thereby influencing the properties of graphene as well. Therefore, in Section 8, we discuss the influence of the changes brought by the external sources into the electronic and magnetic properties of graphene and prospects of their manipulation in a controllable way.

### 1.1. *A sheet of molecular chicken wire*

Graphene can be considered as the building block of many carbon allotropes. It is a two-dimensional crystal with hexagonal structure consisting of a bipartite lattice of two triangular sublattices (Figure 1a). Each atom is tied to its three nearest neighbors via strong $\sigma$ bonds that lie in the graphene plane with angles of 120°. The $\sigma$ bond is a result of the $sp^2$ hybridization of the 2s, $2p_x$, and $2p_y$ orbitals for the three valence electrons. The fourth valence electron is in the $2p_z$ orbital that is orthogonal to the graphene plane. A weak $\pi$ bond is formed by the overlap of half-filled $2p_z$ orbitals with other $2p_z$ orbitals. The transport properties of graphene are determined by these delocalized $\pi$ electrons.

The crystal structure of graphite consists of layers of graphene, with strong intralayer covalent coupling and weak interlayer binding. The weak interlayer coupling supposedly arises due to van der Waals interaction (the separation between the adjacent layers (0.34 nm) is much larger than the nearest neighbor distance

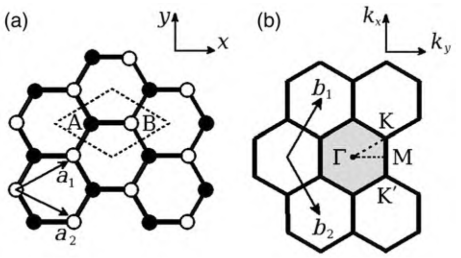

Figure 1. (a) Graphene lattice in real space, and (b) the corresponding reciprocal lattice. The unit cell of graphene contains two atoms A and B. The first Brillouin zone is drawn as shaded hexagon. The basis vectors of the direct lattice and the reciprocal lattice are $a_i$ and $b_i$, $i = 1, 2$, respectively. The high-symmetry points Γ, M and K in the Brillouin zone are also indicated.

between two carbon atoms ($a_{cc} = 0.142$ nm)) and the particular bonding mechanism along the direction normal to the plane. Similarly, if a graphene sheet is rolled up along one axis, it forms a carbon nanotube and it can be formed into a ball to create a fullerene. Due to this, graphene has long been considered a starting point for band structure calculations of graphite [10] and carbon nanotubes, and also for the calculation of their magnetic properties [11,12]. In what follows, we shall present a very brief description of the band structure. A detailed description can be found, for example in [13,14].

As mentioned above, graphene is a honeycomb lattice of carbon atoms. It is a bipartite lattice with two sublattices A and B that are triangular Bravais lattices (Figure 1a). Considering only the $xy$ plane, the unit vectors in real space, $\vec{a}_1$ and $\vec{a}_2$, and the reciprocal lattice vectors $\vec{b}_1$ and $\vec{b}_2$ are shown in Figure 1. The real space lattice vectors are written as

$$\vec{a}_1 = \frac{a}{2}\left(\sqrt{3}, 1\right), \quad \vec{a}_2 = \frac{a}{2}\left(\sqrt{3}, -1\right),$$

where $a = |\vec{a}_1| = |\vec{a}_2| = 0.246\,\text{nm}$ is the lattice constant. The corresponding unit vectors in the reciprocal lattice are

$$\vec{b}_1 = \frac{2\pi}{a}\left(\frac{1}{\sqrt{3}}, 1\right), \quad \vec{b}_2 = \frac{2\pi}{a}\left(\frac{1}{\sqrt{3}}, -1\right),$$

with a reciprocal space lattice constant $4\pi/\sqrt{3}a$. The first Brillouin zone is a hexagon (Figure 1b), where the corners are called the K points. The six corners form two inequivalent groups of K points, traditionally labelled K and K′.

The energy dispersion of $\pi$ electrons in graphene was first derived in 1947 by Wallace [10] within the tight-binding approximation. In this case, the wave function of graphene is a linear combination of Bloch functions for sublattice A

$$\Phi_A = \frac{1}{\sqrt{N}}\sum_{\vec{R}_A} e^{i\vec{k}\cdot\vec{R}_A}\varphi(\vec{r} - \vec{R}_A),$$

and an equivalent function $\Phi_B$ for the B sublattice. Here $N$ is the number of unit cells, $\vec{R}_A$ are the positions of the atom A and $\varphi(\vec{r} - \vec{R}_A)$ is the $2p_z$ orbital of the atom at $\vec{R}_A$. The sum runs over all unit cells, i.e. all possible lattice vectors.

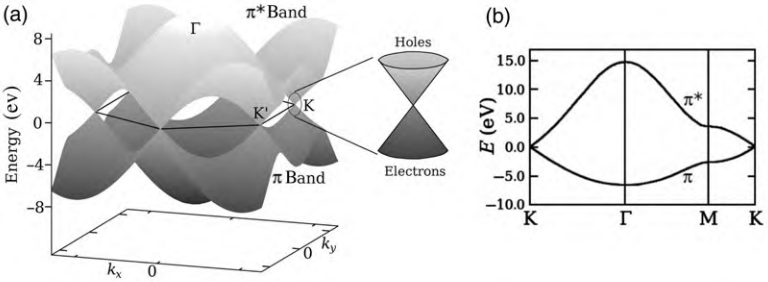

Figure 2. (a) Energy dispersion relation for graphene, drawn in the entire region of the Brillouin zone. Since we ignore the coupling between the graphene sheets, the bands depend only on $k_x$ and $k_y$. The $\pi$ band is completely filled and meets the totally empty $\pi^*$ band at the K points. Near these points both bands have linear dispersion as described in the text. (b) The dispersion along the high-symmetry points ΓMK.

In the nearest neighbor approximation (every A site has three nearest B sites, and vice versa), the energy eigenvalues can be obtained in a closed form [13,14]

$$\mathcal{E}(k_x, k_y) = \pm\gamma_0\left[1 + 4\cos\frac{\sqrt{3}k_x a}{2}\cos\frac{k_y a}{2} + 4\cos^2\frac{k_y a}{2}\right]^{\frac{1}{2}}, \tag{1}$$

where $\gamma_0$ is the transfer integral between the nearest neighbors. The energy dispersion of two-dimensional graphene according to this formula is plotted in Figure 2(a) as a function of the wave vector $\vec{k}$. The upper half of the curves is called the $\pi^*$ or the anti-bonding band while the lower one is $\pi$ or the bonding band. The two bands degenerate at the two K points given by the reciprocal space vectors $\vec{K} = (2\pi/a)(1/3, 1/\sqrt{3})$ and $\vec{K}' = (2\pi/a)(-1/3, 1/\sqrt{3})$ points where the dispersion vanishes. This is also the Fermi energy level $E_{\mathrm{F}}$ in intrinsic (undoped) graphene. There are two atoms per unit cell and hence there are two electrons per unit cell. The lower $\pi$ band is therefore completely filled, which leaves the upper $\pi^*$ band completely empty.

The derivation of this formula neglected the overlap integral between electron orbitals on adjacent lattice sites. Restoring this additional parameter introduces an electron–hole asymmetry to the $\pi$ bands away from the K points. This is shown in Figure 2(b) for parameters quoted in [13].

A full description of the band structure in graphene should also include the consideration of the $\sigma$ bands, since they are the lowest energy bands near the center of the Brillouin zone. However, since most transport properties of bulk graphene are determined by the low-energy band structure near the K points, we mention them only in passing. A description of their inclusion in the tight-binding model can be found in [13], and the presence of these bands within first-principles calculations are discussed in Section 7.

## 1.2. *Massless Dirac fermions*

We now describe how the tight-binding model discussed in the previous section yields the famous *massless Dirac fermions* which have made the study of monolayer graphene so enticing. In this Section, we give a brief overview of the main points: detailed discussion of these results will be given where appropriate in the rest of this review. As noted above, the Fermi energy corresponds to $\mathcal{E}=0$ at the K points. The low-energy properties, corresponding to the electronic states near the Fermi energy, can be described by expanding the energy dispersion around the K points. Writing the graphene wave vector $\vec{q}=\vec{K}+\vec{k}$, such that $|\vec{k}|a \ll 1$, one can write a Taylor expansion of $\mathcal{E}_\pm(\vec{q})$ near $\vec{K}$ which yields

$$\mathcal{E}_\pm(\vec{k}) = \pm\frac{\sqrt{3}}{2}\gamma_0 ak = \pm v_\mathrm{F}\hbar k,$$

where $v_\mathrm{F}=\sqrt{3}\gamma_0 a/2\hbar \approx 10^6\,\mathrm{m\,s^{-1}}$ is the Fermi velocity. This velocity is independent of the carrier density, therefore the energy dispersion corresponds to two cones meeting at the K point (see the inset to Figure 2a) with *linear* dependence on the wave vector. The corresponding density of states is

$$\rho(\mathcal{E}) \propto |\mathcal{E}|,$$

i.e. the density of states is linear and vanishes at zero energy. This is a direct consequence of the linear dispersion near K, in marked contrast to conventional two-dimensional electron gas, where the density of states is a constant.

The unique band structure of graphene just described, brings about profound changes in the electronic properties of the system. In the continuum limit and in the effective-mass approximation, the Hamiltonian in the vicinity of the K point is [15]

$$\mathcal{H}_\mathrm{K}(\vec{k}) = \hbar v_\mathrm{F}\begin{pmatrix} 0 & k_x - \mathrm{i}k_y \\ k_x + \mathrm{i}k_y & 0 \end{pmatrix} = \hbar v_\mathrm{F}\vec{\sigma}\cdot\vec{k} = -\mathcal{H}^T_{\mathrm{K}'}(\vec{k}), \tag{2}$$

where the $\vec{\sigma}=(\sigma_x,\sigma_y)$ is a vector of Pauli matrices. The Hamiltonian therefore describes two-dimensional massless neutrinos [15] with a linear energy dispersion, $\mathcal{E}_\pm(k)=\pm v_\mathrm{F}\hbar k$. The wave functions of these relativistic-like (Dirac) particles have a spinor structure. For the K and K′ points, they are (without normalization)

$$\Psi^\mathrm{K}_{s,\vec{k}} = \mathrm{e}^{\mathrm{i}\vec{k}\cdot\vec{r}}\begin{pmatrix} s \\ \mathrm{e}^{\mathrm{i}\theta_{\vec{k}}} \end{pmatrix}; \qquad \Psi^{\mathrm{K}'}_{s,\vec{k}} = \mathrm{e}^{\mathrm{i}\vec{k}\cdot\vec{r}}\begin{pmatrix} \mathrm{e}^{\mathrm{i}\theta_{\vec{k}}} \\ s \end{pmatrix}, \tag{3}$$

where $s=+1$ for the upper band (electrons) and $-1$ for the lower band (holes), $\tan\theta_{\vec{k}}=k_y/k_x$. The upper and lower terms correspond to the quantum mechanical amplitudes (or *pseudospin*) of finding the particle on one of the two sublattices, A and B. There is a convenient alternative representation of the graphene Hamiltonian which allows the Hamiltonians of the two valleys to be combined into one expression. The basis is written as $\{\phi_A, \phi_B\}$ in the K valley with index $\xi=1$, and $\{\phi_B, \phi_A\}$ in the K′ valley with $\xi=-1$. Then, the Hamiltonian and wave functions for either valley can be written as the $2\times 2$ matrix

$$\mathcal{H}_\xi(\vec{k}) = \xi\hbar v_F\begin{pmatrix} 0 & k_x - \mathrm{i}k_y \\ k_x + \mathrm{i}k_y & 0 \end{pmatrix}; \quad \Psi^\xi_{s,\vec{k}} = e^{\mathrm{i}\vec{k}\cdot\vec{r}}\begin{pmatrix} \xi s \\ e^{\mathrm{i}\theta_{\vec{k}}} \end{pmatrix}. \tag{4}$$

Interestingly, in graphene, the pseudospin direction is associated with the momentum of the particles. This means that the wave functions in the vicinity of the

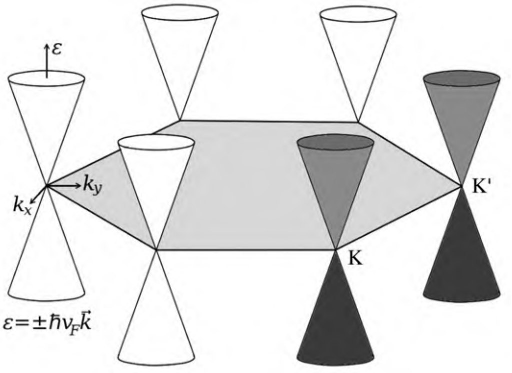

Figure 3. Dirac cones at the Dirac points.

K and K′ points (Dirac points) are *chiral*, or *helical fermions*. One consequence of this is that any backscattering, i.e. scattering of particles from the wave vector $\vec{k}$ to $-\vec{k}$, is suppressed [16]. Particles have opposite chirality in the K or K′ *valleys* or in the electron or hole bands. The energy bands in the vicinity of these Dirac points are two cones meeting at $k=0$ (Figure 3). The charge carriers in graphene are usually described as *massless Dirac fermions* [17]. Experimental observation of full Dirac cone dispersion has been reported recently [18]. The transformation of electrons in graphene to relativistic-like objects have led to many novel effects: anomalous integer quantum Hall effect, Klein's paradox, novel effects at the edges, etc. They are all subjects of our present review.

### 1.3. *How it's made*

Monolayer, bilayer and few-layer graphenes[1] are primarily fabricated in one of three ways. Although this review will focus on the theoretical study of graphene, we shall briefly describe these methods here.[2]

The first method is the mechanical exfoliation of single layers from a bulk graphite sample [21,22]. Due to its weakly-bound layered structure, dry cleaving of highly oriented pyrolytic graphite or single graphite crystals has been very successfully utilized by Novoselov *et al.* to synthesize single-, double- and triple-layer flakes up to 10 μm in size. This technique (also called the *Scotch tape* method) involves peeling flakes from bulk graphite using adhesive tape [21], or cleavage by mechanical rubbing [22]. The number of layers in the resulting flakes can be determined by optical spectroscopy and Raman spectroscopy [23] (Section 3.1). The technical details about the preparation and characterization can be found in the excellent review article by the pioneers of this technique [1]. Mechanically exfoliated graphene flakes were important in determining most of the fundamental properties of Dirac fermions that are expected in an isolated graphene plane.

Exfoliated graphene can be processed to create samples of suspended graphene [24–26] where the monolayer flake is not in contact with a substrate. These samples can be created either by placing a metal grid on top of exfoliated graphene [24] or by depositing metallic electrodes [25,26] before etching away the silicon dioxide substrate from below the graphene. The measured electron mobility is as large as 185,000 $\mathrm{cm^2\,V^{-1}\,s^{-1}}$ at 100 K [26] and 230,000 $\mathrm{cm^2\,V^{-1}\,s^{-1}}$ at 5 K [25]. This is approximately a factor of 10 higher than the largest reported mobility in exfoliated graphene, and matches predictions based on the measurement of phonon-induced disorder and extrapolation from transport measurements on exfoliated graphene samples [27].

The other main route to fabricate graphene samples has been developed by de Heer *et al.* [28–31]. In this method, hexagonal silicon carbide crystals are heated to approximately 1300°C in ultra-high vacuum which allows the Si atoms to evaporate from the surface leaving behind a purely graphitic film. The properties of the residual film vary depending on which face of the SiC crystal is used in the procedure. If the SiC(0001) (silicon-terminated) face is used, high-quality graphene films are deposited which show Dirac cones in their low-energy band structure, although interaction between the graphene and the substrate induces *n*-type doping which shifts the Fermi energy above the Dirac point. Experimental data suggests that the graphene is covalently bound to the substrate via a buffer layer [32] which does not show graphene-like $\pi$ bands due to the additional strain caused by a dilated C–C bond length in this layer [33]. In contrast, when the SiC($000\bar{1}$) (carbon-terminated) face is used, the graphene is not seperated by a buffer layer, but is bound directly to the substrate by weak dispersion forces. Also, multi-layer graphenes grown on this face still exhibit the monolayer-like linear low-energy dispersion because the layers show rotational disorder which minimizes the interactions between them. Magnetospectroscopy of few-layer carbon-face epitaxial graphene [34] also showed the Landau level dispersion characteristic of graphene monolayers. It has been suggested that the interaction between the graphene and the SiC(0001) substrate is not the same for the two sites in the graphene unit cell [35]. This has the effect of opening a band gap at the Dirac points of ~0.26 eV, although this is still controversial as other authors [33,36] claim that many-body effects are the cause of this gap.

Lastly, chemical vapor deposition can be utilized to grow thin graphite films [37,38], and graphene layers [39] which may be patterned and transferred to semiconducting or insulating substrates. In this method [40], hydrocarbon gas is placed near a metal foil surface where the hydrocarbon molecules can be decomposed and carbon atoms are dissolved into the metal. The foil is then allowed to cool (at a predetermined rate) and a carbon film may be formed on the surface. This film can be transferred to a polymer or semiconducting substrate via chemical etching [39]. Graphene monolayers grown in this way can be fully coherent over step edges in the underlying substrate and contain few defects [41,42]. The large size of flakes produced and accompanying high mobility (~4000 $\mathrm{cm^{-2}\,V^{-1}\,s^{-1}}$) make chemical vapor deposition a very promising avenue for the future industrial fabrication of graphene devices.

### 1.4. *Graphene devices*

The relatively short life of experimental research in graphene has limited the number of proposals for devices which might utilize this material. We briefly introduce some device concepts which have been implemented experimentally.

Obviously, the first concept is that of the graphene field effect transistor (FET), but as this is discussed elsewhere in this review, we do not dwell on it now. A comprehensive report on the current state of graphene transitor devices has been written by Lemme [43]. However, two variants do deserve to be mentioned, and they are the high-frequency performance of graphene FETs, and single-electron transistors (SETs). Lin *et al.* [44] demonstrate that a graphene transistor with a gate length of 150 nm may have peak cutoff frequency of 26 GHz, representing a significant step towards utilizing graphene in high-frequency applications, although the authors found the regular $1/f$ behavior of the gain, suggesting that graphene cannot change the operational paradigm of these devices. Other works on high-frequency FETs have been published by Meric *et al.* [45] and Moon *et al.* [46]. Also, Stampfer *et al.* [47] fabricated a fully-tunable single electron transistor from a monolayer graphene nanoribbon and extracted device characteristics from the observed Coulomb diamonds. Additionally, room-temperature spin transport has been measured through graphene transistors [48], with spin polarization to be approximately 10%.

The adsorption of gas molecules on the surface of a graphene flake changes the Hall resistivity, and this effect has been used to develop graphene-based chemical sensors [49]. Micrometer-sized sensors were fabricated which were sensitive to the attaching or detaching of a single gas molecule, producing step-like changes in the resistance. The high sensitivity is a result of the impact of the adsorption on the electronic properties of the graphene flake, which is discussed in detail in Section 8.2.

The mechanical properties of graphene may also be employed in the creation of devices. For example, Bunch *et al.* [50] have created the ‘world’s thinnest balloon’ and claim that it is impermeable to gases. They suggest that this property may be utilized in membrane sensors for pressure changes in small volumes, as selective barriers for filtration of gases, as a platform for imaging of graphene-fluid interfaces and for providing a physical barrier between two phases of matter. Similarly, Stolyarova *et al.* [51] demonstrated that gaseous bubbles can be trapped between a graphene monolayer and the surface of an $SiO_2$ substrate, and subsequently manipulated by an AFM tip. This has the potential to be applied in ‘lab-on-a-chip’ devices.

Graphene may also be used as a novel information storage device, as suggested by Standley *et al.* [52]. Retention times of over 24 h, and operation over many thousands of cycles without significant degradation of the device were reported. Finally, the high transparency, large conductivity, high chemical and thermal stability and good flexibility make ‘graphene window devices’ [53] a natural candidate for solar cells and other next-generation optoelectronic devices. Blake *et al.* [54] argued that graphene, with its low resistivity, high transparency and chemical stability would offer improved durability and simpler technology for future optoelectronic devices.

The properties of graphene are so fascinating that there are reports of attempts to recreate many of those exotic properties in a high-mobility modulated two-dimensional electron gas confined in an AlGaAs/GaAs quantum well [55]. The electronic dispersion in this hexagonal superlattice is expected to be Dirac-like with the pseudospin degree of freedom. Creation of such artificially engineered systems has the obvious advantages over natural graphene because of the possibility to tune the parameters. This would provide unique opportunities to study

Dirac-fermion physics in a conventional two-dimensional electron gas confined in semiconductor systems nanopatterned with honeycomb geometry.

The physics of graphene is a challenging and fascinating subject at the nanoscale. Its impact is already felt both in fundamental scientific research and potential industrial applications. From Dirac electrons in condensed matter to future 'valleytronics' in graphene nanodevices, graphene has unleashed limitless potential to impact our lives as we look through the magical quantum world at the nanoscale, a world that is not much different from an Alice-in-Wonderland world that plays by its own rules.[3] We are yet to completely understand most of those rules, but we hope that this review will help understand some.

## 2. Graphene in a magnetic field

### 2.1. *Landau levels in graphene*

Just as for non-relativistic particles, the motion of relativistic charges in graphene in a strong perpendicular magnetic field is quantized, which results in discrete energy levels (Landau levels). In a conventional electron gas (non-relativistic) Landau quantization produces equidistant energy levels, which is due to the parabolic dispersion law of free electrons. In graphene the electrons have relativistic dispersion law, which strongly modifies the Landau quantization of the energy levels and the positions of the levels.

The Landau quantization of the energy levels in graphene in a perpendicular magnetic field has been studied [11] within the tight-binding model [56,57] and within the effective-mass relativistic model [15,58]. The tight-binding approach is the more fundamental one and it is valid for a wider energy range. In many applications of graphene in a magnetic field only the low-energy processes are important, which can be efficiently described within the effective-mass approximation.

The effective-mass Hamiltonian of a single electron in graphene in a uniform perpendicular magnetic field has a form of a 4 × 4 matrix [15,58]

$$\mathcal{H}_{\mathrm{Dirac}} = v_{\mathrm{F}} \begin{pmatrix} 0 & \pi_x - \mathrm{i}\pi_y & 0 & 0 \\ \pi_x + \mathrm{i}\pi_y & 0 & 0 & 0 \\ 0 & 0 & 0 & \pi_x + \mathrm{i}\pi_y \\ 0 & 0 & \pi_x - \mathrm{i}\pi_y & 0 \end{pmatrix}, \tag{5}$$

where $\vec{\pi} = \vec{p} + e\vec{A}$ is the generalized momentum and $\vec{A}$ is the vector potential. In the above expression we disregard the spin of the electron, taking into account the fact that all energy levels obtained will have additional twofold degeneracy due to spin. For a single electron this degeneracy can be lifted by the Zeeman interaction.

The four-component wave functions corresponding to the Hamiltonian (5) have the form

$$\Psi = \begin{pmatrix} \Psi_{\mathrm{A}}^{\mathrm{K}} \\ \Psi_{\mathrm{B}}^{\mathrm{K}} \\ \Psi_{\mathrm{A}}^{\mathrm{K}'} \\ \Psi_{\mathrm{B}}^{\mathrm{K}'} \end{pmatrix}, \tag{6}$$

where $\Psi_{\mathrm{A}}^{\mathrm{K}}$ and $\Psi_{\mathrm{B}}^{\mathrm{K}}$ are envelope wavefunctions at A and B sites for the valley K, and $\Psi_{\mathrm{A}}^{\mathrm{K}'}$ and $\Psi_{\mathrm{B}}^{\mathrm{K}'}$ are envelope wavefunctions at A and B sites for the valley K′. For a magnetic field orthogonal to the graphene layer, the vector potential can be chosen in the Landau gauge, $\vec{A} = (0, Bx)$. Then the eigenfunctions of the Hamiltonian (5) are labelled by $(j, n, k)$. Here $j$=K, K′ is the valley index, which describes the valley pseudospin, $n = 0, \pm 1, \pm 2, \pm 3, \ldots$ is the Landau level index and $k$ is the wave vector along the $y$ axis. If we take into account the electron spin then we need to multiply the wavefunction (6) by the two-component spin function.

The Hamiltonian (5) can be easily diagonalized, which results in the discrete Landau energy level. The energies of the Landau levels depend only on the index $n$ and have the following form:

$$\varepsilon_n = \hbar\omega_B^{\mathrm{Dirac}}\,\mathrm{sgn}(n)\sqrt{|n|}, \tag{7}$$

where $\omega_B^{\mathrm{Dirac}} = \sqrt{2}v_{\mathrm{F}}/l_B$ and $l_B = \sqrt{\hbar/eB}$ is the magnetic length. The Landau level index, $n$, can be positive or negative. The positive values correspond to electrons (conduction band), while the negative values correspond to holes (valence band). This expression shows that, in contrast to the case of conventional 2DES, the Landau levels in graphene are not equidistant and the largest energy separation is between the zero and the first Landau level. The typical energy separation between the Landau levels in graphene achieved in experiments is much larger than the corresponding inter-level separation in normal 2D layers. For example, the energy difference between the lowest Landau levels ($n = 0$) and the next Landau levels ($n = \pm 1$) is $\Delta E \approx 400\,\mathrm{K}\sqrt{B(\mathrm{Tesla})}$, which for $B = 20$ Tesla is 1800 K. In what follows, we will see that such a large electron energy gap allows one to observe the quantum Hall effect in graphene, even at room temperature.

The wavefunctions corresponding to the Landau levels (7) are given by the following expressions [15,58]:

$$\Psi_{n,k}^{\mathrm{K}} = \frac{C_n}{\sqrt{L}}\exp(-\mathrm{i}ky)\begin{pmatrix} \mathrm{sgn}(n)(-\mathrm{i})\phi_{|n|-1,k} \\ \phi_{|n|,k} \\ 0 \\ 0 \end{pmatrix}, \tag{8}$$

for valley K and

$$\Psi_{n,k}^{\mathrm{K}'} = \frac{C_n}{\sqrt{L}}\exp(-\mathrm{i}ky)\begin{pmatrix} 0 \\ 0 \\ \phi_{|n|,k} \\ \mathrm{sgn}(n)(-\mathrm{i})\phi_{|n|-1,k} \end{pmatrix}, \tag{9}$$

for valley K′. Here $C_n = 1$ for $n = 0$, and $C_n = 1/\sqrt{2}$ for $n \neq 0$,

$$\phi_{n,k} = (2^n n!\sqrt{\pi}l_B)^{-\frac{1}{2}}\mathrm{e}^{-z^2/2}H_n[(x - kl_B^2)/l_B] \tag{10}$$

is the standard wavefunction for a non-relativistic electron at the $n$th Landau level, $H_n(x)$ are the Hermite polynomials, and

$$\mathrm{sgn}(n) = \begin{cases} 0 & (n = 0), \\ n/|n| & (n \neq 0). \end{cases} \tag{11}$$

In terms of the occupation of the sublattices A and B, the wavefunctions (8,9) have an interesting property. Specifically, the wavefunctions at Landau levels $n \neq 0$ always have non-zero amplitudes on both sublattices A and B, while the wavefunctions at the Landau level $n = 0$ have non-zero amplitude only on one sublattice: B sublattice for valley K or A sublattice for valley K′. This property of the wavefunctions of the Landau levels in graphene makes the $n = 0$ Landau level very special for different magnetic applications of graphene.

Taking into account the spin degree of freedom, we can conclude that each Landau level has fourfold degeneracy, which corresponds to twofold degeneracy due to spin and twofold degeneracy due to the valley, i.e. the *flavor* [59], or valley pseudospin [60]. The above description is a single-electron picture of pure graphene. In a many-electron system of real graphene the inter-electron interactions and disorder are important and can introduce splitting of the levels and lift their degeneracy. These topics will be discussed below.

In the presence of an uniform electric field, Lukose *et al.* [61] predicted that the Landau levels are profoundly modified, leading to a collapse of the spectrum when the value of the electric to magnetic field ratio exceeds a certain critical value.

Experimentally, the Landau levels in graphene have been observed by measuring cyclotron resonances of the electrons and holes in infrared spectroscopy experiments [34,62,63], and by measuring tunneling current in scanning tunneling spectroscopy experiments [64–66]. In infrared spectroscopy experiments the Landau level optical transitions were studied. There is a crucial difference between the Landau level optical transitions for non-relativistic electrons in conventional 2DES and relativistic electrons in graphene. For non-relativistic electrons there is the Kohn theorem, which states that the energy of Landau level transitions is equal to the cyclotron energy, regardless of the number of electrons (i.e. the filling factor of the Landau levels), and uninfluenced by the inter-electron interactions. The frequencies of all optical transitions in non-relativistic system are equal to the cyclotron frequency. In the graphene system the Kohn theorem [67] is not applicable. In this case, the frequencies of optical transitions are influenced by the interaction between electrons and the number of electrons, i.e. the filling factor. Since the Landau levels in graphene are not equidistant, all frequencies of optical transitions in graphene are different from each other. The cyclotron optical transitions in a graphene system are of two types: (i) intraband transitions, i.e. transitions between the electron (hole) states; (ii) interband optical transitions, i.e. transitions between the electron and hole states (conduction and valence bands). Since in graphene both conduction and valence bands have the same symmetry, the optical transition selection rule has the same form for both intra- and inter-band transition, and is given by the relation [63]

$$\Delta n = |n_2| - |n_1| = \pm 1. \tag{12}$$

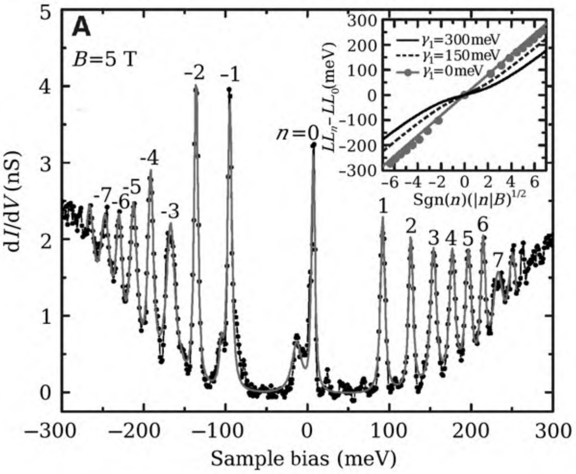

Figure 4. Direct measurement of Landau quantization in epitaxial graphene. Data points show the tunnelling differential conductance spectra versus sample bias of Landau levels in multilayer graphene at $B = 5$ Tesla. Landau level indices are marked. The grey line shows a fit to a series of Voigt line shapes at the Landau level peak positions. Inset: Landau level peak position versus square root of Landau level index and applied field from the peak position in A. Errors in peak positions are smaller than the symbol size (Reprinted figure with permission from D.L. Miller *et al.*, Science, 324, p. 924, 2009 [64]. Copyright © (2009) The American Association for Advancement of Science.).

For example, the allowed optical transitions (absorption) from the Landau level $n = -1$ are $n = -1 \rightarrow n = 0$ (intra-band transition) and $n = -1 \rightarrow n = +2$ (inter-band transition). In usual non-relativistic systems the selection rule for inter-band optical transitions is $n_1 = n_2$.

In scanning tunnelling spectroscopy experiments, the Landau levels are directly observed as the pronounced peaks in the tunnelling spectra [64–66]. From the positions of these peaks the energy of the Landau levels are directly extracted. In Figure 4, typical experimental results of scanning tunneling measurements are shown, where the peaks in the tunneling differential conductance reveal the positions of the Landau levels.

From the experimentally measured cyclotron resonances, the electron Fermi velocity has been obtained [34,62–66]. The electron velocity $v_F \approx 1.1 \times 10^6\,\mathrm{m\,s^{-1}}$ was obtained in [34,62–64], but a smaller value $v_F \approx 0.79 \times 10^6\,\mathrm{m\,s^{-1}}$ was reported in [65]. The reduction of $v_F$ in [65] was attributed to electron–phonon interaction due to strong coupling with the graphite substrate.

The effective-mass approximation of the electron dynamics in graphene in a uniform magnetic field is valid only at low energies, i.e. for low-lying Landau levels. The properties of higher Landau levels can be described within the tight-binding model [56,57]. The Hamiltonian of the tight-binding model has the following form:

$$\mathcal{H}_{\text{tight-binding}} = \sum \varepsilon_i c_i^\dagger c_i + \sum_{<i,j>} t_{ij} c_i^\dagger c_j, \tag{13}$$

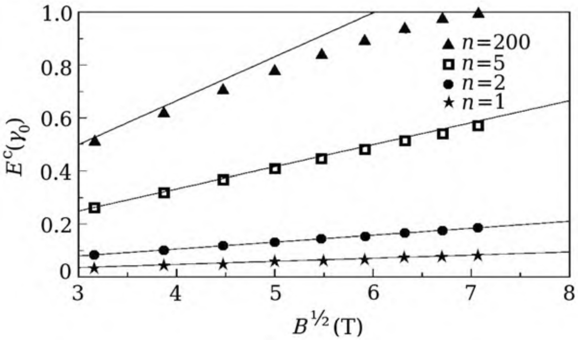

Figure 5. The variation of the low Landau-level energies with square root of magnetic field. The Landau-level energy are obtained within the effective-mass approximation (solid lines) and tight-binding model (symbols). Magnetic field is in Tesla (T) (Reprinted from Physica E, 40, J.H. Ho *et al.*, Landau levels in graphene, 1722–1725 [57]. Copyright © (2008), with permission from Elsevier.).

where $c_i$ is the electron annihilation operator. The magnetic field in the tight-binding model is incorporated through the Peierls substitution

$$c_i^\dagger c_j \to c_i^\dagger c_j \exp\left(\int_i^j \vec{A}\mathrm{d}\vec{r}\right). \tag{14}$$

The Landau levels within the tight-binding model have been obtained numerically [56,57]. The results of the calculations show that the effective-mass approximation is valid at low energies, $\varepsilon \lesssim 1\,\mathrm{eV}$, but at higher energies there are deviations from Equation (7). For example, at $B=30$ Tesla the deviation from Equation (7) occurs at the Landau level $n=5$ (Figure 5). At high energies the magnetic field also affects the degeneracy of the levels [57]. For example, at energies $\varepsilon \gtrsim 2.5\,\mathrm{eV}$ the valley degeneracy is lifted, resulting in twofold (spin only) degeneracy of the Landau levels.

The non-linear features of the energy dispersion law in graphene have been studied experimentally by magneto-optical transmission spectroscopy [68]. The graphene system has been studied in magnetic fields up to 32 Tesla and within the energy range from the far infrared to the visible. It was found that the low-energy part of the energy spectrum is well described by the linear relativistic equation, while at energies higher than 0.5 eV the deviation from the linear dispersion was observed. For example, at the highest studied energy of 1.25 eV, the deviation from the linear dispersion is around 40 meV.

The parameter which controls the magnetoelectronic properties of graphene within the tight-binding model is the magnetic flux passing through a hexagonal ring of the graphene lattice [69]. As a function of this flux the energy dispersion, the density of states, and magnetoabsorption spectra all have the oscillating behavior [69]. The lattice model of graphene in a magnetic field, introduced beyond the Peierls substitute, was studied in [70,71]. Taking into account the higher order magnetic terms, i.e. the diamagnetic shift and shrinkage of the wave functions, in the lattice Hamiltonian these authors found lifting of two-fold degeneracy of the lowest Landau levels in high magnetic fields.

## 2.2. *Anomalous quantum Hall effect*

### 2.2.1. *Experimental observation of the quantum Hall effect in graphene*

Just as for the conventional non-relativistic electron systems [72,73], the Landau quantization of the energy levels in graphene results in the quantization of the Hall conductance, i.e. the quantum Hall effect. In the quantum Hall effect regime, the Hall conductance exhibits a plateau when the Fermi energy, $E_F$, falls between the Landau levels. Every time the Fermi energy crosses a Landau level, the Hall conductance, $\sigma_{xy}$, jumps by an amount of $g_s\, e^2/h$, where $g_s$ is the degeneracy of the Landau level. In graphene, each Landau level has fourfold degeneracy due to valley and spin, i.e. $g_s = 4$. Based on this simple picture of the quantum Hall effect, we expect that the Hall conductance in graphene should show plateaus at $\sigma_{xy} = (4e^2/h)N$, where $N$ is an integer. It so happens that the unique properties of the lowest Landau level ($n = 0$) introduces a shift in quantization of the Hall conductance. This shift is related to the electron–hole symmetry of the graphene layer. The Landau level with $n = 0$ is robust, i.e. it has zero energy regardless of the value of the magnetic field, and it has the properties of both electrons and holes. This quantum anomaly of the $n = 0$ Landau level makes this level effectively twofold degenerate for electrons and twofold degenerate for holes [74]. As a result, the quantization of the Hall conductance occurs at half-integer values

$$\sigma_{xy} = (4e^2/h)\left(N + \frac{1}{2}\right). \tag{15}$$

The half-integer (or anomalous) quantum Hall effect corresponds to the filling factors $\nu = 4(N + \frac{1}{2}) = \pm 2, \pm 6, \pm 10, \ldots$. This sequence of filling factors is different from that of the conventional semiconductor quantum Hall effect (where the plateaus are at $\nu = \pm 4, \pm 8, \pm 12, \ldots$) and this anomalous behavior gives the phenomenon its name (see, e.g. [75]). This quantization rule can be derived from the Kubo formalism [76–79] applied to relativistic electrons in graphene [74,80–82]. The half-integer quantum Hall effect has been observed experimentally [17,83–85]. The typical experimental results for the magnetoresistance and Hall resistance are shown in Figure 6. The Hall resistance shows plateaus at filling factors $\nu = 4(N + \frac{1}{2})$, while the magnetoresistance vanishes. A good quality sample studied in [85] (mobility of electrons was higher than $10^4\,\mathrm{cm^2\,V^{-1}\,s^{-1}}$) allows one to observe plateaus at large filling factors. The quantum Hall effect is clearly seen at filling factors $\nu = \pm 2$ and $\nu = \pm 6$. A developing plateau at $\nu = 10$ is also visible.

An important breakthrough has occured recently. The quantum Hall effect has been observed in epitaxial graphene layers grown on silicon carbide [86,87], thus illustrating the similarity of fundamental electronic properties of epitaxial and exfoliated graphene films. The growth conditions and electrical characteristics of epitaxial graphene films strongly depend on the type of the face of SiC. The growth of graphene on the C-face is rapid and results in graphene films with high mobility around $20{,}000\,\mathrm{cm^2\,V^{-1}s^{-1}}$ [86]. The formation of graphene films on the Si-face is slower and can be easily controlled, but the mobility of the carrier is much smaller with the typical value around $1500\,\mathrm{cm^2\,V^{-1}\,s^{-1}}$. For the high-mobility epitaxial graphene on the C-face, the quantum Hall plateaus corresponding to filling factors $\nu = 2, 6, 10$, and 14 have been observed [86]. For low-mobility epitaxial graphene

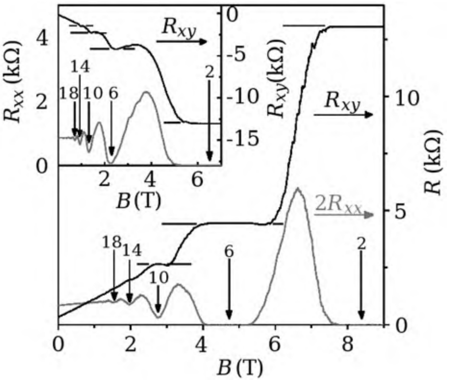

Figure 6. Hall resistance ($R_{xy}$) and magnetoresistance ($R_{xx}$) versus the magnetic field at $T = 30$ mK. The vertical arrows and the numbers on them indicate the values of the corresponding filling factor, $\nu$, of the quantum Hall state. The horizontal lines correspond to $h/e^2\nu$ values. The inset shows the quantum Hall effect for a hole gas, measured at 1.6 K (Reprinted with permission from Y. Zhang *et al.*, Nature, 438, p. 201, 2005 [85]. Copyright © (2005) Nature Publishing Group.).

grown on the Si-face, only the lowest quantum Hall effect with filling factors $\nu = 2$, 6, and 10 have been reported [87]. These results bring epitaxial graphene a step closer to becoming a scalable platform for graphene-based electronics.

One important difference between the quantum Hall effect in graphene and that in usual non-relativistic systems is that the quantum Hall effect in graphene survives even at room temperature [83,84,88]. The reason for such robust behavior of the quantum Hall states is the large activation energy, i.e. the cyclotron energy. For example, at $B = 45$ Tesla the energy gap is 2800 K, which exceeds the thermal energy at room temperature by a factor of 10. The quantum Hall effect has been observed at room temperatures even in a sample with low mobility, $\mu = 4000\,\mathrm{cm}^2\,\mathrm{V}^{-1}\,\mathrm{s}^{-1}$ [83]. These properties of the quantum Hall effect in graphene are in stark contrast to what we have seen in non-relativistic systems, where the quantum Hall effect can be realized only at low temperatures and in samples with high electron mobility.

In [89,90] the activation energies of the quantum Hall states have been extracted from the Arrhenius plots (temperature dependence). The excitation gaps for $\nu = \pm 2$ and $\nu = 6$ quantum Hall states have been analyzed. The excitation gaps are affected by the Landau level broadening, which depends on the magnetic field and the strength of the disorder. Without any Landau level broadening the excitation gaps are equal to the energy gaps between the nearest sharp Landau levels. The broadening of the Landau levels introduces a constant offset of the excitation gaps from the theoretical value for the sharp Landau levels (Figure 7). For the quantum Hall state at $\nu = 6$, the experimental results are consistent with the picture of broad Landau levels with the broadening around 400 K. The $\nu = \pm 2$ gap, however, behaves totally differently. For example, at a high magnetic field the $\nu = \pm 2$ gap, approaches the bare Landau-level separation. This behavior can only be explained by the unique nature of the $n = 0$ Landau level: with increasing magnetic field the $n = 0$ Landau level becomes very sharp. The density of states, which illustrates the sharp nature of the $n = 0$ Landau level, is shown schematically in Figure 7.

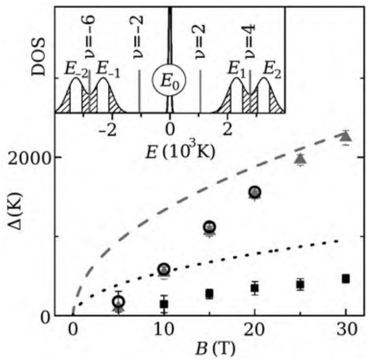

Figure 7. Energy gap between two Landau levels as a function of magnetic field for $\nu = 2$ (full triangles), $\nu = -2$ (open circles), and $\nu = 6$ (full squares) as deduced from the Arrhenius plots. The dashed and dotted lines are the expected (theoretically) energy gaps for sharp Landau levels. The inset shows schematically the density of states for a sharp $n = 0$ Landau level and broadened higher Landau levels for electrons and holes at 30 Tesla. The form and width of the higher Landau levels were extracted from the experimental data. Extended states are represented by the white areas, localized states by the dashed areas (Reprinted figure with permission from A.J.M. Giesben *et al.*, Physical Review Letters, 99, 206803, 2007 [89]. Copyright © (2007) by the American Physical Society.).

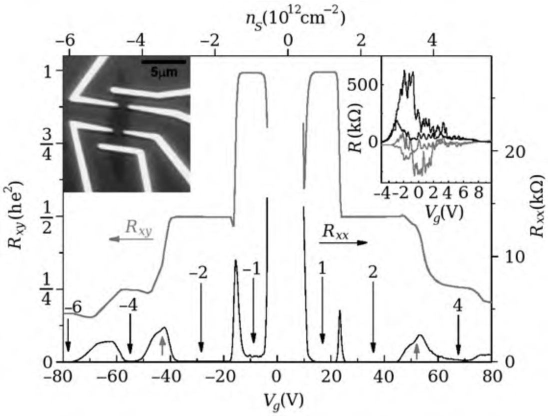

Figure 8. $R_{xx}$ and $R_{xy}$ measured in the device shown in the left inset, as a function of gate voltage, $V_g$, at $B = 45$ T and $T = 1.4$ K. $-R_{xy}$ is plotted for $V_g > 0$. The numbers with the vertical arrows indicate the corresponding filling factor, $\nu$. Gray arrows indicate developing quantum Hall states at $\nu = \pm 3$. $n_s$ is the sheet carrier density derived from the geometric consideration. Right inset: $R_{xx}$ and $R_{xy}$ or another device measured at $B = 30$ T and $T = 1.4$ K in the region close to the Dirac point. Left inset: an optical microscope image of a graphene device used in this experiment (Reprinted figure with permission from Y. Zhang *et al.*, Physical Review Letters, 96, 136806, 2006 [92]. Copyright © (2006) by the American Physical Society.).

At large magnetic fields, $B > 20$ Tesla, and in high-mobility samples (mobility as high as $5 \times 10^4$ cm$^2$ V$^{-1}$s$^{-1}$), new quantum Hall plateaus at filling factors $\nu = 0, \pm 1, \pm 4$ have been reported in the literature [86,91,92]. The new quantum Hall plateaus are shown in Figure 8 with clear quantization of the Hall resistance and vanishing

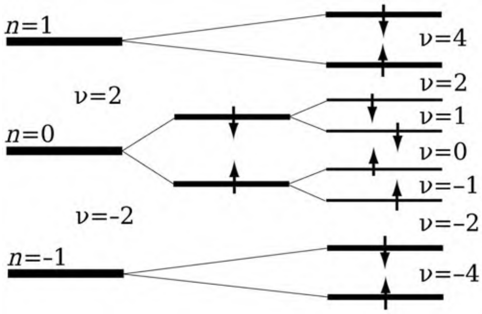

Figure 9. Schematic illustration of the hierarchy of the lifting the degeneracy of the Landau levels in strong magnetic fields. Here $n$ is the Landau level index and $\nu$ describes the corresponding quantum Hall effect. The arrows next to the lines illustrate the direction of the spin at the corresponding energy levels. The fourfold degeneracy of the Landau level $n=0$ is completely lifted. For the $n=\pm 1$ Landau levels only the twofold spin degeneracy is lifted and each level remains twofold valley degenerate.

magnetoresistance. Such plateaus originate from lifting of the fourfold degeneracy of the Landau levels. The quantum Hall effect at $\nu=0, \pm 1$ indicates that the fourfold degeneracy of the Landau level $n=0$ is completely lifted [86,91,92], so that the Hall conductance, $\sigma_{xy}$, increases in steps of $e^2/h$ as the Fermi level passes through the Landau levels. The fact that only $\nu=\pm 4$ quantum Hall plateaus are observed means that the fourfold degeneracy of the Landau levels $n=\pm 1$ is only partially resolved. The experiments in a tilted magnetic field [86,92] show that for the Landau level $n=1$ the twofold spin degeneracy is lifted, leaving the twofold valley degeneracy unbroken.

To distinguish the origin of the broken symmetry (either spin or valley), experiments in a tilted magnetic field have been performed [91]. The spin splitting, which is related to the Zeeman energy, depends on the total magnetic field, while the valley (sublattice) splitting depends only on the perpendicular component of the magnetic field. This is because the valley splitting is caused by the electron–electron interaction and the corresponding ground state is the valley ferromagnet (see the next section). The results of magnetotransport measurements show that the minimum magnetoresistance, which is determined by the inter-level splitting, depends on the total magnetic field for $\nu=\pm 4$, and depends on the perpendicular component of the magnetic field for $\nu=\pm 1$ [91]. These results show that the states $\nu=0$ and $\nu=\pm 1$ arise from the lifting of the spin and valley degeneracy of the Landau level $n=0$, respectively [91]. The order of the lifting of the degeneracy of the Landau levels $n=0$ and $n=\pm 1$ in graphene is illustrated in Figure 9.

Although the behavior of the Hall conductance, $\sigma_{xy}$, is consistent with the lifting of the degeneracy of the Landau level $n=0$, the properties of the magnetoresistance, $R_{xx}$, are unexpected. For the usual quantum Hall effect in non-relativistic systems the magnetoresistance, $R_{xx}$, shows a minimum at the quantum Hall plateaus and activated behavior as a function of temperature. Such a behavior is observed in graphene for $\nu=\pm 1$ Hall states, but the $\nu=0$ Hall state does not show the minimum resistance [91]. There is also no activated behavior at $\nu=0$. In Figure 10 the magnetoresistance of a graphene sample is shown for three values of magnetic field.

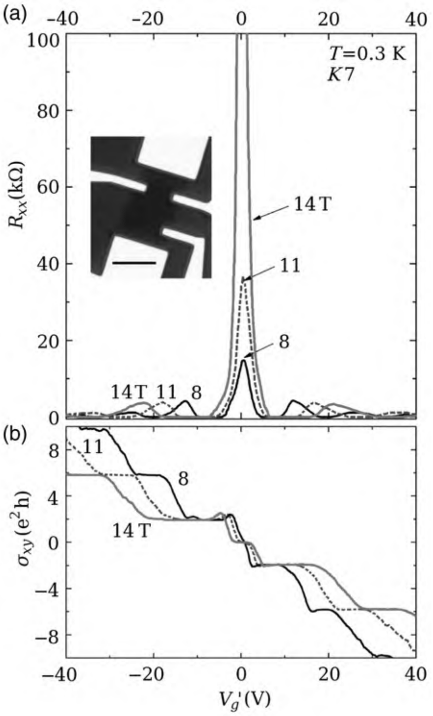

Figure 10. The magnetoresistance $R_{xx}$ (a) and Hall conductivity $\sigma_{xy}$ (b) versus gate voltage, $V'_g$, at 0.3 K with the magnetic field fixed at 8, 11, and 14 T. Peaks of $R_{xx}$ at finite gate voltage correspond to the filling of the $n=1$ and $n=2$ Landau levels. At zero bias voltage the peak in $R_{xx}$ grows to 190 $k\Omega$ at 14 Tesla. The inset shows the sample with Au leads deposited. The bar indicate 5 μm. Panel (b) shows the quantization of Hall conductance at the values $(4e^2/h)(n+\frac{1}{2})$. At 0.3 K, $\sigma_{xy}=0$ in a 2-V interval around $V'_g=0$ (Reprinted figure with permission from J.G. Checkelsky *et al.*, Physical Review Letters, 100, 206801, 2008 [93]. Copyright © (2008) by the American Physical Society.).

The magnetoresistance maximum (not minimum) is clearly seen at zero filling factor (zero bias).

The $\nu=\pm1$ are the usual quantum Hall states with a minimum resistance and activation behavior. The activation energy at $\nu=\pm1$ has a non-linear magnetic field dependence, which was attributed to the many-body effects indicating a many-body origin of the $\nu=\pm1$ states [91].

A detailed analysis of the $\nu=0$ quantum Hall state has shown that this state can be in two phases: metallic or insulating, which are characterized by finite and infinitely large values of the magnetoresistance, $R_{xx}$ [93,94], respectively. The transition from the metallic to the insulating phase occurs with increasing magnetic field at some critical value $B_c$. In all samples studied in [94] the critical magnetic field is around $B_c \approx 30$ Tesla. The actual value of the critical magnetic field depends on the disorder strength in a non-trivial way, namely, with increasing disorder the critical magnetic field increases [94]. The phase transition of the $\nu=0$ quantum Hall state was identified as the Berezinskii–Kosterlitz–Thouless phase transition, for which the magnetic field plays the role of the effective temperature. In two-dimensional systems such a transition is described by the XY model. Within this model the ordered phase is destroyed at the transition point by unbinding of pairs of topological excitations, the corresponding separation (correlation length), $\xi$, depends on the deviation of the magnetic field (effective temperature) from the critical value in the following form:

$$\xi = a \exp[b/\sqrt{1 - B/B_c}], \tag{16}$$

where $a$ is the lattice constant and $b$ is a number of the order 1. The expression (16) fits the experimental data [94], which indicates that at $\nu = 0$ the system shows the Berezinskii–Kosterlitz–Thouless phase transition to a high-field insulating ordered state.

Recent experiments performed in ultraclean suspended graphene samples [95,96] illustrate an insulating nature of the $\nu = 0$ quantum Hall state. The device is fully insulating at high magnetic fields ($B > 5$ Tesla) and at low temperature ($T < 10\,\mathrm{K}$), while at higher temperature the system shows an activated behavior with an energy of 60 K [96]. The distinctive features of the suspended graphene compared to the graphene on substrate are very high quality of graphene samples and enhanced inter-electron interaction strength. The enhancement of the electron–electron interactions is due to the small value of dielectric constant ($\epsilon = 1$) of suspended graphene.

A strong increase in low-temperature resistivity, $\rho_{xx}$, in graphene samples with a relatively large amount of disorder have been observed in [97]. In terms of the conductivity, the graphene system at the charge neutrality point has shown a zero-value plateau in the Hall conductivity, $\sigma_{xy}$, and a minimum in the longitudinal conductivity, $\sigma_{xx}$. Such a behavior was explained in [97] as due to opening of a gap, e.g. due to the Zeeman splitting, in the density of states at the $n = 0$ Landau level. Due to the presence of large disorder, the opening of the gap was observed only for the $n = 0$ Landau level, for which the width of the Landau level is much smaller compared to that in higher Landau levels.

### 2.2.2. *Symmetry breaking: theoretical models*

Experimental observation of the $\nu = 0, \pm 1, \pm 4$ quantum Hall effect opens the question of a mechanism of a symmetry breaking in graphene, which results in lifting of the degeneracy of the Landau levels and the additional quantum Hall plateau. The problem of symmetry breaking in graphene systems in a magnetic field has been studied theoretically in detail [59,75,98–111]. A review of the different aspects of spontaneous symmetry breaking in graphene is available in [107]. Here we discuss only the main mechanisms of symmetry breaking and lifting of the Landau level degeneracy in graphene. In general, the following mechanisms can break the symmetry in graphene quantum Hall systems: (i) disorder can lift the twofold valley degeneracy. (ii) Electron–electron interactions can lift both valley and spin degeneracies. For example, the exchange part of the electron–electron interaction favors the quantum Hall ferromagnetic state. (iii) Zeeman interaction, which is an explicit symmetry breaking term in the Hamiltonian. The Zeeman interaction can lift only the spin degeneracy. (iv) Explicit terms in the Hamiltonian, which can lift the valley symmetry. These terms originate from the graphene lattice structure.

### 2.2.3. *Symmetry breaking: disorder effects*

Within the noninteracting electron system the main mechanism of symmetry breaking is the interaction with the disorder potential, which introduces the intervalley coupling and splits the valley subbands. Such a potential should be short-ranged with the length scale of the order of the lattice constant [75,105]. An example of a short-range potential is a scatterer localized at a particular A or B site with a random amplitude. Such a potential introduces the following term into the relativistic Hamiltonian (5)

$$U(r) = \begin{pmatrix} 1 & 0 & z_{\mathrm{A}}^{*} z_{\mathrm{A}}' & 0 \\ 0 & 0 & 0 & 0 \\ z_{\mathrm{A}}'^{*} z_{\mathrm{A}} & 0 & 1 & 0 \\ 0 & 0 & 0 & 0 \end{pmatrix} u_s \delta\left(\vec{r} - \vec{R}_{\mathrm{A}}\right) + \begin{pmatrix} 0 & 0 & 0 & 0 \\ 0 & 1 & 0 & z_{\mathrm{B}}^{*} z_{\mathrm{B}}' \\ 0 & 0 & 0 & 0 \\ 0 & z_{\mathrm{B}}'^{*} z_{\mathrm{B}} & 0 & 1 \end{pmatrix} u_s \delta\left(\vec{r} - \vec{R}_{\mathrm{B}}\right), \tag{17}$$

where $z_X = \mathrm{e}^{\mathrm{i}\vec{K}\vec{R}_X}$, $z'_X = \mathrm{e}^{\mathrm{i}\vec{K}'\vec{R}_X}$, $X = \mathrm{A}$, B and $u_s = (\sqrt{3}a^2/2)U_s$, $U_s$ is the random amplitude of the on-site potential. The first and second terms in Equation (17) correspond to the scatterer on sites A and B, respectively (Figure 11).

It is easy to see that the short-range potential (17) has very different effects on the lowest Landau level, $n = 0$, and on higher Landau levels, $|n| > 0$. Indeed, the amplitudes of the wavefunctions in the $n = 0$ Landau level is non-zero only on one

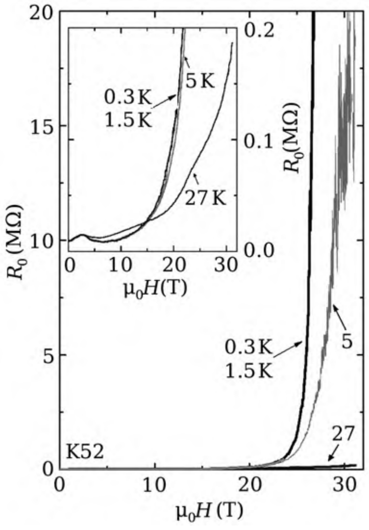

Figure 11. Main panel: divergence of the maximum magnetoresistance, $R_0$, at the Dirac point with $B$ at $T = 0.3$, 1.5, 5, and 27 K. At 27 K, the increase in $R_0$ is quite moderate (to 190 $k\Omega$ at $H = 31$ Tesla). At $T = 0.3$ K, however, $R_0$ exceeds 20 $M\Omega$ above 27 T. The curves at 0.3 and 1.5 K undergo a 1000-fold increase (40 $k\Omega$ to 40 $M\Omega$) in the narrow field interval $17 - 27$ T. In high $B$, the 5 K curve deviates significantly from them. The inset shows the behavior of $R_0$ versus $B$ in greatly expanded scale (×100) (Reprinted figure with permission from J.G. Checkelsky *et al.*, Physical Review B, 79, 115434, 2009 [94]. Copyright © (2009) by the American Physical Society.).

of the sublattices, either A or B. As a result the intervalley matrix element of the potential (17) is zero for the states of the lowest Landau level, $n=0$. Therefore, if the Landau level mixing is disregarded then the random on-site (short-range) potential does not lift the valley degeneracy for the $n=0$ Landau level [105]. For higher Landau levels even the on-site potential introduces intervalley coupling, which results in lifting of the valley degeneracy. If the Landau level mixing is taken into account then even at the lowest Landau level, the short-range potential introduces the intervalley coupling [75].

Disorder-induced intervalley coupling and mixture in the lowest Landau level results also in anomalous electron localization properties [110]: increasing the strength of the on-site random potential introduces *delocalization*, instead of localization in the lowest Landau level. This anomalous behavior is closely related to the Landau level mixing and it is correlated with the disorder-induced valley depolarization of the Landau level states [110] due to mixing of the valleys.

In the lowest Landau level, the intervalley coupling can be introduced even without the Landau level mixing through the randomness in the hopping intergral between two neighboring sites [104,105,112]. Such randomness can be realized through the local lattice distortion or due to scatterers localized between the neighboring sites. The shift from $t$ to $t+\delta t$ in the hopping integral between the neighboring atoms at sites A and B results in the following potential term in the relativistic Hamiltonian [105]

$$U(r)=\begin{pmatrix} 0 & z_{\mathrm{A}}^{*}z_{\mathrm{B}} & 0 & z_{\mathrm{A}}^{*}z'_{\mathrm{B}} \\ z_{\mathrm{B}}^{*}z_{\mathrm{A}} & 0 & z_{\mathrm{A}}^{*}z'_{\mathrm{A}} & 0 \\ 0 & z_{\mathrm{A}}^{\prime *}z_{\mathrm{B}} & 0 & z_{\mathrm{A}}^{\prime *}z'_{\mathrm{B}} \\ z_{\mathrm{B}}^{\prime *}z_{\mathrm{A}} & 0 & z_{\mathrm{B}}^{\prime *}z'_{\mathrm{A}} & 0 \end{pmatrix} u_h\delta(\vec{r}-\vec{r}_i), \tag{18}$$

where $u_h=(\sqrt{3}a^2/2)\delta t$. It is easy to see that even in the lowest Landau level the intervalley matrix elements are non-zero.

The randomness in intervalley hopping integrals can be reformulated in terms of an effective random magnetic field [104]. If the variations of the hopping integrals between the site $j$ and the nearest neighbor sites (there are three such sites) are $\delta t_i$, $i=1,2,3$, then a vector potential for valleys K and K′ at point $j$ is [104]

$$a_X=\frac{c}{e}\sum_{i=1,2,3}\delta t_i \mathrm{e}^{\mathrm{i}\vec{X}\vec{e}_i}, \tag{19}$$

where $X=\mathrm{K}$ or $\mathrm{K}'$. Such a vector potential introduces a random magnetic field, $\delta h$, pointing in the $z$ direction (orthogonal to the graphene layer), which results in a Zeeman-like interaction for the pseudospin order parameter. The typical fluctuation of the random magnetic field is around 0.1–1 Tesla [104]. Although the weak random magnetic field, $\delta h$, is orthogonal to the graphene plane, it produces an easy-plane anisotropy which favors the XY valley ferromagnetic state [104]. The XY ferromagnetic system shows the Berezinskii–Kosterlitz–Thouless transition to the ordered state. Due to the valley anisotropy-induced random magnetic field, the twofold valley degeneracy of the Landau level is lifted. The Zeeman energy lifts the twofold spin degeneracy. Taking into account both the effective random magnetic field and the Zeeman interaction, we obtain a complete lifting of the fourfold degeneracy of the Landau level. In the lowest Landau level the valley anisotropy induced by the random magnetic field is around few degrees of Kelvin at an uniform magnetic field of 30 Tesla, while the Zeeman splitting at $B = 30$ Tesla is around 50 K. This energy scale is consistent with the hierarchy of lifting the degeneracy of the $n = 0$ Landau level, as shown in Figure 9. Therefore the $\nu = 1$ quantum Hall state is valley and spin polarized while the $\nu = 0$ state is spin-polarized and valley-unpolarized.

The disorder in graphene not only results in valley symmetry breaking but also destroys the quantum Hall effect as in non-relativistic systems. The effect of disorder on the existence of the quantum Hall states and electron localization in a strong magnetic field has been studied numerically within the tight-binding model with random on-site potential [99,106,110]. The corresponding Hamiltonian has the following form:

$$\mathcal{H}_{\text{tight-binding}} = \sum \varepsilon_i c_i^\dagger c_i + t \sum_{<i,j>} c_i^\dagger c_j, \tag{20}$$

where the hopping integral $t$ is assumed to be constant and the disorder is introduced through the randomness in the values of the on-site energies, $\varepsilon_i$. In this approach, the mixing between the Landau levels is taken into account automatically and the intervalley coupling is introduced for all Landau levels. It was found that the most robust quantum Hall state against the disorder strength is the $\nu = \pm 2$ state [99] for a system without symmetry breaking and the $\nu = \pm 1$ state [106] for a system with lifted degeneracy of the Landau levels.

### 2.2.4. *Symmetry breaking: the effect of electron–electron interaction*

The disorder potential does not affect the twofold spin degeneracy. The simplest mechanism of breaking the spin symmetry is the Zeeman interaction, $g\mu_B B$, which splits the single particle spin levels. The $g$-factor of electrons in graphene is close to 2, resulting in the Zeeman energy $g\mu_B B \approx 1.5B$[Tesla] K. Another mechanism of breaking the spin symmetry is related to the long-range Coulomb interaction through the formation of the ferromagnetic state [59,98,101,103,106]. The quantum ferromagnetic state is stabilized by the exchange part of the Coulomb interaction. This symmetry breaking mechanism works well for both spin and valley symmetries.

In the case of the valley symmetry the Coulomb interaction Hamiltonian has also explicit lattice symmetry-breaking terms [59,101,103]. These terms can be obtained from the exact expression for the Coulomb repulsion Hamiltonian within the lattice model

$$\mathcal{H}_S = \frac{1}{2} \sum_{\vec{x}, \vec{x}'} V(\vec{x} - \vec{x}') n_x n_{x'}, \tag{21}$$

where $V(r)$ is the Coulomb interaction potential and $n_x$ is the total electron number operator. Rewriting the above expression in the continuum approximation, one can obtain the following terms in the interaction Hamiltonian in a continuum theory [59,103]:

(i) SU(4) spin and valley symmetric Hamiltonian, $\mathcal{H}_S$.

$$\mathcal{H}_S = \frac{1}{2}\int d^2\vec{x}d^2\vec{x}'\rho_{\text{total}}(\vec{x})V(\vec{x}-\vec{x}')\rho_{\text{total}}(\vec{x}'), \tag{22}$$

where $\rho_{\text{total}}$ is the total electron density operator.

(ii) Valley symmetry breaking term, $\mathcal{H}_{BS,1}$, is due to backscattering processes and has the following form [59,103]:

$$\mathcal{H}_{BS,1} = -u_2\Big[J_+^\dagger J_+ + J_-^\dagger J_-\Big], \tag{23}$$

where $u_2 \approx (4/3)a^2(e^2/4\pi\epsilon a_0)$, $J_+ = \psi^\dagger_{\mathrm{K,A}}\psi_{\mathrm{K}',B}$ and $J_- = \psi^\dagger_{\mathrm{K,B}}\psi_{\mathrm{K}',\mathrm{A}}$. Here $_{X,A}$ and $\psi_{X,B}$ are annihilation operators for valley $X = \mathrm{K}, \mathrm{K}'$ corresponding to sublattices A and B, respectively.

(iii) Valley symmetry breaking term, $\mathcal{H}_{BS,2}$, reflects the lattice-scale physics [59,103]. These terms originate from the fact that the two sublattices are shifted with respect to each other. As a result, two electrons at the same continuous point interact stronger if they belong to the same sublattice than if they belong to different sublattices. This symmetry breaking term has the following form:

$$\mathcal{H}_{BS,2} = -\int d^2\vec{x}\sum_{\vec{r}} v_1(\vec{r})\rho_{\text{stag}}(\vec{x}+\vec{r})\rho_{\text{stag}}(\vec{x}). \tag{24}$$

Here $\vec{r}$ corresponds to the positions of sites of one of the sublattice, $\rho_{\text{stag}}$ is the staggered electron density between sublattices A and B [59,103] and

$$v_1(\vec{r}) = \frac{\sqrt{3}a^2}{8}\Big[V(\vec{r}+1/\sqrt{3}\hat{y}) - V(r)\Big], \tag{25}$$

for $r \neq 0$. This symmetry breaking term is algebraically small and is of the order of $(a/l_B)$ compared to the Coulomb energy, $(e^2/\epsilon l_B)$ [59,101,103], where $a$ is the lattice constant in graphene. This lattice symmetry breaking term can also be understood in terms of the analogy of the two valley system and the usual bilayer non-relativistic electron system. Here each layer corresponds to a single valley, and the distance between the layers is of the order of the lattice constant, $a$. Therefore, the asymmetry is controlled by the small parameter $a/l_B \sim 0.03$ at $B \approx 30$ Tesla. The interaction described by the Hamiltonian $\mathcal{H}_{BS,2}$ is short-ranged, but one should be careful when dealing with the lowest Landau level, $n = 0$. As we discussed in the previous section, at the lowest Landau level the short-range interaction does not introduce the intervalley coupling, i.e. the intervalley matrix element is zero. Therefore, when considering the lowest Landau level the finite range of the interaction potential $v_1$ should be taken into account. As a result, the valley symmetry breaking term becomes additionally suppressed by a factor of $a/l_B$ in the lowest Landau level [59,103]. There are also interaction-induced umklapp scattering processes, which also introduce the valley symmetry breaking terms. These processes are exponentially small in $a/l_B$ and are considered in [101].

The SU(4) symmetric interaction Hamiltonian (22) results in spin and valley ferromagnetic ordering, i.e. spontaneous symmetry breaking at corresponding Landau filling factors [98,106]. The direction of spin or pseudospin ordering in the quantum ferromagnetic state is determined by small explicit symmetry breaking terms in the Hamiltonian. Such symmetry breaking terms can result in easy axis or easy plane ferromagnetic states with ferromagnetic order perpendicular or parallel to the graphene layer, respectively [59,103]. In the case of spin, the explicit symmetry breaking term is the Zeeman Hamiltonian, which results in easy axis ferromagnetic ordering.

For valley pseudospin we need to consider the lattice-related symmetry breaking Hamiltonians (23), (24). It was shown that at odd filling factors the symmetry breaking Hamiltonian (24) provides the leading symmetry breaking interaction. This type of Hamiltonian results in easy axis valley ferromagnetic state at the lowest Landau level ($\nu = \pm 1$ quantum Hall states) and easy plane ferromagnetic state at the Landau level $n = \pm 1$ ($\nu = 3$ and 5 quantum Hall states) [59,103]. The explicit numerical analysis of a finite electron system within the tight-binding model with Coulomb interaction supports this conclusion [106].

The easy axis valley ferromagnetic state at $n = 0$ Landau level ($\nu = \pm 1$) means that all electrons at filling factor $\nu = 1$ occupy one valley only:

$$|\nu = -1\rangle = \prod_m c^\dagger_{\uparrow \mathrm{K}, m} |\mathrm{vac}\rangle. \tag{26}$$

Since the wavefunctions of a single valley at $n = 0$ Landau level occupy only one sublattice, the easy axis valley ferromagnetic ordering means that the electrons reside on one sublattice producing a charge density wave. For the easy plane ferromagnetic state realized at $\nu = 3$ and $\nu = 5$ the Berezinskii–Kosterlitz–Thouless transition is expected [59,103]. The effect of the symmetry breaking Hamiltonian (23) has been studied in [101]. It was shown that this type of valley symmetry breaking term results in easy-plane valley ferromagnetic ordering.

Disorder suppresses the exchange ferromagnetic ordering and there is a critical disorder strength above which the corresponding quantum Hall effect is destroyed. A numerical analysis of the tight-binding model of graphene in a strong magnetic field shows that the critical disorder strength for the $\nu = 3$ ferromagnetic state ($n = 1$ Landau level) is much smaller than the critical disorder strength for the $\nu = 1$ state ($n = 0$ Landau level). A similar conclusion was reached in [98] using the Stoner criterion for the formation of quantum Hall ferromagnetism. In [98] the inter-electron interaction was treated within the Hartree–Fock approximation and the disorder was introduced within the self-consistent Born approximation. Within this approach the phase diagram (Figure 12), illustrating the sensitivity of quantum Hall states to the strength of the disorder, was obtained [98].

The stability of exchange-induced ferromagnetic ordering is determined by the strength of inter-electron interactions. Without the disorder the inter-electron interactions completely characterize the energy. Formation of the ferromagnetic ordering within the finite-size system has been studied numerically in [113], where only the spin degree of freedom was taken into account. For the Landau levels $n = 0$, 1, 2, and 3 the formation of spin-ordered states, i.e. ferromagnetic states, for a partially occupied Landau level, the corresponding filling factor $\frac{1}{2}$ has been obtained.

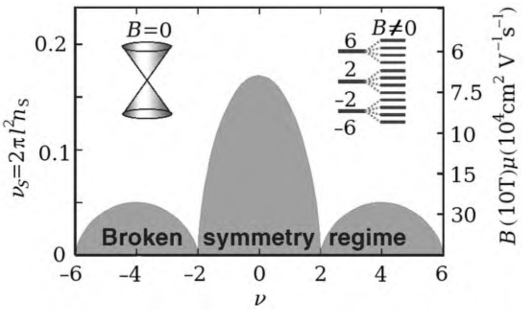

Figure 12. Phase diagram for SU(4) quantum Hall ferromagnetism in the $n=0$ and $n=1$ Landau levels of graphene. The ordered region is bounded by a maximum value of $\nu_s$, the ratio of the density of Coulomb scatterers to the density of a full Landau level. $\nu_s$ is inversely proportional to the product of the sample mobility and the external field strength and order near integer filling factors requires the minimum values for this product indicated on the right-hand vertical axis (Reprinted figure with permission from K. Nomura and A.H. MacDonald, Physical Review Letters, 96, 256602, 2006 [98]. Copyright © (2006) by the American Physical Society.).

For each quantum Hall state, both the ground state Coulomb energy and the activation gaps have been found. The activation gap is one of the important parameters, which characterizes the stability of the corresponding quantum Hall state with respect to disorder and temperature. Due to the unique structure of the Landau wavefunctions in graphene, the interaction-induced activation energy of the spin-ordered states is largest for the $n=1$ Landau level. These results illustrate that the electron correlations are dominant for the $n=1$ Landau level and the ferromagnetic ordered quantum Hall state should be the most stable. This behavior is different from the non-relativistic system, where the largest excitation gap is expected in the lowest Landau level.

The charged excitations of the quantum ferromagnetic states are skyrmions, which are similar in structure to the skyrmionic states in usual multi-component non-relativistic systems. The properties of skyrmions at the *n*th Landau level are determined by the relative strength of the Coulomb interaction within the *n*th Landau level and a symmetry breaking term, e.g. the Zeeman coupling. The interaction within that Landau level is obtained from the expression (22) by taking the projection of the Hamiltonian $\mathcal{H}_S$ onto the *n*th Landau level. Due to the special structure of the wavefunctions belonging to different Landau levels (Equations (8) and (9)), the projection of the Coulomb interaction Hamiltonian onto the *n*th Landau level takes the following form [98,101]:

$$\mathcal{H}_{S,n}=\frac{1}{2}\sum_{\sigma,\sigma'}\sum_{q}\frac{2\pi e^2}{\epsilon q}[F_n(ql_B)]^2\rho_{n,\sigma}(-\vec{q})\rho_{\sigma^n\sigma^{n\prime}}(\vec{q}), \tag{27}$$

where the form factor is given by the following expression:

$$F_0(x)=L_0(x^2/2) \tag{28}$$

$$F_n(x)=\frac{1}{2}\left[L_n\left(x^2/2\right)+L_{n-1}\left(x^2/2\right)\right], \tag{29}$$

where $x = ql_B$, and $L_m(x)$ are the Laguerre polynomials. In the above expressions (27)–(29), a magnetic field specific Gaussian factor, $\exp[-(ql_B)^2/4]$, is absorbed in the definition of the electron density. Therefore the form factors have a polynomial form [101]. The Gaussian factor can also be introduced not only in the electron density but also in the form factors themselves [98].

In the usual two-component non-relativistic systems the skyrmionic excitations exist only in the lowest Landau level (filling factor $\nu = 1$). In graphene the Coulomb interaction is several times stronger than in non-relativistic systems, e.g. GaAs. As a result, the skyrmion excitations survive even in higher Landau levels, $|n| \leq 3$ [59,102]. The charge of such excitations is ±1 for any integer filling [102].

Another interaction-induced mechanism for spontaneous symmetry breaking was introduced in a series of publications [100,108,109,111]. The order parameter in this approach is the gap (the Dirac mass) in the energy dispersion of relativistic electrons. This gap originates from the spontaneous excitonic condensation catalyzed by the magnetic field (magnetic catalysis). The presence of the gap, $\Delta$, in the energy dispersion splits the lowest Landau level, but does not affect the degeneracy of the highest Landau level. For example, the energies of the lowest Landau levels become $\pm\Delta$ and each level is twofold spin degenerate, while the energies of the higher Landau levels are

$$\varepsilon_n = \pm\sqrt{2\hbar v_{\mathrm{F}}^2 |n| eB + \Delta^2}. \tag{30}$$

Therefore for the higher Landau levels the gap changes only the dispersion relation, but does not change the level degeneracy. This fact has a straightforward effect on the quantization of the Hall conductance. Due to the splitting of only the lowest Landau level, there is an additional Hall plateau at $\nu = 0$. Therefore the graphene system with a dynamically generated gap shows Hall conductance quantization at $\nu = 0$ and $\nu = \pm 4(N + \frac{1}{2})$. Taking the Zeeman splitting into account, Gusynin *et al.* [100] reproduced the quantum Hall effect at $\nu = 0, \pm 1, \pm 2N$, $N = 1, 2, \ldots$. The degeneracy of the highest Landau levels is lifted only by the Zeeman interaction. In Figure 13, a schematic illustration of the Landau quantization with dynamical excitonic gap, $\Delta$, and Zeeman splitting, $\mu_B B$, is shown. There are two types of mass order parameters (dynamical gaps), which can be introduced into the model. The dynamical gaps correspond to singlet and triplet contributions with respect to the valley symmetry group [108,109,111]. In general, the dynamical gap order parameters coexist with quantum ferromagnetic order parameters and should be considered simultaneously [108].

Generation of the dynamical gap in a strong magnetic field was studied in [114] within the extended Hubbard model on a honeycomb lattice. The extended Hubbard model takes into account both on-site and nearest neighbor repulsions. The transition to the charge density wave state and an antiferromagnetic state has been illustrated within the model of [114]. Similar to the magnetic catalysis model [100,108,109,111], the generation of the dynamical gap explains the quantum Hall effect at $\nu = 0$ and ±1.

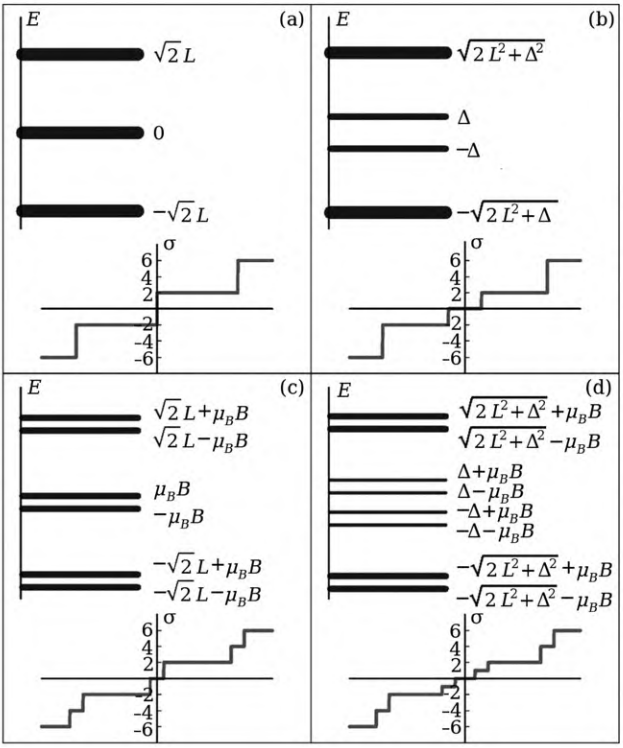

Figure 13. Schematic illustration of the spectrum of the Hall conductivity in $n=0$ and $n=1$ Landau levels for four different cases. (a) $\Delta=0$ and no Zeeman term. (b) Non-zero $\Delta$ and no Zeeman term. (c) $\Delta=0$ and the Zeeman term is taken into account. (d) Both $\Delta$ and the Zeeman term are non-zero. Thickness of the lines represents the degeneracy ×4, ×2 and ×1 of the level; $L=\sqrt{\hbar v_F^2 eB}$. (Reprinted with permission from V.P. Gusynin *et al.*, Physical Review B, 74, 195429, 2006 [100]. Copyright © by the American Physical Society.)

### 2.2.5. *Symmetry breaking: lattice distortion*

The twofold valley degeneracy in graphene can be lifted by an out-of-plane lattice distortion [115]. In a perpendicular magnetic field the distortion of the lattice can lower the total energy of the system. This energy includes both the elastic energy of the lattice and the energy of the electronic system. The distortion of the lattice is described as the relative shift of the sublattices A and B towards and away from a substrate by some distance [115]. Due to interaction with the substrate, the sublattices A and B acquire different on-site energies, which effectively results in effective mass of electrons in graphene and lower the energy of electron in the system. Therefore the electrons preferably occupy the sublattice with the lower on-site energy, spontaneously breaking the valley symmetry.

The gain in the energy of electronic system in graphene due to the distortion of the lattice is determined by the strength of the distortion and increases with the magnetic field [115]. This gain should be compared with the energy cost of the distortion, i.e. with the elastic energy of the lattice. Minimization of the total energy

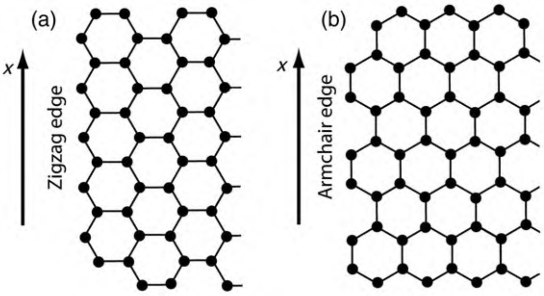

Figure 14. Graphene honeycomb lattice with (a) zigzag and (b) armchair edge terminations.

of the system, which includes the elastic energy of the lattice and the energy of electrons, determines the strength of the spontaneous lattice distortion. A detailed analysis of the graphene system in a magnetic field shows that spontaneous lattice distortion lifts the valley degeneracy only in the lowest Landau level, $n = 0$ [115], while the $n > 0$ Landau levels remain twofold valley degenerate.

The mechanism of lifting of twofold valley degeneracy based on magnetic-field-induced lattice distortion crucially depends on the asymmetric interaction of graphene layer with substrate. If the interaction with substrate is suppressed, e.g. in a suspended graphene, then the spontaneous lattice distortion does not occur.

The magnetic field can also induce lattice instability and lift the valley degeneracy in a suspended graphene even without a substrate if the graphene surface is curved. The example of such a system is the carbon nanotube. A strong magnetic field perpendicular to the nanotubes axis results in lattice instability towards in-plane or out-of-plane distortions [116–119]. The in-plane instability has the Kekule pattern, which is a network of hexagons with alternating short and long bonds.

### 2.2.6. *Edge states in a strong magnetic field*

The half-integer quantum Hall effect in graphene can be understood from the viewpoint of the edge states as well. In the edge state description of the quantum Hall effect, the Hall conductance is determined by the number of edge state bands crossing the Fermi level. In graphene there are two main types of edges: (i) armchair edge and (ii) zigzag edge (Figure 14). Even without a magnetic field, these edges have different properties, e.g. at the zigzag edge, zero energy surface states are observed. In a magnetic field the structure of the quantum Hall edge modes also depends on the type of the edge [104,109,120–125].

Within the continuum model, the difference between the two types of edges originates from different boundary conditions imposed at the edge. For the zigzag edges, the wavefunction vanishes on a single sublattice across the edge, while for the armchair edge, the wavefunction vanishes on both sublattices at the edge [122,123]. To find the structure and the energy dispersion of the edge states, the relativistic Dirac equation with appropriate boundary conditions should be solved. For each valley the corresponding wavefunctions are the two-component functions, i.e. $(\psi_{\mathrm{K,A}}, \psi_{\mathrm{K,B}})$ and $(\psi_{\mathrm{K',A}}, \psi_{\mathrm{K',B}})$ for valleys K and K$'$, respectively. Excluding one of the components from the Dirac equations, we obtain the system of equations for valleys K and K′ in the following form [123]:

$$\frac{1}{2}\left(-\partial_y^2+(y-y_p)^2+1\right)\;_{\mathrm{K,A}}=\lambda\psi_{\mathrm{K,A}};\tag{31}$$

$$\frac{1}{2}\left(-\partial_y^2+(y-y_p)^2-1\right)\;_{\mathrm{K',A}}=\lambda\psi_{\mathrm{K',A}},\tag{32}$$

where the edge is along the $x$ axis, the vector potential is $A_x=-By$, $A_y=0$, and along the $x$ axis the wavefunctions are propagating waves, $\exp(ip_xx)$. Here $\lambda=(\varepsilon/\varepsilon_0)^2$, $\varepsilon_0=\hbar v_0(2eB/\hbar c)^{\frac{1}{2}}$, $y_p=-p_x$, and $y$ and $p_x$ are measured in units of $l_B$ and $\hbar/l_B$, respectively.

Equations (31) and (32) determine the wavefunctions and corresponding energies of the Landau levels in graphene. Without any boundaries the Landau quantization with $\lambda\propto n$, i.e. $\varepsilon\propto\sqrt{n}$, and wavefunctions in the form of Hermite polynomials, $H_n(y-y_p)$, localized at $y_p$, can be obtained from Equations (31) and (32). The energies of the states do not depend on the electron position, $y_p$, within the layer, resulting in high degeneracy of the Landau levels. When $y_p$ becomes close to the boundary of the system, the degeneracy of the Landau levels is lifted. Such dispersive edge states can be obtained from Equations (31) and (32) by introducing the corresponding boundary conditions.

Then for the armchair edge termination the boundary condition takes the form

$$\;_{\mathrm{K,A}}=\psi_{\mathrm{K',A}},\quad \psi_{\mathrm{K,B}}=\psi_{\mathrm{K',B}}\tag{33}$$

at the boundary and for the zigzag edge the boundary condition is

$$\;_{\mathrm{K,A}}=0,\quad \psi_{\mathrm{K',A}}=0.\tag{34}$$

For higher Landau levels, $|n|>0$, there is not much difference in the energies of the edge states between the zigzag and armchair terminations. In both cases, the edge boundary conditions violate the valley symmetry at the edge, resulting in lifting of the twofold valley degeneracy at the boundary, shown schematically in Figure 15. For the armchair edge the boundary condition introduces inter-valley mixing, while for the zigzag edge the boundary condition itself violates the valley symmetry, but does not introduce the mixture between the K and K′ valleys. Thus only for the zigzag edge the valley indexes, K and K′, can be assigned to the edge states (Figure 15).

The lowest Landau level ($n=0$) behaves differently for zigzag and armchair edges. For the armchair edge, the lowest Landau band disperses and there is one pair of particle-like and one pair of hole-like edge states [104,109,120–125]. The appearance of both particle-like and hole-like edge states at $n=0$ Landau level is a direct manifestation of the relativistic nature of electrons in graphene and can be understood from Equations (27) and (28). The solutions of these equations provide the value of the effective energy, $\lambda$, which is proportional to the square of the real energy, $\lambda=(\varepsilon/\varepsilon_0)^2$. Therefore any positive solution of Equations (27) and (28) produce two real solutions: one with positive energy, $\varepsilon=\varepsilon_0\lambda^{\frac{1}{2}}$, and another with the negative energy, $\varepsilon=-\varepsilon_0\lambda^{\frac{1}{2}}$. The states with the positive and negative energies

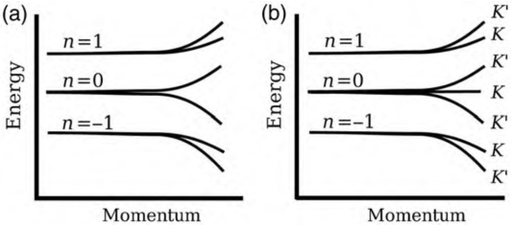

Figure 15. Graphene energy spectrum shown schematically as a function of momentum, $p_x$, near the armchair (a) and zigzag (b) edges. Here $n$ is the Landau level index. (a) For the armchair edge the boundary condition at the edge introduces inter-valley mixing. In this case the valley indexes, K or K′, cannot be assigned to the edge states. (b) For the zigzag edge the boundary condition violates the valley symmetry and lifts the valley degeneracy. There is no inter-valley mixture for the zigzag edge and each edge state belongs to a specific valley. The corresponding valleys are shown by labels K and K′.

correspond to the particle-like and hole-like states, respectively. By counting the number of edge bands at different positions of the Fermi level, it is easy to see that the existence of particle-like and hole-like states at the zero Landau level explains the half-integer quantum Hall effect.

For the zigzag edge, there are two types of edge states: dispersionless (with zero energy) and current-carrying surface states [104,109,120–125]. These two surface states belong to different valleys. The existence of zero-energy state can be understood from the special structure of the electron wavefunctions at the lowest Landau level. That is, in the K valley the $n=0$ Landau states reside on the B sublattice only which automatically satisfies zigzag boundary conditions, $\psi_{\mathrm{K,A}}=0$. For the K′ valley we obtain the dispersive states, which satisfy $\psi_{\mathrm{K',A}}=0$. Similar to the armchair edge, such boundary condition result in two types of edge states: particle-like and hole-like states. The edge states at the lowest Landau level are shown schematically in Figure 15.

The effect of disorder and electron–electron interactions on the structure of the edge states have been studied in [124], where edge reconstruction has been observed. Such reconstruction is more pronounced for a partially occupied Landau level, i.e. in the regime of the fractional quantum Hall effect.

The properties of the $\nu=0$ quantum Hall state are closely related to the structure of the edge states at the lowest Landau level [126]. The $\nu=0$ state can be attributed to either valley or spin splitting. Depending on whether the spin or valley symmetry is broken, the $\nu=0$ quantum Hall state has completely different properties. The system becomes either quantum Hall metal or quantum Hall insulator. We consider the armchair edge termination, for which the lowest Landau band consists of particle-like and hole-like edge states belonging to two different valleys (Figure 15a). Both types of states are twofold spin degenerate. Therefore the valley symmetry in this case is broken near the edge. If the valley symmetry is also broken in the bulk of the system (Figure 16a), then there are no current-carrying edge states at zero energy (Fermi level) and the system shows insulating properties. The edge levels in this case are twofold spin degenerate. If the spin symmetry is broken in the bulk of the graphene layer (Figure 16b) then at zero energy there are counter-propagating

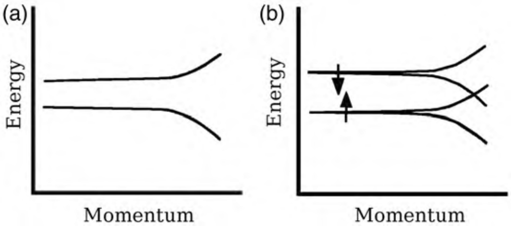

Figure 16. Energy spectrum of graphene shown schematically as a function of momentum, $p_x$, near the armchair edge for the lowest Landau level: (a) the case of broken valley symmetry (valley-polarized $\nu = 0$ quantum Hall state); (b) the case of broken spin symmetry (spin-polarized $\nu = 0$ quantum Hall state). The arrows next to the lines illustrate the direction of spin at the corresponding energy levels.

gapless edge modes [126]. In the experiments [92] the $\nu = 0$ quantum Hall system shows a peak in the magnetoresistance near the Dirac point (zero energy). This observation supports the picture of spin symmetry breaking as the origin of $\nu = 0$ quantum Hall state [126]. In [127], a simple technique has been proposed to measure the chirality of the quantum Hall edge states. This method can be used to clarify the nature of the edge states at the $\nu = 0$ quantum Hall effect.

The properties of counterpropagating edge states of opposite spin at $n = 0$ Landau level have been explored in [128] to explain the results of the experiment reported in [94], where the transition from the metallic to an insulating $\nu = 0$ quantum Hall state was observed. In [128], magnetic impurities were also introduced. Such impurities can flip the electron spin and introduce backscattering between the counterpropagating edge states. Each edge model is described as a one-dimensional Luttinger liquid with Luttinger parameter $\mathcal{K}$. The value of the parameter depends on the magnetic field strength and the details of the edge potential. In such a system the Kondo (magnetic) impurities introduce the critical value, $\mathcal{K}_c$, of the parameter $\mathcal{K}$, so that for $\mathcal{K} > \mathcal{K}_c$ the system is in an insulating state, while for $\mathcal{K} < \mathcal{K}_c$ it is in a metallic phase.

The condition of the existence of the gapless edge states in graphene with zigzag and armchair edges was analyzed in [109] within the approach based on the dynamical generation of the Dirac mass gap due to the magnetic catalysis. The condition is determined by the relative strength of the mass order parameters and the quantum Hall ferromagnetic order parameters.

### 2.3. *Fractional quantum Hall effect*

Observation of the fractional quantum Hall effect [72,73] in high-mobility planar electron gas at large magnetic fields allows one to study the collective behavior of two-dimensional electrons. Theoretical aspects of this problem in graphene have been addressed in a few publications [129–133], where a finite size system has been studied within the scheme of direct diagonalization of the Hamiltonian matrix or within the trial-wavefunction approach. The properties of the fractional quantum Hall effect in graphene can be determined by Haldane's pseudopotentials, $V_m$ [134],

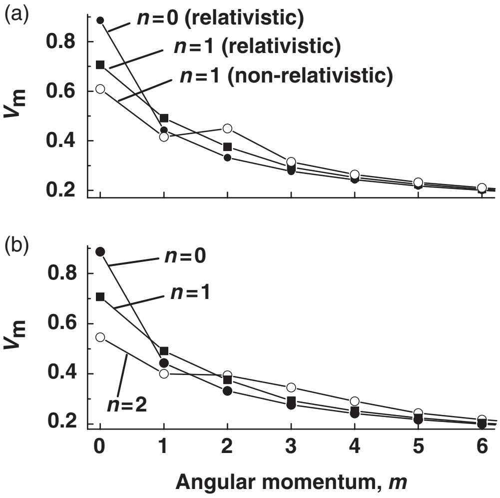

Figure 17. Pseudopotentials calculated from Equation (35) are shown as a function of the relative angular momentum (a) for relativistic and for non-relativistic two-dimensional electrons in the first two Landau levels, and (b) for relativistic electrons in various Landau levels. The energies are measured in units of $e^2/\varepsilon l_B$ (reproduced from [129]).

which are the interaction energies of two electrons with relative angular momentum $m$. The pseudopotentials for the $n$th Landau level has the following form [129,130,132,133]

$$V_m^{(n)} = \int_0^\infty \frac{\mathrm{d}q}{2\pi} q V(q) [F_n(q)]^2 L_m(q^2) \mathrm{e}^{-q^2}, \tag{35}$$

where $V(q) = 2\pi e^2/(\epsilon l_B q)$ is the Coulomb interaction in the momentum space, and $F_n(q)$ is the form factor corresponding to the $n$th Landau level (see Equations (28) and (29)). For non-relativistic electrons in graphene, the corresponding form factors are $F_n(q) = L_n(q^2/2)$. Comparing this expression with Equations (28) and (29), it is possible to see that the inter-electron interactions for the relativistic and non-relativistic electrons are same for $n = 0$ and different for $n > 0$.

In Figure 17 the pseudopotentials for relativistic and non-relativistic systems are shown. The behavior of the relativistic and non-relativistic pseudopotentials are clearly different. For relativistic electrons, the suppression of the pseudopotential for $n = 1$ as compared to $n = 0$ occurs only for $m = 0$, while for all other values of $m$, we have $V_m^{(1)} > V_m^{(0)}$. For non-relativistic electrons, there is also a suppression of the pseudopotential for $m = 1$. The behavior of relativistic pseudopotentials for different Landau levels is shown in Figure 17(b). At all values of the relative angular momentum, $m$, except for $m = 1$, there is a monotonic dependence of the pseudopotentials on the Landau level index, $n$: the pseudopotential decreases with increasing $n$ for $m = 0$ and increases with increasing $n$ for $m > 1$. In contrast, for the angular momentum $m = 1$, the dependence of the pseudopotential on the Landau index is non-monotonic: the pseudopotential has the maximum value at $n = 1$.

The special dependence of the relativistic pseudopotential on the angular momentum and Landau level index has a profound influence on the interaction energy scale of the fractional quantum Hall states at different Landau levels [129,130,132,135]. By looking at the values of the pseudopotentials we can reach a conclusion about the relative strength and stability of the fractional quantum Hall effect in graphene, as compared to the conventional non-relativistic systems. For example, since the electron wave functions at the lowest Landau level in graphene are identical to the lowest Landau level wavefunctions in the conventional (non-relativistic) electron systems, the relativistic pseudopotentials at $n = 0$ in graphene are exactly equal to the corresponding pseudopotentials of the non-relativistic systems [129]. Therefore, without the inter-Landau level coupling, the properties of the fractional quantum Hall state at $n = 0$ Landau level in graphene are the same as for the non-relativistic systems. The specific feature of the quantum Hall system in graphene is that the electrons now have spin and valley degrees of freedom, which would open up the possibility for spin and valley-polarized or unpolarized ground states and the corresponding excitations. The relativistic pseudopotentials at $n > 0$ Landau levels are different from those in the non-relativistic systems. As a result, the fractional quantum Hall states at the $n > 0$ Landau levels should have different properties compared to the non-relativistic systems [129]. Since at the $n = 1$ Landau level the pseudopotentials are enhanced compared to the non-relativistic ones, the fractional quantum Hall states at the $n = 1$ Landau level should be more stable in the relativistic graphene system.

Apalkov and co-workers [129,130] investigated the energy spectra of the fractional quantum Hall states in graphene for a finite-size system within the spherical geometry [72], where the magnetic field strength is determined by the magnetic field fluxes, $2S$, though the sphere in units of the flux quanta. Here $2S$ is an integer and $S$ is also the angular momentum of the single-electron states. It was shown that the ground state of $\nu = \frac{1}{3}$ and $\nu = \frac{1}{5}$ are spin and valley polarized at both $n = 0$ and $n = 1$ Landau levels [130]. The excitation gaps in the fractional quantum Hall systems are determined by the interaction strength at the corresponding Landau levels. The results shown in Figures 18 and 19 for $\nu = \frac{1}{3}$ and $\frac{1}{5}$ quantum Hall states at $n = 0$ and $n = 1$ Landau levels clearly illustrate the enhancement of the energy scale at the $n = 1$ Landau level compared to that at the $n = 0$ Landau level. That is, both valley-polarized and valley unpolarized excitation gaps at the $n = 1$ Landau level are larger than those at the $n = 0$ Landau level. This enhancement is especially pronounced for the $\nu = \frac{1}{3}$ state, for which the pseudopotential at small values of the angular momentum determine the inter-electron interaction strength. At $\nu = \frac{1}{5}$ the excitation spectra for the $n = 1$ and $n = 0$ Landau levels are almost the same. Although larger energy gaps at $n = 1$ Landau level are observed for the $\nu = 1/m$ states, this is not a general rule for other fractional Hall states. The pseudopotential at zero relative angular momentum, $m = 0$, is the strongest for the $n = 0$ Landau level. Therefore, for the fractional quantum Hall states for which the on-site interaction with $m = 0$ is dominant, the energy gap in the $n = 0$ Landau level is the largest. An example of such a fractional quantum Hall state is the $\nu = \frac{2}{3}$ state. The excitation gap of the valley-unpolarized $\nu = \frac{2}{3}$ state is larger in the $n = 0$ Landau level than that for the $n = 1$ Landau level.

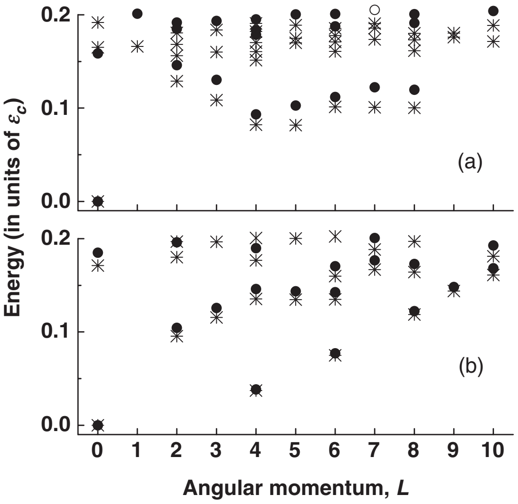

Figure 18. The energy spectra of an eight-electron valley-polarized $\nu = \frac{1}{3}$ fractional quantum Hall system obtained in spherical geometry are shown for different Landau levels: $n = 0$ (stars) and $n = 1$ (full circles). The flux quanta is $2S = 21$. (b) The energy spectra of a six-electron valley-polarized $\nu = \frac{1}{5}$ system is shown for different Landau levels: $n = 0$ (stars) and $n = 1$ (full circles). The flux quanta is $2S = 25$. The energy is shown in units of the Coulomb energy, $\varepsilon_C = e^2/\varepsilon l_B$ (reproduced from [130]).

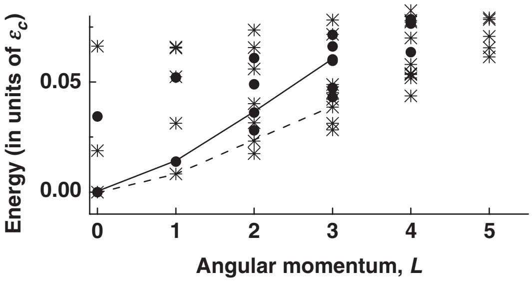

Figure 19. The energy spectra of a six-electron valley-unpolarized $\nu = \frac{1}{3}$ fractional quantum Hall system obtained in the spherical geometry, are shown for different Landau levels: $n = 0$ (stars) and $n = 1$ (full circles). The flux quanta is $2S = 15$. The spin-wave excitations are illustrated by solid ($n = 1$) and dashed ($n = 0$) lines. The energy is shown in units of the Coulomb energy, $\varepsilon_C = e^2/\varepsilon l_B$ (reproduced from [130]).

The single-particle excitations of the fractional quantum Hall states were studied in [135] within a numerical approach. It was shown that at $\nu = \frac{1}{3}$ the excitations are valley skyrmions both at $n = 0$ and $n = 1$ Landau levels. A more complicated situation occurs for the $\nu = \frac{2}{3}$ and $\nu = \frac{2}{5}$ fractional quantum Hall states. The ground states in these two cases are valley-unpolarized at $n = 0$ Landau level and valley-polarized in the $n = 1$ Landau level. The single-particle excitations are valley-unpolarized except at the $\nu = \frac{2}{5}$ state in the $n = 1$ Landau level, for which the excitation has the skyrmion-like valley texture.

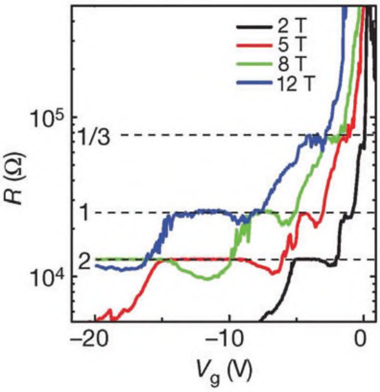

Figure 20. Gate voltage dependence of resistance for a suspended graphene sample is shown at different magnetic fields and at temperature 1.2 K. The plateaus at $\nu = 1, 2$ and $\frac{1}{3}$ are clearly visible. (Reprinted with permission from X. Du *et al.*, Nature, 462, p.192, 2009 [95]. Copyright © (2009) Nature Publishing Group.)

In [136], the ground state of the electron system with partial filling factor was studied within a mean-field approach. The competition between the uniform state, Wigner crystal (with one electron per unit cell) and the bubble crystal (with more than two electrons per unit cell) was considered. It was shown that at all filling factors (except integer) the Wigner crystal state has the lowest energy at the lowest Landau levels, $n = 0, 1$. At $n > 1$ a bubble crystal with two electrons per unit cell is realized at intermediate values of the filling factor, while at all other filling factors the Wigner crystal state occurs. This approach does not take into account the strongly correlated fractional quantum Hall states (Laughlin liquids) [72,73] realized at special fractional filling factors, e.g. $\nu = \frac{1}{3}$. Such states will have the lowest energy at these filling factors.

The fractional quantum Hall effect has been recently observed experimentally [95,96] in specially prepared suspended graphene samples. In such suspended samples, the disorder, which is usually due to the substrate, is strongly suppressed, which has made it possible to observe the fractional quantum Hall effect at the filling factor $\frac{1}{3}$ (Figure 20). The fractional quantum Hall state is a strongly correlated electron state, which at $\nu = \frac{1}{3}$ is the Laughlin liquid state [137]. The activation gap of such a state is determined by the strength of the inter-electron interaction, i.e. by the Coulomb energy, $\varepsilon_C = e^2/\varepsilon l_B$. The activation gap of the $\nu = 1/3$ quantum Hall state was analyzed in [138] based on the two-terminal conductance measurements [95,96]. The activation gap was found to be around 4.4 K and the corresponding fractional quantum Hall effect is clearly visible up to 10 K (the fractional quantum Hall effect in conventional 'non-relativistic' systems usually appear at much lower temperatures, i.e. below 1 K). The experimentally obtained activation gap is much smaller than the theoretically predicted value which, for the experimental parameters of [95,96] is around 40 K [138]. This discrepancy can be attributed to the presence of disorder in the system. Observation of the strong enhancement of interaction effects in suspended graphene can be clearly attributed to the small value of the dielectric constant, $\varepsilon \approx 1$, in suspended graphene.

## 3. Bilayer graphene

Bilayer graphene consists of two graphene monolayers, typically arranged in the Bernal (AB) stacking arrangement. It is a fascinating and complex system in its own right, distinct from both the monolayer and the traditional two-dimensional electron system (2DES) even though it shares some characteristics of each. The study of bilayer graphene started in 2006 with the publication of three papers describing its properties for the first time [139–141]. McCann *et al.* [139] demonstrated that the low-energy band structure of neutral bilayer graphene is gapless and exhibits a variety of second-order effects, and described an unusual sequence of Landau levels. Experimental descriptions of this material were published by Ohta [140], who described the low-energy band structure as well as the formation of a gap at the K point when a transverse electric field is applied (in this case by negatively charged dopants), and by Novoselov *et al.* [141] who measured the quantized Hall conductance as predicted by McCann and Falko. In addition to the quadratic low-energy band structure, with its associated effective mass, the chiral nature of the charge carriers is manifest in the Berry's phase and other properties. The bilayer shares many other physical properties with the monolayer, such as the exceptionally high electron mobility (with mean free path in the sub-micron range), and high mechanical stability. Massive chiral particles do not exist in standard field theory, and this makes the bilayer graphene system a promising venue in which the effects of chirality can be distinguished from those of the Dirac spectrum in comparison with monolayer graphene and traditional 2DESs. One unique feature of bilayer graphene is the ability to open a tunable band gap by engineering a potential difference between the two layers. This may be done either by gating, or by external dopants. This tunable gap (as opposed to the gap in a 2DES which is an intrinsic effect of the crystal structure and therefore not tunable), along with the high electron mobility and simplicity of fabrication techniques opens the possibility of many applications of bilayer graphene in the construction of devices.

Here we present a summary of the properties of this material, and in particular seek to show the similarities and differences between it and the monolayer. We begin in Section 3.1 by discussing the fabrication and identification of bilayer flakes from an experimental point of view. Then, in Section 3.2, the commonly-used tight-binding model is introduced including the effective low-energy description. In Section 3.3 we review the theoretical predictions for the opening of a band gap at the K points, and discuss the experimental evidence for this gap. When bilayer graphene is placed in a strong magnetic field, it exhibits a unique integer quantum Hall effect, and this is reviewed in detail in Section 3.4. The impact of electron–electron interactions is often neglected in the theoretical work, but they may have important consequences and we review analytical and numerical studies of their effects in Section 3.5. Phonon anomalies in this material, and the coupling between electrons and phonons are discussed in Section 3.6, and finally we present a few of the devices which have been proposed to utilize bilayer graphene in Section 3.7.

### 3.1. *Sample fabrication and identification*

Fabrication techniques for bilayer graphene are similar to those for the monolayer material. In the case of mechanically exfoliated flakes, the 'Scotch tape' part of the process deposits many flakes of varying thicknesses onto the substrate, so the process of identifying which flakes are mono- or bilayers becomes the key part of the technique. Bilayer samples have also been made on silicon carbide substrates by the sublimation of the silicon atoms on heating, a process called epitaxial growth. In this section, we describe the optimization of the visibility of graphene, and in particular the ideal conditions for distinguishing the number of layers of exfoliated flakes. We then review other diagnostic techniques, such as atomic force microscopy and Raman spectroscopy which proved to be useful tools in characterizing graphene.

### 3.1.1. *Optical identification of exfoliated bilayer graphene*

The visibility of graphene is a key issue for the mechanical microcleavage fabrication technique, and in 2007, four papers were published [142–145] discussing the visibility of graphene and few-layer graphene on dielectric substrates. Defining the optical contrast (or visibility) to be

$$V = (R - R_0)/R_0,$$

where $R_0$ is the reflection coefficient of the bare substrate, and $R$ is the reflection coefficient of the substrate with a graphene flake present, all authors reported that the visibility of the bilayer is twice as high as that of the monolayer in the visible frequency range. All authors also recommended using substrates with $\mathrm{SiO_2}$ of width $\approx$280 nm. While Blake *et al.* [142] modelled the enhanced reflection of visible light due to constructive interference of light caused by the additional optical path length introduced by the presence of graphene, Abergel *et al.* [143] gave a complimentary analysis considering the effect of the conductivity of the graphene flake at the boundary between the air and the substrate. They gave an analytical condition for the peak visibility, finding that the frequency of incident light $\omega$, the oxide width $d$, and dielectric function $\varepsilon_o$ should be arranged such that

$$\omega \approx \frac{c\left(n + \frac{1}{2}\right)\pi}{d\sqrt{\epsilon_o}\cos\alpha_o}, \tag{36}$$

where $n$ is an integer which labels the resonance, $c$ is the speed of light and $\sin\alpha_o = \sin\alpha/\sqrt{\epsilon_o}$. This approach was supplemented by Nair *et al.* [146] in the publication of measurements of the absorption of visible light by suspended graphene, showing that the absorption scales linearly with the number of layers for energies below about 1 eV and that the constant of proportionality is exactly the fine structure constant $\alpha = e^2/\hbar c$ (Figure 21). Abergel *et al.* [143] noted that since the optical conductivity of bilayer graphene has a peak at $\gamma_1 \approx 400\,\mathrm{meV}$, then the visibility of the bilayer will be enhanced with respect to the monolayer in the far infra-red frequency range. This was subsequently observed by Kuzmenko *et al.* [147].

Wang *et al.* [148] discussed several pertinent differences between the monolayer and bilayer optical properties, including the van Hove singularity which is present in the bilayer, but not in the monolayer. This effect causes the sign of the peak normalized reflectivity to be opposite in the two materials. Additionally, the normalized reflectance exhibits a peak when the photon energy is

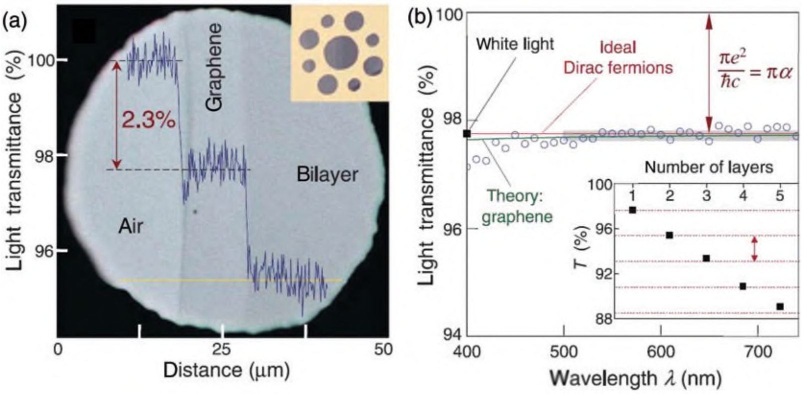

Figure 21. (Colour online) Looking through one-atom-thick crystals. (a) Photograph of a 50 μm aperture partially covered by graphene and its bilayer. The line scan profile shows the intensity of transmitted white light along the yellow line. (Inset) The sample design: A 20 μm thick metal support structure has several apertures of 20, 30, and 50 μm in diameter with graphene crystallites placed over them. (b) Transmittance spectrum on single layer graphene (open circles). Slightly lower transmittance for $\lambda < 400$ nm is probably due to hydrocarbon contamination. The red line is the transmittance $T = (1 + 0.5\pi\alpha)^{-2}$ expected for two-dimensional Dirac fermions, whereas the green curve takes into account a non-linearity and triangular warping of graphene's electronic spectrum. The gray area indicates the standard error for the measurements. (Inset) Transmittance of white light as a function of the number of graphene layers (squares). The dashed lines correspond to an intensity reduction by $\pi\alpha$ with each added layer (Reprinted figure with permission from R.R. Nair *et al.*, Science, 320, 1308, 2008 [146]. Copyright © (2008) The American Association for the Advancement of Science.).

equal to the interlayer coupling energy $\gamma_1$ corresponding to the inter-band excitations becoming accessible. The gate-induced changes in the reflectivity are also significantly different, with the monolayer showing a difference which is roughly constant with the photon energy, but the bilayer peaking at $\gamma_1$. Note that the detail explanation of the theory of optical conductivity can be found in [149–151].

Ni *et al.* [152] measured the visibility of multi-layered graphene on an $SiO_2$ substrate, and fitted their data to the bulk graphite refractive index ($n_G = 2.6 - 1.3i$). They did not find good agreement between the calculations using Fresnel's equations and the experiment, and instead found that the refractive index $n = 2.0 - 1.1i$ fitted better.

Abergel *et al.* [143] also discussed the visibility of graphene on SiC substrates, Roddaro *et al.* [144] presented computations of the observed color of the graphene flakes, Casiraghi *et al.* [145] discussed Raleigh spectroscopy and flakes with larger numbers of layers, and also the dependence of the visibility on the aperture size of the detection device. Gaskell *et al.* [153] measured the contrast in reflection for graphene flakes mounted on glass substrates and also found a linear increase in visibility with the number of layers, linking this to the fine structure constant (Figure 22), after Nair *et al.* [146]. Gao *et al.* proposed a method for flake identification which utilized the color difference between the substrate and the graphene, and discussed various alternative dielectric materials for use in the substrate.

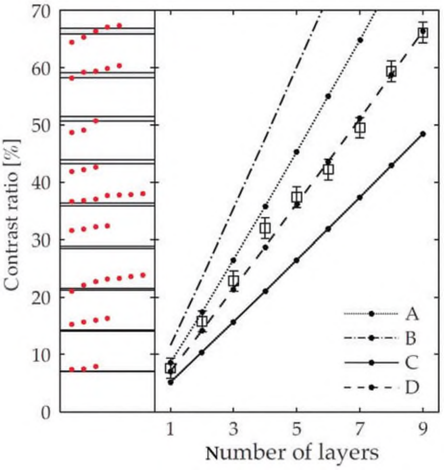

Figure 22. Left: Measured contrast ratios for 41 unique graphitic flakes. Theoretical contrast ratios based on the Fresnel theory with $m$-layer graphene conductance $Z_0G = m\pi\alpha$ are plotted as bands for a substrate refractive index $n_s = 1.522 \pm 0.004$. Right: Contrast ratios for each layer, including error due to camera non-linearity and lamp power fluctuation, compared with Fresnel theory with reported graphite induces (A) $n_g = 2.675 - 1.35i$ [154], (B) $n_g = 2.52 - 1.94i$ [155], graphene index reported by Ni *et al.* [152] (C), and universal conductance (D) (Reprinted figure with permission from P.E. Gaskell *et al.*, Applied Physics Letters, 94, 143101, 2009 [153]. Copyright © (2009) American Institute of Physics.).

### 3.1.2. *Atomic force microscopy and miscellaneous diagnostic techniques*

Atomic force microscopy is a technique which can be employed to measure the relative height of a graphene flake above the substrate, and thus determine the number of layers present in the flake. Obraztsova *et al.* [156] carried out a statistical analysis of the atomic force microscopy (AFM) measurements of the height of many graphene flakes to determine the systematic dependence of the height on the number of layers. They demonstrated (Figure 23) that the peaks in the histograms of measured heights occur at 0.35 nm intervals, corresponding to the predicted interlayer spacing in few-layer graphite flakes. The height of the first layer in a given flake varies due to the differing strength of interactions between the substrate and the flake, and the height of graphene in one plateau varies due to the intrinsic rippling or corrugation of the flake. Their study shows that the flake height is a reliable way of determining the number of layers on a plateau on a given flake, but the low throughput of the AFM technique means that other diagnostic techniques are more promising for the identification stage of the exfoliation fabrication method.

Stacking faults have been observed by Warner *et al.* [157] in exfoliated bilayer and few-layer samples by tunnelling electron microscopy (TEM) measurements. The relative rotation of the layers can be distinguished and the experimental data is fitted well by considering two decoupled monolayers. High-resolution TEM is a good tool for determining the stacking faults for flakes up to six layers thick.

When bilayer graphene is deposited on a (metallic) ruthenium substrate [158], the upper layer is screened from the substrate by the lower layer, which couples strongly to the metal. The authors claim that the linear band structure is regained in the upper

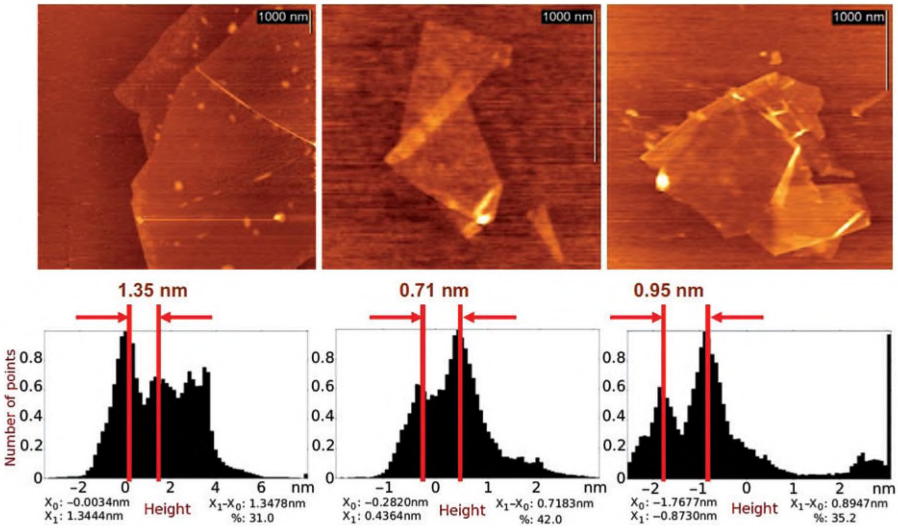

Figure 23. The atomic force microscopy images of three different arbitrary graphene flakes and the distribution of the height values over their surface points (Reprinted with permission from E.A. Obraztsova, A.V. Osadchy, E.D. Obratztsova, S. Lefrant, and I.V. Yaminsky, Physica Status Solidi b, 245, p. 2055, 2008 [156]. Copyright © (2008) Wiley-VCH Verlag GmbH & Co. KGaA.).

layer, and that scanning tunnelling microscopy (STM) images of the flake show both carbon sublattices indicating that the AB symmetry is restored.

### 3.1.3. *Raman spectroscopy*

Both the optical imaging and AFM methods of determining the number of layers in a graphene flake are time-consuming processes. Raman spectroscopy has a much higher throughput, and is therefore a promising candidate for a much faster identification technique, and several authors have claimed that it can reliably distinguish the number of layers in a flake. Raman spectroscopy is intimately related to the phonon modes in the sample being probed. Ferrari *et al.* [23] have shown that the doubly-degenerate $2D$ peak in monolayer graphene splits into four non-degenerate modes in the bilayer. This splitting causes the $2D$ peak to broaden in a systematic way (Figure 24a), to gain a shoulder on its low-energy tail, and to shift slightly upward in frequency. This is also seen in experiments carried out by Graf *et al.* [159], where spatially-resolved Raman spectroscopy can distinguish between mono- and bilayer portions of a single flake (Figure 24b). Also noticeable in this figure is a dramatic increase of intensity, and a slight downward shift (by $\approx 3\,\mathrm{cm}^{-1}$) of the $G$ peak, relative to the monolayer.

The Raman spectrum of two overlapping monolayer flakes has been investigated by Poncharal *et al.* [160]. Figure 25(a) shows the $G$ and $D$ band regions of the 633 nm Raman trace of monolayer and overlapping graphene. There is a slight downward frequency shift and narrowing of the $G$ peak in the overlapping flakes. Figure 25(b) shows the trace for the $2D$ band in the same flakes, with that of the Bernal stacked bilayer for comparison. The splitting of the $2D$ band into four peaks

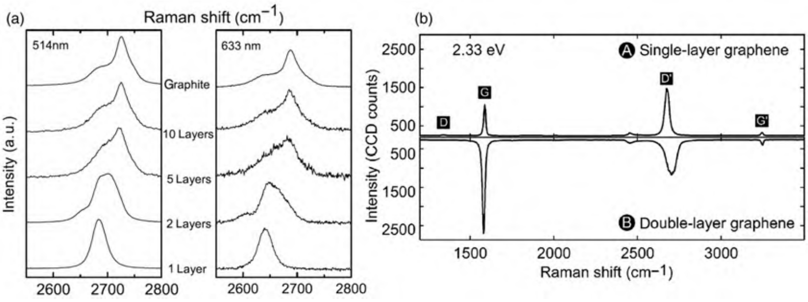

Figure 24. (a) The 2D peak shown in Raman spectra in bilayer graphene (Reprinted figure with permission from A.C. Ferrari *et al.*, Physical Review Letters, 97, 187401, 2006 [23]. Copyright © (2006) by the American Physical Society.). (b) Raman spectra of single- and double-layer graphene (Reprinted with permission from D. Graf *et al.*, Nano Letters, 7, 238, 2007 [159]. Copyright © (2007) by the American Chemical Society.).

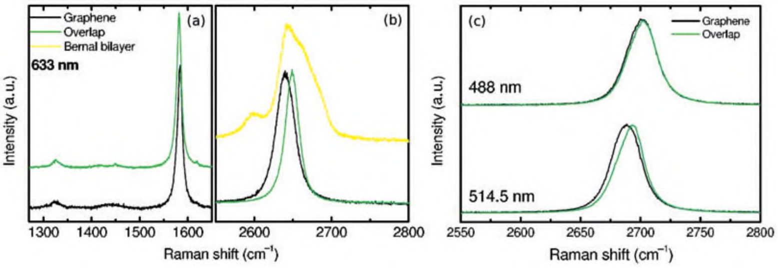

Figure 25. (Colour online) (a),(b) Raman spectra of a single graphene sheet (black lines), Bernal bilayer (yellow lines) and two overlapping misoriented graphene sheets (green lines) at 633 nm. (a) *G* and *D* band range of the graphene and overlapping configuration. Curves have been vertically offset for clarity and normalized on the *G* peak. (b) 2*D* band region for single graphene sheet and overlap compared to the Bernal-stacked bilayer. The overlapping graphene spectrum consists of a single peak clearly shifted compared to monolayer graphene. It strongly differs from the Bernal-stacked bilayer. Its width (19 cm$^{-1}$) is smaller than the monolayer graphene peak (26 cm$^{-1}$). (c) Raman spectrum at 488 nm (top) and 514.5 nm (bottom). The difference in Raman shift is reduced compared to the traces at 633 nm in (a, b). The slight asymmetry is due to experimental shortcomings (Reprinted figure with permission from P. Poncharal *et al.*, Physical Review B, 78, 113407, 2008 [160]. Copyright © (2008) by the American Physical Society.).

in the bilayer is completely absent from the overlapping region. Therefore, the authors conclude that the coupling between the two layers in the overlapping region is minimal. However there is an upward shift in the peak frequency, and the peak is ~20% narrower than in the monolayer case. The authors describe why they think (in contrast to other works, [161,162]) that neither the renormalization of the Fermi velocity nor the opening of a gap at the charge neutrality point cause this frequency shift. Instead, they suggest that the weak coupling between the two monolayers causes a modification of the phonon spectrum, which manifests in Raman trace while leaving the electronic spectrum unaltered.

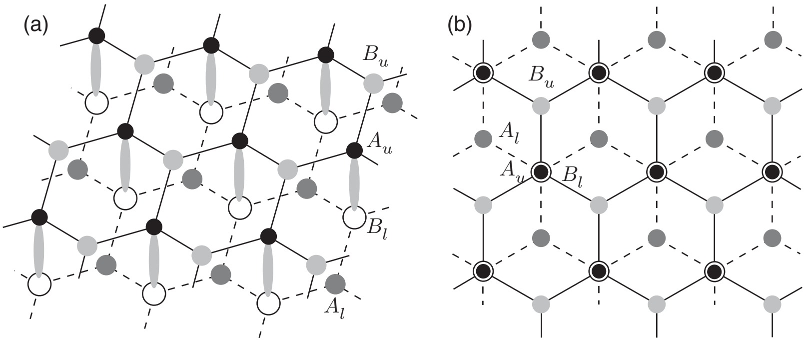

Figure 26. The bilayer lattice in (a) isometric, and (b) top-down projections. The upper (lower) layer is shown in solid (dashed) lines, the interlayer dimer bonds are in grey. The A atoms in the top layer are directly above the B atoms in the lower layer.

## 3.2. *Tight-binding model*

In this section we introduce the commonly-used tight-binding model for bilayer graphene. It is a natural extension of the model used for the monolayer, although additional complexity is introduced by the various interlayer hopping elements. We shall describe each of these and the effect that they have on the low-energy spectrum. Discussion of the interlayer potential is deferred until Section 3.3.

### 3.2.1. *Nearest neighbor and next-nearest neighbor models*

The bilayer crystal lattice is shown in Figure 26. The two monolayer lattices are shown as solid lines for the upper lattice (where the two lattice sites are labelled by a subscript '*u*') and the lower lattice in dashed lines (labelled by a subscript '*l*'). The two lattices are offset from each other in the *xy* plane so that the $A_u$ sublattice is directly above the $B_l$ sublattice, and it is between these pairs of atoms that the interlayer dimer bonds are formed. The $B_u$ and $A_l$ atoms are not directly bonded to the opposite layer. This arrangement is known as Bernal stacking, and is the stacking arrangement which is most commonly considered. Other possible arrangements are AA stacking, where the two lattices are directly above each other and bonds form between the same sublattices, and the turbostratic arrangement where the upper layer is rotated with respect to the lower layer and so interlayer bonding is haphazard and noticeably weaker. The AB stacking arrangement was experimentally verified in epitaxial graphene by Ohta *et al.* [163].

In order to construct the tight-binding model for bilayer graphene, we follow the same scheme as for the monolayer. Assuming that the $sp^2$-hybridized electrons are inert, we consider the $p_z$ electrons only, which form the $\pi$ bands as in the monolayer.[4] Since there are four atomic sites per unit cell, the wave function can be written as a four component spinor in the following basis:

$$\{\psi_{A_l}, \psi_{B_u}, \psi_{A_u}, \psi_{B_l}\}.$$

The intralayer nearest neighbor hopping elements (characterized by the vectors such as $\vec{R}$ in Figure 27(b)) with the transfer integral $t$ (which was also denoted by $\gamma$

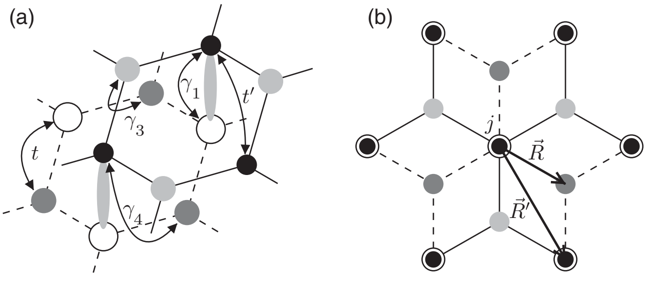

Figure 27. (a) Designation of couplings in the tight-binding model of bilayer graphene. Intralayer couplings are the nearest neighbor (A ↔ B) with energy $t$, and the next-nearest neighbor (A↔A and B↔B) with energy $t'$. Interlayer couplings are $A_u \leftrightarrow B_l$ with energy $\gamma_1$; $A_l \leftrightarrow B_u$ with energy $\gamma_3$; and $A_u \leftrightarrow A_l$ and $B_u \leftrightarrow B_l$ with energy $\gamma_4$. (b) Illustration of the twelve nearest and next-nearest neighbor lattice sites about site $j$. The vectors $R$ and $R'$ appear in the tight-binding formalism.

in Section 2.2) and the next-nearest neighbor hops with vectors like $\vec{R}'$ and transfer integral $t'$ are trivially the same as in the monolayer case, so we concentrate on describing the various interlayer couplings, which are illustrated in Figure 27(a). The most important interlayer coupling is the dimer bond between the $A_u$ and $B_l$ lattice sites. The strength of this coupling is parametrized by the transfer integral $\gamma_1$, and since there is no projection of the vector connecting these two lattice sites on the $xy$ plane, there is no momentum dependence in the matrix element. The next-nearest neighbor interlayer couplings are the $A_l \leftrightarrow B_u$ hops parametrized by $\gamma_3$, and the $A_l \leftrightarrow A_u$ and $B_l \leftrightarrow B_u$ hops parameterized by $\gamma_4$. In each case, the momentum dependence is the same function $f(\vec{k})$ as for the intralayer nearest neighbor hops. Finally, the presence of the dimer bond may induce an additional asymmetry between the two sublattices within each layer, which we account for this by including the parameter Δ. Therefore, the tight-binding Hamiltonian for the $\pi$ bands of neutral bilayer graphene can be written as

$$\mathcal{H}_\pi = \begin{pmatrix} t'g(\vec{k}) & \gamma_3 f(\vec{k}) & \gamma_4 f(\vec{k})^* & tf(\vec{k})^* \\ \gamma_3 f(\vec{k})^* & t'g(\vec{k}) & tf(\vec{k}) & \gamma_4 f(\vec{k}) \\ \gamma_4 f(\vec{k}) & tf(\vec{k})^* & \Delta + t'g(\vec{k}) & \gamma_1 \\ tf(\vec{k}) & \gamma_4 f(\vec{k})^* & \gamma_1 & \Delta + t'g(\vec{k}) \end{pmatrix}, \tag{37}$$

where $f(\vec{k}) = \sum_{i=1}^{3} \exp(i\vec{k}\cdot\vec{R}_i)$, $g(\vec{k}) = \sum_{i=1}^{6} \exp(i\vec{k}\cdot\vec{R}'_i)$, and the superscript asterisk denotes complex conjugation. The values of the transfer matrix elements which appear in the Hamiltonian are still controversial. It seems that they may vary between exfoliated and epitaxial graphene, and theoretical calculations do not currently agree completely with experimental measurement. In Table 1 we collect the values as currently known. The most thorough experimental determination of the tight-binding parameters was carried out by Kuzmenko *et al.* [164], who used infra-red spectroscopy to compare detailed reflection spectra with the predictions of the tight-binding model. They fitted their data to nine free parameters, including the four tight-binding parameters shown in Table 1, the interlayer gap, scattering rate, temperature and position of the charge-neutrality point. The spectrum

Table 1. Tight-binding parameters for bilayer graphene, given in eV.

| | $t \equiv \gamma$ | $\gamma_1$ | $\gamma_3$ | $\gamma_4$ | $\Delta$ |
|---|---|---|---|---|---|
| Kuzmenko [147] (IR spec.) | | 0.378 | | | 0.015 |
| | | (0.005) | | | (0.005) |
| Kuzmenko [164] (IR spec.) | 3.16 | 0.381 | 0.38 | 0.14 | 0.022 |
| | (0.03) | (0.003) | (0.06) | (0.03) | (0.003) |
| Zhang [165] (IR spec.) | 3.0 | 0.40 | 0.3 | 0.15 | 0.018 |
| Malard [166] (Raman) | 2.9 | 0.30 | 0.10 | 0.12 | |
| Malard [167] (Raman) | 3.0 | 0.35 | 0.13 | 0.13 | |
| Min [168] (*ab initio*) | 2.6 | $\approx$0.34 | 0.3 | | |
| Gava [169] (*ab initio*) | −3.4013 | 0.3963 | 0.3301 | 0.1671 | |

Notes: Methods of determination of the parameters include infra-red spectroscopy (IR spec.), Raman spectroscopy (Raman), and *ab initio* density functional theory calculations (*ab initio*). Note that Min *et al.* claim that $\gamma_1$ varies slightly with the interlayer potential $U$. Bracketed values are stated uncertainties.

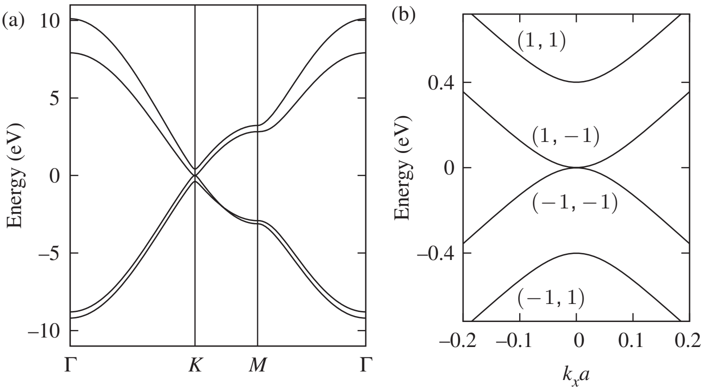

Figure 28. (a) The $\pi$ bands in bilayer graphene along the high symmetry directions. The tight-binding parameters are taken from Zhang [165]. We have ignored the intra-plane next-nearest neighbor hopping parametrized by $t'$ (i.e. we have set $t' = 0$). (b) The low-energy spectrum for $k_y = 0$ in the nearest neighbor tight-binding model, (i.e. for $\gamma_3 = \gamma_4 = t' = \Delta = 0$). The bands are labelled by the pair of values $(\chi, \alpha)$ (Equation (39)). The higher energy bands ($\alpha = 1$) are split by $\gamma_1$ from the low-energy bands ($\alpha = -1$), which are degenerate exactly at the K point. In this case, all four bands are isotropic.

associated with this Hamiltonian is shown in Figure 28, where we have taken the tight-binding parameters given by Zhang *et al.* [165].

Mucha-Kruczyński *et al.* [170] have proposed a method for determining the size and sign of various tight-binding parameters by utilizing angle-resolved photoemission spectroscopy (ARPES) data. Variation of the intensity of constant energy maps reveal the wave function symmetry due to trigonal warping, band gaps and intralayer site asymmetry. The location of the bottom of the split band immediately gives the size of the interlayer coupling $\gamma_1$, and for energies greater than $\gamma_1$, the relative intensity of the signal from the low-energy and split bands determines the sign of this parameter. The magnitude and direction of the trigonal warping of the low-energy band structure are set by the ratio $\gamma_3/\gamma_1$, so once $\gamma_1$ is accurately known, the analysis of the constant energy maps near the charge neutrality point reveals the sign and magnitude of $\gamma_3$. The band gaps can also be characterized, and the relative contributions from the intralayer asymmetry $\Delta$ and the interlayer bias $U$ can be distinguished.

The Hamiltonian in Equation (37) is valid for the $\pi$ bands across the whole Brillouin zone. However, the low-energy properties of bilayer graphene are determined by the electrons near the Fermi surface, which (for moderate doping or gating) is located near the six K points. We therefore expand the momentum dependence of $\mathcal{H}_\pi$ near the two inequivalent points, and assign the valley index $\xi$ (such that $\xi = +1$ in the K valley, and $\xi = -1$ in the K$'$ valley) to be a new quantum number for the system. This causes the basis to expand to contain eight elements, not counting the spin degree of freedom. It is convenient to swap the order of the components in the K$'$ valley, so that the basis is

$$\{\psi_{\mathrm{A}_l}, \psi_{\mathrm{B}_u}, \psi_{\mathrm{A}_u}, \psi_{\mathrm{B}_l}\} \text{ in the K valley, and}$$
$$\{\psi_{\mathrm{B}_u}, \psi_{\mathrm{A}_l}, \psi_{\mathrm{B}_l}, \psi_{\mathrm{A}_u}\} \text{ in the K}' \text{ valley.}$$

Using this basis, we can write the low-energy Hamiltonian in valley $\xi$ by expanding the functions of momentum to the leading order about the K points as

$$\mathcal{H}_\xi = \begin{pmatrix} \frac{3}{4}t'a^2|\vec{k}|^2 & \xi v_3 \pi & \xi v_4 \pi^\dagger & \xi v \pi^\dagger \\ \xi v_3 \pi^\dagger & \frac{3}{4}t'a^2|\vec{k}|^2 & \xi v \pi & \xi v_4 \pi \\ \xi v_4 \pi & \xi v \pi^\dagger & \Delta + \frac{3}{4}t'a^2|\vec{k}|^2 & \gamma_1 \\ \xi v \pi & \xi v_4 \pi^\dagger & \gamma_1 & \Delta + \frac{3}{4}t'a^2|\vec{k}|^2 \end{pmatrix}, \tag{38}$$

where $v = \sqrt{3}at/(2\hbar)$ is the Fermi velocity of monolayer graphene, $v_3 = \sqrt{3}a\gamma_3/(2\hbar)$ and $v_4 = \sqrt{3}a\gamma_4/(2\hbar)$ are the velocities associated with the interlayer hops, $\pi = p_x + \mathrm{i}p_y$, and $\vec{p} = \hbar\vec{k} = -\mathrm{i}\hbar\vec{\nabla}$.

In the simplest case (the nearest neighbor approximation), with $\gamma_3 = \gamma_4 = \Delta = t' = 0$, we see that the spectrum near the K point is quadratic:

$$E_{\mathrm{nn}} = \chi\sqrt{v^2p^2 + \gamma_1^2/2 + \alpha\gamma_1\sqrt{v^2p^2 + \gamma_1^2/4}}, \tag{39}$$

where $\chi = \pm 1$ refers to the conduction and valence band, and $\alpha = \pm 1$ to the low-energy and split branches illustrated in Figure 28(b). A cross-over to a linear spectrum occurs at $p \approx \gamma_1/2v$, corresponding to the electron density $n^{\mathrm{lin}} \approx \gamma_1^2/(4\pi\hbar^2v^2) \approx 4 \times 10^{12}\,\mathrm{cm}^{-2}$ [139], which is lower than the density at which the higher energy band becomes occupied: $n^{(2)} \approx 2\gamma_1^2/(\pi\hbar^2v^2) \approx 8n^{\mathrm{lin}}$ [139]. The equivalent energy is approximately $\gamma_1/5$.

The qualitative features of this model have been confirmed in optical experiments by Wang *et al.* [148] and Kuzmenko *et al.* [147,164]. Wang *et al.* spectulated that disagreements between the predicted and observed reflectivity properties could be due to excitonic effects altering the optical spectrum. Kuzmenko *et al.* [147] observed peaks in the reflectivity associated with the onset of various inter-band transitions, and were able to extract parameters for the tight-binding model from them. However there were some features which required additional couplings to be considered in the tight-binding model before they could be explained, and we shall discuss them later.

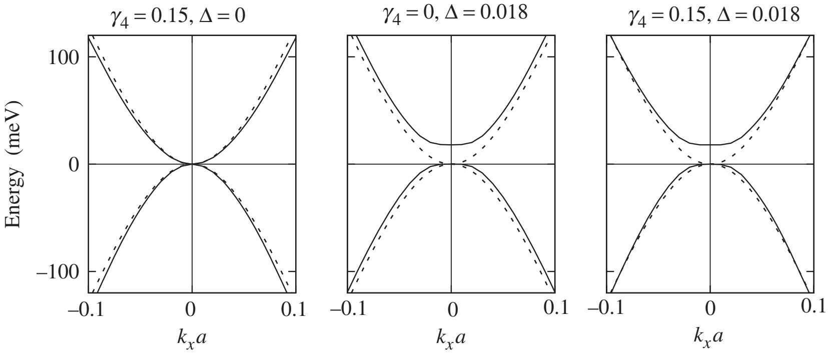

Figure 29. Detail of the effect of $\gamma_4$ and $\Delta$ (the intralayer site asymmetry induced by the presence of the dimer bond) on the low-energy spectrum near the K point. In each case the solid line represents the labelled tight-binding parameters with $\gamma_3 = t' = 0$, and the dashed lines correspond to $\gamma_3 = \gamma_4 = \Delta = t' = 0$. The $k_x$ momentum is measured from the K point, and $k_y = 0$ throughout.

The effects of the interlayer hop parametrized by $\gamma_4$, and the onsite assymmetry $\Delta$ is shown in Figure 29, where we plot numerical solutions of the Hamiltonian in Equation (38) with $\gamma_3 = t' = 0$, and various values of $\gamma_4$ and $\Delta$. We see that $\gamma_4$ introduces a small electron–hole asymmetry, and that $\Delta$ increases the conduction band energy near the K point. The combined effect is shown in the third panel of Figure 29. At larger momentum ($k_x a \sim 0.1$), the combined effects of $\gamma_4$ and $\Delta$ cancel, leaving the bands almost unchanged.

Note that in this section, the overlap matrix has been neglected (see, e.g. Mucha-Kruczyński *et al.* [170], or the book by Saito *et al.* [13]). This has an effect on the band structure, including introducing an asymmetry between the electron and hole bands, although only minimal effect is observed on the low-energy part near the K points.

An analysis of the real space Green's function of bilayer graphene near the K points has been carried out by Wang *et al.* [171]. They derive analytical expressions for the Green's function, and plot the local density of states (LDOS) to compare with experimental scanning tunnelling microscopy images of bilayer flakes. They predict that the lattice sites not involved in the dimer bonds have the highest electron density for electrons with energy below the interlayer coupling $\gamma_1$. This is in contrast to monolayer flakes where the two lattice sites are equivalent and the LDOS are identical to each other. The difference in the LDOS, $\Delta\rho_0(\varepsilon)$ is given by

$$\Delta\rho_0(\varepsilon) = \begin{cases} 0 & |\varepsilon| > \gamma_1 \,, \\ \dfrac{S\gamma_1}{2\pi t^2} & |\varepsilon| < \gamma_1 \,, \end{cases}$$

where $S = 3\sqrt{3}a^2/2$ is the area of the unit cell in real space.

Lopes dos Santos *et al.* [162] used the continuum limit of the tight-binding formulation to consider the effect on the spectrum of a small rotation (parametrized by the angle $\theta$) between the two graphene layers. The main consequence of the rotation is that the Dirac cones in each layer are shifted in momentum space, so that the doublet of zero energy states in the lower layer cannot couple via the interlayer dimers to the zero energy states in the upper layer. Instead, they couple to three sets of finite energy states, at $\pm v\Delta K$, where $\Delta K = 2\ \sin(\theta/2)$. The effect of this altered coupling is that the Dirac cones are preserved, although their energy is shifted downward by an amount $6\tilde{t}_{\perp}^{2}\ \sin(\theta/2)/(v\Delta K)$. The Fermi velocity is also renormalized so that $\tilde{v}/v = 1 - 9\left[\tilde{t}_{\perp}/(v\Delta K)\right]^{2}$, where $\tilde{v}$ is the modified interlayer hopping parameter at the reciprocal lattice vectors, and this reduced velocity constitutes an experimental tool for identifying twisted bilayers. The twist also generates an electric potential difference between the layers, but the absence of coupling between the zero energy states in each layer prevents the opening of a gap at the Dirac point. Finally, an electron–hole asymmetry develops, which shifts the Fermi energy away from the Dirac point at half-filling.

Katsnelson *et al.* [172] showed that, as in the monolayer, the ripples[5] which are intrisic to graphene [24,173] cause the Hamiltonian to be modified by an effective gauge field. This induces zero energy states, which the authors prove (via the Atiyah-Singer theorem) to be topologically protected. The number of these states is determined by the total 'flux' in the sample.

### 3.2.2. *Trigonal warping*

The next-nearest neighbor couplings may have important effects in the low-energy limit. Chiefly, the direct coupling between atomic sites not involved in the dimer bond (the $\mathrm{A}_l$ and $\mathrm{B}_u$ sites), which is parametrized by the hopping integral $\gamma_3$ causes the low-energy spectrum to become anisotropic. This effect is called trigonal warping, is detectable in ARPES measurements [174,175], and has a significant effect on the weak localization properties of bilayer graphene [176,177]. It is included in the tight-binding formalism with the transfer integral $\gamma_3$ which leads to the velocity $v_3 = \sqrt{3}a\gamma_3/(2\hbar)$. The spectrum associated with the nearest neighbor Hamiltonian with the trigonal warping terms was given by McCann [139] as

$$\epsilon_{\pm}^{(\alpha)} = \pm\sqrt{\frac{1}{2}\gamma_1^2 + \left(v^2 + \frac{1}{2}v_3^2\right)p^2 + (-1)^{\alpha}\sqrt{\Gamma}}, \tag{40a}$$

where $\alpha = 1, 2$ represents the lower and higher energy bands respectively, and

$$\Gamma = \frac{1}{4}\left(\gamma_1^2 - v_3^2p^2\right)^2 + v^2p^2\left(\gamma_1^2 + v_3^2p^2\right) + 2\xi\gamma_1 v_3 v^2 p^3 \cos(3\phi). \tag{40b}$$

In Figure 30(a) we show this spectrum for the parameters given by Zhang *et al.*, but with $\gamma_4 = \Delta = t' = 0$, so that we reveal the effects of the trigonal warping only. Plotting the energy along the line $k_y = 0$, the spectrum is asymmetrical about $k_x = 0$, although electron–hole symmetry is still present since the sublattice symmetry is not broken. For small energies, a Lifshitz transition occurs whereby the Fermi surface breaks into one central region with area $A_c \approx \pi\epsilon^2/(\hbar v_3)^2$ and three elliptical 'leg' regions with area $A_l \approx A_c/3$. The center of the leg regions are at momenta with magnitude $\gamma_1 v_3/v^2$ and angles 0, $2\pi/3$, and $4\pi/3$. The electron density at which this transition in the shape of the Fermi surface will occur is $n_L \approx (v_3/v)^2\ n^{\mathrm{lin}} \approx 1\times10^{11}\,\mathrm{cm}^{-2}$,

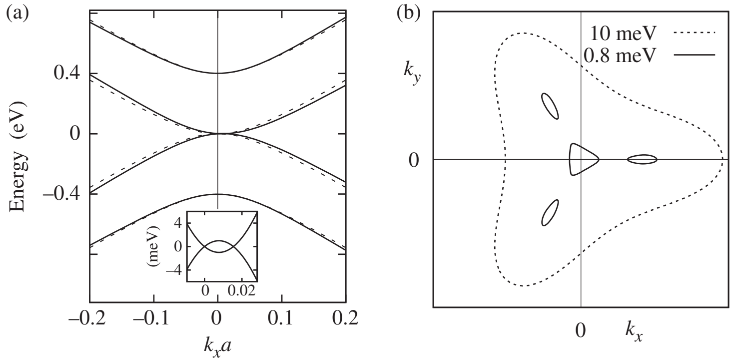

Figure 30. (a) Effect of inclusion of trigonal warping (solid line) in spectrum. The dashed line is for $v_3 = 0$. An asymmetry about $k_x = 0$ is introduced, but electron–hole symmetry persists. The inset shows the very low energy spectrum, and the band overlap of $\approx 2$ meV induced by the trigonal warping. (b) Isoenergetic lines in momentum space for $v_3/v = 0.1$. For $E \approx 1$ meV the Fermi surface splits into four pockets.

where $n^{\text{lin}}$ is the density corresponding to the cross-over from the quadratic to the linear spectrum, discussed after Equation (39). The trigonal warping has a substantial effect on the low-energy transport properties of the bilayer.

### 3.2.3. *Effective low-energy theory*

In 2006, McCann and Falko [139] introduced a low-energy effective model for bilayer graphene. In essence, it is an expansion of the Hamiltonian in the parameter $\varepsilon/\gamma_1$ which effectively excludes the atomic sites involved in the dimer bond. Starting from the Hamiltonian in Equation (38), with $\gamma_4 = t' = \Delta = 0$, and including the interlayer bias $U$ discussed in Section 3.3, four blocks can be identified:

$$\mathcal{H}_{11} = \xi\Big(U\sigma_z/2 + v_3[\sigma_x p_x - \sigma_y p_y]\Big), \quad \mathcal{H}_{22} = -\xi U\sigma_z/2 + \gamma_1\sigma_x,$$
$$\mathcal{H}_{21} = \mathcal{H}_{12} = \xi v(\sigma_x p_x + \sigma_y p_y).$$

The $4 \times 4$ Green's function associated with $\mathcal{H}_\xi$ can also be split into $2 \times 2$ blocks, and the approach taken by McCann was to compute the block $G_{11}$ involving only the lower band states, and use it to identify the effective low-energy Hamiltonian. In particular, using $G^{(0)}_{aa} = (\mathcal{H}_{aa} - \epsilon)^{-1}$,

$$G = \left(\mathcal{H}_\xi - \epsilon\right)^{-1} = \left.\begin{matrix} G_{11}^{(0)-1} & \mathcal{H}_{12} \\ \mathcal{H}_{21} & G_{22}^{(0)-1} \end{matrix}\right)^{-1}.$$

Simple evaluation of the equation $GG^{-1} = 1$ gave

$$G_{11}^{-1} + \epsilon = \mathcal{H}_{11} - \mathcal{H}_{12}G_{22}^{(0)}\mathcal{H}_{21}.$$

Now, the low-energy effective Hamiltonian $\mathcal{H}_2$ is identified with the Green's function $G_{11}$ as $\mathcal{H}_2 = G_{11}^{-1} + \epsilon$ so that the Schrödinger equation for this Hamiltonian was written as

$$\mathcal{H}_2\psi = \epsilon\psi \Rightarrow \left[\mathcal{H}_{11} - \mathcal{H}_{12}G_{22}^{(0)}\mathcal{H}_{21}\right] \quad = \epsilon\psi.$$

Making a Taylor expansion of $G_{11}^{(0)}$ in the small parameters $\epsilon/\gamma_1$ and $U/\gamma_1$, substituting in the Schrödinger equation for the $2 \times 2$ Hamiltonian, moving all terms containing energy to the right-hand side, and rearranging for $\mathcal{H}_2$ gives

$$\mathcal{H}_2 = -\frac{v^2}{\gamma_1}\begin{pmatrix} 0 & \pi^{\dagger 2} \\ \pi^2 & 0 \end{pmatrix} + \xi v_3\begin{pmatrix} 0 & \pi \\ \pi^\dagger & 0 \end{pmatrix} + \frac{\xi U}{2}\left[\begin{pmatrix} 1 & 0 \\ 0 & -1 \end{pmatrix} - \frac{2v^2}{\gamma_1^2}\begin{pmatrix} \pi^\dagger\pi & 0 \\ 0 & -\pi\pi^\dagger \end{pmatrix}\right]. \tag{41}$$

This expression is interesting in a number of ways. Firstly, the kinetic energy now comes with factors of $\pi^2$, which ensures that the energy dispersion is quadratic in this limit. This corresponds to the electrons gaining a finite effective mass at the bottom (top) of the conduction (valence) band, and the Dirac spectrum disappears. However, the chirality of the electrons persists because the sublattice pseudospin is still a relevant degree of freedom. The linear momentum term now carries the velocity $v_3 \sim v/10$. Therefore, this term is important at low momentum and its effect on the band structure (called trigonal warping) is discussed in Section 3.2.2. The final term in this expression contains contributions to the Hamiltonian from the interlayer asymmetry potential. Since the decoupled lattice sites retained in this model are in opposite layers, the low-energy band structure keeps its dependence on $U$ via the first term in the bracket as it was in the four band case. Further discussion of this term is deferred until Section 3.3. The second term in the bracket is sometimes called the kinetic asymmetry, and is due to the depletion of charge on the $A_u$, $B_l$ dimer sites. Using a more compact notation, this equation can also be written as the final result of McCann and Falko [139]:

$$\mathcal{H}_2 = -\frac{1}{2m}(\vec{\sigma} \cdot \vec{p})\sigma_x(\vec{\sigma} \cdot \vec{p}) + \xi v_3 \vec{\sigma}^t \cdot \vec{p} + \frac{\xi U}{2}\sigma_z + \frac{\xi U}{2m\gamma_1}(\vec{\sigma} \cdot \vec{p})\sigma_z(\vec{\sigma} \cdot \vec{p}), \tag{42}$$

where $m = \gamma_1/(2v^2)$ is the effective mass induced by the curvature of the bands, and the superscript $t$ denotes the transpose of the matrix.

## 3.3. *Band gap in bilayer graphene*

### 3.3.1. *Band gap in the tight-binding model*

The symmetry governing the degeneracy of the highest valence and lowest conduction bands at the K points in neutral bilayer graphene is the inversion symmetry. If this symmetry is broken, then a gap is expected to appear in the low-energy spectrum [139,178,179]. This breaking of symmetry can be modelled within the tight-binding approximation by assuming that the two layers are at different electrostatic potentials (Figure 31(a)) so that the difference between them is parametrized by the energy $U$. The Hamiltonian corresponding to the full bilayer

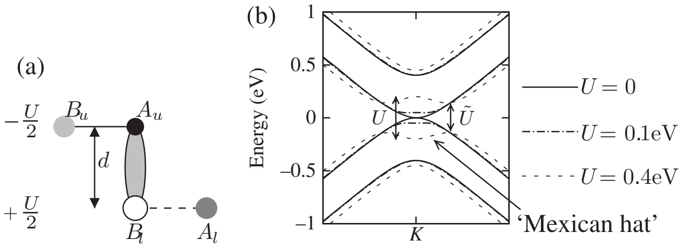

Figure 31. (a) Side-on view of the bilayer lattice, with the interlayer potential $U$ and the interlayer separation $d$ labelled. (b) Low-energy tight-binding bands for three values of the gap $U$, with $\gamma_3 = \gamma_4 = \Delta = t' = 0$, $t = 3$ eV and $\gamma_1 = 0.4$ eV. The gap at the K point is $U$, whereas the minimum splitting between the bands occurs at $\tilde{U}$.

system with broken inversion symmetry is given by $\mathcal{H} = \mathcal{H}_0 + \mathcal{H}_U$, where $\mathcal{H}_0$ is discussed fully in Section 3.2, and

$$\mathcal{H}_U = \begin{pmatrix} \xi U/2 & 0 & 0 & 0 \\ 0 & -\xi U/2 & 0 & 0 \\ 0 & 0 & -\xi U/2 & 0 \\ 0 & 0 & 0 & \xi U/2 \end{pmatrix} = \frac{\xi U}{2} \sigma_z \otimes \sigma_z, \tag{43}$$

which corresponds to the lower layer being at potential $+U/2$, and the upper layer at $-U/2$. The factor of $\xi$ is necessitated by the definition of the bases in the two valleys. The effect of the inclusion of this term is illustrated in Figure 31(b) for the nearest neighbor tight-binding model. We see that for moderate values of the interlayer potential (often called the bias potential), a gap does indeed appear at the K point, but the quadratic profile of the low-energy dispersion is retained. For higher values of the bias, the quadratic nature is replaced with the 'Mexican hat' dispersion [180]. The band structure associated with this simplified Hamiltonian is

$$\epsilon^2 = v^2 p^2 + \gamma_1^2/2 + U^2/4 + \alpha \sqrt{v^2 p^2 (U^2 + \gamma_1^2) + \gamma_1^4/4},$$

where $\alpha = 1$ designates the split bands, and $\alpha = -1$ gives the low-energy bands. From this expression, it is straightforward to compute that the gap exactly at the K point is $U$, and that the minimum separation of the conduction band and valence band is

$$\tilde{U} = \frac{\gamma_1 U}{\sqrt{U^2 + \gamma_1^2}} \quad \text{at momentum} \quad p^2 = \frac{U^2}{4v^2} \frac{U^2 + 2\gamma_1^2}{U^2 + \gamma_1^2}.$$

The two quantities are labelled in Figure 31(b). Therefore, $U \approx \tilde{U}$ for bias up to $U = 0.2$ eV.

In the preceding analysis, the size of that gap was treated as a phenomenological parameter. In a typical experimental setup, the source of the symmetry breaking is either a gating arrangement, or a number of dopants placed on one face of the graphene bilayer. Two studies [178,181] have related the characteristics of the gate or the dopant concentration to the size of the gap in the context of the continuum limit of the tight-binding model. We shall discuss first-principles calculations of these effects in Section 3.3.3. The excess charge density $n = n_1 + n_2$ is distributed between both layers because of the incomplete screening, so that there is a potential energy difference [178]

$$U = U_0 + e^2 n_2 L^2 / C_b \tag{44}$$

between the two layers. In this expression, $U_0$ is the bare asymmetry parameter which gives a finite asymmetry at zero density (due to, e.g. uncontrolled doping in the fabrication process, or interactions between the graphene flake and the substrate), $L^2$ is the flake area and $C_b = \varepsilon_r \varepsilon_0 L^2 / d$ is the capacitance of the bilayer with dielectric constant $\varepsilon_r$. The gap is calculated self-consistently, and Figure 32(a) shows the calculated value of the gap for three values of the bare asymmetry. Figure 32(b) shows the densities on the two individual layers for a finite bare asymmetry $U_0 = \gamma_1/5 = 78\,\mathrm{meV}$. The result of the screening is to reduce the zero density gap so that $U(0) < U_0$. In the limiting case $\gamma_1$, $\epsilon_\mathrm{F} \gg |U|$, an analytic expression for $U(n)$ can be derived. Integrating the wave function amplitudes to find the layer density of the partially occupied bands, the densities are

$$n_{1(2)} \approx \frac{\mathrm{sgn}(\epsilon_\mathrm{F})\, p_\mathrm{F}^2}{2\pi\hbar^2} \pm \frac{\gamma_1 U}{2\pi\hbar^2 v^2}\left[\frac{\epsilon_0}{\gamma_1} + \frac{\epsilon_0^2}{\gamma_1^2} - \frac{1}{2}\ln\left(\frac{\epsilon_0}{\gamma_1}\right)\right],$$

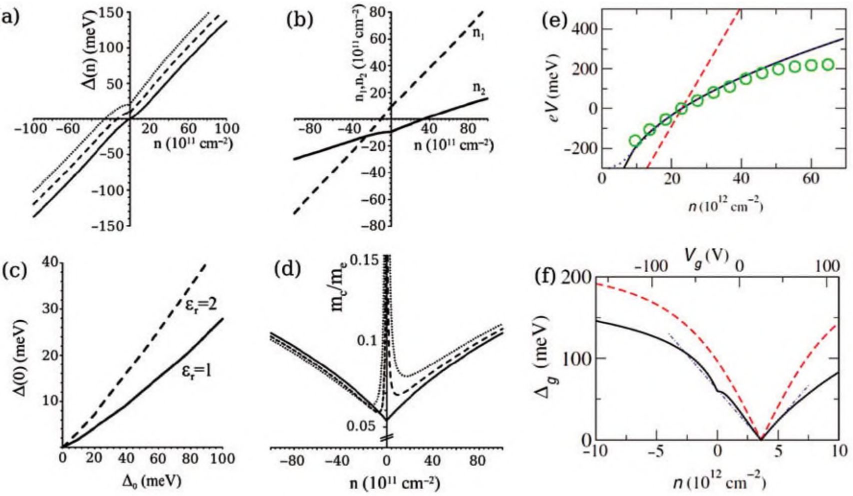

Figure 32. (a) Numerical evaluation of the bilayer asymmetry $U(n)$ for different values of the bare asymmetry: $U_0 = 0$ (solid line), $U_0 = \gamma_1/10 = 39\,\mathrm{meV}$ (dashed line) and $U_0 = \gamma_1/5 = 78\,\mathrm{meV}$ (dotted line), using typical parameter values $\gamma_1 = 0.39\,\mathrm{eV}$, $d = 3.55\,\text{Å}$, $\varepsilon_r = 1$ and $v = 8.0 \times 10^5\,\mathrm{m\,s^{-1}}$. (b) Layer densities $n_2$ (solid) and $n_1$ (dashed) as functions of $n$ for $U_0 = \gamma_1/5 = 78\,\mathrm{meV}$. (c) $U(0)$ as a function of $U_0$ for $\varepsilon_r = 1$ (solid line) and $\varepsilon_r = 2$ (dashed). (d) The cyclotron mass in units of the bare electronic mass for different values of $U_0$ as in (a). (e) $U(n)$, where the solid and dotted lines are the result of the self-consistent procedure for $\gamma_1 = 0.2\,\mathrm{eV}$ and $\gamma_1 = 0.4\,\mathrm{eV}$, respectively; the dashed line is the unscreened result; the circles represent $U(n)$ measured by ARPES [140]. (f) Band gap $\tilde{U}$ as a function of density (bottom axis) and gate voltage (top axis): solid and dashed lines are for the screened and unscreened cases, respectively. The thin dashed-dotted line is a linear fit to the screened result at small biases. ((a)–(d) Reprinted with permission from E. McCann, Physical Review B, 74, 161403, 2006 [178]. Copyright © (2006) by the American Physical Society); ((e) and (f) Reprinted with permission from E.V. Castro *et al.*, Physical Review Letters, 99, 216802, 2007 [181]. Copyright © (2007) by the American Physical Society.)

where the 'ungapped' energy is $\epsilon_0 = (\gamma_1/2)\left[\sqrt{1 + 4v^2 p_F^2/\gamma_1^2} - 1\right]$. In the limit discussed, $v^2 p_F^2 \approx \epsilon_F^2 + \gamma_1 |\epsilon_F|$ so that $\epsilon_0$ is independent of $U$ and Equation (44) is used to find

$$U \approx \frac{U_0 + e^2 L^2 n/(2C_b)}{1 + \Lambda\left[\frac{\epsilon_0}{\gamma_1} + \frac{\epsilon_0^2}{\gamma_1^2} - \frac{1}{2}\ln\left(\frac{\epsilon_0}{\gamma_1}\right)\right]}.$$

This approximation is valid for intermediate densities $U, \tilde{U} \ll |\epsilon_F| < \gamma_1$ where $\epsilon_F \approx \epsilon_0$. The effectiveness of the screening is given by the parameter $\Lambda = e^2 L^2 \gamma_1/(2\pi\hbar^2 v^2 C_b)$, which depends on the model parameters, as illustrated in Figure 32(c). Here $U(0)$ is shown as a function of $U_0$ for $\varepsilon_r = 1$ (solid line) and $\varepsilon_r = 2$ (dashed line). It is clear that the gap increases with the dielectric constant.

According to Castro *et al.* [181], the screened potential difference between the two layers is given by

$$U = \left(2 - \frac{n}{n_0} + \frac{\Delta n(n, V)}{n_0}\right)\frac{n_0 e d}{2\epsilon_0},$$

where $\Delta n(n, V)$ is the induced charge imbalance between the two layers, which is calculated through the weight of the wave functions in each layer. This charge imbalance produces an internal electric field which screens the external one. Figure 32(e) shows the comparison of the screened and unscreened calculations with experimental data taken in ARPES measurements by Ohta *et al.* [140]. The unscreened model cannot accurately describe the experimental data, whereas the results of the self-consistent procedure do. The theoretical dependence of the gap on the electron density is shown in Figure 32(f), along with a linear fit (valid in the small gap regime only). The theory predicts saturation of the gap $U \approx \gamma_1$ at large biases.

Pereira *et al.* [182] performed an analytical study of the effect of a band gap and changing electron density on the length of the interlayer dimer bonds. In their model, the atoms not involved in the bonding are assumed to be static, and a uniform displacement of the $A_u$ and $B_l$ atoms towards each other is considered assuming that the Fermi energy is in the conduction band. The Mexican hat shape of the band structure plays a role by changing the topology of the Fermi surface, and introducing non-monotonicity into the displacement. Two densities,

$$n^* = \frac{g\mathcal{A}_c V^2}{4\pi v^2} \quad \text{and} \quad n^{**} = \frac{g\mathcal{A}_c(V^2 + 2\gamma_1^2)}{4\pi v^2}$$

characterize the behavior, where $\mathcal{A}_c$ is the area of the unit cell. The quantity $n^*$ designates the density which corresponds to the Fermi level being at the top of the Mexican hat, and sets the scale for the minimum of the lattice displacement. As the density is increased further, the displacement saturates with the onset of saturation being marked by $n^{**}$. Since there are a number of poorly-known parameters in the model, the quantitative results are unreliable.

### 3.3.2. *Experimental evidence of gap*

Experimental verification of the predicted band structure of gapped bilayer graphene has been obtained in two ways. Firstly, it has been shown by Ohta *et al.* [140] that

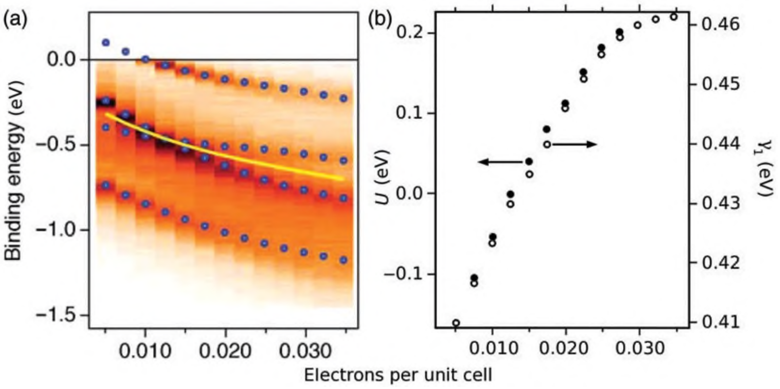

Figure 33. (Colour online) Variation of states at the K point with increasing potassium coverage. (a) The image map shows the energy distribution curve at K as a function of potassium coverage. The blue markers are the fitted positions of the tight-binding $\pi$ and $\pi^*$ bands, and the yellow line indicates $E_D$. The closing and reopening of the gap between $\pi$ and $\pi^*$ states are clearly shown. (b) The influence of doping concentration on the band parameters $U$ (filled dots) and $\gamma_1$ (open circles) (Reprinted figure with permission from T. Ohta *et al.*, Science, 313, p. 951, 2006 [140]. Copyright © (2006) The American Association for the Advancement of Science.).

*n*-type doping of a bilayer graphene flake by potassium atoms causes an increase in the total charge density on the upper layer which generates a static electric field which was characterized by $U$. Since the screening length ($\sim$4 Å) is comparable to the interlayer separation ($d \approx 3.4$ Å), the screening of this charge is incomplete and a net dipole field results between the two layers. Ohta and Bostwick [140,179] used ARPES to determine the low-energy band structure of the bilayer and hence determined the gap and other band structure parameters. Figure 33(a) shows the evolution of the four $\pi$ bands as the concentration of potassium dopants increases. At minimal doping, the remnant charge asymmetry from the manufacturing process and substrate interactions causes the bilayer to be slightly positively doped and a small gap is seen between the middle two bands. For the doping of approximately 0.012 electrons per unit cell, the bilayer is overall charge-neutral and the gap closes. Increasing the doping further provides overall negative charge density and the gap reopens. Figure 33(b) shows the evolution of the interlayer potential difference $U$ as a function of the dopant concentration (filled dots). For moderate dopant density, the change in the potential is linear and moves through zero at approximately 0.012 electrons per unit cell, precisely coinciding with the closing of the gap. Castro *et al.* [181] also demonstrated the existence of a gap by chemically doping a bilayer in the case of a finite magnetic field.

The second method of producing a gap in the low-energy spectrum is to use electronic gating. Infra-red spectroscopy [183,184] has shown band gaps of up to 250 meV (Figure 35) which have a slight nonlinear dependence on both photon energy and electronic density. An example device is shown in Figure 34(a), where a top gate is fabricated over an AB-stacked graphene bilayer (Figure 34b). The presence of this gate and the back gate allow two electrical displacement fields $D_b$ of the back gate and $D_t$ of the top gate (Figure 34c) to be

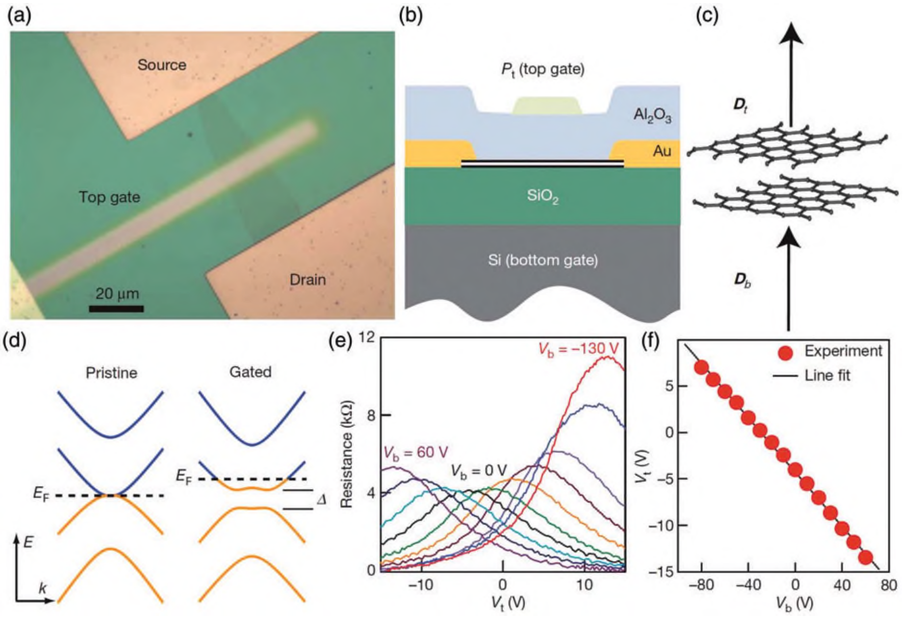

Figure 34. Dual-gated bilayer graphene. (a) Optical microscopy image of the bilayer device (top view). (b) Illustration of a cross-sectional side view of the gated device. (c) Sketch showing how gating of the bilayer induces top ($D_t$) and bottom ($D_b$) electrical displacement fields. (d) Left, the electronic structure of a pristine bilayer has zero band gap (where $k$ denotes the wave vector.) Right, upon gating, the displacement fields induce a non-zero band gap $U$ and a shift of the Fermi energy $E_F$. (e) Graphene electrical resistance as a function of top gate voltage $V_t$ at different fixed bottom gate voltages $V_b$. The traces are taken with 20 V steps in $V_b$ from 60 V to $-100$ V and at $V_b = -130$ V. The resistance peak in each curve corresponds to the charge-neutrality point (CNP) where $D_b = D_t$ for a given $V_b$. (f) The linear relation between top and bottom gate voltages that results in bilayer CNPs (Reprinted figure with permission from Y. Zhang *et al.*, Nature, 459, p. 820, 2009 [184]. Copyright © (2009) Nature Publishing Group.).

independently controlled. The average of these fields breaks the inversion symmetry of the graphene flake and opens the gap at the charge neutrality point. The difference of these fields leads to a net carrier doping, so that the position of the Fermi level and the size of the band gap may be controlled independently (Figure 34d). If the back gate voltage is fixed and the top gate voltage swept, traces such as those in Figure 34(e) are found, showing that the charge-neutrality point (corresponding to the peak in the resistance) shifts, and the magnitude of the peak resistance increases with both increasing positive and negative back gate voltage. This increase in the peak resistance may be linked to an increasing magnitude of the band gap.

The infra-red spectroscopy measurements show that the absorption peak near $\gamma_1 \approx 0.4$ eV associated with the inter-band optical transitions splits into two when the top gate is applied. One peak moves downwards in energy with increasing gate voltage, the other upwards, as in the left-most panel of Figure 35. This behavior is explained by noting that peak 1 is due to transitions between the lower and upper conduction bands, while peak 2 is due to transitions from the upper valence band to the upper conduction band. Therefore, if a gap is present between the upper valence

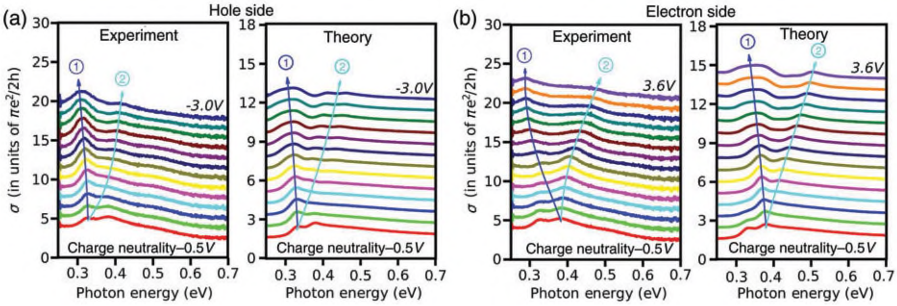

Figure 35. Experimental and theoretical spectra of the IR conductivity in units of $\pi e^2/2h$ for (a) the hole side and (b) the electron side as a function of photon energy. Charge neutrality occurs at $V = -0.5\,\text{V}$. In the case of hole doping, the traces correspond to $V = -0.5$, $-0.8$, $-1.0$, $-1.2$, $-1.4$, $-1.6$, $-1.8$, $-2.0$, $-2.2$, $-2.4$, $-2.6$, $-2.8$ and $-3.0\,\text{V}$ from bottom to top. In the electron side, the traces are for $V = -0.5$, $-0.4$, $-0.3$, $-0.2$, 0.0, 0.2, 0.4, 0.8, 1.2, 1.6, 2.0, 2.4, 2.8, 3.2 and 3.6 V. The theoretical data is obtained via the Kubo formula (Reprinted figure with permission from K.A. Mak *et al.*, Physical Review Letters, 102, 256405, 2009 [183]. Copyright © (2009) by the American Physical Society.).

and lower conduction bands, and the Fermi energy is located in the conduction band, the energy of the transition associated with peak 1 will decrease, whereas that associated with peak 2 will increase. The energy gap between the two peaks is then precisely the band gap. The left-hand plots in both Figure 35(a) and (b) are experimental data showing exactly this trend. A maximum gap of ~200 meV is seen for a gate voltage of 3.6 V. The peaks also broaden because the bands are not exactly parallel, so a wider range of transition energies are allowed for stronger gating.

As has already been stated, one of the attractive prospects for the utilization of graphene in technological applications is in ballistic field-effect transistors. The external tunability of the band gap in the biased bilayer is particularly exciting in this context, and attempts have been made to implement current-switching devices using this idea [185]. Transport measurements showed a gate-induced insulating state and significantly non-Ohmic current–voltage characteristics at low temperatures, but the band gap revealed by these transport measurements was significantly lower than predicted by theory, and current switching was unobtainable at high temperature. While these experiments may demonstrate the proof of principle for these devices, there are still many challenges to be overcome. In addition, the careful analysis of the low-temperature data revealed that the transport is best described by disorder induced by variable range hopping in an insulating material where impurity states localized in the band gap are the predominant mechanism for transport. Thermally activated transport did not qualitatively explain the experimental results.

### 3.3.3. Ab-initio *simulations*

Various studies have been carried out on the effect of the interlayer electric field using first principles techniques [168,169,186–188]. There is some confusion in the literature because for the two main approximations for the exchange and correlation potentials, the local density approximation (LDA) and generalized gradient

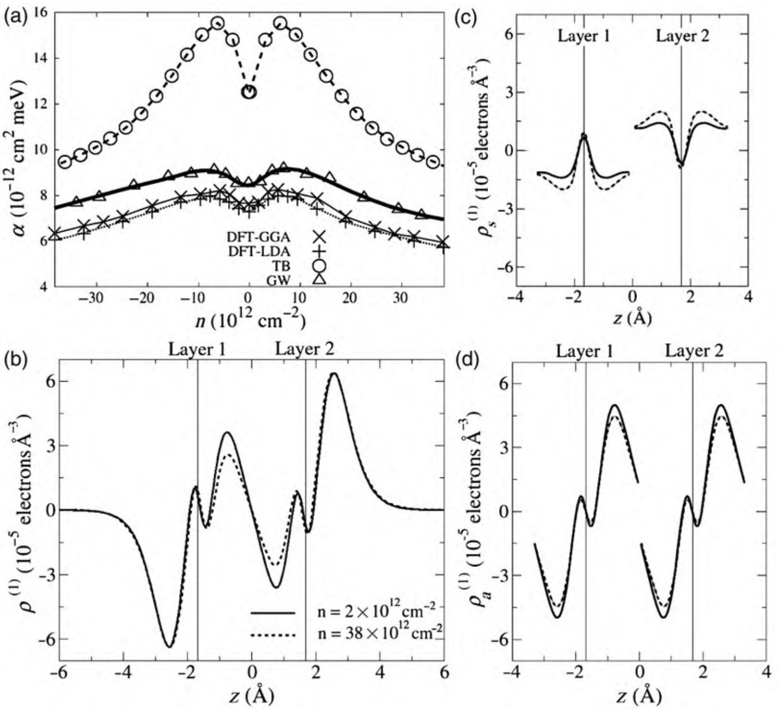

Figure 36. (a) $\alpha$ (as defined in Equation (45)) as a function of doping $n$, for an electronic temperature of 300 K calculated with DFT-GGA (crosses), and DFT-LDA (pluses), calculated using the TB model with $\gamma_0 = 3.1\,\text{eV}$ and $\gamma_1 = 0.4\,\text{eV}$ (circles) and using the GW correction (up-triangles). The continuous thick line is the fit of the GW result. (b) Planar average of the linearly induced charge (per unit volume) $\rho^{(1)}$ for bilayer graphene in the presence of an external electric field $E_{\text{av}} = 1.6 \times e/(2\varepsilon_0)10^{12}\,\text{cm}^{-2}$ for doping level $n = 2 \times 10^{12}\,\text{cm}^{-2}$ (continuous line) and $n = 38 \times 10^{12}\,\text{cm}^{-2}$ (dashed line). (c) The symmetric component, $\rho_s^{(1)}$; (d) the antisymmetric component $\rho_a^{(1)}$, with respect to each layer, of the linearly induced charge $\rho^{(1)}$ shown in (b) for the same doping levels (Reprinted figure with permission from P. Gava *et al.*, Physical Review B, 79, 165431, 2009 [169]. Copyright © (2009) by the American Physical Society.).

approximation (GGA) have been shown to give quantitatively different results for the optimum interlayer spacing $d$ and the band gap $U$.

The most thorough study was published by Gava *et al.* [169] in which they describe the size of the gap as a function of the doping and the external electric field. They demonstrate first that the size of the gap is linearly dependent on the charge imbalance between the two layers, and define the linear coefficient as

$$U(n, E_{\text{av}}) = \alpha(n)(n_1 - n_2), \qquad (45)$$

where $n_{1,2}$ are the densities on the two layers, and $E_{\text{av}}$ is the applied electric field. In the absence of electronic screening, $\alpha$ is independent of the doping, and $\alpha^{\text{bare}} = \frac{de^2}{2\epsilon_0} = 30.3 \times 10^{-12}\,\text{cm}^2\,\text{meV}$. The DFT results within the LDA, GGA and GW approximations are compared to tight-binding results employing a simple electrostatic model to account for the screening in Figure 36(a). It is clear from the figure that while all four estimations give the same qualitative dependence, the tight-binding approximation gives a significantly higher slope than any of the first principles results. There are two possible reasons for this discrepancy: The crude electrostatic model used in the self-consistent process in the tight-binding model, and systemic differences in the calculated band structures between the first principles and tight-binding results. The authors demonstrate that both factors play a significant role. The differences in charge transfer which lead to the reduced screening between the two models is illustrated in Figure 36(b–d). The linearly induced charge (per unit volume) is

$$\rho^{(1)}(z; n, E_{\mathrm{av}}) = \frac{\partial \rho(z; n, E_{\mathrm{av}})}{\partial E_{\mathrm{av}}} E_{\mathrm{av}} \approx \frac{1}{2}[\rho(z; n, E_{\mathrm{av}}) - \rho(z; n, -E_{\mathrm{av}})],$$

where $\rho(z;\, n,\, E_{\mathrm{av}})$ is the planar average of the charge density (per unit volume) at doping $n$ and in the presence of an external average electric field $E_{\mathrm{av}}$. The charge density $\rho^{(1)}$ is antisymmetric with respect to $z = 0$ (which corresponds to the point half-way between the two graphene planes) and is plotted in Figure 36(b). We see that the electronic screening is characterized by the charge transfer between the two layers, and an intralayer polarization (which is also present in the monolayer). The density is decomposed into a symmetric component $\rho_s^{(1)}$ and an antisymmetric component $\rho_a^{(1)}$ with respect to each individual layer defined by

$$\rho_{s/a}^{(1)}(z) = \frac{1}{2}\left\{\rho^{(1)}(z) \pm \rho^{(1)}[\mathrm{sgn}(z)d - z]\right\}.$$

These are shown in Figure 36(c) and (d), respectively. Clearly, these quantities are related to the inter- and intralayer charge transfer, respectively. The antisymmetric contribution is very similar to the induced charge in a single monolayer, and is of the same order of magnitude as the total induced charge in the bilayer. On this basis, the authors conclude that the intralayer polarization gives an important contribution to the screening properties of the system. This contribution is not taken into account in the tight-binding approximation, and is the major contribution to the discrepancy between these two models. The authors also show that the GW correction adds a contribution to the density dependence of the linear parameter $\alpha$ (Figure 36a) which can be explained within a perturbation theory analysis. Also, the temperature dependence of the linear parameters is small.

Other notable works include the comparison of the AB and AA stacking arrangements by Huang *et al.* [188] and Aoki *et al.* [186], in which they demonstrate that AB stacking is energetically favorable over the AA arrangement. Also, Min *et al.* [168] published the first systematic DFT study of the gapped bilayer, showing that the size of the gap saturates with increasing interlayer potential. They also claim that the exchange potential may contribute to the discrepancies between the DFT and tight-binding results, and that the logarithmic divergence of the screening ratio at small gate voltage (demonstrated within the tight-binding model by McCann [178]) is reproduced in their calculations. Yu *et al.* [189] considered the polarizability of graphene stacks within the LDA approximation, and they also found the same qualitative picture sketched above. Specifically, the gap saturation was at approximately 0.25 eV, although the gap size at fields where electric breakdown will start to occur in $SiO_2$ was 0.17 eV. They also investigated the distribution of charge between layers and sublattices, finding that an external field induces a significant electron concentration on one layer, with a positive charge cloud on the other, and that the lattice sites not involved in the dimer ($\gamma_1$) bonding have higher density. Finally, atomistic calculations have been presented by Fiori *et al.* [187] to assess the practicality of FET devices implemented in gapped bilayer graphene. They claim that there is no conceptual issue, but that the band gap is not wide enough to support a sufficiently high on/off current ratio.

## 3.4. *Quantum Hall effect*

The quantum Hall effect in bilayer graphene is a fascinating manifestation of the massive chiral nature of the low-energy quasiparticles. When a magnetic field with a large component perpendicular to the graphene plane is applied, the electron spectrum splits into Landau levels (LLs), just as in a traditional two-dimensional electron system, or as in monolayer graphene (Section 2.1). However, the form of the dependence of the energy of these levels on the magnetic field, level index, density and other parameters are qualitatively different from both of these examples. The chiral nature of the electrons is reflected in the presence of zero-energy levels, and the increased Berry's phase manifests in the doubled degeneracy of these levels. The quadratic low-energy dispersion is represented by the linear dependence of the LL spectrum on the magnetic field, and the near-linear dependence on the LL index. We shall begin in this section by presenting the experimental evidence for the novel quantum Hall effect in bilayer graphene. Then, in order to describe the behavior of the low-energy Landau levels, the two band tight-binding model introduced by McCann *et al.* [139] will be used in Section 3.4.2 to demonstrate the main features. The magneto-optical properties are discussed in Section 3.4.3, the trigonal warping is included in Section 3.4.4 and electron–electron interactions and the perculiar properties of the zero modes are reviewed in Section 3.4.5.

### 3.4.1. *Experimental picture*

The first report of an observation of the quantum Hall effect in bilayer graphene was given by Novoselov *et al.* [141]. Using samples obtained by the microcleavage technique and fashioned into multi-terminal transistor devices, the low-temperature transport properties were measured in strong magnetic fields. Figure 37(a) shows typical traces of the longitudinal and transverse resistivities at fixed electron density as a function of the magnetic field. Plateaus in the Hall resistivity accompanied by dips in the longitudinal resistivity are clearly seen. The sequence of QHE plateaus is described by $\rho_{xy} = h/4ne^2$ (where $n$ is an integer designating the level), as would be expected in a traditional two-dimensional electron system with spin and valley degeneracies. However, a significant discrepancy with this case is manifest at small filling factors, as shown in Figure 37(b): the expected level at zero density is not present, leading to a double-sized step across the zero density point, and indicating a Landau level with doubled degeneracy relative to the higher Landau levels. The absence of a plateau at zero energy resembles the behavior of the massless Dirac fermions observed in the monolayer material (Section 2.2). Figure 37(c–f) shows that

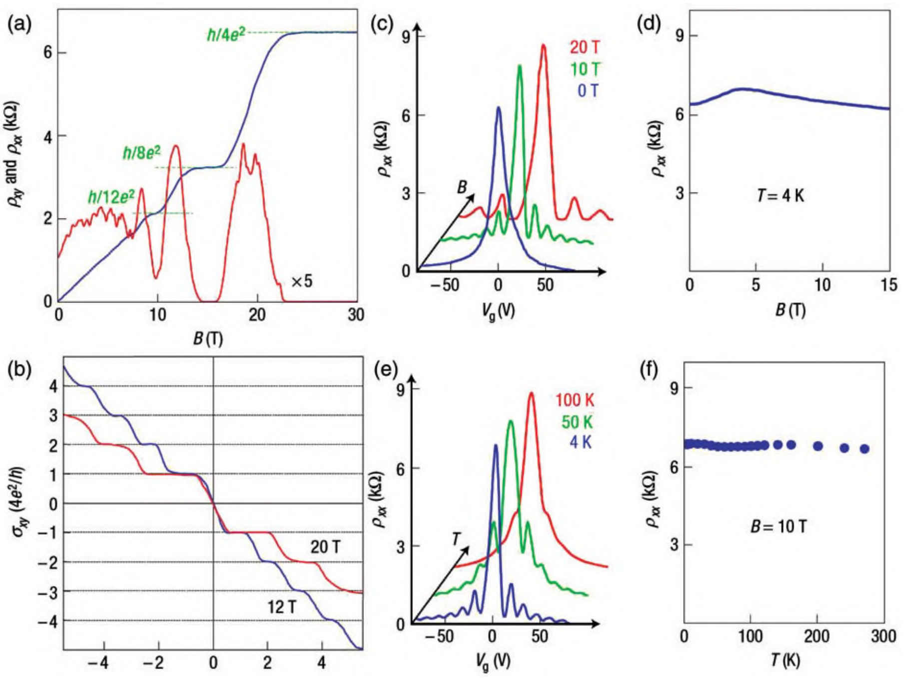

Figure 37. (a) Hall resistivities $\rho_{xy}$ and $\rho_{xx}$ measured as a function of $B$ for fixed concentrations of electrons $n \approx 2.5 \times 10^{12}\,\mathrm{cm}^{-2}$ induced by the electric field effect. The known geometry of the devices allowed the authors to convert the measured resistance into $\rho_{xx}$ with an accuracy of better than 10%. (b) $\sigma_{xy}$ plotted as a function of $n$ at a fixed $B$ and temperature $T = 4\,\mathrm{K}$. Positive and negative $n$ correspond to field-induced electrons and holes, respectively. $\sigma_{xy}$ crosses zero without any sign of the zero-level plateau that would be expected for a conventional 2D system. (c–f) Resistivity of bilayer graphene near zero concentration as a function of magnetic field and temperature. The peak in $\rho_{xx}$ remains of the order of $h/4e^2$, independent of $B$ (c,d) and $T$ (e,f). This yields no gap in the Landau spectrum at zero energy (Reprinted figure with permission from K.S. Novoselov *et al.*, Nature Physics, 2, p. 177, 2006 [141]. Copyright © (2006) Nature Publishing Group.).

the height of the $\rho_{xx}$ peak is only weakly dependent on magnetic field and temperature, which again contrasts starkly with the traditional two-dimensional case.

### 3.4.2. *Tight-binding description of low-energy Landau levels*

The main features of the Landau level spectrum are best exhibited in the low-energy effective model introduced by McCann and Falko [139] and discussed in Section 3.2.3. The leading term in the two-band Hamiltonian for bilayer graphene is

$$\mathcal{H} = -\frac{1}{2m}(\vec{\sigma} \cdot \vec{p})\sigma_x(\vec{\sigma} \cdot \vec{p}),$$

which corresponds to the continuum limit of the nearest neighbor tight-binding theory in the K valley. To account for a magnetic field characterized by the vector potential $\vec{A}$, we employ the generalized momentum operator $\vec{p} - q\vec{A}$, where $q = -e$

such that $e > 0$ is the electron charge. In that case, the matrix form of the Hamiltonian becomes

$$\mathcal{H} = -\frac{1}{2m}\begin{pmatrix} 0 & (p_x + eA_x - \mathrm{i}p_y - \mathrm{i}eA_y)^2 \\ (p_x + eA_x + \mathrm{i}p_y + \mathrm{i}eA_y)^2 & 0 \end{pmatrix}.$$

We shall work within the Landau gauge defined by $\vec{A} = Bx\vec{\ell}_y$ so that the magnetic field $\vec{B} = \vec{\nabla} \times \vec{A} = B\vec{\ell}_z$. In this case, the $\pi$ and $\pi^\dagger$ operators correspond to lowering and raising operators for the basis of magnetic oscillator functions given by $\varphi_m = \mathrm{e}^{\mathrm{i}k_y y}\,\phi_m(x)$. These functions are defined so that

$$\pi\phi_0 = 0, \quad \pi\phi_m = -\frac{\mathrm{i}\hbar}{l_B}\sqrt{2m}\phi_{m-1}, \quad \pi^\dagger\phi_m = \frac{\mathrm{i}\hbar}{l_B}\sqrt{2(m+1)}\phi_{m+1}, \qquad (46)$$

where $l_B = \sqrt{\hbar/(eB)}$ is the magnetic length, and the indices $m \geq 0$ are integers. Using these relations in the Schrödinger equation gives the spectrum of discrete levels $\varepsilon_{\mathfrak{n}}^{\pm}$ and associated wave functions $\Phi_{\mathfrak{n}}^{\pm}$ as[6]

$$\varepsilon_0 = 0, \quad \Phi_0 = \begin{pmatrix} \phi_0 \\ 0 \end{pmatrix}; \quad \varepsilon_1 = 0, \quad \Phi_1 = \begin{pmatrix} \phi_1 \\ 0 \end{pmatrix};$$

$$\varepsilon^{\pm}_{|\mathfrak{n}|\geq 2} = \pm\hbar\omega_c\sqrt{|\mathfrak{n}|(|\mathfrak{n}|-1)}, \quad \Phi^{\pm}_{|\mathfrak{n}|\geq 2} = \frac{1}{\sqrt{2}}\begin{pmatrix} \phi_{|\mathfrak{n}|} \\ \pm\phi_{|\mathfrak{n}|-2} \end{pmatrix},$$

where $\omega_c = eB/m = \hbar/(\lambda_B^2 m) = 2\hbar v^2/(\lambda_B^2\gamma_1)$ is the cyclotron frequency in bilayer graphene. Each of these levels is four-fold degenerate due to the combined two-fold spin and valley degeneracies. This derivation illustrates the existence of the eight-fold degenerate zero energy state, since the Hamiltonian $\begin{pmatrix} 0 & \pi^{\dagger 2} \\ \pi^2 & 0 \end{pmatrix}$ along with the relations in Equation (46) shows clearly that it is possible to act twice with $\mathcal{H}$ on the wave function $\begin{pmatrix} \phi_1 \\ 0 \end{pmatrix}$ and return a zero eigenvalue. In the monolayer case (Section 2.1), the Hamiltonian contains only linear powers of $\pi$, so it is possible to act only once to return the zero eigenvalue. The magnetic field dependence of these levels is contained entirely in $\omega_c = eB/m$, so that the Landau levels depend linearly on the field, in contrast to the monolayer where they show $\sqrt{B}$ dependence. Also, the Landau level spacing (i.e. the dependence on $\mathfrak{n}$) shows that the levels are nearly equally spaced, apart from the lowest few where the deviation of $\sqrt{|\mathfrak{n}|(|\mathfrak{n}|-1)}$ from equal spacing is not small. The eightfold degeneracy in the $\varepsilon = 0$ Landau levels is unusual amongst two-dimensional systems, and suggests that electron–electron interactions in a bilayer could give rise to a number of strongly correlated quantum Hall states. We defer its discussion until Section 3.4.5.

A more complete picture of the behavior of the Landau levels in bilayer graphene is given by the full four-band tight-binding model. In this case, the Hamiltonian in the same basis as used previously, i.e. where the wave function component orders are swapped between the K and K′ valleys is [190]

$$\mathcal{H} = \begin{pmatrix} U_0 - \xi U/2 & 0 & 0 & \xi v\pi^\dagger \\ 0 & U_0 + \xi U/2 & \xi v\pi & 0 \\ 0 & \xi v\pi^\dagger & U_0 + \xi U/2 & \gamma_1 \\ \xi v\pi & 0 & \gamma_1 & U_0 - \xi U/2 \end{pmatrix},$$

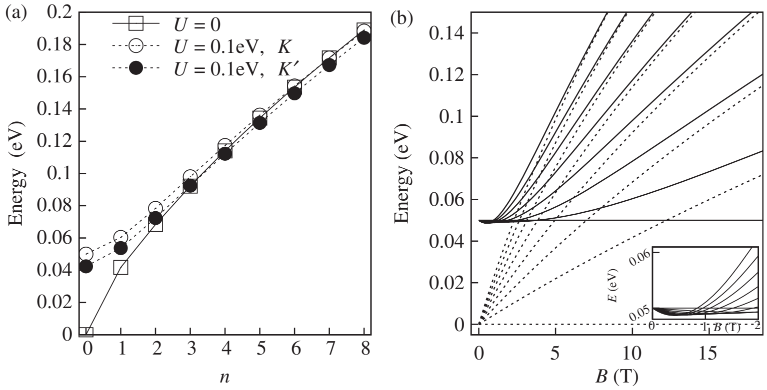

Figure 38. (a) The low-energy Landau levels as a function of level index $n$ for zero and finite gap $U$ at $B = 10$ Tesla. The lifted valley degeneracy is manifest for finite gap. (b) The first eight Landau levels as a function of magnetic field for zero and finite gap $U$ in the K valley only. The gap causes additional level crossings at small magnetic field, and it is clear that the $n = 0$ level is constant as a function of field. The inset shows the LL spectrum for low magnetic field, displaying the additional crossings induced by the interlayer asymmetry. We have taken $\gamma_1 = 0.4\,\text{eV}$, $v = 1.0 \times 10^6\,\text{m s}^{-1}$ and $U_0 = 0$ throughout.

where $U_0$ is the average potential of the two layers, $U$ is the total energy difference between the two layers, and as before, $\pi = p_x + eA_x + \mathrm{i}(p_y + eA_y)$. The eigenvalues associated with this Hamiltonian are the solutions of the quartic polynomial

$$\begin{aligned}&\left[(E_b(n,B) - U_0 + \xi U/2)^2 - (n+1)w^2\right]\left[(E_b(n,B) - U_0 - \xi U/2)^2 - nw^2\right]\\&\quad - \left[(E_b(n,B) - U_0)^2 - U^2/4\right]\gamma_1^2 = 0,\end{aligned}$$

where $w = \sqrt{2}\hbar v / l_B$. Solutions to this equation cannot be written in a simple form (as they could for $E^2$ in the zero magnetic field case), so we present numerical evaluations of the eigenvalues in Figure 38. In this case, the labels of the Landau levels are defined as follows. The conduction and valence band each have their own ladder of levels, with indices $n = 0, 1, \ldots$. To distinguish one band from another, we use the label $b = c, v$ for the conduction and valence bands, respectively. The presence of a potential difference between the two layers gives rise to the splitting of the zero energy LL. The Mexican hat structure of the zero-field energy relation is replicated in the Landau level spectrum at low fields [175] by the fan of levels which cross each other in a complicated pattern (see the inset to Figure 38b). Pereira *et al.* [190] display a comparison of these levels with those derived from the two band approximation discussed above. They find that the two-band theory underestimates the Landau level energy at moderate field, but that the qualitative features of the levels are the same.

Some particular cases of this equation are easy to evaluate. Firstly, the $U = 0$ case yields the exact eigenvalues

$$E_b(n,B) = \pm\sqrt{\frac{(2n+1)\hbar^2 v^2}{l_B^2} + \frac{\gamma_1^2}{2} \pm \sqrt{\left(\frac{\hbar^2 v^2}{l_B^2} + \frac{\gamma_1^2}{2}\right)^2 + \frac{2n\gamma_1^2\hbar^2 v^2}{l_B^2}}},$$

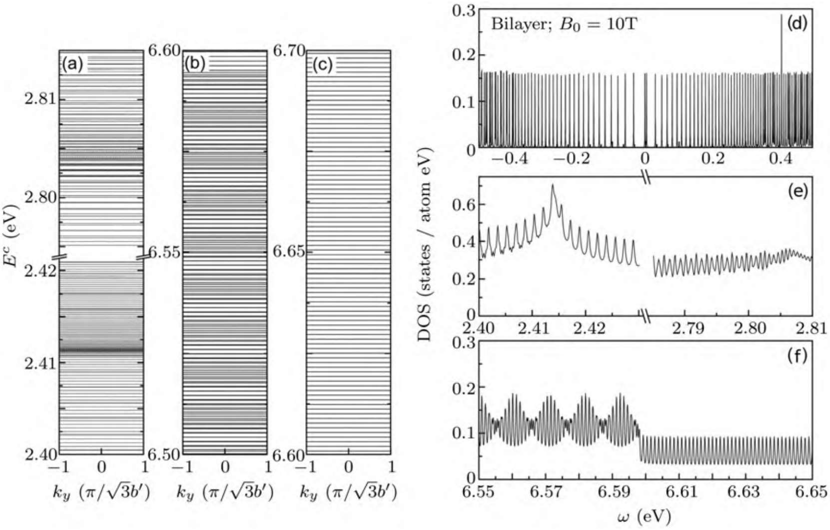

Figure 39. The (a) moderate- and (b,c) high-energy LLs of bilayer graphene at $B = 10$ Tesla. Density of states of bilayer graphene for $B = 10$ Tesla at (d) low, (e) moderate and (f) high energies (Reprinted figure with permission from Y.H. Lai *et al.*, Physical Review B, 77, 085426, 2008 [193]. Copyright © (2008) by the American Physical Society.).

where $b = c$ corresponds to the leading positive sign, and $b = v$ to the negative sign. This expression readily reduces to $E_b(0, B) = 0, \pm\sqrt{\hbar^2 v^2/l_B^2 + \gamma_1^2/2}$ for the $n = 0$ levels. In the symmetric case (i.e. when $U = 0$), both bands have $E(0, B) = 0$ as a solution, restoring the doubly degenerate lowest Landau level.

The Hofstadter butterflies for bilayer graphene have been examined by Nemec *et al.* [191], and transport properties in the case where the chemical potential exceeds $\gamma_1$ has been investigated by Nakamura *et al.* [192].

The Landau level spectrum for the high-energy bands of bilayer graphene was investigated by Lai *et al.* [193]. They used the tight-binding model without the continuum limit to explicitly diagonalize Hamiltonians corresponding to finite-sized bilayer graphene flakes in a magnetic field. They focused on three energy regions: the low-energy region where the results of analytical solutions of the continuum limit of the model were recovered; the high-energy limit where the Landau levels are composed of electrons originating from the split bands at zero field (Figure 39b and c) and the intermediate regime (Figure 39a). The intermediate regime corresponds to the region where the LL density is largest (Figure 39d–f), where a phenomenological broadening of $\Gamma = 0.5$ meV has been included) because the zero-field density of states is highest at the $M$ point of the Brillouin zone. The non-uniformity of the LLs is due to the unequal spacing of LLs in this energy range (not captured in the low-energy approximation to the tight-binding model described above), and is enhanced by the presence of the second group of LLs arising from the split bands. This analysis also includes the interlayer couplings parametrized by $\gamma_3$ and $\gamma_4$, and the intralayer next-nearest neighbor hop $t'$.

### 3.4.3. *Magneto-optical properties of bilayer graphene*

The magneto-optical properties of bilayer graphene were first discussed theoretically by Abergel and Falko [151] who took the non-interacting picture of electrons in bilayer graphene and calculated the selection rules and optical strengths for inter-Landau level transitions.

The selection rules derived within the two-band low-energy effective theory (with Landau levels labelled by $\mathrm{n} \in \{\ldots, -2, 0, 1, +2, \ldots\}$ as explained in the Endnote 6) are stated as follows: transitions between levels for which the magnitude of the LL index differ by one are allowed. For circularly polarized light with right-handed orientation (such that $\vec{\ell}_{\oplus} \propto \vec{\ell}_x - \mathrm{i}\vec{\ell}_y$), the allowed transitions increase the magnitude of the Landau level index. For left-handed polarization ($\vec{\ell}_{\ominus} \propto \vec{\ell}_x + \mathrm{i}\vec{\ell}_y$), allowed transitions decrease the Landau level index by one. This is illustrated in Figure 40(a), where arrows represent transitions corresponding to the absorption of radiation by the graphene flake. The associated absorption spectrum and a comparison with the monolayer spectrum is shown in Figure 40(b). Several points bear discussion, the first of which being that the LL spectrum is denser in the bilayer, so that the transition energies are smaller and the spectrum of peaks more tightly packed. This is a direct manifestation of the finite zero-field density of states at the charge-neutrality point in bilayer graphene. Secondly, the peak height shows a different pattern from the monolayer. Apart from a significantly larger lowest-energy peak, all peaks have the same height, in contrast to the monolayer peaks which steadily decrease in height. These selection rules also make it possible to distinguish experimentally between two possible ground states of the half-filled quantum Hall system. If the splitting $\hbar\beta\omega_c$ between the $n = 0$ and $n = 1$ levels is smaller than the Zeeman energy, then the arrangement of electrons between these two levels depends on the details of the correlations between them.[7] It is possible to imagine two model scenarios: first, if the interaction between spins and the magnetic field is strong

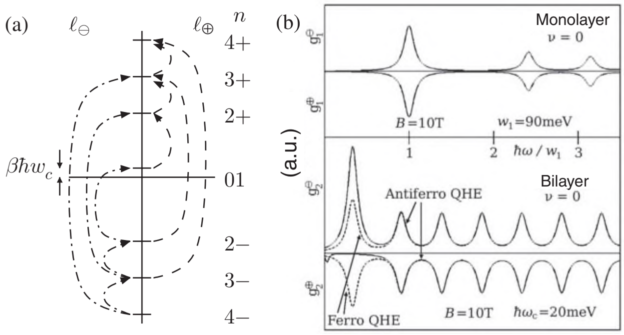

Figure 40. (a) Selection rules for inter-Landau level transitions in bilayer graphene. Allowed transitions in $\ell_{\oplus}$-polarized light increase the magnitude of the LL index by one, $\ell_{\ominus}$-polarized light allow transitions which reduce the magnitude of the LL index by one. (b) Monolayer (top) and bilayer (bottom) far infra-red absorption spectra in $\ell_{\oplus}$ and $\ell_{\ominus}$ polarizations for $B = 10$ Tesla and filling factor $\nu = 0$. Dashed and solid lines describe absorption by ferro- and antiferromagnetic states, respectively. The energy normalization is with respect to $w_1 = \sqrt{2}\hbar v / l_B$ (from [151]).

enough to overcome the gap between the levels, it will be energetically favorable for electrons to align their spins and fill half the states of both levels. This state is labelled ‘ferromagnetic’ as a description of the spin ordering. Second, if the correlations or other interactions force the $n = 0$ level to be filled and the $n = 1$ level to be empty, then we label the state ‘antiferromagnetic’. The lowest absorption peak is determined by the $2- \rightarrow 1$ and the $1 \rightarrow 2+$ transitions, so the relative shape of this peak in the two polarizations acts as a probe of the electron ordering of these states. If the antiferromagnetic state is formed, there are electrons in only the $n = 0$ level, so the $1 \rightarrow 2+$ transition is not accessible and the peak in the $\ell_\oplus$ polarization in absent. On the other hand, if the ferromagnetic state is formed, the $n = 1$ is half-filled, so that both transitions are allowed. Therefore there are peaks in the absorption spectra of both polarizations. Additionally, the very low-energy peak corresponding to the $0 \rightarrow 1$ transition is only present in the $\ell_\oplus$ polarization.

The optical transitions in bilayer graphene were also examined within the four-band model in the single particle approximation by Pereira *et al*. [190] as a function of the asymmetry gap and magnetic field. They give analytical expressions for the oscillator strength for transitions, and show the dependence of the transition energy on the magnetic field (Figure 41a). The transition energies are only weakly dependent on the field strength for $B < 5$ Tesla, in contrast with both the monolayer and unbiased bilayer cases. Oscillator strengths for the same transitions are shown in Figure 41(b). There is an asymmetry between the conduction and valence band intra-band transition energies, which increases as the gap size increases, as shown in Figure 41(c). The oscillator strengths also are strongly effected by the gap, as shown in Figure 41(d).

The cyclotron resonance absorption has been studied experimentally, firstly by Sadowski *et al.* [34] who found signatures of the monolayer single particle description in few-layer epitaxial graphene samples, and more recently by Henriksen *et al.* [194]. In the latter work, infra-red spectroscopy was used to

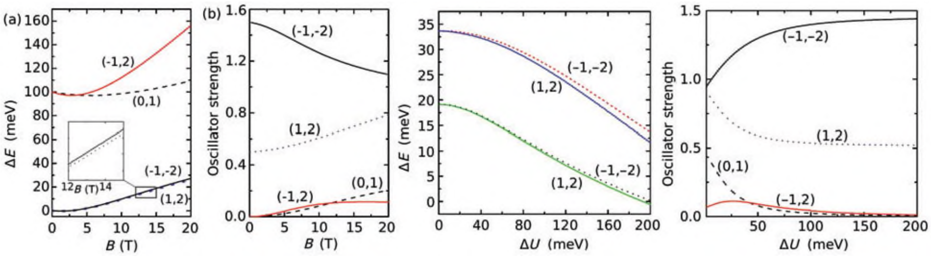

Figure 41. (Colour online) (a) Transition energies in a biased ($U = 100$ meV) graphene bilayer, as a function of the magnetic field $B$ for the dipole-allowed transitions: $0+ \rightarrow 1+$ (black dashed line), $1+ \rightarrow 2+$ (blue dotted line), $1- \rightarrow 2-$ (black solid line), and $1- \rightarrow 2+$ (red solid line), and we use the four-band notation to label the Landau levels. (b) Oscillator strengths as a function of magnetic field for the transitions described in (a). (c) Transition energies as a function of the gap for $1+ \rightarrow 2+$ (blue solid line), and $1- \rightarrow 2-$ (red dashed line) transitions for $B = 20$ Tesla, and $1+ \rightarrow 2+$ (green solid line) and $1- \rightarrow 2-$ (black dotted line) for $B = 10$ Tesla. (d) Oscillator strengths for dipole-allowed transitions in a graphene bilayer as a function of the interlayer potential difference at $B = 5$ Tesla.

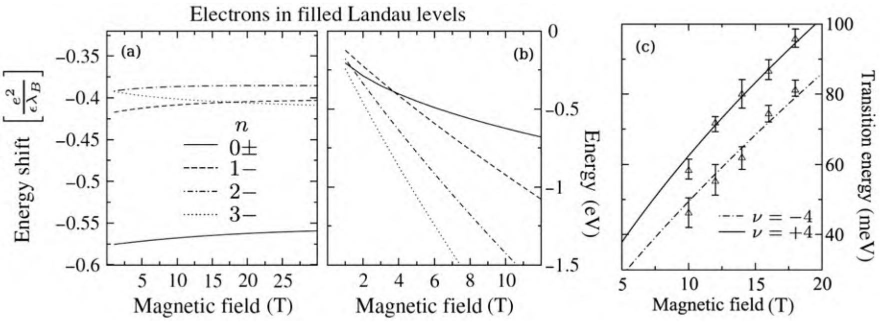

Figure 42. (a) Energy shift per electron of filled LLs. (b) The absolute energy per electron of filled LLs showing the crossing between the $n = 0\pm$ degenerate level and the higher LLs in the valence band. In both plots, $U = 0$. (c) Electron–hole asymmetry in the inter-LL optical transition energy. The experimental data (represented as points) are taken from [194, Figure 2]. The authors take $\gamma_1 = 0.4\,\text{eV}$, and $v = 0.95 \times 10^6\,\text{m s}^{-1}$ (from [195]).

measure the absorption spectrum of bilayer graphene and several significant differences were found between the expected results detailed above and the experimental data. Firstly, a significant (≈20%) electron–hole asymmetry was found for interband transitions. The authors speculated that this asymmetry was either intrinsic, or caused by residual charged impurities. Next, while the transition energies between higher levels follow a roughly $\sqrt{B}$ dependence, those involving the lowest Landau levels were linear in $B$. Additionally, the authors could not get their data to fit the single particle predictions using a single set of fitting parameters ($\gamma_1$ and $v$).

Several attempts have been made to explain these puzzling data. Firstly, Abergel and Chakraborty [195] used an exact diagonalization scheme [72] to point out that the long-range part of the electron–electron interaction is important in this system. They claim that the shift in the energy of a filled LL is significantly higher for the zero-energy LLs than for the higher energy LLs, as shown in Figure 42(a) and (b). This induces a large asymmetry in the energies of transitions that start in the zero-energy levels compared to those that finish in those levels. As shown in Figure 42(c), a single set of fitting parameters ($\gamma_1 = 0.4\,\text{eV}$, $v = 0.95 \times 10^6\,\text{ms}^{-1}$) describe the transitions involving the $n = 0$, 1 levels well. Mucha-Kruczyński *et al.* [196] calculated the single-particle transition energies including the self-consistent screening, and found that finite zero-bias asymmetry (i.e. $U_0 \neq 0$), combined with the screening could account for the electron–hole asymmetry in higher Landau levels. Huang *et al.* [197] studied wide bilayer nanoribbons numerically, finding Landau levels and optical spectra with many of the same features as the bulk system. Kusminskiy *et al.* [198] also included screening via the Thomas–Fermi approximation as a correction to the Hartree–Fock renormalized Landau levels, and found similar agreement between the experimental data and their theory. It is therefore clear that interlayer screening and many body effects are crucial in this system.

### 3.4.4. *The effect of trigonal warping on the Landau level spectrum*

The effects of the next-nearest neighbor hops characterized by $\gamma_3$ can be ignored for $\hbar/l_B > v_3 m$ [139], however, for a weak magnetic field, the trigonal warping and associated Lifshitz transition (Section 3.2.2) adds significant complexity to the low-lying Landau levels. Strong $\gamma_3$ coupling makes Landau levels with $|n| \geq 3$ gain energy, while the $|n| = 2$ levels approach zero in energy [151]. The coupling also allows additional inter-Landau level transitions for the low-lying electrons, with transitions between states for which $|n| = |n'| \pm 2$ and $|n| = |n'| \pm 4$ now permitted, but with reduced optical strength $(v_3 m l_B/\hbar)^2$. This is reflected in the trace of the absorption spectrum. For example, the new peak present at $\omega/\omega_c$ corresponds to transitions $3- \to 1$ and $1 \to 3+$.

### 3.4.5. *Electron–electron interactions in the zero-mode Landau levels*

The zero-mode Landau levels are those described in the two-band model by the indices $n = 0$ and $n = 1$. This model gives their energies as

$$E_0 = \frac{1}{2}\xi U, \quad \text{and} \quad \mathrm{E}_1 = \frac{1}{2}\xi U\big(1 - 2\hbar\omega_c/\gamma_1\big),$$

where, as before, $U$ is a phenomenological parameter which denotes the interlayer gap. The splitting of these two levels due to the kinetic term is $2\hbar\omega_c U/(2\gamma_1) \approx 8.2 \times 10^{-3}\ UB$. Ezawa [199,200] has predicted that the Coulomb interactions will split the eight-fold degeneracy into four two-fold degenerate bands, which are further split by Ising QH ferromagnetism at $\nu = \pm 1, \pm 3$. Therefore, the step in the QHE at zero density will be split into eight plateaus. Misumi *et al.* [201] study the effect of an in-plane electric field on the quartet of states which is split into the positive energy range by the layer asymmetry. In this case, a field-dependent gap $\omega_c\sqrt{(U/\gamma_1)^2 + 2(el_B \mathbf{E}_\parallel/\omega_c)^2}$ is opened between the $(0, K, \pm)$ and $(1, K, \pm)$ levels, which may be detectable in QHE measurements. As the in-plane field strength is increased, the contribution to the dielectric constant and electric susceptibility from these levels enhance those functions around $\nu = 2$. The low-energy excitations and intra-Landau level cyclotron resonance were studied by Barlas *et al.* [202] within the Hartree–Fock approximation. They give Hund's rules for the filling of the octet of levels defined by the $n = 0\pm$ states, where for high field and relatively small gap, the filling order goes such that real spin polarization is maximized, followed by valley pseudospin (which in the $n = 0\pm$ levels is the same as a which-layer pseudospin because of the form of the electron wave functions), followed by the LL pseudospin. This process gives rise to a finite LL pseudospin polarization at any odd-integer filling factor. Within the Hartree–Fock approximation, the low-energy collective modes show a roton minimum at $ql_B \approx 2.3$, there is no contribution to the exciton gap from electron–electron interactions at $q = 0$, and the band splitting approaches the Hartree–Fock theory result as $q \to \infty$. At odd-integer filling factors, there are intra-Landau level cyclotron resonance modes with frequency $\omega_{\mathrm{LL}} = 2\hbar v^2 U/(l_B\gamma_1)^2$ which may lead to QHE plateaus forming at these filling factors if $\omega_{\mathrm{LL}}\tau > 1$.

Abergel and Chakraborty [195] studied the effects of the long-range Coulomb interaction between electrons in the zero-mode octet within an exact diagonalization scheme [72] which allowed exact evaluation of the Coulomb matrix elements and inclusion of exchange and correlation effects. They found finite valley polarization

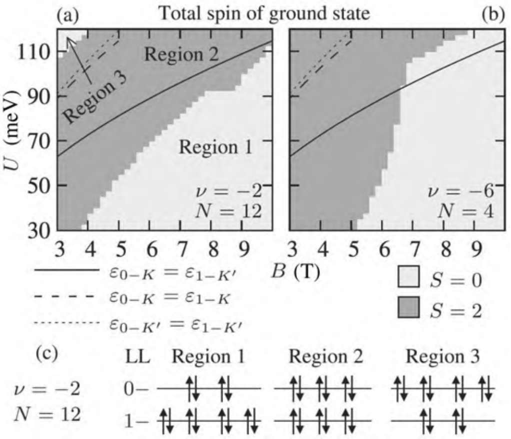

Figure 43. The total spin of the ground state of the (a) $\nu = -2$ and (b) $\nu = -6$ systems. The lines show the crossing points of the single-particle states. The graining is due to the finite interval between data points. (c) The occupancy of the single electron states in the interacting many body ground state for each region of the plot in (a).

at $\nu = -2$, $-6$ over a wide range of gap sizes and magnetic fields. Also, as shown in Figure 43, there is finite spin polarization for certain ranges of fields, corresponding to the interplay between the exchange energy and the splitting of the Landau levels as influenced by the size of the asymmetry gap. The filling of electron states within the octet explains the appearance of the spin polarization. In region 2 (the darker shaded areas), the pairing of electrons within the same Landau level is incomplete, allowing the exchange interaction to minimize the total energy by aligning the unpaired electrons' spins. In regions 1 and 3, all electrons are paired, so the exchange interaction is unable to rearrange the electrons' spins in this way.

Misumi and Shizuya [201,203] discussed the ground state and collective excitations of the zero modes, and their effects on the electronic susceptibility and dielectric constant. Ando [204] analyzed the coupling of electrons in LLs to optical phonon modes and investigated the shift in energy and mode broadening due to this coupling.

Another manifestation of the electron–electron interactions in the zero energy LLs is the gradual lifting of the eight-fold degeneracy as the magnetic field is increased. Transport measurements have shown that in suspended bilayer graphene [205] and exfoliated bilayer graphene on an $SiO_2$ substrate [206], quantum Hall plateaus appear for every integer value of the filling factor. The higher mobility of electrons in suspended bilayer graphene (Feldman *et al.* report $\mu = 1.5 \times 10^5\,\text{cm}^2\,\text{V}^{-1}\,\text{s}^{-1}$ at electron density of $n = 2 - 3 \times 10^{11}\,\text{cm}^{-2}$ compared to the exfoliated samples of Zhao *et al.* who measure $\mu = 1 \times 10^4\,\text{cm}^2\,\text{V}^{-1}\,\text{s}^{-1}$ at $n = 4 \times 10^{12}\,\text{cm}^{-2}$) mean that the degeneracy lifting happens at smaller magnetic field than in the exfoliated flakes. The heirarchy of degeneracy lifting is shown in Figure 44, where a schematic representation of the evolution of the Landau level degeneracy is given. We have marked the approximate fields at which each new

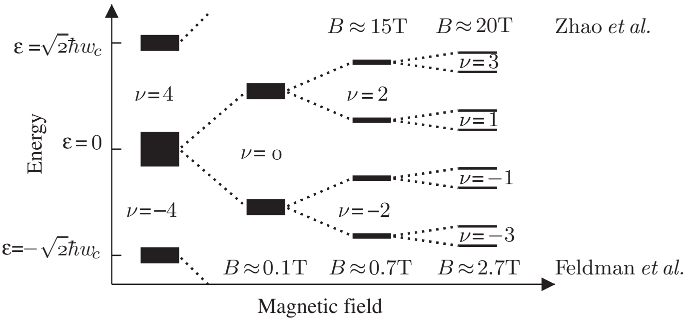

Figure 44. The order of Landau level degeneracy removal as magnetic field strength increases. The thickness of the line marking the Landau level indicates the degeneracy. The dotted lines mark the splitting of degenerate Landau levels. The magnetic field labels refer to the beginning of the emergence of each regime in the suspended case [205] (lower) and exfoliated case [206] (upper).

regime begins to present itself in the two experiments. Both authors note that disorder and Zeeman splitting are unlikely mechanisms for lifting the degeneracy (since the energy scales of these two effects are much smaller than the energy gaps), and interaction with charged impurities is unlikely because the effect is more apparent in the suspended samples. The authors of both papers therefore claim that it is electron–electron interactions which are responsible for this lifting of the degeneracy.

### 3.5. *Electron–electron interactions in bilayer graphene*

Although the electron–electron interactions do not seem to play an important role in the transport measurements conducted on bilayer graphene, they may have a significant effect on other physical properties of this system, especially the magnetism of the ground state. We therefore review the theoretical work on this topic. A variety of analytical techniques have been applied to this problem, and the key issue which discriminates between them is the role of screening. Screening is always more important in the bilayer than the monolayer, because there is a finite density of states at the K point, but in the gapped bilayer, the density of states shows a square-root divergence at the band edge, meaning that screening is particularly efficient in this case. Therefore, on-site Hubbard models have been considered for the biased bilayer, while the Hartree–Fock approximation, the RPA and variational techniques have been applied to the ungapped bilayer.

Nilsson *et al.* [207] were the first to examine the possibility of a magnetic ground state in bilayer graphene. Using a variational method, they found that a trial ground state with finite-spin polarization at half filling produced a lower total energy than the unpolarized system when the exchange energy associated with the long-range Coulomb interaction was taken into account. The parameter $Q$ describes the ‘size’ of the electron or hole pockets in the density, and is taken to be the variational parameter. If the variational state is assumed to be such that there is one electron pocket in the up-spin channel, and one hole pocket in the down-spin channel at each K point, then $n_{1,\uparrow}(p) = \theta(Q - p)$, $n_{1,\downarrow} = 0$ on the first layer, and $n_{2,\uparrow} = 1$, $n_{2,\downarrow} = 1 - \theta(Q - p)$ on the second layer. The authors demonstrate that the optimal $Q$ is $Q_{\min} = 0.05\gamma_1$, and that the system favors the formation of spin polarized electron and hole pockets. This calculation does not include the exchange interaction between electrons in opposite K points. Adding this energy favors a state with net ferromagnetism, and lifts the degeneracy between trial ground states with and without the $Z_2$ symmetry. The induced ferromagnetism is predicted to be up to the order of $10^{-5}$ $\mu_B$ per carbon atom. Short-range interactions were also considered in a Hubbard model, and *c*-axis antiferromagnetism is predicted.

Hwang *et al.* [208] applied the RPA to ungapped bilayer graphene to derive the polarization function, and hence discuss the dielectric properties and associated screening, the Kohn anomaly, Friedel oscillations and the RKKY interaction. Using the two band model, intrinsic (i.e. undoped) bilayer graphene is shown to have a constant polarization function $\Pi^0(q) = \frac{gm}{2\pi}\log 4$ (where $g = 4$ is the band degeneracy factor, and $m$ is the effective mass) so that the dielectric function is $\epsilon(q) = 1 + \frac{gme^2}{\kappa q}\log 4$. Also, this constant polarization function means that the Coulomb potential has no oscillatory terms (i.e. no Friedel oscillations), in contrast to the monolayer and traditional 2DES. The asymptotic radial dependence is $1/r^3$, as opposed to $1/r$ in the monolayer.

In extrinsic bilayer graphene, there are contributions to the polarizability from both the intra- and inter-band transitions. This quantity is plotted in Figure 45, where the intra-band, inter-band, and total polarizations are shown separately. In the bilayer, the polarizability is constant for $q < k_F$, but for $q > k_F$ the cancellation between the intra- and inter-band contributions is not exact due to the enhanced backscattering associated with the inter-band transitions. Therefore, the polarization function increases up to $q = 2k_F$. At this point, the chirality-induced enhancement to the wide angle scattering generates a cusp (with discontinuous first derivative): behavior which is in line with the 2DES, but sharply opposed to that of the SLG. In the large momentum limit, the polarization converges to the constant $\frac{gm}{2\pi}\log 4$ because the inter-band processes dominate over the intra-band ones. This is again different from the 2DES, where the polarizability falls as $1/q^2$. The cusp at

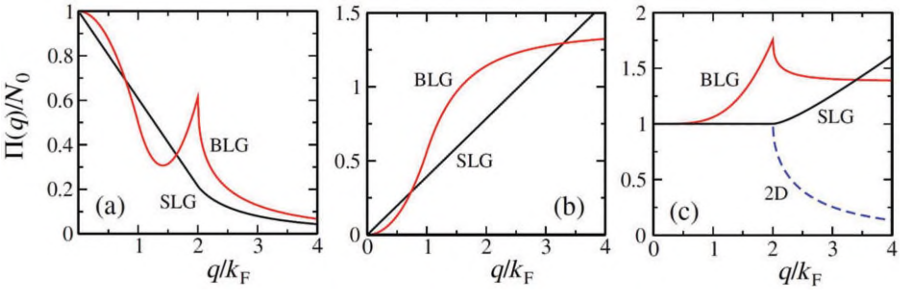

Figure 45. Calculated (a) intraband, (b) interband, and (c) total static polarizability of bilayer graphene. For comparison, the single-layer polarizabilities are shown. In (c), the authors also show the regular 2D static polarizability (dashed line) (Reprinted figure with permission from E.H. Hwang and S. Das Sarma, Physical Review Letters, 101, 156802, 2008 [208]. Copyright © (2008) by the American Physical Society.).

$q = 2k_F$ leads to Friedel oscillations and a strong Kohn anomaly (Section 3.6). Finally, the authors discussed the RKKY interaction between two magnetic impurities. For an intrinsic bilayer, the magnetic moments are not correlated due to the constant polarization function, and there is no net magnetic moment. In doped BLG, the singularity at $q = 2k_F$ restores the oscillatory term in the RKKY interaction, and behavior very similar to the 2DES is recovered.

In the case of the biased bilayer, the presence of the non-trivial Fermi surface at low density causes behaviour which departs from the standard Fermi liquid type. Stauber *et al.* [209] investigated this regime using the first-order correction to the electron self energy which renormalizes the band parameters such that

$$E(k) \approx \Delta_1 - \alpha_1 k^2 + \lambda_1 k^4, \quad \Delta_1 = \Delta - \frac{e^2}{\epsilon_0}\Delta k, \quad \alpha_1 = \alpha + \frac{e^2}{4\epsilon_0}\frac{\Delta k}{k_\times},$$
$$\lambda_1 = \lambda - \frac{3e^2}{64\epsilon_0}\frac{k_{\max}^3 - k_{\min}^3}{k_\times^3},$$

where $\Delta k = k_{\max} - k_{\min}$, and $k_\times = k_{\max}k_{\min}$ and $\Delta$, $\alpha$, and $\lambda$ are the bare band parameters. The momenta $k_{\min}$ and $k_{\max}$ are the lower and upper extent of the Fermi ring. This renormalization means that for $\lambda_1 \leq 0$, the spectrum is unbounded and an instability may occur in the non-interacting system. To examine this possibility, the authors include the exchange part of the Coulomb interaction between electrons. When this contribution is considered with the bare band parameters, it is found that the Fermi ring is unstable with respect to ferromagnetism, with a second-order transition. When the renormalization due to the self-energy corrections is included, this tendency is reduced, (although there is a critical density at which the phase transition will occur) and the magnetization is saturated at $n > 5 \times 10^{11}\,\mathrm{cm}^{-2}$. At low densities, the ferromagnetic ordering is not affected by the self-energy corrections and will be present at $T = 0$. The authors also examined the polarization function in the Mexican hat regime, and it was found that the electron gas in the biased bilayer deviates from the standard Landau Fermi liquid theory for intermediate energies, and at low energies, the Fermi liquid result is obtained except at wave numbers which directly connect two parallel parts of the Fermi surface. The presence of two Fermi lines implies that the Friedel oscillations have period $\pi/b$ (where $2b = k_{\max} - k_{\min}$). Finally, the plasmon spectrum shows features typical of a 2DES, although the energy scale is larger than the traditional systems by virtue of the low electron mass.

The logarithmic divergences which appear within the Hartree–Fock approximation of the band parameter renormalization can be removed by adding Thomas–Fermi screening to the calculation [198]. When this screening is taken into account, the renormalized bands disperse more slowly than in the Hartree–Fock case.

Ferromagnetism has been investigated in the Hubbard model near the band edge by Castro *et al.* [210]. They claim that the high density of states at the band edge, and resulting screening of the long-range part of the Coulomb interaction makes this model applicable in this context. There is a critical value of the gap, $U_c$ above which the ferromagnetism becomes unavoidable because of the change in band parameters for the up-spin and down-spin bands. To illustrate this, Figure 46(a) shows the Hartree–Fock bands for three different values of the gap $U$. In the case $U < U_c$, there is no splitting between the different spin bands and the magnetization $m$ and

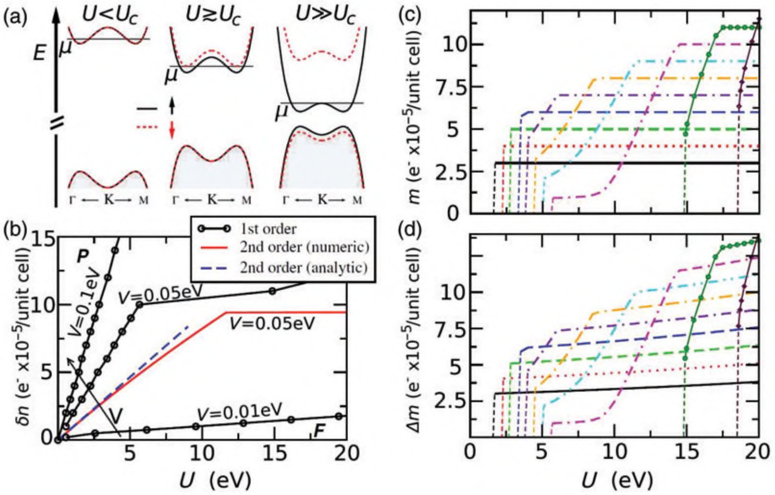

Figure 46. (a) Hartree-Fock bands for ↑ (solid lines) and ↓ (dashed lines) spin polarizations. (b) The $U$ vs $\delta n$ phase diagram at $T = 0$: symbols are inferred from (c) and signal a first-order transition; lines stand for the second-order transition. (c) The $T = 0$ solution for magnetization. (d) The $T = 0$ solution for the layer difference in magnetization. In (c) and (d), the successive lines represent different layer asymmetry in the electron density, with the lowest magnetization corresponding to the smallest density imbalance (Reprinted with permission from E.V. Castro *et al.*, Physical Review Letters, 100, 187803, 2008 [210]. Copyright © (2008) by the American Physical Society.).

interlayer magnetization difference $\Delta m$ are both trivially zero. When the gap is a little above the critical value ($U \gtrsim U_c$), the degeneracy of the spin states in the conduction band is lifted which gives rise to a finite magnetization, $m \neq 0$. That the degeneracy in the valence band is not lifted means that $\Delta m \approx m$, as shown in Figure 46(c) and (d). When $U \gg U_c$, the valence band does become non-degenerate, and the magnetization is opposite in the two layers, so that $\Delta m > m$. Finite temperature does not change this picture to any great extent. Also, it is clear that $|\delta n| < |\Delta n|$ implying that the electron density is above the Dirac point in one plane, and below it in the other. This is natural, since the tight-binding model shows that valence band states are located mainly in the layer at low potential, and conduction band states are located mainly in the layer at high potential. Finally, Figure 46(b) illustrates a comparison of the self-consistent analysis (lines with dots) and the approximate analytical estimates assuming a second-order transition. It is clear that the ferromagnetic-paramagnetic transition in this system is actually first order.

The electron compressibility is a physically measurable quantity which reveals much information about the interaction effects in electron gases. The compressibility of the bilayer has been calculated within the Hartree–Fock approximation by Kusminskiy *et al.* [211]. At very small doping, compressibility is negative and divergent, as in a 2DES. The inter-band contribution tends to move the region of negative compressibility to smaller densities, so that this contribution reduces compressibility. However, similar calculations for the compressibility of the monolayer [212] produce a 10–15% renormalization of the electron velocity, similar to that found in experiment [213].

Table 2. Table of phonon frequencies.

| Γ-point mode | Yan *et al.* [215] | Saha *et al.* [214] |
|---|---|---|
| $E_g$ | 1587 | 1594.1 |
| $E_u$ | 1592 | 1598.9 |
| $E_g \Rightarrow E^*$(low) | | 35.0 |
| $A_{1g} \Rightarrow A^*$(low) | | 76.8 |
| $A_{1g} \Rightarrow A^*$(high) | | 900.8 |
| $A_{2u}$ | | 903.3 |
| *K*-point mode | | |
| $E$ | 1318 | |

Note: Units are $\text{cm}^{-1}$ throughout.

For more details on the nature of plasmon dispersion and compressibility in monolayer and bilayer graphene, see Section 4.

### 3.6. *Phonon anomalies and electron–phonon coupling*

Phonons and the electron–phonon coupling are important topics because of the intimate links that the subject has with Raman spectroscopy, a key experimental tool in the study of graphene.

First-principles studies of phonons in mono-, bi- and few-layer graphenes have been carried out [214,215]. Saha *et al.* [214] determine the dependence of the energy of various low-momentum phonon modes on the number of layers and find strong layer dependence for out-of-plane modes, and relatively weak layer dependence for in-plane modes. In Table 2, we summarize the available data for the frequency of the phonon modes discussed. Yan *et al.* [215] show how the $E_{2g}$ peak splits into two modes which are split by approximately $5\,\text{cm}^{-1}$.

Various authors have discussed phonon anomalies in bilayer graphene, so a brief outline of the physics is in order. For reference, the original description of phonon anomalies in monolayer graphene was given by Piscanec *et al.* [216], but in this section we describe the phonons in bilayer graphene only. Yan *et al.* [217] show the change of phonon frequency $\omega_{\text{ph}}$ as a function of the Fermi energy (Figure 47d), with the anomaly occurring when the inter-band electron–hole excitation is in resonance with the phonon mode. The change of phonon frequency with the tuning of the Fermi energy is given by

$$\hbar\omega_{\text{ph}}(E_{\text{F}}) - \hbar\omega_{\text{ph}}(0) \sim -\lambda \int_0^{2|E_{\text{F}}|} dE_{e-h} \frac{2E_{e-h}}{\hbar^2\omega_{\text{ph}}^2 - E_{e-h}^2} \sim \lambda \ln\left|1 - \frac{2|E_{\text{F}}|}{\hbar\omega_{\text{ph}}}\right|,$$

where λ is the electron–phonon coupling parameter. This anomaly was observed experimentally by Das *et al.* (Figure 48a), whereas it has not yet been observed in the monolayer. Yan *et al.* speculate that the reason for this is the intrinsic charge inhomogeneity in graphene causes a larger variation in the Fermi energy in the monolayer than it does in the bilayer, and to be qualitative about this idea, the authors show the evolution of the anomaly size as a function of charge non-uniformity. This anomaly was not seen by later experiments [218], and this is probably due to the large

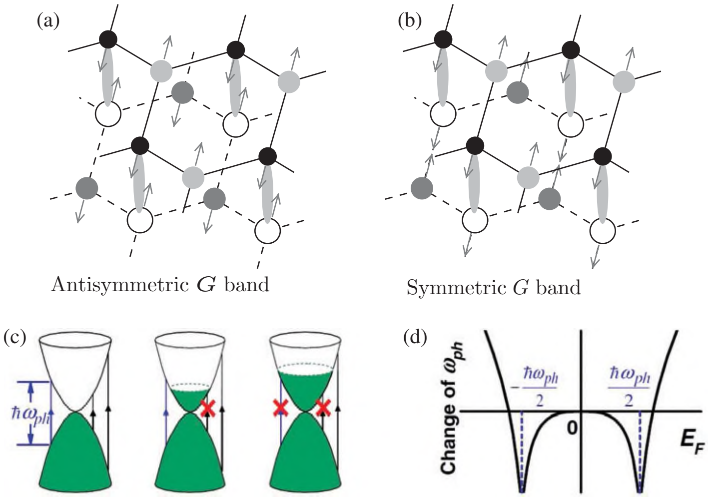

Figure 47. Phonon modes in bilayer graphene where the grey arrows represent the direction of vibration of each atom. (a) The antisymmetric *G* band mode is a distortion of the zigzag lines where the layers are out of phase. (b) The symmetric *G* band mode is a distortion of the zigzag lines where the layers are in phase. (c) Vertical ($q = 0$) inter-band electron–hole pair transitions in a gapless 2D semiconductor with three different Fermi levels. Shaded regions are filled with electrons, and the transition indicated by the arrow is the resonance with the long-wavelength optical phonon (From [217]). (d) Predicted change of phonon energy as a function of the Fermi energy. The two phonon anomalies show up at $E_F = \pm\hbar\omega_{ph}/2$ (Reprinted figure with permission from J. Yan *et al.*, Physical Review Letters, 101, 136804, 2008 [217]. Copyright © (2008) by the American Physical Society.).

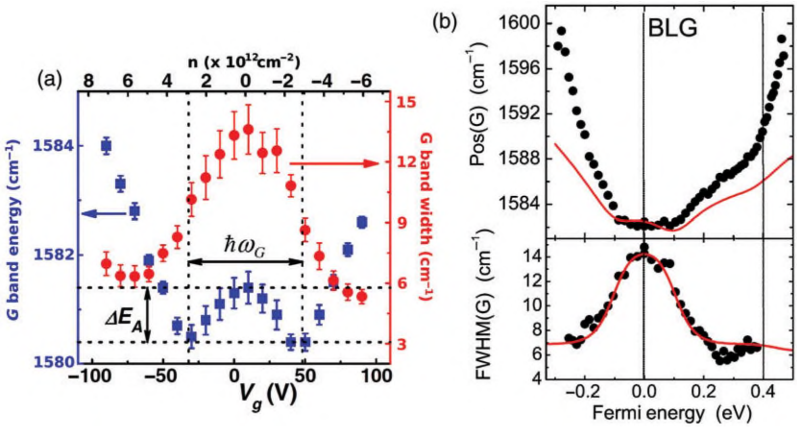

Figure 48. (a) Experimental energy and linewidth of the *G* band. Two phonon anomalies are clearly resolved in the phonon energy (Reprinted figure with permission from J. Yan *et al.*, Physical Review Letters, 101, 136804, 2008 [217]. Copyright © (2008) by the American Physical Society.). (b) The position of the *G* peak, and its full width at half-maximum plotted as a function of Fermi energy (Reprinted figure with permission from A. Das *et al.*, Physical Review B, 79, 155417, (2009) [219]. Copyright © (2009) by the American Physical Society.).

charge non-uniformity, and because these experiments were carried out at room temperature. Malard *et al.* measured the phonon frequency shift when a finite interlayer asymmetry potential is applied. The breaking of the layer symmetry allows the antisymmetric mode to become active in Raman spectra, causing the $G$ band to split into two peaks (see schematic representation of the displacements associated with each phonon mode in Figure 47a and b). Frequency differences of $\sim 15\,\mathrm{cm}^{-1}$ are observed between the two modes for large negative bias, and comparison with theoretical predictions shows that the measured shift of the symmetric phonon is significantly larger than predicted, while the shift of the antisymmetric phonon is in line with predictions. Symmetry analysis of bilayer graphene phonons in the presence of an external electric field [219] reproduces the qualitative features. Castro Neto *et al.* [220] have used a simple one-loop calculation within the tight-binding model to compute the electronic susceptibility of bilayer graphene, and related it to the frequency shift of the phonon mode due to the electron–phonon coupling. They find that the shift is linear in the electron density $n$, and negative:

$$\delta\omega_{\vec{Q}}^{\mathrm{bil}} \propto -\left(\frac{\partial t}{\partial l}\right)^2 \frac{n}{M_C \omega_{\vec{Q}} \gamma_1},$$

where $M_C$ is the mass of a carbon atom, $l$ is the lattice constant, with $\partial t/\partial l \approx 6.4\,\mathrm{eV}\,\mathrm{\AA}^{-1}$, and $\omega_{\vec{Q}}$ is the frequency of a phonon with wave vector $\vec{Q}$.

On the other hand, Das *et al.* [221] report that the $G$ peak frequency is renormalized as a function of doping, outside of a the range $-0.1\,\mathrm{eV} < E_\mathrm{F} < 0.1\,\mathrm{eV}$, which corresponds to the $\hbar\omega_0/2$ anomaly discussed above. There is also a kink at $E_\mathrm{F} \approx 0.4\,\mathrm{eV}$. These results are explained with reference to the doping and dynamic effects, and the presence of the kink is related to the Fermi energy moving to the split band. This phonon anomaly has also been discussed theoretically by Ando [204] within the one-loop approximation for the phonon self energy. The logarithmic singularity in the frequency shift is derived for the symmetric $G$ mode when the interlayer potential is zero, but a finite-disorder potential curtails the singularity and broadens the phonon mode. On the other hand, the antisymmetric $G$ mode does not display the singularity and the broadening is significantly reduced for $E_\mathrm{F} < \gamma_1$ because inter-band transitions are suppressed. In the case of finite-interlayer bias, the screening is taken into account self-consistently by Ando [222]. The presence of the band gap modifies the phonon renormalization, the symmetric and antisymmetric $G$ modes mix strongly, and an asymmetry between the phonon frequencies at positive and negative electron concentrations is induced. This asymmetry becomes considerable when the gap size is of the order of the phonon frequency, and in this case, resonant inter-band contributions between the two low-energy bands and the frequency of the low-frequency mode (dominantly symmetric) are reduced strongly, and broadened.

### 3.7. *Device proposals utilizing bilayer graphene*

In this section we outline some of the devices that have been proposed which utilize bilayer graphene in their operation. Transistor and current switching devices were discussed in Section 3.3, so we do not repeat that material here. We shall describe two proposals for valleytronic devices (utilizing the valley quantum number as a

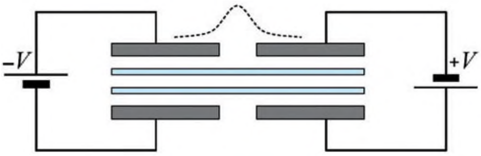

Figure 49. Side view of a gated bilayer graphene configuration with the voltage kink. The region where the interlayer voltage changes sign (the channel) supports bands of chiral zero modes (dashed line). The conventional (non-topological) confinement would correspond to the same polarity of bias on both sides of the channel (Reprinted figure with permission from I. Martin *et al.*, Physical Review Letters, 100, 036804, 2008 [223]. Copyright © (2008) by the American Physical Society.).

controllable two-state system), and two for employing the pseudospin (i.e. the sublattice index) in the same way.

Martin *et al.* [223] describe a device which utilizes a split gating arrangement to confine electrons in zero modes in a 1D channel (Figure 49). These electrons are chiral in the valley index, so that their direction of propagation is determined by which valley they are in. A valley filter may be observed by applying a potential difference along the voltage kink, since the resulting current would consist of only one valley species. A valley valve can be implemented by placing two such filters in series. If the polarity of the filters is the same then current will pass, if it is opposite then current will not flow. The polarity of each valve can be reversed by swapping the orientation of the bias potentials on each side of the channel.

Abergel and Chakraborty [224] demonstrated that irradiating gated bilayer graphene with intense, circularly polarized, terahertz frequency light leads to the creation of valley polarized dynamical states in the gapped region of the spectrum. By passing an arbitrary current through these states, the current is polarized into the valley in which the states reside. Swapping the polarization of the top gate, or the orientation of the circular polarization of the light causes the valley in which the dynamical states form to be swapped also. Currents of the order of a tenth of a pico-Amp, and valley polarizations above 99% are predicted to be obtained. These devices can be used individually to generate valley polarized currents, or in series to implement switching devices. The valley-polarized currents exist in the bulk of the bilayer graphene (rather than localized at a sample edge, or in a narrow channel), and may be used as an analogue of spin-polarized currents in spintronics. The fact that this device relies on a bulk effect also gives it the distinct advantage that the details of the edges make no difference to its operation, which makes the device significantly easier to fabricate than those that utilize specific properties of certain edge geometries in their operation.

San-Jose *et al.* [225] propose a pseudospin valve employing gapped bilayer graphene. Their device consists of two-gated regions which are biased so that there is a finite gap at the charge-neutrality point which induces an out-of-plane component of the pseudospin. If the two regions have opposite polarity and the distance between the two regions is small enough, then electron will be unable to rotate its pseudospin quickly enough to allow it to penetrate the region of opposite polarization and reflection will occur at the interface between the two regions. Conversely, if the two regions are arranged with the same polarity, no such reflection will take place.

Pseudo-magnetoresistance of approximately 100% were suggested for optimal device dimensions of a pseudospin transistor.

Min *et al.* [226] proposed pseudospin ferromagnetism in gated bilayer graphene, which may have analogous applications to the real spin in spintronic systems. They demonstrated that high-gate voltage polarizes the pseudospin, and speculate that pseudospin-transfer torques, and easy switching behavior can be accomplished.

## 4. Many-body and optical properties of graphene

In this section, we discuss some of the novel electronic properties of graphene, where the electron–electron interactions traditionally play an important role. We begin in Section 4.1 with a discussion of the measurement of compressibility in monolayer graphene [213] and the reported theoretical studies [227] to understand the experimental results. In Section 4.2 we discuss the theoretical studies of plasmon dispersion in monolayer and bilayer graphene. We also review the properties of graphene in an intense electromagnetic field (EMF) in Section 4.3.

### 4.1. *Electronic compressibility*

In an interacting electron system of uniform density, the (inverse) electronic compressibility $\kappa^{-1} \propto \partial\mu/\partial n$ (where $\mu$ is the chemical potential and $n$ is the electron density) is a fundamental physical quantity that is intimately related to the strength of inter-electron interactions [228,229]. First measured for a two-dimensional electron gas in 1992 [230], the compressibility provides valuable information about the nature of the interacting ground state, particularly in the strong coupling regime where (in addition to the exchange energy) the Coulomb interaction is known to play a dominant role. In this section, we begin by reviewing the surprising experimental results by Martin *et al.* [213] for the compressibility of monolayer graphene, and continue to describe attempts to understand them from a theoretical point of view. We then review the same physics in the bilayer material, highlighting the intriguing differences between these two systems.

#### 4.1.1. *Monolayer graphene*

A recent report on the measurement of electronic compressibility in monolayer graphene revealed behavior which was totally unexpected [213]. In this work, scanning single-electron transistor microscopy was used to measure the change of local electrostatic potential (and thereby change in local chemical potential) of a graphene sample when the carrier density was modulated [213]. The observed results for the local inverse compressibility were found to be quantitatively described by the kinetic energy alone (with the electron velocity renormalized by 10–15%) and the authors speculated that the exchange and correlation energy contributions to the compressibility either cancel each other out or are negligibly small. This interesting puzzle has remained unsolved because the approximate theoretical schemes adopted by various authors to investigate electron correlations in graphene [231,232] do not find any such cancellations. Similarly, the recently reported Hartree–Fock studies of compressibility [211,212] in monolayer and bilayer graphene do not consider electron correlations at all, although they do correctly predict the velocity renormalization.

Abergel *et al.* [227] investigated the role of electron correlations in monolayer and bilayer graphene. They showed how in monolayer graphene, two fundamental properties of the system, namely, the linear energy dispersion and chirality conspire to allow complete cancellation of exchange and correlation contributions just as was observed in the experiment [213]. On the other hand, in bilayer graphene where the low-energy quasiparticles are massive chiral fermions, the parabolic dispersion does not allow this cancellation of the two energies, and the kinetic energy retains a dependence on the electron correlation function which manifests in the electron compressibility.

As discussed elsewhere in this review (Sections 1.2 and 5.2), the low-energy charge carriers in monolayer graphene behave as massless Dirac fermions described by a single-particle Hamiltonian which is linear in momentum $\vec{p}$. The eigenstates of the Hamiltonian are uniquely labelled by quantum numbers representing the wave vector $\vec{q} = \vec{p}/\hbar$, the band (conduction/valence) $b$, valley (pseudospin) $\xi$ and the $z$-component of the real electron spin $\sigma$. The wave functions are of the form, $(\vec{r}) = e^{i\vec{q}\cdot\vec{r}}\chi$, where $\chi$ is, in the most general case, an eight-component spinor [3]. The wave function can be written in an abbreviated basis by ignoring the spin, and swapping the order of the sublattice components in the two valleys to recover the Hamiltonian given in Section 1.2.

A full analytical study of the many-electron system in graphene is clearly an impossible task. However, most of the clues to the puzzle involving the measured compressibility described above can be found at the level of two electrons, which is amenable to a fully analytic solution. One could therefore start with a two-electron system where the electrons occupy the states $\psi_\alpha$ and $\psi_\beta$ with $\alpha$ and $\beta$ corresponding to the full sets of quantum numbers $(\vec{q}_{\alpha,\beta}, b_{\alpha,\beta}, \xi_{\alpha,\beta}, \sigma_{\alpha,\beta})$. Let us denote by $\varphi$ the antisymmetric non-interacting two-electron wave function

$$\varphi(\vec{r}_1, \vec{r}_2) = \frac{1}{\sqrt{2}}\left[\psi_\alpha(\vec{r}_1)\psi_\beta(\vec{r}_2) - \psi_\beta(\vec{r}_1)\psi_\alpha(\vec{r}_2)\right], \tag{47}$$

where the subscript labels refer to the independent coordinates of the two electrons. The correlations due to the mutual Coulomb interaction are introduced by multiplying the free-particle wave function by a generic correlation factor $F$ as

$$\Psi = F(\vec{r}_1, \vec{r}_2)\varphi(\vec{r}_1, \vec{r}_2). \tag{48}$$

At this stage, a precise definition of $F$ is not necessary. The only requirements are that it should be a real function, and to preserve the antisymmetry of the correlated wave function $\Psi$ it is assumed to be symmetric with respect to exchange of the particle coordinates, i.e. $F(\vec{r}_1, \vec{r}_2) = F(\vec{r}_2, \vec{r}_1)$.

In order to evaluate the two-particle energy we have to normalize the wave function $\Psi$. A straightforward calculation gives

$$||\Psi||^2 = \langle\Psi|\Psi\rangle = \int d\vec{r}_1\, d\vec{r}_2\, F(\vec{r}_1, \vec{r}_2)^2 \left\{1 - \frac{1}{2}\delta_{\xi_\alpha \xi_\beta}\left[1 + b_\alpha b_\beta \cos(\theta_\alpha - \theta_\beta)\right]\cos Q\right\},$$

where $Q = (\vec{q}_\beta - \vec{q}_\alpha)\cdot(\vec{r}_1 - \vec{r}_2)$ and $\theta_{\alpha,\beta}$ are the polar angles of the momenta $\vec{q}_{\alpha,\beta}$.

Evaluation of the expectation value of the kinetic part of the non-interacting two-body Hamiltonian leads us to

$$\begin{aligned} T^{\mathrm{mon}} = \frac{1}{2}\hbar v_{\mathrm{F}} \int \mathrm{d}\vec{r}_1\, \mathrm{d}\vec{r}_2\, F \Bigg\{ & \frac{1}{4}\mathrm{i}\delta_{\sigma_\alpha\sigma_\beta}\delta_{\xi_\alpha\xi_\beta}\Big[\mathrm{e}^{\mathrm{i}Q} Z^1_{\alpha\beta}\big(1 + b_\alpha b_\beta \mathrm{e}^{-\mathrm{i}(\theta_\beta-\theta_\alpha)}\big) \\ & + \mathrm{e}^{\mathrm{i}Q} Z^2_{\beta\alpha}\big(1 + b_\alpha b_\beta \mathrm{e}^{\mathrm{i}(\theta_\beta-\theta_\alpha)}\big) + \mathrm{e}^{-\mathrm{i}Q} Z^1_{\beta\alpha}\big(1 + b_\alpha b_\beta \mathrm{e}^{\mathrm{i}(\theta_\beta-\theta_\alpha)}\big) \\ & + \mathrm{e}^{-\mathrm{i}Q} Z^2_{\alpha\beta}\big(1 + b_\alpha b_\beta \mathrm{e}^{-\mathrm{i}(\theta_\beta-\theta_\alpha)}\big)\Big] \\ & - \mathrm{i}b_\beta\bigg(\cos\theta_\beta \frac{\partial F}{\partial x_1} + \cos\theta_\beta \frac{\partial F}{\partial x_2} + \sin\theta_\beta \frac{\partial F}{\partial y_1} + \sin\theta_\beta \frac{\partial F}{\partial y_2} + 2\mathrm{i}q_\beta F\bigg) \\ & - \mathrm{i}b_\alpha\bigg(\cos\theta_\alpha \frac{\partial F}{\partial x_1} + \cos\theta_\alpha \frac{\partial F}{\partial x_2} + \sin\theta_\alpha \frac{\partial F}{\partial y_1} + \sin\theta_\alpha \frac{\partial F}{\partial y_2} + 2\mathrm{i}q_\alpha F\bigg)\Bigg\}, \end{aligned}$$

where we use the shorthand

$$Z^j_{\alpha\beta} = \big(b_\beta \mathrm{e}^{\mathrm{i}\theta_\beta} + b_\alpha \mathrm{e}^{-\mathrm{i}\theta_\alpha}\big)\frac{\partial F}{\partial x_j} - \mathrm{i}\big(b_\beta \mathrm{e}^{\mathrm{i}\theta_\beta} - b_\alpha \mathrm{e}^{-\mathrm{i}\theta_\alpha}\big)\frac{\partial F}{\partial y_j} + \mathrm{i}q_\beta F\Big(b_\beta + b_\alpha \mathrm{e}^{\mathrm{i}(\theta_\beta-\theta_\alpha)}\Big).$$

Due to the linearity of the single-particle Hamiltonians in the momentum operators, only first-order derivatives appear in the integrand. Terms in $T$ of the form

$$\int \mathrm{d}\vec{r}_j\, F\frac{\partial F}{\partial x_j} = \frac{1}{2}\int \mathrm{d}\vec{r}_j \frac{\partial}{\partial x_j}F^2,$$

clearly vanish due to the antisymmetry of the integrand. Most of the terms left after the volume integration cancel each other as a consequence of the spinor structure of the single-particle wave functions. The only surviving terms sum to

$$T^{\mathrm{mon}} = \hbar v_{\mathrm{F}}(b_\alpha q_\alpha + b_\beta q_\beta)||\Psi||^2,$$

that is, the kinetic energy expectation value $\langle \mathcal{T}^{\mathrm{mon}}\rangle$ is simply the sum of the single free-particle kinetic energies,

$$\langle \mathcal{T}^{\mathrm{mon}}\rangle = \frac{T^{\mathrm{mon}}}{||\Psi||^2} = \hbar v_{\mathrm{F}}(b_\alpha q_\alpha + b_\beta q_\beta) = T_0 = \frac{\langle\varphi|\mathcal{T}^{\mathrm{mon}}|\varphi\rangle}{||\varphi||^2} \tag{49}$$

and does not depend on the correlation function $F$ at all. Similar cancellations are expected for higher electron numbers, although analytical expressions become intractable even at the level of three electrons. This is a very interesting result since complete cancellation of correlation contributions to the kinetic energy has never been observed in conventional electron systems. It creates an unusual situation with interesting consequences, as described in [227]. In the thermodynamic limit, the potential energy (per particle) $\mathcal{V}$ is usually expressed in the form

$$\langle \mathcal{V}\rangle = n\int \mathrm{d}\vec{r}\,[g(r) - 1]V_{\mathrm{Coul}}(r),$$

where $n$ is the single particle number density, $V_{\text{Coul}}$ is the Coulomb potential and $g(r)$ is the pair correlation function which, for $\vec{r} = \vec{r}_1 - \vec{r}_2$, is given by

$$g(|\vec{r}|) = \frac{N(N-1)}{||\Psi||^2 n^2} \int \mathrm{d}\vec{r}_3 \ldots \mathrm{d}\vec{r}_N \, |\Psi(\vec{r}_1, \vec{r}_2, \vec{r}_3, \ldots, \vec{r}_N)|^2,$$

where $N$ is the total number of electrons. The energy (per particle) functional $\mathcal{E}^{\text{mon}}$ is now

$$\mathcal{E}^{\text{mon}} = t_0 + \langle \mathcal{V} \rangle = t_0 + n \int \mathrm{d}\vec{r} \, [g(r) - 1] V_{\text{Coul}}(r), \tag{50}$$

where $t_0 = T_0/N$ is the kinetic energy per particle. Its variation with respect to $g(r)$ (an essential step in determining the optimal $g(r)$ and hence the optimal $F$) would yield an unusual Euler–Lagrange equation, $V_{\text{Coul}}(r) = 0$, which is clearly not the case in graphene [233]. To resolve this dilemma, Abergel *et al.* noted that the energy functional $\mathcal{E}^{\text{mon}}$ is actually not bounded below: one can choose correlations such that the potential energy takes arbitrarily large negative values. This implies that to determine the optimal $g(r)$, the energy functional derived above is not sufficient and additional physical constraints, for example, that $g(r)$ should correspond to the correct number of states in the bands would be necessary[8]. Clearly, determination of the optimal pair-correlation function for massless Dirac fermions in graphene is a challenging problem [234]. However, the expression for the functional $\mathcal{E}^{\text{mon}}$ is of the correct form, i.e. once the correct pair-distribution function $g(r)$ is found, one could evaluate the correct energy from the above form of the energy functional.

Let us now turn our attention to the electron compressibility. To that end, we first evaluate the variation $\delta_n \mathcal{E}^{\text{mon}}$ of $\mathcal{E}^{\text{mon}}$ with respect to $n$ [227]:

$$\delta_n \mathcal{E}^{\text{mon}} = \frac{\partial t_0}{\partial n} \delta n + \delta n \int \mathrm{d}\vec{r} \, [g(r) - 1] V_{\text{Coul}}(r) + n \int \mathrm{d}\vec{r} \, V_{\text{Coul}} \frac{\delta g(r)}{\delta n} \delta n.$$

From this we can read the derivative as

$$\frac{\partial \mathcal{E}^{\text{mon}}}{\partial n} = \frac{\partial t_0}{\partial n} + \int \mathrm{d}\vec{r} \, [g(r) - 1] V_{\text{Coul}} + n \int \mathrm{d}\vec{r} \, V_{\text{Coul}} \frac{\delta g(r)}{\delta n}.$$

The compressibility will then be proportional to

$$\frac{\partial^2 \mathcal{E}^{\text{mon}}}{\partial n^2} = \frac{\partial^2 t_0}{\partial n^2} + 2 \int \mathrm{d}\vec{r} \, V_{\text{Coul}} \frac{\delta g(r)}{\delta n} + n \int \mathrm{d}\vec{r} \, V_{\text{Coul}} \frac{\delta(\delta g(r)/\delta n)}{\delta n}.$$

Deriving the functional dependence of $g(r)$ on $n$ in a closed form is an almost impossible task. Extensive studies of conventional two-dimensional electron systems have indicated that $g(r)$ varies only slightly as a function of density [229], except at very low densities where it starts to develop a prominent peak as a precursor to Wigner crystallization [235]. Since in graphene the Wigner crystallization is not a possibility (in the absence of an external magnetic field) [236], and no other phase transitions expected at the density range of interest, we expect the variation $\delta g(r)/\delta n$ to vanish or to be negligibly small. Alternatively, we could consider a slightly less stringent condition $\int \mathrm{d}\vec{r} \, V_{\text{Coul}} \frac{\delta g(r)}{\delta n} = 0$, which implies that the interaction energy depends linearly on the density of Dirac electrons. The compressibility is then described entirely by the kinetic energy

$$\kappa^{-1} = \frac{\partial^2 \mathcal{E}^{\text{mon}}}{\partial n^2} = \frac{\partial^2 t_0}{\partial n^2},$$

in accordance with the experimental observation [213]. In arriving at this striking result, there are two basic properties of monolayer graphene that play crucial roles: the linear energy dispersion and chirality of massless Dirac electrons [227].

This immediately invites the question: what happens in bilayer graphene, where the low-energy charge carriers behave as massive chiral fermions and as such the Hamiltonian is quadratic in momentum operators near the charge neutrality point?

### 4.1.2. *Bilayer graphene*

In bilayer graphene, as discussed above, there are four atoms per unit cell, so in principle the basis employed in the tight binding model should be doubled in size. However, a low-energy effective theory is employed which considers only the atomic sites which are not involved in the inter-layer dimer bond, and so reduce the basis to only eight components. The authors of [227] used the effective two band model detailed in Section 3.2.3 and obtained from the Hamiltonian corresponding to the first term of Equation (42). The wave functions associated with this Hamiltonian are

$${}_{\alpha}(\vec{r}) = \frac{\mathrm{e}^{\mathrm{i}\vec{q}_\alpha\cdot\vec{r}}}{\sqrt{2\mathcal{A}}} \left. \begin{matrix} -\mathrm{e}^{-2\mathrm{i}\theta_\alpha} \\ 1 \end{matrix} \right).$$

With these basis states, an intermediate expression for the kinetic energy looks as follows:

$$\begin{aligned}
T^{\text{bi}} = & \frac{1}{2}(\epsilon_\alpha + \epsilon_\beta) \\
& - \int \mathrm{d}\vec{r}_1 \mathrm{d}\vec{r}_2 \, \frac{\hbar^2}{4m} F \mathrm{e}^{-\mathrm{i}Q} \Big\{ \mathrm{i}q_\beta \Big( \big[\cos\theta_\beta + \cos(2\theta_\alpha - \theta_\beta)\big] \frac{\partial F}{\partial x_1} \\
& + \big[\sin\theta_\beta + \sin(2\theta_\alpha - \theta_\beta)\big] \frac{\partial F}{\partial y_1} \Big) + \mathrm{i}q_\alpha \Big( \big[\cos\theta_\alpha + \cos(\theta_\alpha - 2\theta_\beta)\big] \frac{\partial F}{\partial x_2} \\
& + \big[\sin\theta_\alpha - \sin(\theta_\alpha - 2\theta_\beta)\big] \frac{\partial F}{\partial y_2} \Big) \Big\} \\
& - \int \mathrm{d}\vec{r}_1 \mathrm{d}\vec{r}_2 \, \frac{\hbar^2}{4m} F \mathrm{e}^{\mathrm{i}Q} \Big\{ \mathrm{i}q_\alpha \Big( \big[\cos\theta_\alpha + \cos(\theta_\alpha - 2\theta_\beta)\big] \frac{\partial F}{\partial x_1} \\
& + \big[\sin\theta_\alpha - \sin(\theta_\alpha - 2\theta_\beta)\big] \frac{\partial F}{\partial y_1} \Big) + \mathrm{i}q_\beta \Big( \big[\cos\theta_\beta + \cos(2\theta_\alpha - \theta_\beta)\big] \frac{\partial F}{\partial x_2} \\
& + \big[\sin\theta_\beta + \sin(2\theta_\alpha - \theta_\beta)\big] \frac{\partial F}{\partial y_2} \Big) \Big\},
\end{aligned}$$

where terms containing second derivatives of $F$ which are identically zero on integration, and those which trivially sum to zero are already excluded. The integrals of terms with single derivatives of $F$ are finite:

$$\int \mathrm{d}\vec{r}_1\,\mathrm{d}\vec{r}_2\,\mathrm{e}^{\pm\mathrm{i}Q}F\frac{\partial F}{\partial x_1} = \mp\mathrm{i}\big(q_{\beta x} - q_{\alpha x}\big)\frac{\mathcal{A}^2\tilde{F}^2}{8} = -\int \mathrm{d}\vec{r}_1\,\mathrm{d}\vec{r}_2\,\mathrm{e}^{\pm\mathrm{i}Q}F\frac{\partial F}{\partial x_2}$$

and similarly for terms containing derivatives with respect to $y$. After some lengthy algebra, one gets [227]

$$T^{\mathrm{bi}} = \frac{1}{2}(\epsilon_\alpha + \epsilon_\beta) + \frac{\hbar^2}{4m}\frac{\mathcal{A}^2\tilde{F}^2}{2}\cos\big(\theta_\alpha - \theta_\beta\big)\Big\{\Big(q_\alpha^2 + q_\beta^2\Big)\cos\big(\theta_\alpha - \theta_\beta\big) - 2q_\alpha q_\beta\Big\}. \tag{51}$$

When compared with the kinetic energy in monolayer graphene (Equation (49)), the non-cancellation exhibited in Equation (51) is a feature of the sublattice structure of the electronic wave function in bilayer graphene, resulting from the quadratic nature of the low-energy dispersion relation. On evaluation of the remaining integrals and after some elementary algebra, the energy functional is found to be

$$\mathcal{E}^{\mathrm{bi}} = t_0 + \langle\mathcal{V}\rangle + \frac{\hbar^2}{8m}\frac{\tilde{F}^2}{||\Psi||^2}\cos(\theta_\alpha - \theta_\beta)\Big[(q_\alpha^2 + q_\beta^2)\cos(\theta_\alpha - \theta_\beta) - 2q_\alpha q_\beta\Big], \tag{52}$$

where $\tilde{F}$ is the Fourier transform of the correlation function. Comparing the case of monolayer graphene, Equation (50), one can easily see that there is a non-zero contribution of electron correlations to the kinetic energy in the above functional (Equation (52)), and therefore taking the derivatives with respect to $n$ yield a compressibility which depends non-trivially on them. It is clear that this additional term will also be present in the many-body energy, as its integral over momentum is manifestly finite. It is also expected that for bilayer graphene where the excess electron density is high enough that the Fermi energy is in the energy range where the linearity of the spectrum is restored, the effect of the correlations in the energy functional will again be suppressed. Quantitative computation of this term requires precise knowledge of the radial dependence of $F$, and the relation between $F(r)$ and $g(r)$ (where several choices of approximate schemes are available in the literature e.g. [237]). Most importantly, however, an experimental observation of a shift in compressibility from the pure kinetic energy contribution (unlike what was observed for monolayer graphene) would provide a way to directly determine the strength of electron correlations in that system.

## 4.2. *Plasmon dispersion in graphene*

In this section, we discuss the Coulomb screening properties and collective excitations in monolayer and bilayer graphene. We focus on the work of Wang and Chakraborty [238,239], although some parts of their results were previously calculated by Wunsch *et al.* [240]. Later papers which contain analytical results for the plasmon spectrum and other dynamical properties of graphene include references [208,209,241–246].

### 4.2.1. *Monolayer graphene*

In the pseudospin space, the zero-magnetic-field Hamiltonian of a spin-up electron which experiences a non-negligable SOI that is parameterized by a momentum

$\vec{p} = \hbar\vec{k}$ measured from the K point is [238,247,248] $\mathcal{H} = v_{\mathrm{F}}\vec{p}\cdot\vec{\sigma} + \Delta_{\mathrm{so}}\sigma_z$ with $\vec{\sigma} = (\sigma_x, \sigma_y, \sigma_z)$ the Pauli matrices. Here $\Delta_{\mathrm{so}}$ is the strength of the SOI[9]. The eigenstates of the Schrödinger equation are readily obtained as

$$\Psi^{\lambda}_{\vec{k}}(\vec{r}) = \mathrm{e}^{\mathrm{i}\vec{k}\cdot\vec{r}} \left. \begin{matrix} 1 + \sin(\alpha_{\vec{k}} + \lambda\pi/2) \\ -\mathrm{e}^{\mathrm{i}\phi_{\vec{k}}}\cos(\alpha_{\vec{k}} + \lambda\pi/2) \end{matrix} \right),$$

with energy $E^{\lambda}_{\vec{k}} = \lambda\sqrt{\Delta^2_{\mathrm{so}} + \hbar^2 v_{\mathrm{F}}^2 k^2}$ for $\lambda = +1$ denoting the conduction band and $\lambda = -1$ the valance band. Here tan $\phi_k = k_y/k_x$, tan $\alpha_k = \hbar v_{\mathrm{F}} k/\Delta_{\mathrm{so}}$, and $k = \sqrt{k_x^2 + k_y^2}$.

The RPA Coulomb interaction in the Fourier space $U(q,\omega)$ obeys the equation [250,251]

$$U(q,\omega) = v_0 + v_0\hat{\Pi}_0(q,\omega)U(q,\omega) \tag{53}$$

with the electron–hole propagator

$$\hat{\Pi}_0(q,\omega) = 4\sum_{\lambda,\lambda',\vec{k}} |\, g^{\lambda,\lambda'}_{\vec{k}}(\vec{q})|^2 \, \frac{f[E^{\lambda'}_{\vec{k}+\vec{q}}] - f[E^{\lambda}_{\vec{k}}]}{\omega + E^{\lambda'}_{\vec{k}+\vec{q}} - E^{\lambda}_{\vec{k}} + i\delta}, \tag{54}$$

as illustrated by the Feynmann diagram in Figure 50. Here $v_0 = e^2/(2\epsilon_0\epsilon_i q)$ is the two-dimensional Coulomb interaction (in Fourier space) with the high-frequency dielectric constant [252] $\epsilon_i = 1$ and $g^{\lambda,\lambda'}_{\vec{k}}(\vec{q})$ is the interaction vertex.

The factor of four in Equation (54) comes from combined degeneracy of the spin (two-fold) and valley (also two-fold) quantum numbers; the vertex factor reads

$$|\, g^{\lambda,\lambda'}_{\vec{k}}(\vec{q})|^2 = \frac{1 + \lambda\lambda'\cos\alpha_{\vec{k}+\vec{q}}\cos\alpha_{\vec{k}} + \lambda\lambda'\sin\alpha_{\vec{k}+\vec{q}}\sin\alpha_{\vec{k}}(k + q\cos\theta)}{2|\vec{k} + \vec{q}|},$$

with $\theta$ being the angle between $\vec{k}$ and $\vec{q}$. Since the chiral property of the system prohibits the intra-band backward scattering at $\vec{q} = 2\vec{k}$ and the inter-band vertical transition at $\vec{q} = 0$ under the Coulomb interaction, we have $|\, g^{\lambda,-\lambda}_{\vec{k}}(0)|^2 = |\, g^{\lambda,\lambda}_{\vec{k}}(2\vec{k})|^2 = 0$. The collective excitation spectrum is obtained by finding the zeros of the real part of the dielectric function $\hat{\epsilon}(q,\omega) = 1 - v_0(q)\hat{\Pi}_0(q,\omega)$.

In the presence of the SOI, an energy gap opens between the conduction and valence bands and the semimetal electronic system is converted into a narrow gap semiconductor system. At the same time, a gap is opened between its intraband single-particle continuum $\omega \leq \omega_{\mathrm{L}} \equiv \hbar v_{\mathrm{F}} q$ and its interband single-particle continuum $\omega \geq \omega_{\mathrm{H}} \equiv 2\sqrt{\Delta^2_{\mathrm{so}} + \hbar^2 v_{\mathrm{F}}^2 q^2/4}$. However, the system differs from a normal narrow gap semiconductor due to its peculiar chiral property. Here we have chosen the magnitude of the SOI strength to be around 0.08–0.1 meV [247,253]. The result

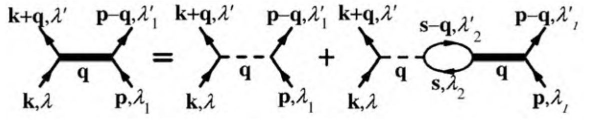

Figure 50. Diagrammatic illustration of the RPA dressed Coulomb interaction.

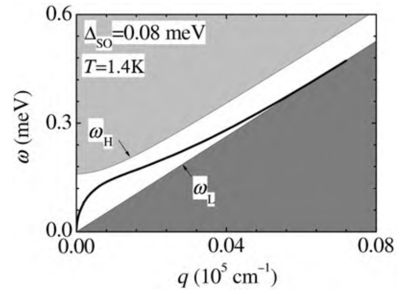

Figure 51. Plasmon spectrum (thick curve) of an electron gas in intrinsic graphene ($E_F = 0$) at temperature $T = 1.42$ K with $\Delta_{SO} = 0.08$ meV. Intra- (dark shaded) and inter- (light shaded) band single-particle continuums are also shown. $\omega_L$ and $\omega_H$ are the lower and upper borders separating the white (EHC gap) and shaded areas, respectively (see also [240]).

can be easily applied to Dirac gases with different $\Delta_{so}$ by scaling the energy and wavevector in units of $\Delta_{so}$ and $k_{so} = \Delta_{so}/(\hbar v_F)$, respectively.

At zero temperature or for $T \ll \Delta_{so}$, the intraband transition is negligible and $\epsilon_r > 0$. There is no plasmon mode in the system. With an increase in the temperature, holes appear in the valence band and electrons in the conduction band. The intraband transitions are enhanced and contribute to the electron–hole propagator of Equation (54) and a dip in $\epsilon_r$ at the intra-band electron-hole excitation continuum (EHC) edge $\omega_L$. This dip in $\epsilon_r$ results in plasmon modes above $\omega_L$. For $\Delta_{so} = 0$ where $\omega_H = \omega_L$, the intraband (interband) single-particle continuum occupies the lower (upper) part of the $\omega$–$q$ space below $\omega_L$ (above $\omega_L$) and the plasmon mode are Landau damped. In the presence of the SOI, i.e. for $\Delta_{so} \neq 0$, a gap of width $\omega_H - \omega_L$ is opened between the intra- and interband single-particle continuum and an undamped plasmon can exist in this gap, as shown in Figure 51. This plasmon mode may perhaps be observed in experiments.

The appearance of the undamped plasmon mode in the presence of the SOI is a result of the interplay between the intra- and inter-band correlations which can be adjusted by varying the temperature of the system in experiments. To show the temperature range in which an undamped plasmon mode exists, Figure 52 shows $\epsilon_r(\omega_L)$ (dotted curve) and $\epsilon_r(\omega_H)$ (solid curve) as functions in the temperature $T$ at $q = 0.05 \times 10^5\,\text{cm}^{-1}$. For $\Delta_{so} = 0.08\,\text{meV}$, an increase of the temperature from $T = 0$ leads to an increase in the ratio of the intra- to the inter-band correlation while $\epsilon_r$ in the EHC gap ($\omega_L \leq \omega \leq \omega_H$) decreases and crosses zero. There is no undamped plasmon mode when the inter-band correlation dominates at $T \leq 1.1\,\text{K}$ and when the intra-band correlation dominates at $T \geq 3.3\,\text{K}$. In the temperature regime 1.1 K $\leq T \leq 3.3\,\text{K}$ or $T \approx 2\Delta_{so}$ when the intra- and inter-band correlations match, however, $\epsilon_r(\omega_L) < 0$ while $\epsilon_r(\omega_H) > 0$ and one undamped plasmon mode exists.

Therefore, the SOI converts the Dirac electronic system into a narrow gap semiconductor with chiral properties. As a result, an undamped collective excitation was found to exist in the spectral gap of the single-particle continuum and is perhaps observable in the experiments. There have been a steady flow of reports in the literature on the electronic properties of graphene. Interestingly, the SOI-dependent

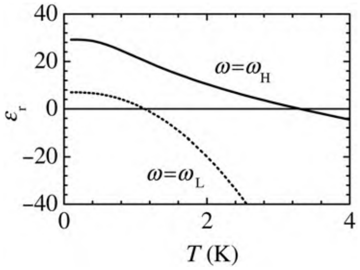

Figure 52. Temperature dependence of the real part of the dielectric function at the edges of the intra- and intersubband single-particle continuum $\omega_L$ (dotted curve) and $\omega_H$ (solid curve) at $q = 0.05 \times 10^5\,\mathrm{cm}^{-1}$.

dielectric function derived in [238] was employed by other authors to explore the possibility of Wigner crystallization in graphene [236].

After Wang and Chakraborty [238] reported their study of Coulomb screening and plasmon spectrum in monolayer graphene with zero or finite gap and doping at zero or finite temperature, a series of works have been reported on the many-body effects in graphene. Analytical results for dynamical polarization of graphene were reported within the RPA [240,241]. Instead of considering only the spin-orbit introduced energy gap, Qaiumzadeh and Asgari [242] assumed an unspecified energy gap of arbitrary width for doped monolayer graphene and studied the corresponding ground-state properties in the RPA. They concluded that the conductance and the charge compressibility decrease with the band gap. Almost during the same time, Pyatkovskiy [243] also derived analytically the dielectric function of gapped graphene at zero temperature and repeated the plasmon spectrum result of Wang and Chakraborty. In addition, the effect of plasmons on the energy band in graphene has been estimated and compared with the experimental result [254–256]. Hill, Mikhailov and Ziegler [246] have recently reported results on the dielectric function and plasmon dispersion based on the tight-binding band structure and take the non-Dirac effect of graphene dispersion band into account, including the anisotropy and the nonlinearity of the energy band. Those effects influence the plasmon spectrum, in terms of the anisotropic plasmon spectrum and extra plasmon mode. Coulomb screening and collective excitations spectrum in monolayer graphene using the RPA was also reported by other authors [257,258]. The magneto-optical excitations in monolayer graphene has also been investigated [259]. Finally, a THz source has been proposed based on the stimulated plasmon emission in graphene [260] and the absorption of THz electromagnetic radiation in gapped graphene has been estimated [261].

### 4.2.2. *Bilayer graphene*

While monolayer graphene has quasiparticles described by a chiral Dirac gas, bilayer graphene is best thought of as a chiral Fermi gas near the K points [139,140,207,262] (Section 3). Consequently, a comparison of their physical properties would offer new understanding and provide interesting predictions about the different behaviors between these two fundamental systems. Wang and Chakraborty [239] were the first to employ the RPA to address some of the interesting properties of the Coulomb screening and the collective excitations in bilayer graphene.

In the effective-mass approximation [139,262], the electrons in the K valley are described by a Hamiltonian with a mixture of linear and quadratic terms in the wave vector $k$ (see the first two terms of Equation (42) in Section 3.2.3). The eigenfunction of the above Hamiltonian is $\Psi^{\lambda}_{\vec{k}}(\vec{r}) = \frac{\mathrm{e}^{\mathrm{i}\vec{k}\cdot\vec{r}}}{\sqrt{2}}\left(c\mathrm{e}^{\mathrm{i}\phi_{\vec{k}}}\lambda\right)$ with the energy $E^{\lambda}_{\vec{k}} = \lambda\hbar^2 k\sqrt{k^2 - 2k_0 k\cos 3\varphi + k_0^2}/2m$ and the pseudospin angle $\lambda\phi_{\vec{k}}$. Here $\varphi = \arg(\vec{k}_+)$, $\phi_{\vec{k}} = \arg(k\mathrm{e}^{-2\mathrm{i}\varphi} - k_0\mathrm{e}^{\mathrm{i}\varphi})$ with $\arg(z)$ being the argument $\theta$ of a complex $z = |z|\mathrm{e}^{\mathrm{i}\theta}$, $k_0 \approx 10^8/\sqrt{3}\mathrm{m}^{-1}$ is the wave vector difference between the central pocket and any of the three 'leg' pockets in the same valley (Section 3.2.2.), and $\lambda = 1(-1)$ for the conduction (valence) band.

Just as for the case of the monolayer graphene [238] and other spin systems [251], we find that the dielectric matrix of a graphene bilayer is a unit matrix multiplied by a dielectric function

$$\hat{\varepsilon}(q,\omega) = 1 - v_q\hat{\Pi}_0(\vec{q},\omega), \tag{55}$$

with the bare Coulomb interaction $v_q = e^2/(2\varepsilon_0 q)$ and the electron–hole propagator is written explicitly in Equation (54). Near the central Dirac point at $k = 0$, the intraband backward scattering and interband vertical Coulomb scattering are forbidden and $|g^{\lambda,-\lambda}_{\vec{k}}(0)|^2 = |g^{\lambda,\lambda}_{\vec{k}}(-2\vec{k})|^2 = 0$. The same rules also hold for the three satellite Dirac points. For a large $k$ ($k \gg k_0$), $|g^{\lambda,-\lambda}_{\vec{k}}(0)|^2 = |g^{\lambda,-\lambda}_{\vec{k}}(-2\vec{k})|^2 = 0$, but $|g^{\lambda,\lambda}_{\vec{k}}(-2\vec{k})|^2 = 1$, i.e. the intraband backward transition is allowed but both the interband backward and vertical transitions are forbidden. The above selection rules together with the energy dispersion of the carriers indicate that the electrons (holes) close to the bottom (top) of the conduction (valence) band have very different behaviors from those away from the bottom (top).

The Coulomb screening is dictated by the response of the electron liquid to a pertubation. The static dielectric function at zero temperature versus $q$ is plotted in Figure 53(a). Its long wavelength limit is given by the properties of the four pockets around each of the Dirac points. The central point has an isotropic velocity $v_0 = \hbar k_0/(2m) = 10^5\,\mathrm{m\,s^{-1}}$ (with energy $E_0 = \hbar^2 k_0^2/2m = 3.9$ meV) while the satellite ones have the elliptic form of equi-energy lines with a minimum velocity equal to $v_0$ along their radial direction and a maximum of $3v_0$ along the azimuthal direction. The static dielectric constant at $q = 0$ is estimated to be $\varepsilon_s = 1 + 3e^2/(8\varepsilon_0\hbar v_0) \approx 105$. This value is much bigger than that of the monolayer graphene (4.5) [238]. This means that the long-range Coulomb interaction is much more strongly screened for the bilayer system, using a much bigger density of states near the Fermi energy in a bilayer graphene.

Another characteristic of bilayer graphene is its screening anisotropy, especially for scattering at a distance range of about 10 nm. This is shown by the difference between the solid and the dotted curves in Figure 53(a) and (b), corresponding to the directions of $\vec{q}$ pointing to any satellite from the central Dirac points ($\alpha = 0$) or connecting any two satellites ($\alpha = \pi/6$). Here $\alpha$ is the angle between $\vec{q}$ and the $x$-axis. At $q = \sqrt{3}k_0 = 10^8\,\mathrm{m}^{-1}$, the wavevector distance between any two satellite Dirac points, the anisotropy of $\varepsilon_s$ reaches its maximum with a mismatch of 20% along the different directions. The shoulder near $q = k_0 = 0.58 \times 10^8\,\mathrm{m}^{-1}$ in the solid curve

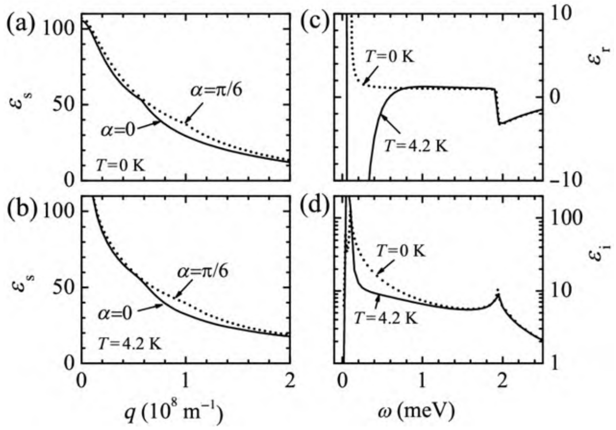

Figure 53. (a) The static dielectric function $\varepsilon_s$ versus the wavevector $q$ along the direction $\alpha = 0$ (solid) and $\pi/6$ (dotted) at $T = 0$. (b) The same as (a) but at $T = 4.2$ K. (c) The real part of the dielectric function $\varepsilon_r$ versus frequency $\omega$ at $T = 0$ (dotted) and at $T = 4.2$ K (solid). (d) The imaginary part of the dielectric function $\varepsilon_i$ versus $\omega$ at $T = 0$ (dotted) and at $T = 4.2$ K (solid). In (c) and (d), $q = 0.005 \times 10^8\,\mathrm{m}^{-1}$ and $\alpha = 0$. In the limit $\omega \to \infty$, $\varepsilon_r$ gradually approaches to one while $\varepsilon_i$ approaches to zero.

reflects the strong scattering between the carriers in the central and the $\varphi = 0$ satellite Dirac points. At a finite temperature, the energy pockets near the Dirac points are partially occupied and the intraband scattering strength is greatly enhanced. As a result, the static dielectric function near $q = 0$ increases rapidly, as shown in Figure 53(b) at $T = 4.2$ K. The effect of finite temperature is shown in Figure 53(c) and (d) for $q = 0.005$ along $\alpha = 0$, at $T = 0$, 4.2 K.

For $\omega > E_0/2$, the dielectric function of bilayer graphene is similar to that of a normal Fermi gas and its temperature dependence is weak. The step of $\varepsilon_r$ and the peak of $\varepsilon_i$ near $\omega = E_0/2 = 2$ meV correspond to the single-particle excitations coupling states with vanishing group velocity and wavevectors equal to half of the vector from the central pocket to a satellite pocket. For small $\omega$, however, the dielectric function becomes more sensitive to the temperature and shows characteristics of the Dirac gas. One sign of the Dirac gas is the lack of Coulomb screening ($\varepsilon_r \approx 1$) in the energy window between 1 and 2 meV. Another sign is that a low-energy plasmon mode appears only at a finite temperature. As shown in Figure 53 (c), $\varepsilon_r$ has no negative value for the energy $\omega < E_0/2$ at $T = 0$ but evolves into a deep negative dip at a finite temperature $T = 4.2$ K, when the energy pockets near the Dirac points are partially occupied. As a result, one observes a weakly Landau damped plasmon mode of dispersion $\omega \sim \sqrt{q}$ at $T = 0$ and a couple at finite temperatures.

The collective excitations of the electronic liquid in bilayer graphene are also a subject of interest. Figure 54(a) shows the plasmon spectrum of intrinsic bilayer graphene ($E_F = 0$). The dispersion of the weakly Landau-damped mode is indicated by the thick curve and has $\sqrt{q}$ dependence. Interestingly, the plasmon mode exists only at energy higher than $E_0/2$, i.e. double the depth of the energy pockets in the

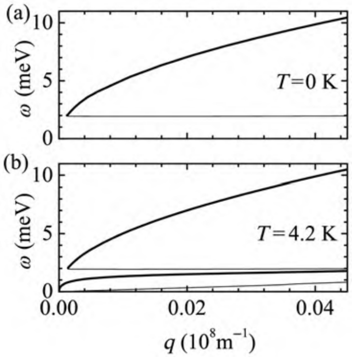

Figure 54. The plasmon spectrum of an undoped bilayer graphene at $T = 0$ (a) and at $T = 4.2\,\mathrm{K}$ (b). The thick curves indicate the weakly Landau damped modes while the thin curves represent the strongly damped modes.

Dirac points. At a finite temperature $T = 4.2\,\mathrm{K}$, another weakly damped plasmon mode shows up at the energy lower than $E_0/2$ and also has a dispersion of $\sqrt{q}$ near $q = 0$, as illustrated in Figure 54(b). The plasmon mode of higher energy that exists at $T = 0$ is not sensitive to the temperature. This temperature dependence of the low- and high-energy plasmon spectra represents a marked difference between electron gases having linear (without the collective excitations) and quadratic (with the collective excitations) energy dispersion at $T = 0$. The electronic states in bilayer graphene are similar to the Fermi type at high energies but revert to Dirac type at low-energy.

The carrier density of the system can be changed by doping [140]. For a typical doping density of $10^{12}\ \mathrm{cm}^{-2}$ [140,262], the Fermi energy is high enough above the bottom of the conduction band that the linear $k$ term in the Hamiltonian can be neglected. The electrons then have quadratic dispersion but with chirality and $\phi = -2\varphi$. Near $q = 0$, the plasmon dispersion in doped bilayer graphene has $\sqrt{q}$ dependence, as shown by the solid curve in Figure 55, and shares the same dispersion $\omega_p^{2D} = [n_e e^2 q/2\varepsilon_0 m]^{\frac{1}{2}}$ with a normal two-dimensional Fermi gas. To see the effect of the chirality, for comparison we plot as a dotted curve the plasmon dispersion of a normal two-dimensional Fermi gas with two valleys. The two curves overlap for the small $q$ but separate as $q$ increases. The maximum difference in the dispersion appears near $q = \sqrt{2}k_{\mathrm{F}}$ when $\vec{k}$ and $\vec{k} + \vec{q}$ form a right angle in the Fermi plane and the corresponding transition is forbidden in the bilayer graphene due to the chiral scattering properties.

The bilayer plasmon frequency is smaller than that of the monolayer because the dielectric properties of the monolayer are weaker. Hwang and Das Sarma [208] derived analytical expression of static dielectric function for bilayer graphene with moderate doping when the linear Hamiltonian term can be neglected. With the analytical expression, they could estimate the screened static Coulomb potential and show the Kohn anomaly near $q = k_{\mathrm{F}}/2$, the Friedel oscillation and the form of RKKY interaction in bilayer graphene. See Section 3.5 for a description of this work.

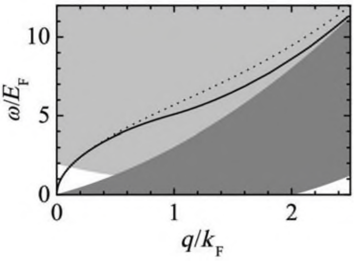

Figure 55. The plasmon spectrum of a doped bilayer graphene (solid curve) with a typical carrier density of $10^{12}\,\mathrm{cm}^{-2}$. Correspondingly, $E_F = 36.3\,\mathrm{meV}$ and $k_F = 1.77 \times 10^8\,\mathrm{m}^{-1}$. The plasmon spectrum in the same system but without chirality is plotted as a dotted curve for comparison. Intra- (dark shaded) and inter- (light shaded) band single-particle continuums are also shown.

The magneto-plasmons in bilayer graphene were considered in a self-consistent analytical framework by Tahir *et al.* [263]. They derived expressions for the plasmon frequency, and compared their results to those for monolayer graphene and traditional 2DESs. The light effective mass of the electrons in the bilayer, and the relatively weak dielectric properties of graphene ensures that the plasmon frequency is approximately two times higher than that of, for example, GaAs–AlGaAs heterojunctions. The magnetoplasmon and Weiss oscillation has been studied in mono- and bilayer graphene [264,265]. The Boltzman equation has been used to study the electronic transport in bilayer graphene [266]. Then the effects of site dilution disorder on the electronic properties, such as self-energies, the density of states, the spectral functions and both DC and AC transport properties, in graphene multilayers have also been studied [267].

Theoretical approaches described in this section were recently employed by Wang and Chakraborty to investigate the Coulomb screening and plasmon spectrum in a bilayer graphene under a perpendicular electric bias [268]. The potential bias applied between the two graphene layers opens a gap in the single-particle energy spectrum and makes the semimetal bilayer graphene into a semiconductor. As a result, the dielectric function for the Coulomb interaction and the propagator function were found to be modified significantly [268]. The potential bias also opens a gap in the single-particle excitation spectrum and softens the collective modes. This may result in undamped collective modes that are observable in experiments. Experimental observation of plasmon modes with long lifetime might prove to be beneficial for future device applications.

### 4.3. *Graphene in a strong electromagnetic field*

Graphene also displays unique and intriguing properties when it is irradiated by strong electromagnetic fields (EMFs), such as laser light. Floquet theory (the temporal analogue of Bloch theory) has been applied [224,269] to determine the quasienergy spectrum and dynamical density of states, in this situation.

The time-periodic EMF is represented by a vector potential, and the minimal coupling substitution made in the Hamiltonian. The Floquet theory is then applied, so that the overall wave function of Floquet state $\alpha$ is written as $\Psi_\alpha(t) = e^{-i\varepsilon_\alpha t}\Phi_\alpha(t)$ where $\Phi_\alpha(t+T) = \Phi_\alpha(t)$, with $T = 2\pi/\Omega$. The Floquet Hamiltonian may be diagonalized numerically to produce the spectrum of quasienergies $\varepsilon_\alpha$ and the wave functions $\Phi_\alpha(t)$, which may then be used to calculate physical quantities such as the density of states, or the electronic current. As an example, Oka *et al.* [269] showed that an intense, circularly polarized EMF parametrized by frequency $\Omega$ and intensity $F$ generates spectral gaps at $\omega = \pm\Omega/2$, and at the Dirac point. The gap at the Dirac point is initially quadratic in the intensity: $2\kappa \sim 2A^2/\Omega$, but takes the asymptotic behavior $2\kappa \sim 2A - \Omega$. Here $A = F/\Omega$, where $F$ is the field strength (intensity). This gap exists both in bulk monolayer graphene, and in graphene nanoribbons. The authors then use the Keldysh approach to calculate the current through a finite-sized, irradiated monolayer graphene sample and find that a dc Hall current in induced in the ribbon.

Fistul *et al.* [270] have shown that an intense EMF may mitigate the Klein effect in a *n-p* junction and allow electrostatic confinement of electrons. It does this by creating a dynamical band gap, which forbids the tunnelling of quasiparticles through the potential barrier via hole states, as in the Klein effect. Instead, electrons may only tunnel via interband processes which are strongly suppressed. The size of the gap is dependent on the intensity and frequency of the radiation, so the authors claim that structures such as QDs or *n–p–n* transistors may be engineered by this technique. Photon-assisted tunnelling was also considered in the context of bilayer graphene by Shafranjuk [271]. López-Rodríguez and Naumis describe analytical results within the Floquet formalism [272] and Wright *et al.* [273] have shown that bilayer ribbons show enhanced optical conductivity in the terahertz and far infra-red frequency ranges.

Abergel and Chakraborty [224] considered irradiated bilayer graphene, both with and without the gap-generating bias potential. When the bilayer was unbiased, a similar picture was found to that of the monolayer, with dynamical gaps being generated at the charge-neutrality point, and at $\omega = \pm n\Omega/2$, with $n$ an integer. These gaps are manifest in the density of states, as shown in Figure 56. In the case when there is a finite gap at zero energy (evidenced by the low density of states), the radiation may cause dynamical states to be created in the gapped region (see, e.g. the finite density of states for $\omega < 5\,\mathrm{meV}$ in the K valley for $F = 5\,\mathrm{kV/cm}$ in Figure 56(a)). The most fascinating observation to be made from Figure 56 is that for $U \neq 0$, the density of states is not the same in each valley, since the orientation of the circular polarization of the irradiating field couples more strongly to electrons in one valley than in the other. If the polarization of the radiation is reversed, or the direction of the bias potential $U$ is swapped, then the strong and weak couplings are also reversed. In particular, the radiation-induced density of states in the gapped region is, in some cases, only present in one valley. For example, for $F = 1\,\mathrm{kV\,cm^{-1}}$ and $U = 10\,\mathrm{meV}$, there is finite density of states in the K valley for $\omega < U/2$, but not in the K$'$ valley. The authors go on to show how irradiated bilayer graphene may be used as a valley filter for an electron current. By irradiating one part of a graphene flake, and attempting to pass current through this section, electrons will only pass if there is a finite density of states through which they can propagate. Therefore, tuning the radiation so that the density of states is in one valley or the other immediately yields a valley-polarized current. This effect was demonstrated theoretically by

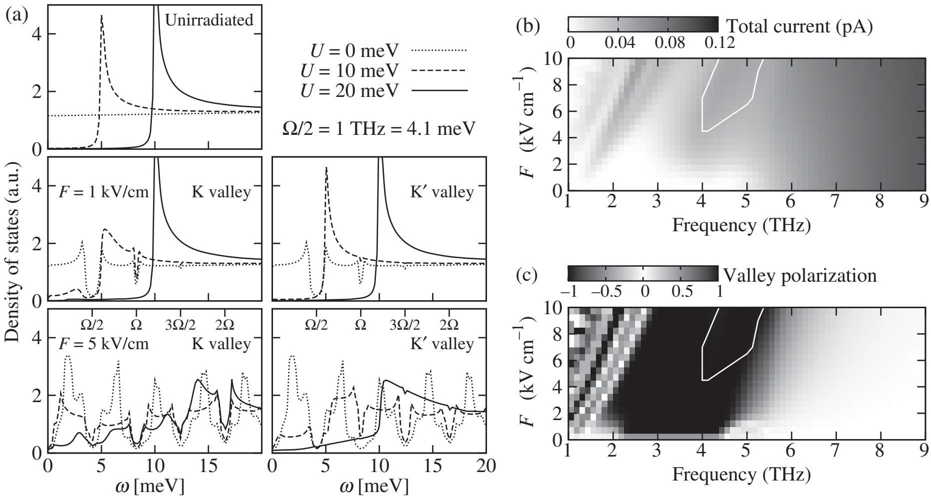

Figure 56. (a) Density of states in irradiated bilayer graphene for three field intensities and three gap sizes. (b) The total current, and (c) the valley polarization of electron transport through an irradiated bilayer graphene device. In (b) and (c), $U = 20$ meV, and the transverse (current-driving) bias is 12 meV. The white contours denote the region of simultaneous high valley polarization (>98%) and significant current flow (>0.08 pA).

computing the current through the device via a tunnelling approach. The two graphitic 'leads' are described by appropriate Hamiltonian for unirradiated bilayer graphene. The central (irradiated) region is linked to the leads via coupling Hamiltonians which assume that the momentum and energy of the electron must be conserved at the boundary. The valley component of the charge current in the right-hand (outgoing) lead is $J_\xi = -\langle \mathrm{d}N_R^\xi/\mathrm{d}t \rangle$, where $N_r^\xi$ stand for the number operator of $\xi$-valley electrons in the right lead. A nonequilibrium Green's function method is used to compute the current of electrons in the $\xi$ valley, which is

$$J_\xi = -\frac{2e}{h}\int \frac{d^2\vec{k}}{(2\pi)^2}\sum_{\alpha_\xi}\mathrm{Tr}\left\{\bar{\Gamma}_{\alpha_\xi}\Im\bar{G}^r(E_{\alpha_\xi})\right\}\left[f_c(E_{\alpha_\xi}) - f_R(E_{\alpha_\xi})\right],$$

where $f_{c,R}$ is the occupation of electrons in the central region or right-hand lead, $G^r$ is the full retarded Green's function in the central region, $\Gamma$ contains the inter-region coupling parameters, $\alpha$ labels the Floquet states, $E$ is the energy of an electron in the lead and Tr denotes the trace over the matrix structure (designated by the overbar). The Green's function is calculated using the Floquet states, and includes the self energy due to the two graphitic leads.

This filter device can produce electrons in either valley, simply by reversing the polarity of the incident light, or the sign of the bias potential $U$. In Figure 56(b) and (c), the total current through irradiated bilayer graphene is shown, along with the simultaneous valley polarization. The area where the polarization is greater than 98%, and the current is greater than 0.08 pA is shown by the white contour.

## 5. Zero-field transport in graphene

Transport properties in graphene and bilayer graphene are among the most exciting observations in these new materials. What is so special about them? First of all, graphene is a genuine two-dimensional electronic system. Second, it is a semimetal at the charge neutrality point and a metal away from the charge neutrality point. This means that the Fermi surface, responsible for transport at low temperatures, consists either of two (slightly deformed) circles away from the charge neutrality point which shrink to two Dirac points exactly at charge neutrality. Moreover, the fact that graphene has two bands, touching each other only at the two Dirac points (Section 1), provides intra- and interband scattering, where the latter leads to a number of interesting features such as Klein tunnelling and a constant optical conductivity.

Transport processes can be distinguished by the type of scattering of the (quasi) electrons in the material. First of all, the electrons are scattered by the honeycomb lattice, which leads to the formation of Bloch states if the lattice is perfectly periodic. This case is also known as ballistic transport, in which the boundary conditions play a crucial role. Then there can be scattering by non-periodic structures (impurities, lattice defects and lattice deformations). This leads to diffusion of the electrons, under certain conditions also to Anderson localization. And finally, there is scattering between the electrons themselves due to Coulomb interaction and electron–phonon interaction.

The basis for calculating quantum transport properties is either the linear response theory (Kubo formalism) or the evaluation of transmission coefficients (Landauer–Büttiker formalism). Both approaches have been used frequently for graphene and gave the same results for comparable quantities. In the following, we will employ the Kubo formalism because it provides more flexibility for calculating general physical properties such as thermal effects and optical conductivities. Away from the neutrality point a classical (Boltzmann) approach was successful [274–276] and will be discussed briefly.

### 5.1. *Basic experimental facts*

Already the first experiments on graphene by Novoselov *et al.* [17] and Zhang *et al.* [85] revealed very characteristic transport properties in graphene. Graphene as well as a stack of two graphene sheets (i.e. a graphene bilayer) are semimetals with remarkably good conducting properties [1,17,85]. These materials have been experimentally realized with external gates, which allow a continuous change of charge carriers.

Besides the quantum Hall effect (Section 2), it was found that the longitudinal conductivity changes linearly as a function of gate voltage $V_g$ with a negative slope for holes and a positive slope for electrons. There is a minimal conductivity $\sigma_{\min}$ near the charge neutrality point (cf. Figure 57). The latter has attracted some attention because its value seems to be very robust in terms of sample quality and temperature [1,27,277,278]. More recent experiments by Du *et al.* [26] on suspended graphene, however, indicated that below $T \approx 150\,\mathrm{K}$ the minimal conductivity decreases linearly with decreasing $T$ and reaches the extrapolated value $\sigma_{\min} \approx 2e^2/h$ at $T = 0$. A similar result was found by Danneau *et al.* [279]. This clearly

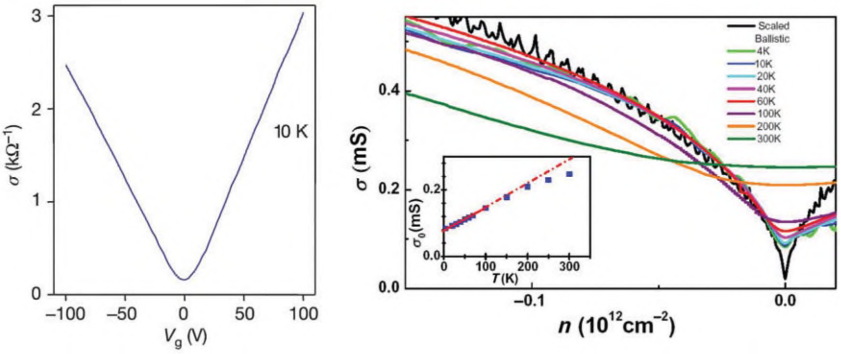

Figure 57. Measured conductivities in graphene. The linear behavior of the conductivity as a function of the gate voltage is shown for graphene on a substrate at fixed temperature $T = 10\,\mathrm{K}$ (left panel) (Reprinted figure with permission from K.S. Novoselov *et al.*, Nature, 438, p. 197, 2005 [17]. Copyright © (2005) Nature Publishing Group.) and for suspended graphene at several temperatures (right panel) (Reprinted figure with permission from X. Du *et al.*, Nature Nanotechnology, 3, p. 491, 2008 [26]. Copyright © (2008) Nature Publishing Group). The inset on the right panel shows the behavior of the minimal conductivity.

indicates that the main mechanism of transport in graphene at the NP is diffusion, possibly with a very large mean-free path. Away from the NP the linear behavior has not always been observed but also a sublinear behavior. One possible reason is that the linear behavior is due to long-range scattering by charged impurities, which may not be present in suspended graphene [26].

*Role of disorder* – Disorder might play an important role in the physics of graphene. First of all, a two-dimensional lattice is thermodynamically unstable. It is known that this is the origin of the strong corrugations in graphene in the form of ripples. Another source of disorder are (charged) impurities in the substrate, which probably affect the transport properties substantially. Recent experiments on suspended graphene have been able to eliminate this type of disorder. Experimental evidence of strong effects of disorder comes from the observation of puddles of electrons and holes at the charge neutrality point [213]. In a recent experiment with hydrogenated graphene (graphane), disorder is added by an inhomogeneous coverage by hydrogen atoms. This leads to the formation of localized states which causes a non-metallic behavior characterized by a variable-range hopping conductivity [280].

*Role of electron–electron interaction* – There is no clear evidence for an effect of electron–electron interaction on transport properties. This is supported by recent theoretical findings, based on perturbative renormalization group calculations [232,281,282], that Coulomb interaction provides only a correction of 1–2% for the optical conductivity [283]. This is in good agreement with the experiments on the optical transparency of graphene [146,284].

*Role of electron–phonon interaction* – Although there is a remarkable electron–phonon interaction [217,285,286] in graphene, its effect on transport properties has not been investigated in detail. Some experimental findings of a gap opening was associated with electron–phonon interaction [287] but in most samples the conductivity is explained by non-interacting particles. The optical conductivity might be affected by the electron–phonon interaction of gated graphene before interband scattering can dominate transport (i.e. when the frequency $\omega$ is less than $E_F/\hbar$) [284].

### 5.2. *Low-energy approximation and random fluctuations*

The linear approximation of the tight-binding model for monolayer graphene was introduced in Section 1.2. Here we focus on the low-energy properties near the nodes of neutral graphene, taking into account also random scattering caused by ripples and impurities. Moreover, a random gap can appear. The reason in the case of monolayer graphene is that fluctuations appear in the coverage of the monolayer graphene by additional non-carbon atoms [280,288]. In the case of bilayer graphene with a dual gate [140,185] the random gap is caused by the fact that the graphene sheets are not planar but create ripples [24,289,290]. As a result, electrons experience a randomly varying gap along each graphene sheet.

The two bands in monolayer graphene and the two low-energy bands in bilayer graphene represent a spinor-1/2 wave function. This allows us to expand the corresponding Hamiltonians in terms of Pauli matrices $\sigma_j$ as

$$\mathcal{H} = h_1\sigma_1 + h_2\sigma_2 + \sum_{j=0}^{3} v_j\sigma_j. \tag{56}$$

Near each node the coefficients $h_j$ read in low-energy approximation [291]

$$h_j = \mathrm{i}\nabla_j \quad \text{(monolayer graphene)}, \tag{57a}$$

$$h_1 = \nabla_1^2 - \nabla_2^2, \quad h_2 = 2\nabla_1\nabla_2 \quad \text{(bilayer graphene)}, \tag{57b}$$

where $(\nabla_1, \nabla_2)$ is the 2D gradient, $v_1$ is a random scalar potential, $v_{2,3}$ the two components of a random vector potential and $v_3$ a random gap. This is a gradient expansion of the monolayer graphene and bilayer graphene tight-binding Hamiltonians around the nodes K and K′.

It is assumed here that randomness scatters only at small momentum such that intervalley scattering, which requires a large momentum at least near the nodes [292], is not relevant and can be treated as a perturbation. Then each valley contributes separately to the density of states and to the conductivity, and the contribution of the two valleys is additive. This allows us to consider the low-energy Hamiltonian in Equations (56), (57) for each valley separately, even in the presence of randomness. Within this approximation the gap term $v_3 \equiv m$ is a random variable with mean value $\langle m_r \rangle = \bar{m}$ and variance $\langle (m_r - \bar{m})(m_{r'} - \bar{m}) \rangle = g\delta_{r,r'}$. The following analytic calculations will be based entirely on the Hamiltonian of Equations (56) and (57). In particular, the average Hamiltonian $\langle \mathcal{H} \rangle$ can be diagonalized by Fourier transformation and is

$$\langle \mathcal{H} \rangle = p_1\sigma_1 + p_2\sigma_2 + \bar{m}\sigma_3 \tag{58}$$

for monolayer graphene with eigenvalues $E_p = \pm\sqrt{\bar{m}^2 + p^2}$. For bilayer graphene, the average Hamiltonian is

$$\langle \mathcal{H} \rangle_m = (p_1^2 - p_2^2)\sigma_1 + 2p_1p_2\sigma_2 + \bar{m}\sigma_3, \tag{59}$$

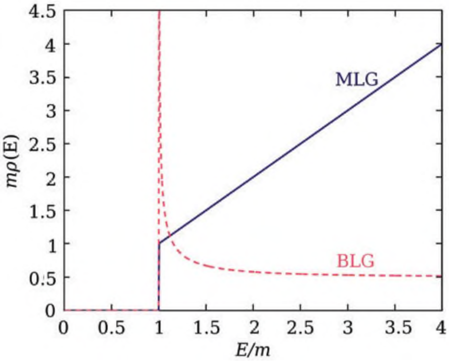

Figure 58. Density of states for monolayer graphene and bilayer graphene with a uniform gap (from [293]). Bilayer graphene has a singularity at the gap edge.

with eigenvalues $E_k = \pm\sqrt{\bar{m}^2 + p^4}$. In order to apply results from these calculations to monolayer graphene or bilayer graphene we must include a degeneracy factor $\gamma = 4$, referring to the two valleys K and K′ and the two-fold spin degeneracy of the electrons.

### 5.2.1. *Density of states*

Transport properties at temperature $T = 0$ are connected to the density of states $\rho(E_{\mathrm{F}})$ at the Fermi level $E_{\mathrm{F}}$ and the diffusion coefficient $D$ through the Einstein relation for the conductivity:

$$\sigma(\omega = 0) \propto D\rho(E_{\mathrm{F}}). \tag{60}$$

In the absence of disorder, the density of states of 2D Dirac fermions opens a gap, as soon as a nonzero term $m$ appears in the Hamiltonian of Equation (56), since the low-energy dispersion is $E_p = \pm\sqrt{m^2 + p^2}$ for monolayer graphene and $E_p = \pm\sqrt{m^2 + p^4}$ for bilayer graphene (cf Figure 58). At low energies, the density of states of monolayer graphene is

$$\rho(E) = |E|\Theta(|E| - m), \tag{61}$$

where $\Theta(x)$ is the Heaviside function. For bilayer graphene the density of states is

$$\rho(E) = \frac{|E|}{2\sqrt{E^2 - m^2}}\Theta(|E| - m). \tag{62}$$

The density of states for both cases are shown in Figure 58. Random fluctuations of $m$ can fill the gap with states by band broadening and by the development of Lifshitz tails, as shown in Figure 59.

## 5.3. *Theory of transport*

Transport properties, such as electric and thermal conductivities, can be calculated within either the classical Boltzmann or within the Kubo formalism. The former is

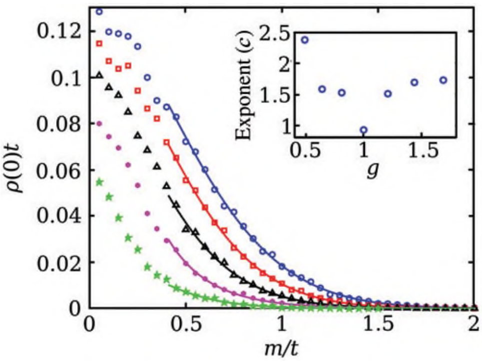

Figure 59. The density of states calculated numerically at the neutrality point for Gaussian random gap for a 200×200 honeycomb lattice for $g = 0.9^2$, 1, $1.1^2$, $1.2^2$ and $1.3^2$ from bottom to top after 400 averages. The symbols denote the numerical data, solid lines are fits using $a\,\exp(-bm^c)$. The inset shows the obtained exponents, $c$, as a function of $g$, which is close to 1.5 (from [293]).

very successful for providing results away from the nodes. At the nodes quantum effects are crucial, so the Boltzmann approach fails and the Kubo formalism must be employed. An alternative to the Kubo formalism is the Landauer formalism. Both formalisms, however, lead to similar results [294]. Therefore, we will restrict the subsequent study on the Kubo formalism after a brief discussion of the Boltzmann approach.

### 5.3.1. *Boltzmann approach*

From the classical Boltzmann theory, where quantum effects are included by choosing a Fermi distribution for the otherwise classical electrons [229], we get for the conductivity the expression

$$\sigma = \frac{1}{2} e^2 v_F^2 \rho(E_F)\tau, \tag{63}$$

where $\tau$ is the scattering time and $v_F$ the Fermi velocity. This relation is very similar to the Einstein relation of Equation (60). In the case of Dirac fermions ($\mathcal{H} = v_F \vec{p} \cdot \vec{\sigma}$), where the density of states is linear in $E_F$, we obtain

$$\sigma = 2\frac{e^2}{h}\frac{E_F \tau}{\hbar}. \tag{64}$$

The scattering time $\tau$ is determined by the distribution of random scatterers. Thus a major problem of calculating transport properties is to evaluate $\tau$, and one possible way to do that is provided by the Boltzmann approach. The latter, based on the classical Boltzmann equation, has been a very successful concept for the discussion of transport in solid-state physics. It is more difficult to apply in graphene, however, as we will discuss next.

When $\tau$ is roughly a constant with respect to $E_F$, as in normal metals, the conductivity in Equation (64) would change linearly with $E_F$. The latter, on the other hand, is related to the density of charge carriers $n$ as $E_F \propto \sqrt{n}$, as a consequence of the linear density of states:

$$n \propto \int_0^{E_F} \rho(E)\mathrm{d}E \approx \int_0^{E_F} E\,\mathrm{d}E = E_F^2/2.$$

Therefore, $\sigma$ would change with $\sqrt{n}$ for monolayer graphene. This is not in agreement with experimental observations on gated graphene on a substrate, where it was found that $\sigma$ changes linearly with $n$ [17]. For bilayer graphene the density of states is constant near the nodes, which is a consequence of the parabolic dispersion. Then we have $n \propto E_F$, and a constant $\tau$ leads to a linear behavior in gated bilayer graphene, in agreement with the experimental observations [27]. From this point of view, bilayer graphene has a more conventional transport behavior than monolayer graphene.

To get a linear behavior also for monolayer graphene, the assumption of a constant $\tau$ must be replaced by a density-dependent $\tau$ that changes linearly with $E_F$: $\tau \sim k_F$. Such a behavior was obtained from the Born approximation of $\tau$ by assuming $V \sim \hbar v\pi/2k_F$ [98]. However, two problems remain within this result: one is the vanishing minimal conductivity, in contrast to the experimental observation of a minimal conductivity at the neutrality points [17]. The other is the absence of a finite offset (i.e. the linear conductivity curves of the holes and the electrons do not meet at $E_F = 0$). This behavior was observed in the experimental curves [278].

At the nodes the Fermi surface are just points and the density of states of monolayer graphene vanishes (i.e. there are no states at the Fermi energy). This implies that a statistical concept, which uses the distribution of charges, may experience some difficulties. Nevertheless, the Boltzmann approach can be applied away from the Dirac point and then the Dirac point is approached at the end. Perturbation theory with short-range scatterers gives for the scattering time [274–276]

$$\tau \propto k_F^{-1} \sim \infty. \tag{65}$$

According to Equation (64), including the Dirac dispersion $E_F \propto k_F$, this leads to a constant nonzero conductivity. Thus, the Boltzmann approach gives us a nonzero minimal conductivity when we consider short-range scatterers. Unfortunately, a divergent scattering time at the Dirac point does not describe a realistic situation because quasiparticles are scattered, e.g. by the ripples or charge inhomogeneities. Moreover, the conductivity is constant also away from the nodes $E_F = 0$ because the wavevectors $k_F$ always cancel each other. Unfortunately, this is again in disagreement with the linearly increasing conductivity of the experiment [17].

In conclusion, the classical Boltzmann approach describes the transport properties qualitatively correct. However, it needs two different types of scattering to obtain the conductivity near the Dirac point and away from the Dirac point properly. The divergent scattering time at the Dirac point cannot be correct though, at least for strong disorder. The subsequent discussion focuses on a more microscopic approach, based on the Kubo formula for linear response to an external electric field, where we start from the Hamiltonian in Equation (56). This will allow us to recover the Einstein relation Equation (60) with a disorder dependent diffusion coefficient $D$, a non-divergent scattering time and the robustness of the minimal conductivity.

### 5.3.2. *Kubo formalism*

A quantum approach to transport starts from a Hamiltonian $\mathcal{H}$ (here for independent electrons) and the corresponding current operator

$$j_k = -\mathrm{i}e[\mathcal{H}, r_k],$$

where $r_k$ is a component of the position operator of the electron. The average current, induced by a weak external electric field $E$, is obtained in terms of linear response as Ohm's law

$$\langle j_k \rangle = \sigma_{kl} E_l,$$

with conductivity $\sigma_{kl}$. The general form of the conductivity in the Kubo formalism can be expressed as a product of one-particle Green's functions $G(z) = (\mathcal{H} + z)^{-1}$ at different energies $z$ [295]. In the following, we exclude an external magnetic field. This leads to a vanishing Hall conductivity $\sigma_{kl} = 0$ for $k \neq l$. Following the notation of [296], there are two contributions to the real part of the longitudinal conductivity as $\sigma = \sigma^I + \sigma^{II}$ with

$$\sigma^I_{kk}(\omega) = -\frac{e^2}{2h}\omega \int \sum_r (r_k - r'_k)^2$$
$$\times \operatorname{Re}\left\{\left\langle \mathrm{Tr}_2\left[ G_{rr'}\left(\frac{1}{2}\omega - \epsilon - \mathrm{i}\delta\right) G_{r'r}\left(-\frac{1}{2}\omega - \epsilon - \mathrm{i}\delta\right)\right]\right\rangle\right\} \kappa_\beta(\epsilon)\mathrm{d}\epsilon$$

and

$$\sigma^{II}_{kk}(\omega) = \frac{e^2}{2h}\omega \int \sum_r (r_k - r'_k)^2$$
$$\times \operatorname{Re}\left\{\left\langle \mathrm{Tr}_2\left[ G_{rr'}\left(\frac{1}{2}\omega - \epsilon - \mathrm{i}\delta\right) G_{r'r}\left(-\frac{1}{2}\omega - \epsilon + \mathrm{i}\delta\right)\right]\right\rangle\right\} \kappa_\beta(\epsilon)\mathrm{d}\epsilon$$

with

$$\kappa_\beta(\epsilon) = f_\beta(\epsilon + \omega/2) - f_\beta(\epsilon - \omega/2)$$

and with the Fermi distribution function $f_\beta(x) = (1 + e^{\beta(x-\mu)})^{-1}$ at temperature $T = 1/k_B\beta$. The brackets $\langle \ldots \rangle$ refer to disorder average and $\omega$ is the frequency of the external electric field. The spinor structure of monolayer graphene and bilayer graphene is taken into account by the trace $\mathrm{Tr}_2$ over $2 \times 2$ matrices.

The expressions of the conductivity are rather complicated which make them difficult to handle. Therefore, for practical calculations it is useful to study certain limits and to apply approximations.

*DC conductivity*: the standard approach to the DC conductivity (i.e. $\omega \rightarrow 0$) is to neglect $\sigma^I$, since for this expression the poles of the Green's functions are in the same half plane. Therefore, any amount of disorder will lead to an exponential decaying Green's functions. Then the summation over the lattice sites $r$ is finite and the prefactor $\omega$ gives a vanishing DC limit $\omega \rightarrow 0$. This allows us to write

$$\sigma_{kk} \approx \sigma_{kk}^{II} = \frac{e^2}{h}\frac{\omega}{2}\int C'(\epsilon, \omega)\kappa_\beta(\epsilon)\mathrm{d}\epsilon, \tag{66}$$

where $C'(\varepsilon, \omega)$ is the real part of

$$C(\epsilon, \omega) = \lim_{\delta \to 0}\sum_r r_k^2 \langle \mathrm{Tr}_2[G(r, 0; \epsilon - \omega/2 - \mathrm{i}\delta)G(r, 0; \epsilon + \omega/2 + \mathrm{i}\delta)]\rangle. \tag{67}$$

A substantial simplification is possible in the zero-temperature limit $T = 0$ which restricts the integration over particle energies $\epsilon$ to a small interval, given by the frequency $\omega$:

$$\sigma_{kk} = -\frac{e^2}{h}\frac{\omega}{2}\int_{\mu-\omega/2}^{\mu+\omega/2} C'(\epsilon, \omega)\mathrm{d}\epsilon. \tag{68}$$

A further simplification comes from the approximation by pulling out the integrand at $\epsilon = \mu$:

$$\sigma_{kk} \approx -\frac{e^2}{2h}\omega^2 C'(\mu, \omega). \tag{69}$$

This expression can be directly compared with the result of the Boltzmann approach in Equation (63).

We begin with a clean sample by ignoring the disorder average in Equation (67) and introduce the pure two-particle Green's function (2PGF)

$$C_0(\mu, \omega) = \lim_{\delta \to 0}\sum_r r_k^2 \mathrm{Tr}_2[G(r, 0; \mu - \omega/2 - \mathrm{i}\delta)G(r, 0; \mu + \omega/2 + \mathrm{i}\delta)], \tag{70}$$

which is for Dirac fermions without scattering and with infinite cutoff [297]

$$C_0(\mu, \omega) = -\frac{1}{8\omega\pi}\left[\frac{8}{\omega} + \frac{1 - 4\mu^2/\omega^2}{\mu}\ln\left(\frac{(1 + 2\mu/\omega)^2}{(1 - 2\mu/\omega)^2}\right)\right]. \tag{71}$$

This becomes at the Dirac point $\mu = 0$ the simple expression

$$C_0(0, \omega) = -2/\pi\omega^2 \tag{72}$$

and with Equation (69) we obtain the well-known DC result [298–300] for the conductivity:

$$\sigma_{kk} = \frac{1}{\pi}\frac{e^2}{h}. \tag{73}$$

*AC conductivity*: for $\omega > 0$ and $T > 0$ the conductivity is a function of $\omega/T$. Therefore, we must keep $T$ finite for the AC conductivity. Moreover, now we must take into account also $\sigma^I$. This gives for Dirac fermions, where we ignore the additional factor 4 that comes from the valley and from the spin degeneracy, the expression [301,302]

$$\sigma_{kk} \sim \frac{\pi}{8}\frac{e^2}{h}\frac{\sinh(\beta\omega/2)}{\cosh(\beta\omega/2)+\cosh(\beta\mu)}.$$

Here the frequency $\omega$ is restricted to the bandwidth of the underlying lattice Hamiltonian. For $\beta\mu \ll \beta\omega \sim \infty$ this becomes a frequency-independent expression [301,303–306]:

$$\sigma_{kk} \sim \frac{\pi}{8}\frac{e^2}{h}.$$

Including the spin and valley degeneracy, this agrees with the experimentally observed plateau of the optical conductivity of $\pi e^2/2h$ [146,284]. There is a correction factor due to Coulomb interaction [281–283]

$$1+\frac{c_1}{1+\alpha\ln(\lambda/\omega)/4},$$

where $\lambda$ is the cut-off of the Dirac spectrum and $\alpha = e^2/\hbar v \approx 2.2$ is the effective fine structure constant. The numerical coefficient $c_1$ has been debated in a number papers, where the most recent value is $c_1 = 0.0125$ [283] that agrees with the previous result in [282].

Another possible correction is due to disorder, always present in realistic graphene samples in the form of ripples and impurities. Disorder leads to an effective scattering of the quasiparticles that can be characterized as a scattering rate. A conventional way of including scattering by random impurities is to introduce a scattering rate $\eta$ in the form of an imaginary term $i\eta$ through the substitution $\omega \to \omega + 2i\eta$ in $C_0(\mu, \omega)$ such that

$$C(\mu,\omega) \approx C_0(\mu,\omega+2i\eta). \tag{74}$$

There are several options to determine the phenomenological parameter $\eta$ (scattering rate or inverse scattering time), for instance, by the Born approximation [229] or the self-consistent Born approximation [229,262,275,276,307–309] which will be discussed in Section 5.5.1. It implies that

$$C_0'(0,\omega+2i\eta) = -2\mathrm{Re}\left(\frac{1}{\pi(\omega+2i\eta)^2}\right) = -\frac{2}{\pi}\frac{\omega^2-4\eta^2}{(\omega^2+4\eta^2)^2}, \tag{75}$$

and with Equation (69) we obtain the following for the conductivity:

$$\sigma_{kk} \approx \frac{e^2}{\pi h}\frac{\omega^2(\omega^2-4\eta^2)}{(\omega^2+4\eta^2)^2}. \tag{76}$$

This is the well-known DC result $e^2/\pi h$ only when the scattering rate $\eta$ is much smaller than the frequency, i.e. in the weak-disorder limit. The reason for this behavior is simply related to the fact that for any $\eta > 0$ the 2PGF decays exponentially on the scale $1/\eta$, always leading to a vanishing DC conductivity. It is not caused by Anderson localization but just by the incorrect evaluation of the

2PGF. This can be cured by introducing an accurate description of the average 2PGF in Equation (67) instead of the product of two averaged one-particle Green's functions.[10]

In the following we will discuss in more detail the effect of disorder on the transport properties, since this is important for applying the theory to the physics of realistic graphene samples. Moreover, in this field there are number of open questions which might be a challange for future studies.

### 5.4. *Perturbation theory for disorder*

The fact that for weak disorder (i.e. for $\eta \ll \omega$) the semiclassical approximation in Equation (76) gives reasonable values for the conductivity suggests that transport properties can be evaluated in terms of perturbation theory with respect to disorder. Since the scattering rate $\eta$ vanishes with vanishing disorder, this quantity might also be available in perturbation theory. Here we use the low-energy Hamiltonian of Equation (56) and treat the random variables $v_j$ as perturbations. A simple case is uncorrelated Gaussian randomness with zero mean and variance

$$\langle v_{jr} v_{j'r'} \rangle = g_j \delta_{jj'} \delta_{rr'} \quad (j = 0, \ldots, 3).$$

The perturbation theory is studied for a finite system of size $L$ and a smallest scale $l$ (e.g. lattice constant or mean free path). Then the change of the perturbed system under a change of the scale $\xi = \ln(L/l)$ can be calculated, for instance, in terms of a one-loop approximation. This perturbative renormalization group (PRG) has been employed for two-dimensional random Dirac fermions of Equation (56) in a large number of papers [298,310–312]. For instance, the solution of the PRG equations for a random gap ($g_3 > 0$, $g_0 = g_1 = g_2 = 0$) indicates that the variance of the random variable and its averaged value $m \equiv \langle m \rangle$ scale to zero, whereas the energy $\epsilon$ is running away on large scales $\xi$:

$$g_3(\xi) = \frac{g_3}{1 + (2g_3/\pi)\xi}, \quad m(\xi) = \frac{m_0}{\sqrt{1 + (2g_3/\pi)\xi}}, \quad \epsilon(\xi) = \epsilon_0 \sqrt{1 + (g_3/2\pi)\xi}. \tag{77}$$

Therefore, the one-loop PRG breaks down on a length scale

$$L_c \sim e^{\pi/g_3} l, \tag{78}$$

which has also been discussed in the literature [299,313]. Nevertheless, the PRG result can give us some useful insight in the transport properties if we restrict the system to a size $L$ smaller than $L_c$. For instance, the density of states is then obtained as [314]

$$\rho(E) \sim \frac{|E|}{2\pi} [1 + 2(g_3/\pi) \ln(L/l)].$$

Thus the density of states always vanishes linearly at the Dirac point $E = 0$, no matter how strong the disorder is. However, the slope of the linear behavior increases with system size $L$ logarithmically. The normalization of the density of states implies that this one-loop result can only be valid for system sizes $L$ up to $L_c$. It can be shown that this characteristic length scale, which appears here only as a limiting case for the calculational method, also plays an important (physical) role for the scattering rate: The scattering rate vanishes for systems smaller than $L_c$.

Transport properties have been studied within this PRG scheme for all $g_j > 0$ [311]. The transport quantities can either be expressed in terms of the length scale $L$, like the density of states above, or in terms of the wavevector $k$, representing an inverse length scale. The wavevector is proportional to the energy and inversely proportional to the wavelength $\lambda$ through the Dirac dispersion $E = v_F k \propto v_F \lambda^{-1}$. Therefore, the one-loop PRG breaks down for wavelengths larger than $\lambda \sim L_c$ which implies for energies $E$ smaller than the critical energy scale

$$E_0 \sim \mathrm{e}^{-\pi/g_0} t,$$

where $g_0$ is the bare variance of the random scalar potential and $t$ is the hopping rate. Then for $|E| \geq E_0$ the conductivity reads [311]

$$\sigma(E) = \frac{8e^2}{\pi h} \ln(|E|/E_0). \tag{79}$$

The diffusion coefficient $D$ and the scattering rate $\eta$ are

$$D = \frac{g_0'}{2\eta\pi} \ln(|E|/E_0), \quad \eta = \pi g_0' \rho(E),$$

where $g_0'$ is essentially the variance of the random scalar potential $g_0$. These results satisfy the Einstein relation $\sigma \propto D\rho$.

The one-loop PRG calculation of random Dirac fermions was also extended to include Coulomb interaction [312]. These calculations indicate a run-away RG flow from the unperturbed fixed point. The search for new fixed points has not been successful yet. Earlier hopes that a specific conformal-invariant field theory could control all the physics of the random Dirac fermions near $E \sim 0$ have also not been fulfilled so far.

The perturbative approach can be extended by the summation over infinitely many subdiagrams for the 2PGF [315]. The result is known as weak localization and describes diffusion in disordered systems. A related idea is the $1/N$ expansion of the 2PGF [316]. This concept has also been applied to graphene [307]. It is a flexible approach that also allows us to study the effect of inter-valley scattering. According to the weak-localization studies by Suzuura and Ando [292], scattering between different valleys (i.e. different nodes of the low-energy spectrum) has a strong effect on the transport properties. The behavior changes from anti-localization, when only intra-valley scattering is included, to localization for inter-valley scattering. This means that, at least for weak disorder, the conductivity is reduced in comparison to the pure system. However, this does not necessarily mean that this type of disorder leads to Anderson localization.

A closer inspection of the weak-localization approaches reveals that these self-consistent results approaches have a deeper physical meaning, namely the appearance of diffusion due to spontaneous symmetry breaking. Therefore, it is easier to start directly from the symmetry analysis and to avoid the complicated diagrammatic calculations, as we will discussion in the next section.

The summation over infinitely many subdiagrams is not only useful for disorder but can also be applied to a perturbation theory for electron–electron [257] or to electron–phonon interaction [305]. It provides self-consistent equations of the Hartree–Fock–Bogoliubov type (i.e. it represents the best fit of the many-body problem by single-particle approximations). Such approximations usually lead to a gap opening, just as in the BCS theory, for arbitrarily weak interaction. It remains a question, however, whether these gaps are real or just artifacts of the single-particle approximation. This problem has been studied in great detail in the case of strongly correlated systems [317].

### 5.5. *Self-consistent approach: scattering rate and diffusion*

The evaluation of the scattering rate in the self-consistent Born approximation (SCBA) reads as the self-consistent equation

$$\eta = 2\mathrm{i}g(\langle\mathcal{H}\rangle + z + \mathrm{i}\eta)^{-1}_{rr}, \tag{80}$$

where $\eta$ can be interpreted as the imaginary part of the self-energy (cf. [309]). A similar equation can be derived from the saddle-point approximation of the average 2PGF [296,318]. This approach avoids the unphysical behavior of the factorized 2PGF in Equation (75) for $\omega < 2\eta$. As a consequence, instead of the single scalar parameter $\eta$, the corresponding self-consistent equation determines a $4 \times 4$ matrix $\hat{Q}$:

$$\hat{Q} = g(\langle\hat{\mathcal{H}}\rangle + z - 2\gamma_j\hat{Q})^{-1}_{rr}\gamma_j, \tag{81}$$

where $\gamma_j = \mathrm{diag}(\sigma_j, \sigma_j)$, and $\hat{\mathcal{H}} = \mathrm{diag}(\mathcal{H}, \mathcal{H})$ is a $4 \times 4$ block diagonal Hamiltonian. $j = 0$ is for a random scalar potential, $j = 1, 2$ for a random vector potential and $j = 3$ for a random gap potential. A special solution of Equation (81) could be of the form

$$\hat{Q}_0 = -\mathrm{i}\frac{\eta}{2}\gamma_j, \tag{82}$$

where $\eta$ is the scattering rate, since it shifts the energy in the Green's function $(\langle\hat{\mathcal{H}}\rangle + z)^{-1}$ by $\mathrm{i}\eta$, like in the semiclassical approach of Section 5.3.2. Now we can insert our special solution in Equation (81) and multiply it by $\gamma_j$. This reduces the matrix equation to a scalar equation (80), the equation of the SCBA. It should be noticed that this equation is the same for all types of randomness, the model specific properties have dropped out. This is a first hint that the reduced equation is not sufficient to describe the physics of disordered monolayer graphene or bilayer graphene. The reason is that with the special ansatz (82) we have completely lost the $4 \times 4$ matrix structure of the equation. A more careful inspection of Equation (81) reveals that $\hat{\mathcal{H}}$ is invariant under a continuous transformation for $j = 1, 2, 3$ (but not for $j = 0$), depending on the type of randomness [296,318]. A consequence of these symmetries is that for $z = 0$ the saddle-point equation is invariant under the global symmetry transformation, and the transformation creates a whole manifold of solutions $\hat{Q}$ with $\hat{Q}^2 = -\eta^2\gamma_0/4$ ($\gamma_0$ is the $4 \times 4$ unit matrix). This is the origin of the nonlinear sigma model, which describes diffusion of particles. We will briefly return to this point in the discussion of the average 2PGF in Section 5.5.1.

It is crucial to notice that the manifold collapses to a single solution if $\eta = 0$. Such a vanishing solution exists, for instance, for a finite monolayer graphene if its linear size $L$ is too small, namely $L < L_c$.[11]

### 5.5.1. *Scaling relation of the two-particle Green's function*

After integration over the manifold of saddle-point solutions, both for monolayer graphene and bilayer graphene, the average 2PGF

$$K_g(q,z) = \sum_r \mathrm{e}^{-\mathrm{i}q\cdot r} \lim_{\delta\to 0} \langle \mathrm{Tr}_2[G(r,0;-z/2-\mathrm{i}\delta)G(r,0;z/2+\mathrm{i}\delta)]\rangle,$$

which is related to $C(\epsilon,\omega)$ in Equation (67) for $\epsilon = 0$ by

$$C(0,\omega) = -\left[\frac{\partial^2 K_g(q,\omega)}{\partial q_k^2}\right]_{q=0},$$

can also be evaluated. For instance, for a random gap with variance $g$ there is a simple relation between the 2PGF of the pure system

$$K_0(q,z) = \sum_r \mathrm{e}^{-\mathrm{i}q\cdot r} \lim_{\delta\to 0} \mathrm{Tr}_2[G_0(r,0;-z/2-\mathrm{i}\delta)G_0(r,0;z/2+\mathrm{i}\delta)],$$

with the one-particle Green's function $G_0(z) = (\langle\mathcal{H}\rangle + z)^{-1}$, and the average 2PGF as [318]

$$K_g(0,\omega) = \frac{(\omega + 2\mathrm{i}\eta)^2}{\omega^2} K_0(0,\omega + 2\mathrm{i}\eta) \equiv \omega^{-2} F(\omega + 2\mathrm{i}\eta). \tag{83}$$

The right-hand side does not depend on the disorder strength $g$ explicitly, only through the scattering rate $\eta$. This is a scaling relation for $K_g(0,\omega)$, where we have pulled out the divergent term $\omega^{-2}$ and introduced the scaling function $F(z) = z^2 K_0(0,z)$ with $z = \omega + 2\mathrm{i}\eta$. The expression for the conductivity in Equation (69) then reads

$$\sigma = -\frac{e^2}{2h} F'(\omega + 2\mathrm{i}\eta), \tag{84}$$

where $F'(z)$ is the real part of $F(z)$. Thus, the conductivity depends only on the variable $\omega + 2\mathrm{i}\eta$ through the scaling function. This is a generalization of the classical Drude formula, where the scaling function of the latter would be $F_{\mathrm{Drude}} \propto i/z$ .

The relation in Equation (83) can be compared with the semiclassical approximation in Equation (74). They do not agree except for the trivial case $\eta = 0$ due to the prefactor $(\omega + 2\mathrm{i}\eta)^2/\omega^2$, obtained from the integration over the saddle-point manifold. For $\eta > 0$ it is important to notice that the average 2PGF always diverges like $\omega^{-2}$, whereas the pure 2PGF is finite for $\eta > 0$. This cures the problem which we have had with the expression in Equation (76) if $\omega < \eta$.

## 5.6. *Numerical simulations*

Analytic calculations are limited because they are either based on a truncated perturbation series or they employ an approximative scheme. Therefore, it is important to use numerical calculations of finite systems as a complementary approach. There are a number of works in which the transport properties have been studied numerically, usually based on the transfer-matrix (or Landauer) approach [321,322]. An interesting result is that the conductivity increases with the system size in the presence of a single valley and potential disorder [323,324]:

$$\sigma(L) \sim \frac{2e^2}{h}\left[\sigma_0 + s\ln(L/\xi)\right], \tag{85}$$

with $\sigma_0$ and $s$ of the order of unity. This logarithmic behavior agrees remarkably well with the one-loop PRG calculation in Equation (79). From the numerical results it is not clear whether or not the logarithmic increase of the conductivity saturates at some finite value, as it is suggested by the breakdown of the PRG, or increases asymptotically. Since it is obvious from the PRG that the behavior must change qualitatively beyond the scale $L_c$, it cannot be ruled out that this scale has not been reached in the numerical calculations.

In contrast to the growing behavior of the conductivity, a random gap term instead of the potential disorder gives a size-independent conductivity [325]

$$\sigma(L) = \frac{1}{\pi}\frac{e^2}{h}, \tag{86}$$

for any strength of the random gap fluctuations but with vanishing average gap. For any non-zero gap, however, the conductivity decays with increasing size $L$. Moreover, the conductivity increases with the strength of the random gap fluctuations for fixed $L$ and fixed average gap. This indicates that the unusual behavior is not related to conventional Anderson localization, since for the latter we expect a decreasing localization length for increasing random fluctuations.

Additionally, Schomerus [326] considered the impact of the leads on transport through weakly doped graphene. He showed that graphitic leads and quantum wires give qualitatively the same transport properties, which can be characterized by a single parameter which is determined by the measurement of the conductance and shot noise of a rectangular undoped graphene strip. This duality is the result of the mode selection mechanism originating from the conical points of undoped graphene, and holds even though the different types of wire support different numbers of propagating modes.

## 5.7. *Metal–insulator transition*

Recent experiments on hydrogenated graphene (graphane) (Section 8.2.3) have revealed that a gap is opened by the adsorption of hydrogen such that graphene can undergo a transition from metallic to insulating behavior [280,288]. The gap opening by hydrogen adsorption is also supported by density-functional calculations [327]. An interesting question in this context is how the transport properties change when we add gradually hydrogen to graphene [280], creating randomly gaps in the graphene sheet [140,185]. The random gap is characterized by two parameters, the average gap $\bar{m}$ and the variance $g$ of the spatial gap fluctuations. If we begin with weak disorder, i.e. $\sqrt{g} \ll \bar{m}$, the minimal conductivity $\sigma_{\min}$ will be zero because there are either no states at the node $E=0$ or these states are localized. Thus the system is insulating with a vanishing conductivity at low temperatures. The spatial gap fluctuations around the mean value $\bar{m}$ have two effects: First, they can close the effective gap by broadening the particle and hole bands and, second, they can create new states inside the gap, such as midgap states [328–330]. Those states are either localized for large $\bar{m}$ (e.g. Lifshitz tails) [280,288,293] or delocalized for small $\bar{m}$ [318]. As we increase the spatial fluctuations of $\delta m$, local regions are formed in which $\delta m \approx 0$ with reasonable probability. Increasing $g$ further, these local regions with $\delta m \approx 0$ start to form a percolating network. It is not necessary to close these gaps completely, since a local gap only reduces the local density of states. Therefore, a quantum percolation transition can take place in the presence of sufficiently large fluctuations of $\delta m$. This is similar to the percolating network picture of charged puddles [331]. A perturbative renormalization-group analysis supports such a transition indirectly. Starting from Equation (77), the term $\bar{m}$ always flows to zero under renormalization. The corresponding fixed point is a free massless Dirac Hamiltonian with DC conductivity $e^2/h\pi$. In other words, the system always flows to a clean metal for sufficiently large system size. However, this renormalization-group analysis is only valid for weak disorder. In case of strong disorder another behavior may appear in which the gap can survive.

More detailed analytic and numerical studies of the metal–insulator transition due to a random gap have revealed that for a vanishing average gap graphene is always metallic [318,325,332]. However, the situation is less clear for a nonzero $\bar{m}$. First, we have the result of the perturbative renormalization group that indicates a metallic behavior, at least for small $g$, and no metal–insulator transition. Moreover, the scaling relation of Equation (84) allows us to obtain the conductivity from the pure 2PGF, where the latter gives the scaling function as

$$F(z) = \frac{2a}{\pi} \frac{z^2}{\bar{m}^2 - z^2} \Theta(m_c^2 - \bar{m}^2)$$

with $a=1$ ($a=2$) for monolayer graphene (bilayer graphene). Thus the conductivity vanishes when the average gap $\bar{m}$ exceeds a critical value $m_c$. Here $m_c$ depends on whether we consider monolayer graphene or bilayer graphene. Its value for a given variance $g$ is much smaller for monolayer graphene than for bilayer graphene [318]:

$$m_c = \begin{cases} \dfrac{2}{l\sqrt{e^{2\pi/g} - 1}} \sim \dfrac{2e^{-\pi/g}}{l} & \text{(monolayer graphene)} \\ g/2 & \text{(bilayer graphene)} \end{cases} . \tag{87}$$

The scattering rate $\eta$ is obtained from Equation (80) for both, monolayer graphene and bilayer graphene, as [318]:

$$\eta^2 = (m_c^2 - \bar{m}^2)\Theta(m_c^2 - \bar{m}^2)/4. \tag{88}$$

Inserting these results into the expression for the DC conductivity of Equation (84) gives us a simple power law

$$\sigma = \frac{a}{\pi}\frac{e^2}{h}\left(1 - \frac{\bar{m}^2}{m_c^2}\right)\Theta(m_c^2 - \bar{m}^2). \tag{89}$$

The factor $a = 2$ of the bilayer may be connected to the fact that the conductivity doubles for the bilayer graphene because of the two conducting sheets. However, in our approach it is related to spectral properties at low energies (linear vs. parabolic). Experiments do not show this doubling in the DC limit but indicate that the minimal conductivity of bilayer graphene is more sensitive to temperature (i.e. it increases strongly with temperature), whereas the minimal conductivity of monolayer graphene is almost independent of temperature [27] or changes linearly with $T$ [26].

The results in Equations (87) and (88) indicate that the effect of disorder is much stronger in bilayer graphene. For monolayer graphene as well as for bilayer graphene, the critical gap value $m_c$ increases with disorder. Thus, a random gap allows diffusive motion of the electrons, provided that the average gap is not too large. This reflects the percolation picture, as mentioned at the beginning of this section. The corresponding phase diagram includes two gapped phases (one for $\bar{m} > m_c$ and one for $\bar{m} < -m_c$) and an intermediate diffusive (metallic) phase with a nonzero minimal conductivity $\sigma_{\min}$ [318] (cf. Figure 60). These results are in qualitative agreement with the numerical simulations for related network models by Cho and Fisher [333] and by Chalker *et al.* [334]. However, more recent numerical simulations by Bardarson *et al.* [325] have questioned the power law in Equation (89) for monolayer graphene: although the prefactor $e^2/\pi h$ agrees very well, the critical value $m_c$ is smaller than the one calculated in Equation (87). Since the latter is a result for an infinite graphene sample, we have also calculated $m_c$ for finite samples and found qualitatively the same finite-size behavior such as the decay of $\sigma(L)$ with increasing size $L$ [332]. Nevertheless, the actual value of $m_c$ for different types disorder remains an open problem. Moreover, the simple power law in Equation (89) may have a different exponent because the self-consistent evaluation of the

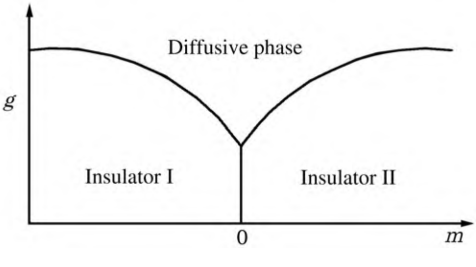

Figure 60. Schematic phase diagram of random-gap Dirac fermions (monolayer graphene) for average gap $\bar{m}$ and disorder strength $g$, obtained from numerical and analytic calculations [318,325,333,334]. There are two gapped phases for $m < -m_c$ and for $m > m_c$ with an intermediate metallic phase. According to Equation (87) the vertical line has a width of $2m_c = 2e^{-\pi/g}$ which is too small to be visible in this plot. The metallic phase for large $g$ has not been observed in recent numerical simulations [325] because $m_c$ was smaller than the value obtained in Equation (87).

conductivity has not been taken into account a renormalization of critical indices near $m_c$. Nevertheless, a recent numerical simulation for Dirac fermions with an uncorrelated random mass confirms a linear power law for the conductivity [335].

The suppression of the gap by random fluctuations can also play an important role in systems where a gap is induced either by an external magnetic field [336,337] or by interaction effects, such as Coulomb interaction [338] and electron–phonon interaction. Disorder, always present in realistic graphene samples, can lead to the randomness of the gap parameter. As a consequence, there is a competition between gap formation by interaction and gap suppression due to disorder. To observe a gap in the transport properties of such a system, the average gap must exceed a critical value. On the other hand, if the average gap is too small or the fluctuations are too large, the metallic behavior can survive.

## 6. Confinement of electrons in graphene

Quantum dots (QDs), or the ‘artificial atoms’ [8,9] are one of the most intensely studied systems in condensed matter physics where the fundamental effects related to various quantum phenomena in confined geometries can be studied but with the unique advantage that the nature of the confinement and the electron density can be tuned externally. However, much of the interest in this system derives from its enormous potentials for applications, ranging from novel lasers to quantum information processing. While the majority of the QD systems investigated are based on the semiconductor heterostructures, in recent years, QDs created in carbon nanotubes have been reported in the literature where the ‘atomic’ properties [339] were clearly elucidated and its importance in technological applications was also demonstrated [340]. Nonrelativistic electrons, the properties of which are described by the Schrödinger equation, can be easily confined by electrostatic confinement potentials, to create well-defined QD and quantum well structures in usual semiconductor systems. The behavior of relativistic electrons in graphene is however completely different. Due to the massless chiral nature of their energy dispersion, electrons in graphene can penetrate through potential barriers of any height. An electron approaching a potential barrier emerges inside the barrier as a hole, which can then freely propagate under the barrier and finally can penetrate through the barrier without any losses. Such electron tunnelling through a barrier of any height and width is known as Klein tunnelling [341–343]. A direct experimental observation of Klein tunnelling was reported in [344,345] where transport through a *n*–*p*-type potential barrier was measured. For an electron normally incident on the potential barrier, perfect transmission was observed, thus indicating a direct manifestation of Klein tunnelling.

Klein tunnelling therefore makes it hard to localize electrons in graphene by a confinement potential and the standard semiconductor QDs and quantum wells realized through the confinement potential cannot be achieved in graphene. The existence of Klein tunnelling for relativistic electrons in graphene and the transition from the Schrödinger bound state to the Dirac unbounded states in a confinement potential was demonstrated in [346]. Different approaches were explored to overcome the problem of electron confinement in graphene.

A straightforward approach, realized experimentally in [47,347–349], is based on ‘mechanical’ cutting of graphene into the desired nanosize shape. Such an island of graphene becomes a QD with characteristic discrete energy levels. The properties of these QDs are determined by the discrete nature of the energy levels and the charging effects due to inter-electron interactions within the QD.

Another approach to create QDs in graphene is to realize the QD through the confinement potential within the graphene layer. Due to Klein tunnelling, the standard confinement potential cannot localize the electron within a finite spatial region. In this case we need to consider not the QD that localizes an electron, i.e. the electron stays within the QD for infinitely long time, but a QD which can trap an electron for long enough time. Such trapping can be realized in a smooth confinement potential and only for states with large transverse momentum [350,351].

Spatial localization of an electron within a QD in graphene layer can be achieved if a finite gap is introduced in the energy dispersion for relativistic electrons. The energy gap can be produced, e.g. by the SOI, through coupling with the substrate, or in a biased graphene bilayer (Section 3). The QDs in graphene can be also introduced through a magnetic confinement potential [352–354]. In this case the nonuniform magnetic field results in electron localization within a finite spatial region, thereby creating a QD.

### 6.1. *QDs in graphene islands*

QDs in islands of graphene have been realized experimentally in [47,347–349]. To extract the discrete energy spectra of the QD islands, tunnelling transport through the system was measured [47,347–349]. Clear Coulomb blockade peaks in tunnelling conductance versus the bias voltage dependence have been observed (Figure 61). The positions of the peaks are determined by the charging and confinement energies within the graphene islands. The unique relativistic dispersion of electrons in graphene results in much larger confinement energy for electrons in graphene islands compared to the confinement energy of non-relativistic electrons. For graphene islands the confinement energy can be estimated as $\sim v_F h/2D$, where $D$ is the size of the island, while for the non-relativistic massive electrons the confinement energy is $\sim h^2/8m^* D^2$, where $m^*$ is an effective electron mass. For example, for a 40 nm QD the confinement energy is found to be $\sim$10 meV [347] for graphene while the energy is around 1 meV for a non-relativistic QD system. The interplay between the confinement energy and the charging energy determines the structure of the conductance peaks in the tunnelling transport experiments.

It was shown experimentally [347] that for large ($>$100 nm) QDs in graphene, i.e. in graphene islands, the Coulomb peaks are periodic and the positions of the peaks are mainly determined by the charging energy. From the Coulomb diamond measurements, a charging energy of 4.3 meV was extracted for 200 nm graphene islands [349]. For small QDs the energy scale is determined by the confinement energy. In this case the peaks of tunnelling conductance are nonperiodic [347] with the typical energy scale of $v_F h/2D$. Another manifestation of the confinement nature of the energy scale for small QDs is the special statistics of the energy levels, i.e. the distribution of the nearest neighbor energy-level spacing. The statistics of the energy levels are determined by the time-reversal symmetry of the Hamiltonian of the system and the

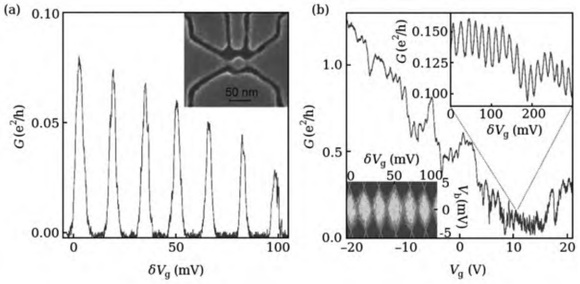

Figure 61. (a) Conductance of a graphene device with the central island of 250 nm in diameter as a function of the gate voltage, $V_g$, in the vicinity of $+15\,V$, $T = 0.3\,K$. The inset shows the smallest 30 nm diameter QD. (b) Conductance of the same device as in (a) over a wide range of $V_g$, and the temperature is 4 K. Upper inset: Zooming into the low-$G$ region reveals hundreds of Coulomb blockade oscillations. The lower inset shows Coulomb diamond: differential conductance as a function of gate voltage (around $+10\,V$) and bias voltage (Reprinted figure with permission from L.A. Ponomerenko *et al.*, Science, 32, p. 356, 2008 [347]. Copyright © (2008) The American Association for the Advancement of Science.).

type of boundary conditions. For non-relativistic systems, the statistics of the energy levels is described by the Poissonian distribution ($P(\delta E) = \exp(-\delta E)$) for classically regular shape of the QD. Here $\delta E$ is the interlevel spacing. For an irregular classically chaotic shape, the distribution takes the Wigner–Dyson form, corresponding to the orthogonal ensemble ($P_O = (\pi/2)\delta E \exp(-(\pi/4)\delta E^2)$) for a system with time-reversal symmetry, and to the unitary ensemble ($P_U = (32/\pi^2)\delta E^2 \exp(-(4/\pi)\delta E^2)$) for a system without the time-reversal symmetry. In non-relativistic systems the time reversal symmetry is usually broken by an external magnetic field.

In graphene, even for the classically regular shape of a QD, the electron dynamics are chaotic and the statistics of energy levels are described by the Gaussian unitary ensemble [355], which corresponds to a system with broken time-reversal symmetry. The mechanism of time-reversal symmetry proposed in [355] is the infinite mass boundary condition. The experimentally measured level statistics [347] illustrates a transition from the Poisson distribution for dots of large size ($>100\,nm$) to the distribution corresponding to chaotic Dirac billiards, for dots of small size ($<100\,nm$) (Figure 62). Experimental results are best fitted by the Gaussian unitary distribution [347].

The results of the numerical analysis of disordered graphene QDs [356,357] show that the statistical properties of QDs strongly depend on the boundary conditions. For example, QDs with abrupt termination at the boundary show a transition from the Gaussian orthogonal ensemble at zero magnetic field to the Gaussian unitary ensemble at finite magnetic fields [356]. Therefore, these systems have time-reversal symmetry. The abrupt termination of the QD introduces inter-valley mixing at the boundary.

Another example of a boundary, considered in [357], is a smooth boundary, i.e. a smooth mass confinement. The smooth boundary condition is introduced through a smooth mass term. This type of boundary condition suppresses inter-valley scattering. It was determined that the statistics of the energy levels for QDs with a smooth boundary corresponds to the Gaussian orthogonal ensemble

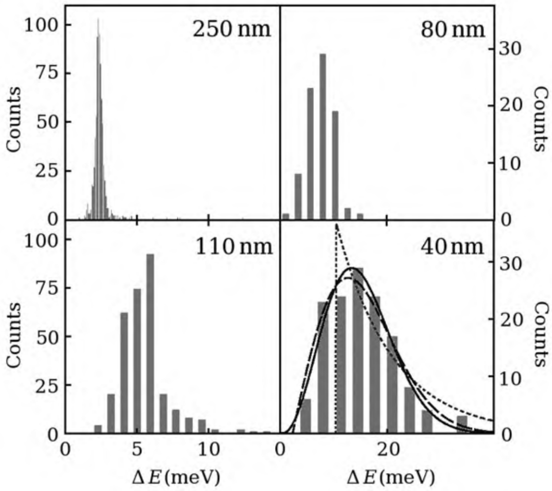

Figure 62. Level statistics in Dirac billiards. The histograms of the nearest neighbor level spacing are shown for QDs of different sizes. The level statistics becomes increasingly non-Poissonian for smaller QDs. This is illustrated for the smallest device, where the solid, dotted and dashed curves are the best fits for the Gaussian unitary, Poisson and Gaussian orthogonal ensembles, respectively. The distributions are shifted from the origin due to Coulomb blockade (Reprinted figure with permission from L.A. Ponomerenko *et al.*, Science, 32, p. 356, 2008 [347]. Copyright © (2008) The American Association for the Advancement of Science.).

for large QDs and the Poisson ensemble for small dots [356]. For small QDs the localized edge states determine the Poissonian statistics, while the contribution of the edge states is suppressed when the size of the dot is increased.

The energy spectra and the charging effects in graphene islands have been studied theoretically in great detail. It was shown that the structure of the electronic states and the energy scales of graphene QDs are determined by the edge type of the QDs, i.e. the boundary conditions, and electron occupation of the QD. There are two main types of edges in graphene QDs: armchair and zigzag, which are shown schematically in Figure 14. The distinctive feature of the armchair edge is that the vector normal to the edge is orthogonal to the bond. These two types of edges determine the basic configurations of QDs with the same type of edges along the whole boundary (Figure 63): trigonal zigzag [358–360], trigonal armchair [358,359], hexagonal zigzag [359–361], and hexagonal armchair [359,361]. A configuration with two types of edges, e.g. rectangular configuration (see Figure 64), has been also studied in the literature [362,363]. In this case there are zigzag edges along the $x$-axis and armchair edges along the $y$-axis. The dangling bonds at the edges of the graphene islands are passivated by hydrogen atoms (not shown in Figures 63 and 64).

The energy spectra of graphene QDs have been studied theoretically by two main methods: within the tight-binding model and within the Dirac relativistic equation. The tight-binding Hamiltonian has the form

$$\mathcal{H}_{\text{tight-binding}} = \sum_i \varepsilon_i c_i^\dagger c_i + \sum_{\langle i,j\rangle} t_{ij} c_i^\dagger c_j \tag{90}$$

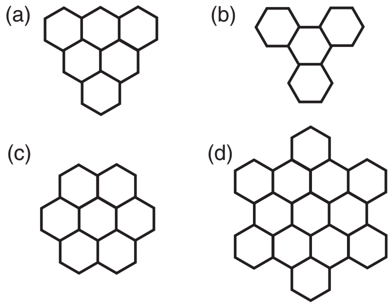

Figure 63. Typical configurations of graphene QDs with same type of the edges: (a) trigonal zigzag; (b) trigonal armchair; (c) hexagonal zigzag and (d) hexagonal armchair.

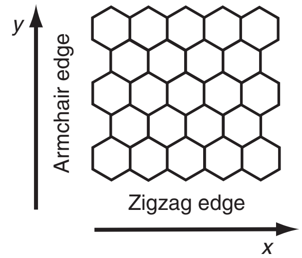

Figure 64. Rectangular QD terminated by both armchair and zigzag edges.

and the relativistic-like low-energy limit was described in Section 1.2. The properties of QDs strongly depend on the type of boundary, e.g. zigzag or armchair edges.

For the continuous Dirac-like equation, the type of the boundary determines the boundary conditions for the electron wave functions. The general energy-independent boundary condition is determined by a $4 \times 4$ matrix, $M$, through the following relation [364,365]:

$$\Psi = M\Psi. \tag{91}$$

For the boundary condition that preserves time reversal symmetry the matrix $M$ is determined by three parameters [365]

$$M = (\vec{\nu} \cdot \vec{\tau}) \otimes (\vec{n} \cdot \vec{\sigma}), \tag{92}$$

where $\tau_i$ and $\sigma_i$ are Pauli matrices in the valley space and the sublattice space, respectively. The matrix $M$ is parametrized by the directions of two three-dimensional vectors, $\vec{\nu}$ and $\vec{n}$. Here the vector $\vec{n}$ is orthogonal to the unit vector normal to the boundary.

The above form of the matrix $M$ introduces two types of boundary conditions. If we denote wave functions in the K valley by $\psi_+$ and those in the K$'$ valley by $\psi_-$, they are [365]: (i) zigzag-type boundary condition: $\psi^{\mathrm{A}}_{+} = \psi^{\mathrm{A}}_{-} = 0$ (any $\psi^{\mathrm{B}}_{+}$ and $\psi^{\mathrm{B}}_{-}$) or $^{\mathrm{B}}_{+} = \psi^{\mathrm{B}}_{-} = 0$ (any $\psi^{\mathrm{A}}_{+}$ and $\psi^{\mathrm{A}}_{-}$); (ii) armchair-type boundary condition: $|\psi^{\mathrm{A}}_{+}| = |\psi^{\mathrm{A}}_{-}|$

and $|\psi^{\mathrm{B}}_{+}| = |\psi^{\mathrm{B}}_{-}|$. The type of the boundary condition is determined by the orientation of the vector, $\vec{T}$, of the period at the edge. This vector is approximately parallel to the edge. If the vector $\vec{T}$ is parallel to the bonds then the boundary condition is of the armchair type. For all other orientations of the vector $\vec{T}$, the boundary conditions are of the zigzag type [365]. Therefore, the zigzag-type boundary conditions are more generic. The zigzag boundary condition does not couple different valleys, while the armchair boundary condition introduces coupling between the two valleys.

There is an other type of boundary condition, which is used in some cases within the continuous Dirac-type model. This is the infinite mass boundary condition. This boundary condition can be realized, for example, through the staggered potential at the zigzag edge. The staggered potential means that the electrostatic potential at two lattice sites (A and B) is different, i.e. $V_A = +\mu$ and $V_{\mathrm{B}} = -\mu$. Similar to the zigzag boundary condition, the infinite mass boundary condition does not mix the valley and at the zigzag boundary takes the form [365]: ${}^{\mathrm{A}}_{+} = \mathrm{i}\psi^{\mathrm{B}}_{+}$ and $\psi^{\mathrm{A}}_{-} = -\mathrm{i}\psi^{\mathrm{B}}_{-}$.

For triangular and trapezoidal geometries of graphene QDs the single-particle energy spectra of the QDs can be found analytically [366,367] within the tight-binding model. For example, for triangular QDs with armchair boundary conditions, the single-particle states are characterized by two integer numbers, $n$ and $m$, and have the following form [367]:

$$\epsilon_{n,m,\pm} = \pm t\left\{3 + 2\cos\left[\frac{4\pi n}{3(N+2)}\right] + 2\cos\left[\frac{4\pi m}{3(N+2)}\right] + 2\cos\left[\frac{4\pi(n+m)}{3(N+2)}\right]\right\}^{\frac{1}{2}},$$

where $N$ is number of carbon atoms per one side of the triangular QD.

The approach based on the tight-binding model is the more fundamental and is valid for QD of any size, while the Dirac equation, being a continuous approximation of the tight-binding model, is valid only for QDs of large size. In [363] a detailed comparison of the electronic eigenstates of a rectangular QD obtained within the framework of the Dirac equation and the tight-binding model was presented. It was found that the graphene QDs with size of $7 \times 8$ is the smallest one for which the Dirac equation is applicable.

Zigzag edges in graphene have unique properties. For example, they can introduce degenerate zero-energy states localized at the edges. The actual existence of zero-energy states depends on the configuration of the QD. As an example, the zero-energy states have been found only for rectangular QDs [362,363] and trigonal zigzag QDs [358–360]. However, no such zero-energy states exist for hexagonal zigzag graphene QDs [359,360]. A sufficient condition for the existence of degenerate zero-energy states in a graphene sample is the sublattice imbalance, i.e. an uncompensated lattice [360]. That is, if $N_A$ is the number of atoms of sublattice A and $N_{\mathrm{B}}$ is the number of atoms of sublattice B in a graphene QD, then the parameter $N_Z = N_{\mathrm{A}} - N_{\mathrm{B}}$ determines the existence of zero-energy states. This parameter is zero for hexagonal zigzag QDs and nonzero for trigonal zigzag QDs [360]. The condition $N_Z > 0$ is the sufficient condition for the existence of zero-energy edge states but it is not the necessary condition. For example, for rectangular QDs there are zero-energy edge states, but the sample is compensated, i.e. $N_Z = 0$.

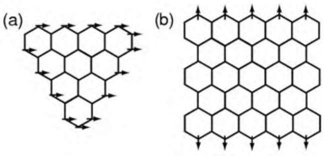

Figure 65. Local magnetization for trigonal zigzag QD (a) and rectangular QD (b). The directions of magnetization shown in the figure are chosen for the sake of clarity.

The degenerate zero-energy edge states, occupied by electrons, leads to ferromagnetic and antiferromagnetic ordering due to the inter-electron exchange interaction. To study the magnetic ordering in graphene QDs, the inter-electron interaction should be introduced, for example, within the density functional theory (DFT) *ab initio* calculations [360,362] or through the Hubbard on-site interaction combined with the Hartree–Fock mean field approach [360,363]. The DFT calculations, although more accurate than the mean field theory, can be performed only for QDs of small size. A comparison of the low-energy spectra of graphene QDs obtained within the Hubbard model and within the DFT approach shows that the Hubbard model captures correctly the low-energy physics of the QD.

The results of the numerical analysis of graphene QDs with zero-energy degenerate states, i.e. for a rectangular QD and a trigonal zigzag QD, illustrate the magnetic ordering in such graphene islands [359,360,362,363]. The magnetic moments are localized on the zigzag edges of the QDs. The type of magnetic ordering is different for rectangular and trigonal dots. For rectangular QDs the stable magnetic phase is antiferromagnetic [362,363], the magnetic structure of which is similar to the magnetic structure of graphene zigzag ribbons, namely, the magnetic moments are localized at two zigzag edges with opposite orientation (Figure 65). The results of *ab initio* DFT calculations show that the antiferromagnetic phase is a stable phase for all rectangular QDs of size larger than $3 \times 3$ [362]. For smaller QDs the stable phase is nonmagnetic [362]. For trigonal zigzag QDs the stable phase is ferromagnetic with the same orientation of magnetic moments (Figure 65), i.e. the electron spins [359,360]. The net local spin mostly sits on the edge of the QD and goes to zero in the centre of the dot.

The signature of the zero-energy degenerate edge states in graphene QDs can be observed in optical absorption experiments [358]. The absorption spectra obtained numerically within the tight-binding model clearly show rich peak structures originating from the edge states [358]. The structure is visible only for zigzag triangular graphene QDs, but does not exist for armchair triangular dots. With increasing size of the dot, the relative contribution of the edge states to the absorption spectra is suppressed. The ratio, $f_{\text{edge}}/f_{\text{all}}$, of the oscillator strength corresponding to the edge states to the total oscillator strength has a maximum value of 0.42 at $N_z = 4$ and decreases to 0.15 at $N_z = 50$. Here $N_z$ is the number of atoms along the edge.

A detailed analysis of Coulomb interaction effects in graphene QDs was reported in [368]. The calculations were done for circular QDs within the massless Dirac equation. It was assumed that the QD has a zigzag-type boundary, which supports degenerate zero-energy edge states. The zigzag boundary condition does not mix the two valleys. In this case each energy level of the QD is twofold valley degenerate and to find the energy spectrum it is enough to consider only one valley. Due to the circular symmetry of the problem the general solution of the Dirac equation is described by the Bessel functions and the two-component wave function for a single valley $s = \pm 1$ has the following form [368]:

$$\left.\begin{matrix} {}^{\mathrm{A}}_{s}(r,\theta) \\ {}^{\mathrm{B}}_{s}(r,\theta) \end{matrix}\right) = \left.\begin{matrix} J_m(kr)\mathrm{e}^{\mathrm{i}ms\theta} \\ -\mathrm{i}J_{m-s}(kr)\mathrm{e}^{\mathrm{i}(m-s)\theta} \end{matrix}\right). \tag{93}$$

The boundary conditions corresponding to the zigzag edge were introduced:

$${}^{\mathrm{A}}_{s}(R,\theta) = 0, \tag{94}$$

where $R$ is the radius of the QD. This boundary condition allows for surface states of the form

$$\left.\begin{matrix} {}^{\mathrm{A}}_{s}(r,\theta) \\ {}^{\mathrm{B}}_{s}(r,\theta) \end{matrix}\right) = \begin{pmatrix} 0 \\ \sqrt{\dfrac{m+1}{\pi R^{2(m+1)}}}r^m\mathrm{e}^{\mathrm{i}sm\theta} \end{pmatrix}. \tag{95}$$

In terms of the tight-binding model with the nearest neighbor hopping, the surface states in which only sublattice B is occupied are degenerate and have zero energy. Introducing next-nearest neighbor hopping to the tight-binding model results in a finite kinetic energy of the surface states and the zero-energy band becomes dispersive [368].

The Coulomb electron–electron interaction has been introduced to describe the charging effects of the dot:

$$\mathcal{H}_C = \frac{e^2}{4\pi\varepsilon_0\varepsilon}\sum_{n<n'}\frac{1}{|\vec{r}-\vec{r}'|}. \tag{96}$$

The charging properties of QDs depend on the electron occupation of the dot. For large number of electrons within the dot, all the surface states are occupied and the Fermi level is far from the neutrality point. In this case the main charging effect is a rigid shift of the electrostatic potential, which results in standard Coulomb blockade effects [368].

A different situation occurs if the number of electrons within the QD is small enough so that the electrons occupy only the surface states [368]. That situation is realized if the Fermi energy is near the neutrality point. In this case the system can be described within the truncated Hilbert state restricted only to the surface states. Since the surface states are almost degenerate, the electrons occupying these states are strongly correlated and the properties of the system are determined by the Coulomb inter-electron interaction. In [368] two trial functions for the correlated ground state were proposed: (i) the Laughlin wave function [72,137]

$$(z_1, z_2, \ldots, z_N) \propto \prod_{i<j}(z_i - z_j)^p, \tag{97}$$

where $z = x + iy$, $N$ is the number of electrons, $p$ is odd and (ii) Wigner crystal-type wave function. Both trial functions show good agreement with the exact numerical results [368].

In [369], a rotating-electron-molecule-type wave function was introduced to describe the correlated electrons at the zero energy edge of the QDs. Based on the numerical diagonalization of the interaction Hamiltonian of the electron system with up to eight electrons, the authors concluded that the rotating-electron-molecule wave function provides a better description of the correlated electron system than the Laughlin trial function or the Wigner crystal [369]. A strongly correlated electron state exists only for the long-range Coulomb interaction. The electron correlations disappear for point-like Hubbard interaction.

A special type of graphene quantum island is a quantum ring. The most non-trivial behavior of the quantum rings is in an external magnetic field. This behavior is due to the Aharonov–Bohm effect [370] and manifests itself as periodic oscillations in the energy spectra and the transport properties as a function of the number of flux quanta through the ring, $\Phi$. The quantum ring in graphene has been realized experimentally [371] and the current through the ring has been studied. The size of the ring is ~1 μm and the system is coherent at temperatures below 1 K. The measured conductance oscillations clearly show the Aharonov–Bohm oscillations (Figure 66). Surprisingly, the amplitude of the conductance oscillations increases with increasing magnetic field strength. This tendency is shown in Figure 66. An analysis of the structure revealed that this behavior does not originate from the magnetic impurities, but rather from the orbital effect of the magnetic field.

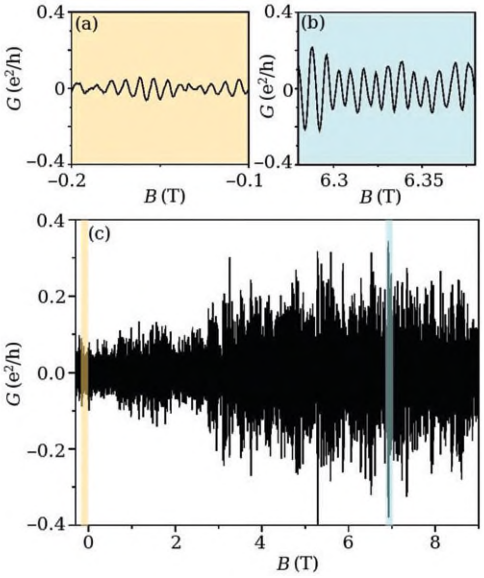

Figure 66. Aharonov–Bohm conductance oscillations measured at a gate voltage +30 V in the different magnetic field range. For $B \sim 3$ Tesla a clear increase of Aharonov–Bohm amplitude is observed. (Reprinted figure with permission from S. Russo *et al.*, Physical Review B, 77, 085413, 2008 [371]. Copyright © (2008) by the American Physical Society.)

Numerical studies of quantum rings were also reported [372–374] within the tight-binding and the continuous Dirac equation approaches. The system is studied as a function of the magnetic field, where the magnetic field in the tight-binding model is introduced through the Peierls substitution. The quantum ring in the form of a disk has been studied in [372] within the Dirac continuous equation. It was shown that even without a magnetic field the quantum ring shows the breaking of the effective time-reversal symmetry, which manifests itself as the lifting of degeneracy between the states with angular momentum $m$ and $-m$ in the same valley in the absence of a magnetic field. Each level, however, still has the double valley degeneracy since the energy of the state with angular momentum $m$ in valley K is equal to the energy of the state with angular momentum $-m$ in the valley K$'$ . A finite magnetic field lifts this twofold degeneracy and breaks the time-reversal symmetry. Finally the energy spectra and the persistent current, defined as $j=-\partial E/\partial\Phi$, show periodic oscillations with the magnetic flux, $\Phi$. Due to breaking of effective time-reversal symmetry at the zero magnetic field, the persistent current for a single valley is non-zero even at $B=0$. The persistent current for both valleys is zero at $B=0$.

In [373] the effect of electron–electron interactions in a cylindrical quantum ring system have been studied. The inter-electron interactions is introduced through the Coulomb Hamiltonian,

$$\mathcal{H}_C=\frac{1}{2}\sum_{i\neq j}\frac{e^2}{4\pi\epsilon}\frac{1}{|\vec{r}_i-\vec{r}_j|}. \tag{98}$$

The exchange Coulomb interaction between the electrons in the same valley is strong, but it is strongly suppressed for electrons in different valleys [373]. This means that there is an exchange contribution for the two-electron singlet valley state (both electrons being in the same valley), but there is no exchange interaction for the triplet valley state (two electrons in different valleys). In a two electron system, by varying the size of the quantum ring the transition from the valley-singlet ground state for small quantum rings to a valley-triplet ground state was observed.

Due to the two types of edges in a quantum ring, i.e. the inner and outer edges, there are two types of edge states [374] in the system. These edge states have been studied within the tight-binding approach in [374] for different geometries of quantum rings: triangular, hexagonal and rhombus. The inner and outer edge states are clearly localized at the inner and outer boundaries of the ring. The edge states behave differently as a function of the magnetic field (magnetic flux). For example, the energy of the outer edge state decreases with increasing magnetic field, while the energy of the inner edge state increases with the magnetic field. This behavior can be understood from a semiclassical picture of the motion of the guiding centre of the edge states in a magnetic field. The guiding centre of the inner edge state moves in the same direction as the cyclotron motion, while the guiding centre of the outer edge state moves in the direction opposite to the cyclotron motion. At the anticrossing point of these two dependencies there is a coupling between the edge states.

### 6.2. *Electron trapping in graphene QDs*

As it was already discussed earlier, the conventional semiconductor QDs based on a confinement by the electric potential, e.g. a gate potential, cannot be realized in graphene due to Klein tunnelling. Although a confinement potential in graphene cannot localize an electron for infinitely long time, it is still possible to realize a confinement potential that can *trap* an electron for finite but relatively long time. That type of trapping exists only for electron states with transverse momentum [350,351]. The transverse momentum introduces locally a gap and corresponding classically forbidden regions, which results in tunnelling barriers and the trapping of an electron.

To illustrate the possibility of electron trapping in graphene, we consider the semiclassical dynamics of relativistic electrons in a one-dimensional confinement potential, $V(x)$. The effective semiclassical Hamiltonian for such a confinement potential takes the form [351]

$$\mathcal{H}_{\mathrm{eff}} = \pm\hbar v_{\mathrm{F}}\sqrt{k_x^2 + k_y^2} + V(x). \tag{99}$$

This expression shows that the transverse momentum, $p_y$, introduces an effective mass for the motion in the $x$ direction. Then for a given transverse momentum there are four classical turning points, which satisfy the following equation:

$$E = \pm\hbar v_{\mathrm{F}}|k_y| + V(x). \tag{100}$$

For a parabolic confinement potential, $V(x) = -(x/x_0)^2 U/2$, the classical turning points are given by the expressions [351]

$$\frac{x_{\mathrm{out}\pm}}{x_0} = \pm\sqrt{2\frac{\hbar v_{\mathrm{F}}|k_y| - E}{U}} \tag{101}$$

$$\frac{x_{\mathrm{in}\pm}}{x_0} = \pm\sqrt{2\frac{-\hbar v_{\mathrm{F}}|k_y| - E}{U}}. \tag{102}$$

The turning points with classically forbidden regions are shown schematically in Figure 67. The electron (hole) bounces between two inner turning points, $x_{\mathrm{in}\pm}$, resulting in quasibound state, i.e. the resonances. These bound states have finite width due to quantum tunnelling through classically forbidden region between points $x_{\mathrm{in}}$ and $x_{\mathrm{out}}$. Such quasibound states result in oscillations of the current through the *p–n–p* junction as a function of the gate voltage [375]. The trapping properties of one-dimensional confinement potential, e.g. a *p–n–p* junction, are suppressed in the presence of disorder. This is because the disorder makes the boundary between different regions less sharp, which introduces additional escape channels from the trapping region. Thus in the presence of disorder the widths of the quasibound states increase, which can be visible in suppression of oscillations of the current through the *p–n–p* junction with variation of the gate voltage [375].

A similar mechanism of trapping exists for the QD-type confinement potential with trapping in both $x$ and $y$ directions [350]. For a cylindrically symmetric confinement potential, the electron angular momentum, which is a transverse

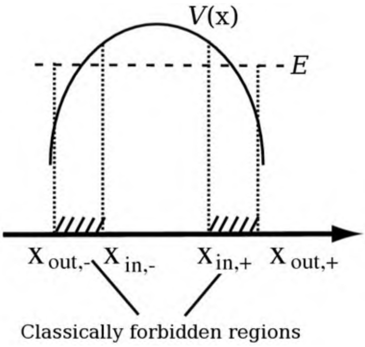

Figure 67. Trapping of an electron in a one-dimensional confinement potential, $V(x)$. The transverse momentum, $p_y$ introduces an effective electron mass in the $x$ direction, which results in four classical turning points, $x_{\text{in}\pm}$ and $x_{\text{out}\pm}$. Two classically forbidden regions are also indicated. The electron is trapped between the inner turning points, $x_{\text{in}\pm}$.

momentum for such a system, introduces a local gap and classically forbidden regions. We assume that the QD is cylindrically symmetric, $V(r)$, and the confinement potential does not introduce any inter-valley mixing. In that case it is enough to consider the states of a single valley only. Then the electron states are described by a two-component wave functions with the following Hamiltonian:

$$\mathcal{H} = \hbar v_{\text{F}} \left. \begin{matrix} 0 & k_x - \mathrm{i}k_y \\ k_x + \mathrm{i}k_y & 0 \end{matrix} \right) + \begin{pmatrix} V(r) & 0 \\ 0 & V(r) \end{pmatrix}. \tag{103}$$

In the cylindrical coordinate, the corresponding Dirac equations become [253]

$$V(r)\psi_1 + \hbar v_{\text{F}} \mathrm{e}^{-\mathrm{i}\theta} \left( -\mathrm{i}\frac{\partial}{\partial r} + \frac{1}{r}\frac{\partial}{\partial \theta} \right) {}_2 = E\psi_1 \tag{104}$$

$$V(r)\psi_2 + \hbar v_{\text{F}} \mathrm{e}^{\mathrm{i}\theta} \left( -\mathrm{i}\frac{\partial}{\partial r} - \frac{1}{r}\frac{\partial}{\partial \theta} \right) {}_1 = E\psi_2, \tag{105}$$

where $\psi_1(r, \theta)$ and $\psi_2(r, \theta)$ are the two components of the wave function, and $E$ is the eigenenergy of a stationary state. For a cylindrically symmetric confinement potential, the solution of the system of equations (104)–(105) can be expressed in the following form:

$${}_1(r, \theta) = \chi_1(r)\mathrm{e}^{\mathrm{i}(m-\frac{1}{2})\theta}, \tag{106}$$

$${}_2(r, \theta) = \chi_2(r)\mathrm{e}^{\mathrm{i}(m+\frac{1}{2})\theta}, \tag{107}$$

where $m = \pm\frac{1}{2}, \pm\frac{3}{2}, \ldots$ is the electron angular momentum. Substituting these expressions into Equations (104)–(105), we obtain

$$V(r)\chi_1 - \mathrm{i}\hbar v_{\text{F}} \frac{\mathrm{d}\chi_2(r)}{\mathrm{d}r} - \mathrm{i}\hbar v_{\text{F}} \frac{m + \frac{1}{2}}{r} \chi_2(r) = E\chi_1 \tag{108}$$

$$V(r)\chi_2 - \mathrm{i}\hbar v_{\text{F}} \frac{\mathrm{d}\chi_1(r)}{\mathrm{d}r} + \mathrm{i}\hbar v_{\text{F}} \frac{m - \frac{1}{2}}{r} \chi_1(r) = E\chi_2. \tag{109}$$

The system of equations (108)–(109) describes the electronic states of a graphene layer with confinement potential $V(r)$ [350].

The semiclassical dynamics corresponding to the system of equations (108)–(109) has been discussed in [350]. The semiclassical approach can be applied if the angular momentum of the electron is large. We are looking for a solution of the system of equations (108)–(109) in the form $\chi_1, \chi_2 \propto \exp(\mathrm{i}q\rho)$. Then under the condition $m \gg 1$ we obtain [350]

$$[E - V(r)]^2 = \hbar^2 v_{\mathrm{F}}^2 \left(\frac{m}{r}\right)^2 + \hbar^2 v_{\mathrm{F}}^2 q^2. \tag{110}$$

This equation describes the semiclassical dynamics. It has two turning points which are determined by the condition $q = 0$, i.e.

$$[E - V(r)]^2 = \hbar^2 v_{\mathrm{F}}^2 \left(\frac{m}{r}\right)^2. \tag{111}$$

Therefore the transverse momentum, $m/r$, introduces a gap (or effective mass) in the semiclassical energy dispersion law.

For a monotonic confinement potential (Figure 68), if $r_0$ is a solution of the equation $E - V(r_0) = 0$ then the two classical turning points can be found from Equation (111) in the following form [350]:

$$r_1 = r_0 - \Delta r_1 = r_0 - \frac{m/r_0}{F/\hbar v_{\mathrm{F}} + m/r_0^2}, \tag{112}$$

$$r_2 = r_0 + \Delta r_1 = r_0 - \frac{m/r_0}{F/\hbar v_{\mathrm{F}} - m/r_0^2}, \tag{113}$$

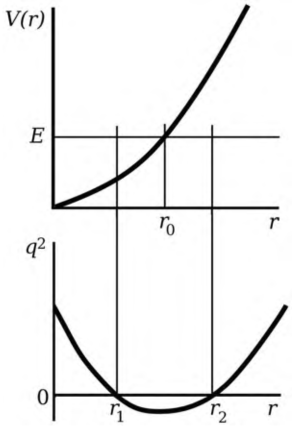

Figure 68. Schematic representation of a cylindrically symmetric confinement potential. The angular motion introduces a transverse momentum, which results in an effective electron mass. The classically forbidden region which is determined by the condition $q^2 < 0$, is realized at large values of the angular momentum. The classical turning points are $r_1$ and $r_2$. The electron is trapped inside the classical region $r < r_1$. Tunnelling through the semiclassical barrier ($r_1 < r < r_2$) determines the escape rate from the trapped region.

where $F = \mathrm{d}V(r)/\mathrm{d}r|_{r=r_0}$. The electron can freely propagate within the classical regions $r > r_2$ and $r < r_1$. The tunnelling barrier between two classical regions introduces the electron trapping in the region of the QD, $r < r_1$. Tunnelling through the classically forbidden region ($r_1 < r < r_2$) determines an escape rate from the QD (Figure 68). Under the condition $F \gg \hbar v_F m/r_0^2$, which results in the relation $\Delta r_1 = \Delta r_2 = m\hbar v_F/Fr_0$, the tunnelling exponent is given by the following expression [350]:

$$R = \exp\left. -\int_{r_0-\Delta r_1}^{r_0+\Delta r_1} |q(r)|\mathrm{d}r\right) = \exp\left(-\frac{\pi\hbar v_{\mathrm{F}} m^2}{2Fr_0^2}\right). \tag{114}$$

Therefore, an efficient electron trapping occurs in a smooth confinement potential, i.e. the slope, $F$, should be small, and at a large angular momentum, $m$. For a confinement potential of the form $V(r) = (u/p)r^p$, the escape rate from the QD becomes

$$R = \exp\left[-\frac{\pi m^2}{p(E/\epsilon_p)^{p+1/p}}\right], \tag{115}$$

where

$$\epsilon_p = [(\hbar v_{\mathrm{F}})^p u/p]^{1/(p+1)}. \tag{116}$$

Then the condition for a small escape rate, i.e. a large tunnelling exponent $R \ll 1$ determines the upper limit of the energy of the strongly trapped state at a given angular momentum, $m$, [350]

$$E < \epsilon_p m^{2p/(p+1)}. \tag{117}$$

Therefore trapping of an electron in a QD realized through a confinement potential is due to the formation of semiclassical tunnelling barrier. The width of the classically forbidden region depends on the transverse momentum, i.e. the angular momentum, and the slope of the confinement potential. Electron trapping can be realized only in a smooth confinement potential, which means that there are no electrons trapped in the confinement potential with sharp boundaries, e.g. a box-like potential. For such a potential the slope $F$ at the boundary of the QD is large and the tunnelling exponent is small. Another requirement for strong electron trapping is a large value of the angular momentum, $m$. At a small $m$ the tunnelling barrier is narrow and the electron can easily escape from the QD.

### 6.3. *QDs with sharp boundaries*

The semiclassical analysis describes an electron dynamics only for large values of the angular momentum. To address the problem of electron trapping at small values of the angular momentum and in a confinement potential with sharp boundaries, the system of equations (108)–(109) should be solved exactly. In [376–378] the system of equations (108)–(109) was analyzed in detail for a confinement potential with sharp boundaries, i.e. box-like potential, which has the following form:

$$V(r) = \begin{cases} 0 & \text{if } r < R \\ V_0 & \text{if } r > R \end{cases}, \tag{118}$$

where $V_0 > 0$ is the strength of the confinement potential and $R$ is the radius of the QD. For such a confinement potential there are no classically forbidden regions and no semiclassical trapping barrier. At the same time it was shown that in this case there are electronic states with very small escape rate [376–378]. Electron trapping in these states is determined by the interference effects within the whole region of the QD. In this case the dependence of the electron trapping time on the parameters of the confinement potential is not exponential but a power law.

The trapped states in the confinement potential can be defined by two methods. In the first method the trapped states are considered as the resonances, which are revealed as the first-order poles of the scattering matrix in the complex energy plane or as the peaks in the scattering cross section. Here the widths of the peaks determine the lifetime of the trapped state. This method has been used in [376], where the scattering cross-section was numerically calculated for a box-like confinement potential. It was shown in [376] that sharp resonances occur only at the energy close to the confinement potential strength, i.e. $E \approx V_0$.

In the second method the trapped states are defined as the time-independent solutions of the Schrödinger equation with purely outgoing boundary conditions. The stationary solutions with outgoing boundary conditions exist only at complex energies. The trapped states in this method are considered as long-lived states in the decay process [378]. The real part of the complex energy is associated with the energy of the trapped state, while the inverse of the imaginary part of the energy determines the lifetime of the decaying state. For example, if $E$ is the complex energy of the trapped state, then the trapping time is $\tau = \hbar/\mathrm{Im}[E]$. Such an approach to the problem of quasibound states was originally introduced by Gamow [379]. The second method allows us to find some analytical expressions which determine the trapping properties of the QD. This method has been used in [377,378]. Here the complex energies, $E$, of the trapped states are determined from the solution of Equations (108)–(109) with outgoing boundary conditions: $\chi_1, \chi_2 \propto \exp(ikr)$ at large distance from the QD.

For the box-like confinement potential it is easy to show that the solution of Equations (108)–(109) takes the following form [378]:

$$\left.\begin{matrix} \chi_1(r) \\ \chi_2(r) \end{matrix}\right) = A \left.\begin{matrix} J_{|m-\frac{1}{2}|}(\varepsilon r/R) \\ \mathrm{i}J_{|m+\frac{1}{2}|}(\varepsilon r/R) \end{matrix}\right), \tag{119}$$

at $r < R$ and

$$\left.\begin{matrix} \chi_1(r) \\ \chi_2(r) \end{matrix}\right) = B \begin{pmatrix} H^{(1)}_{|m-\frac{1}{2}|}[(\varepsilon - \nu_0)r/R] \\ \mathrm{i}H^{(1)}_{|m+\frac{1}{2}|}[(\varepsilon - \nu_0)r/R] \end{pmatrix}, \tag{120}$$

at $r > R$. Here $J_n$ is the Bessel function of the $n$th order, $H_n^{(1)}$is the Hankel function of the first kind, $\varepsilon = RE/\hbar v_F$ is complex, and $\nu_0 = RV_0/\hbar v_{\mathrm{F}}$. The continuity of the wave function determines the energy eigenvalue equation in the following form:

$$\frac{H^{(1)}_{|m-\frac{1}{2}|}(\varepsilon - \nu_0)}{H^{(1)}_{|m+\frac{1}{2}|}(\varepsilon - \nu_0)} = \frac{J_{|m-\frac{1}{2}|}(\varepsilon)}{J_{|m+\frac{1}{2}|}(\varepsilon)}. \tag{121}$$

The energy, $\varepsilon$, in this equation is complex. In terms of the complex energy, the condition of strong trapping means that the imaginary part of the energy is small. Surprisingly, in the box-like geometry of the QD there are special states in which an electron is localized; which means that the imaginary part of the energy of this state is zero and the electron lifetime is *infinitely large* [378]. These states exist only if the dimensional potential strength, $\nu_0$, is a root of the Bessel function $J_{m-\frac{1}{2}}(\nu_0) = 0$. In this case there is a real solution $\varepsilon = \nu_0$ of Equation (121) with infinitely long trapping time.

Therefore a localized state of an electron in a QD with sharp boundary exists only if the confinement potential satisfies the following condition:

$$\nu_0 = \lambda_{n,i}, \tag{122}$$

where $n = m - \frac{1}{2}$ and $\lambda_{n,i}$ is the $i$th root of the Bessel function of the order $n = 0, 1, 2, \ldots$. In this case the energy of a localized state is exactly equal to the strength of the confinement potential, $\varepsilon = \nu_0$. These localized states have infinitely long trapping time and exist at both small and large values of angular momentum, $m$. The typical imaginary part of the energies of the other states are of the order of 1 and the corresponding trapping times are relatively short. Any deviation of the parameters of the confinement potential from the condition (122) of localization introduces an electron escape from the highly trapped state of the QD.

If the condition for localization is weakly violated, i.e. $\delta_\nu \equiv \nu_0 - \lambda_{m-\frac{1}{2},i}$ is small, then it is possible to find the imaginary part of the energy of the highly trapped states [378] from the standard perturbation theory based on Equation (121):

$$\mathrm{Im}[\varepsilon] = \frac{\pi}{2}\left(\frac{\delta_\nu}{\ln \delta_\nu}\right) \tag{123}$$

if $m = \frac{1}{2}$ and

$$\mathrm{Im}[\varepsilon] = \frac{\pi}{[2^m(m - \frac{1}{2})!]^2}\left[1 - \frac{1}{2m}\right]^{2m+1} \delta_\nu^{2m} \tag{124}$$

if $m > \frac{1}{2}$.

Electron trapping in a confinement potential with sharp boundaries is very sensitive to the profile and the parameters of the potential. By varying the parameters of the confinement potential, one can tune the trapping time within the confinement region. These parameters could be the strength of the confinement potential, the radius of the QD or the distance between the QDs in a system of coupled QDs with sharp boundaries [377].

### 6.4. *QDs in a magnetic field: numerical studies*

The semiclassical approach to the problem of trapped states in a confinement potential is applicable only at large values of electron angular momentum. At small angular momentum, even for a smooth confinement potential we need to go beyond the semiclassical approximation. In this case we need to solve the system of equations (108)–(109) exactly. The numerical solution of this system of equations for the confinement potential with a sharp boundary was discussed in Section 6.3. Here we consider the numerical solution of Equations (108)–(109) for a confinement potential with smooth boundary [350]. Similar to the confinement potential with a sharp boundary, the trapped states are defined as the time-independent solutions of the Schrödinger equation with outgoing boundary conditions. Such stationary solutions exist only at complex energies, where the real part of the energy is the energy of the state and the imaginary part of the energy is proportional to the escape rate from the QD, i.e. inversely proportional to the trapping time.

To introduce the outgoing boundary conditions for the system of equations (108)–(109), we consider the solution of these equations at large distances, $r \to \infty$. In this limit, due to the relation $V(r) \gg E \gg \hbar v_{\mathrm{F}}/r$ the confinement potential provides the leading terms in Equations (108)–(109). Therefore, at $r \to \infty$ Equations (108)–(109) take the form

$$V(r)\chi_1 - \mathrm{i}\hbar v_{\mathrm{F}} \frac{\mathrm{d}\chi_2}{\mathrm{d}r} = 0, \tag{125}$$

$$V(r)\chi_2 - \mathrm{i}\hbar v_{\mathrm{F}} \frac{\mathrm{d}\chi_1}{\mathrm{d}r} = 0. \tag{126}$$

The general solution of Equations (125)–(126) can be expressed in the following form:

$$\chi_1 = C_1 \exp\left(\frac{\mathrm{i}}{\hbar v_{\mathrm{F}}} \int^r V(r')\mathrm{d}r'\right) + C_2 \exp\left(-\frac{\mathrm{i}}{\hbar v_{\mathrm{F}}} \int^r V(r')\mathrm{d}r'\right), \tag{127}$$

$$\chi_2 = -C_1 \exp\left(\frac{\mathrm{i}}{\hbar v_{\mathrm{F}}} \int^r V(r')\mathrm{d}r'\right) + C_2 \exp\left(-\frac{\mathrm{i}}{\hbar v_{\mathrm{F}}} \int^r V(r')\mathrm{d}r'\right). \tag{128}$$

The two terms in these solutions correspond to waves propagating towards the QD and away from the dot. Only the solution corresponding to the outgoing waves should be kept, i.e. only the first terms in Equations (127)–(128) should be considered. Thus the outgoing boundary conditions mean that at large distance, the functions $\chi_1$ and $\chi_2$ take the form

$$\chi_1 = -\chi_2 = C_1 \exp\left(\frac{\mathrm{i}}{\hbar v_{\mathrm{F}}} \int^r V(r')\mathrm{d}r'\right). \tag{129}$$

This expression should be considered as the boundary condition for the system of equations (108)–(109) at $r \to \infty$. It is convenient to reformulate the boundary condition (129) in terms of new functions $f(r)$ and $g(r)$ defined by the following expressions:

$$\chi_1 = f(r)\exp\left(\frac{\mathrm{i}}{\hbar v_{\mathrm{F}}}\int^{r} V(r')\mathrm{d}r'\right), \tag{130}$$

$$\chi_1 = -g(r)\exp\left(\frac{\mathrm{i}}{\hbar v_{\mathrm{F}}}\int^{r} V(r')\mathrm{d}r'\right). \tag{131}$$

In terms of the functions $f(r)$ and $g(r)$ the boundary condition (129) becomes $f(r\to\infty) = g(r\to\infty)$. Substituting expressions (130), (131) into the system of equations (108)–(109), we obtain

$$V(r)(f-g) + \mathrm{i}\hbar v_{\mathrm{F}}\frac{\mathrm{d}g}{\mathrm{d}r} + \mathrm{i}\hbar v_{\mathrm{F}}\frac{m+\frac{1}{2}}{r}g = Ef, \tag{132}$$

$$V(r)(g-f) + \mathrm{i}\hbar v_{\mathrm{F}}\frac{\mathrm{d}f}{\mathrm{d}r} - \mathrm{i}\hbar v_{\mathrm{F}}\frac{m-\frac{1}{2}}{r}f = Eg. \tag{133}$$

The system of equations (132)–(133) should be solved numerically with the boundary conditions $f(r=0) = g(r=0) = 0$ at the origin and $f(r\to\infty) = g(r\to\infty)$ far away from the QD [350]. Such a solution exists only at complex energies. For a confinement potential of the form $V(r) = (u/p)r^p$, the complex energy spectra is shown in Figure 69 for different values of electron angular momentum. Only the states with small values of the imaginary part of the energy are shown in Figure 69, i.e. in addition to the states shown in the figure there are many continuum states with large imaginary part of the energy.

The strength of the electron confinement is determined by the ratio of the interlevel spacing, $\Delta E$, to the imaginary part of the energy, Im($E$). For strongly

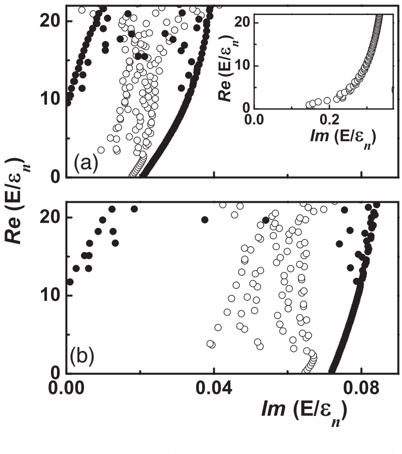

Figure 69. The real and imaginary parts of the energy spectra of an electron in a QD with a confinement potential $V(r) = (u/p)r^p$, shown for various values of the exponent $p$ and the angular momentum $m$: (a) $p=2$, $m=3/2$ (open circles) and $p=2$, $m=19/2$ (solid circles); (b) $p=4$, $m=3/2$ (open circles), $p=4$, $m=9/2$ (stars) and $p=4$, $m=19/2$ (solid circles). The results for $p=2$ and $m=\frac{1}{2}$ are shown in the inset. The energy is in the units of $\epsilon_p = [\hbar v_{\mathrm{F}})^p\ u/p]^{1/(p+1)}$ (reproduced from [350]).

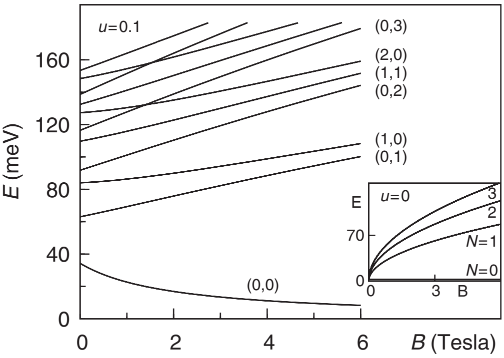

Figure 70. Energy (Fock–Darwin) spectrum of the Dirac QDs with parabolic confinement potential, $V(r)=(u/2)r^2$ is plotted for $u=0.1$ (meV nm$^{-2}$) as a function of magnetic field. The numbers in the parentheses correspond to the two quantum numbers $N$ and $m$, where $m$ is the angular momentum and $N+m=n$ is the Landau level index. The energy spectrum of graphene without confinement potential, i.e. $u=0$, is given in the inset (reproduced from [350]).

trapped states this ratio is large, while for the deconfined continuum states this ratio is of the order of 1. The formation of the confined states in the QD is already visible at angular momentum $m=3/2$, for which the ratio $\Delta E/\mathrm{Im}(E)$ is around 50. With increasing angular momentum the electron states become more confined and the imaginary part of the energy decreases. For example, for $m=9/2$ the ratio $\Delta E/\mathrm{Im}(E)$ is 200, while for $m=19/2$ the ratio $\Delta E/\mathrm{Im}(E)$ is 800, i.e. the electron with these value of angular momentum can be considered as strongly trapped by the confinement potential [350]. Therefore the confined states within the QD can be observed for states with angular momentum greater than $\sim 9/2$.

Properties of the trapped states of a QD in an external magnetic field have been studied numerically in [350]. To find the energy spectra of such a system a finite set of basis wavefunctions, corresponding to an electron in uniform magnetic field, has been introduced. The basis wavefunctions have the form of Equation (8), where the Landau wavefunctions are expressed in terms of the functions with a given angular momentum, $m$. Then the matrix elements of the confinement potential between the basis functions are calculated and the eigenvalues and eigenfunctions of the corresponding Hamiltonian matrix are found. To suppress any escape of particles from the QD, i.e. to consider only the confined states within the QD, the basis functions were restricted only by the functions with positive energies.

The calculated low-lying energy states of the graphene QD in uniform magnetic field and in a parabolic confinement potential, $V(r)=(u/2)r^2$, are shown in Figure 71. At zero magnetic field the energy spectrum reproduces the energy spectrum of the confined states in a parabolic QD. In contrast to conventional nonrelativistic parabolic QD, which has equidistant and degenerate energy spectrum, the spectrum of QDs in graphene is not equidistant and the degeneracy of the levels is lifted. At low magnetic fields, the magnetic length, $l_B$, is larger than the characteristic size, $[(\hbar v_F)^2 u]^{\frac{1}{3}}$, of the confined states in the QD. In this case the magnetic field introduces a mixture between the confined states of the dot [350]. For a large magnetic field the magnetic length becomes smaller than the size of the QD and the electron states can

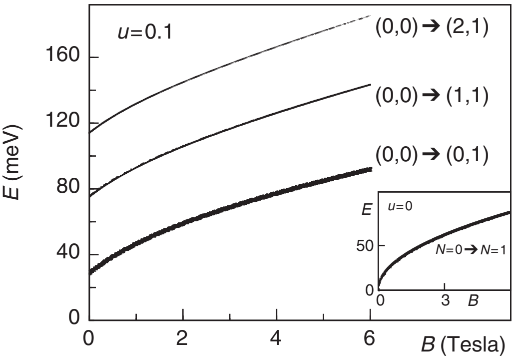

Figure 71. The dipole-allowed optical transitions in a graphene QD with a parabolic confinement potential, $V(r) = (u/2)r^2$ is shown at $u = 0.1$ (meV nm$^{-2}$). Only optical transitions from the ground state are shown. Inset: the optical transitions in graphene without the confinement potential, $u = 0$. The thickness of the lines is proportional to the calculated intensity. From the bottom to the top, the relative intensities are about 1.0, 0.1, 0.02, respectively (reproduced from [350]).

be considered as the Landau level states mixed by the confinement potential. In this case the inter-Landau level coupling lifts the degeneracy of the Landau levels.

The manifestation of mixing of Landau levels by the confinement potential is clearly seen in optical transitions within the QD. The optical transitions from the ground state, $(0, 0)$, of the QD to the excited states are shown in Figure 71. Without a confinement potential the only allowed transition is $(0, 0) \rightarrow (0, 1)$, i.e. from the $n = 0$ to the $n = 1$ Landau levels. The confinement potential introduces mixing of the Landau levels, which results in the allowed optical transitions $(0, 0) \rightarrow (1, 1)$ and $(0, 0) \rightarrow (2, 1)$. The lowest allowed optical transition, i.e. $(0, 0) \rightarrow (0, 1)$ transition, for parabolic confinement potential has an energy [350]

$$\Delta E = [(\hbar v_F)^2 u]^{\frac{1}{3}} + \frac{\sqrt{2}\hbar v_F}{l_B}. \tag{134}$$

This expression reproduces the Landau level separation in graphene at large magnetic fields and inter-level separation for the confined states at zero magnetic field. The expression (134) can also be used to extract the band parameter, $\hbar v_F$, from the optical absorption experiments in graphene in a magnetic field and a confined potential.

### 6.5. *Magnetic QDs*

The combination of a uniform magnetic field and the confinement electrostatic potential can produce strongly confined states [380] even in an ideal graphene system. The origin of such a confinement can be understood from the semiclassical analysis of the electron dynamics. In an uniform magnetic field, Equation (110) takes the form [380]

$$(\hbar v_F)^2 q^2 = [E - V(r)]^2 - (\hbar v_F)^2 (m/r + eBr/2)^2. \tag{135}$$

The classically forbidden region is determined by the condition $q^2 < 0$. Then the electron motion is confined, i.e. an electron cannot classically propagate at large distances, $r \to \infty$, if at large $r$ the right-hand side of Equation (135) becomes negative. This can be realized if the confinement potential increases slower than $r$, e.g. becomes constant at large distance [380]. Therefore at large $r$ the behavior of the electron is determined not by the confinement potential but mainly by the uniform magnetic field, which itself produces intrinsically confined electronic states. The electron confinement by a slow varying electrostatic potential and uniform magnetic field can also be understood as a pinning of intrinsically confined magnetic electronic states by the electrostatic potential. The advantage of this type of confinement is that it can be realized for all values of the electron angular momentum, $m$, and for different types of slow varying electrostatic potential, even non-cylindrically symmetric one. If the confinement potential increases as $V \propto r$ then the system shows confinement–deconfinement transitions, which is controlled by the dot parameters and the strength of the magnetic field [380]. These transitions can also be understood from the semiclassical expression (135). Indeed, if $V = v_0 r$ then from Equation (135) we obtain that the confinement of the state is determined by the sign of the expression $v_0 - \hbar v_F e B$. The electron is confined or deconfined if this expression is negative or positive, respectively.

The confinement of an electron in graphene can also be realized through inhomogeneous magnetic fields [352,353]. For a cylindrically symmetric magnetic QD, the external magnetic field is perpendicular to the graphene plane and the magnitude of magnetic field depends only on radius, $B(r)$. The Dirac equation for a two-component spinor, $\psi = (\psi_1, \psi_2)$, corresponding to a single valley takes the form

$$\vec{\sigma}\left[\vec{p} + \frac{e}{c}\vec{A}(x, y)\right] \ (x, y) = \epsilon\psi(x, y), \tag{136}$$

where $\vec{A}(x, y)$ is the vector potential and $E = v_F \epsilon$. For a cylindrically symmetric magnetic QD, the electron angular momentum is conserved. Then the solution of the Dirac equation has the form of Equations (106)–(107) and the Dirac equation reduced to the following system of equations [352]:

$$\frac{d\chi_1(r)}{dr} - \frac{m + \frac{1}{2} + \phi(r)}{r}\chi_1(r) = \epsilon\chi_2 \tag{137}$$

$$\frac{d\chi_2(r)}{dr} + \frac{m - \frac{1}{2} + \phi(r)}{r}\chi_2(r) = \epsilon\chi_1, \tag{138}$$

where $\phi(r) = \frac{e}{c}\int_0^r dr' r' B(r')$ is the magnetic flux through a disk of radius $r$ in units of the flux quantum.

For the simple model of a magnetic QD for which $B = B_0$ outside a disk of radius $R$ and zero inside the disk, the general solution of the system of equations (137)–(138) can be expressed in terms of the Bessel functions inside the dot and hyperbolic functions $\Phi$ and $\Psi$ outside the dot. The continuity of the two-component wave function determines the energy eigenequation for the magnetic QDs [352]

$$1 - |\tilde{m}|\theta(-\tilde{m})/\delta - \frac{\varepsilon l_B}{\sqrt{2\delta}} \frac{J_{m+\frac{1}{2}}(\epsilon l_B \sqrt{2\delta})}{J_{m-\frac{1}{2}}(\epsilon l_B \sqrt{2\delta})} = \frac{\mathrm{d}}{\mathrm{d}\eta} \ln \Psi(\alpha, 1 + |\tilde{m}|; \eta = \delta), \tag{139}$$

where $l_B = \sqrt{c/eB_0}$ is the magnetic length, $\delta = R^2/2l_B^2$, $\tilde{m} = m - \delta$ and $\alpha = 1 + \tilde{m}\theta(\tilde{m}) - (\varepsilon l_B)^2/2$. The solutions of Equation (139) determine the energies of the localized states of an electron within the magnetic QD. Electrons in these states are strongly confined with zero escape rate.

The many electron system in parabolic magnetic QDs, i.e. $B(r) \propto r^2$, was studied in [354]. Employing Sucher's projector formalism [381], i.e. restricting the Hilbert space to the positive-energy eigenspace for each particle, allowed the authors to obtain the energy spectra of the many electron interacting system. For a two-electron system, a singlet-triplet ground-state spin transition was observed as a function of the inter-electron interaction strength.

### 6.6. *Confinement of massive relativistic electrons in graphene*

Another way to overcome the problem of Klein tunnelling and to confine an electron in a graphene layer is to introduce gap in the energy dispersion, i.e. introduce a finite electron mass. Due to the presence of the gap, there are no freely propagating states (hole states) inside the barrier, which suppresses the Klein tunnelling. The effective electron mass can be introduced through a constant mass term in the Hamiltonian. The QD in this case can be straightforwardly defined through a confinement potential. The final Hamiltonian of the system has the following form [382]:

$$\mathcal{H} = v_{\mathrm{F}} \vec{p} \cdot \vec{\sigma} + \tau \Delta \sigma_z + V(x, y), \tag{140}$$

where $\tau = \pm 1$ corresponds to the two valleys K and K′, $\Delta$ is a constant mass term and $V(x, y)$ is the electrostatic confinement potential. The mass term, $\Delta$, introduces a gap of $2\Delta$. The Hamiltonian (140) generates localized states which decay exponentially away from the QD. The constant mass term can be realized, for example, by introducing the underlying substrate [383].

The mass term appears also in bilayer graphene with different potentials at the two layers [184,384]. The different potentials result from the influence of doping on one of the layer or from an electric field perpendicular to the layer, i.e. by gating. In this case the mass term in the Hamiltonian has the form $((V_1 - V_2)/2)\sigma_z$. Here $V_1$ and $V_2$ are the potentials at two layers. By varying the potential difference between the layers, one can realize the QD with localized states [384]. For example, by introducing a position-dependent potassium doping, the position-dependent mass term can be introduced [384]. A special example of the position-dependent mass term in the Hamiltonian of a single layer of graphene is an infinite-mass boundary conditions [385]. The Hamiltonian of an electron in graphene layer with mass-dependent term then has the form

$$\mathcal{H} = v_{\mathrm{F}} \vec{p} \cdot \vec{\sigma} + \tau V(r) \sigma_z. \tag{141}$$

Then the infinite mass boundary conditions means that the mass of the electron is zero inside the dot, $V(r)=0$ if $r < R$, and infinitely large outside the dot, $V(r)=\infty$ if $r > R$. For a circular confinement, the infinite-mass boundary condition has a simple form

$$_2/\psi_1 = \mathrm{i}\tau \mathrm{e}^{\mathrm{i}\phi} \tag{142}$$

at $r=R$. With this boundary condition the energy eigenequation takes the form [385]

$$\tau J_{m+\frac{1}{2}}(kR) = J_{m-\frac{1}{2}}(kR), \tag{143}$$

where $m = \frac{1}{2}, \frac{3}{2}, \ldots$ is the angular momentum and $k = E/\hbar v_{\mathrm{F}}$. The states of such QDs are strongly confined. Each level has twofold valley degeneracy, which follows from the property $E(m,\tau) = E(-m,-\tau)$ [385]. There is no zero energy state, which leads to the energy gap between the states with positive and negative energies.

## 6.7. *QDs in bilayer graphene*

The Klein paradox which manifests in monolayer graphene indicates that it is impossible to confine electrons by electrostatic methods. This problem is circumvented in bilayer graphene, where the lifting of the band degeneracy by the gap caused by the inter-layer potential suppresses the perfect tunnelling through an electrostatic barrier [376]. Matulis *et al*. calculated the energy spectrum and lifetime (or inverse width) of quasibound states in monolayer and bilayer QDs assuming a step-like potential profile. They found that states in the bilayer with energy lower than the potential step are much narrower (i.e. are much longer-lived) than the corresponding states in the monolayer (Figure 72). The reason for this is the differing behavior of electrons incident on a potential barrier in the two forms of graphene. At normal incidence, the monolayer barrier is completely transparent, while in the bilayer the barrier always reflects the incident electron. The longitudinal component of momentum destroys this perfect behavior, but this nonetheless serves to illustrate why confinement is much better in a bilayer dot.

Similarly, Pereira, *et al*. [386] theoretically considered dots defined by gating or inhomogeneous doping in bilayer graphene. The doping is assumed to generate

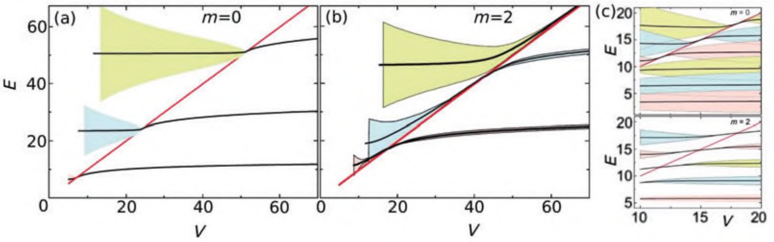

Figure 72. Quasibound states for QD in bilayer: orbital momenta (a) $m=0$, (b) $m=2$. The energies of these states are given by the black curves and its width (i.e. the inverse of the lifetime) by the shadowed regions. The straight slanted line corresponds to $E=V$. (c) The equivalent plots for the monolayer (Reprinted figure with permission from A. Matulis and F.M. Peeters, Physical Review B, 77, 115423, 2008 [376]. Copyright © (2008) by the American Physical Society.).

a quadratic potential which is cut off at some radius $R$ so that the potential difference between the layers $\Delta U$ is, as a function of the radial distance $r$:

$$\Delta U(r) = \begin{cases} \dfrac{U_M r^2}{R^2}, & r/R < 1 \\ U_M, & r/R \geq 1. \end{cases}$$

Unusually, the $m=0$ state (where $m$ is the total angular momentum) is found to have the maximum of its wave function's amplitude at $r \neq 0$. In contrast, $m=1$ is the ground state and the angular momentum phase of $2\pi$ cancels the Berry's phase of $-2\pi$. The energy levels are also not symmetric in their angular momentum: the authors find that $E(m) = -E(-m)$, in contrast to the usual semiconductor case with parabolic confinement. The energy levels are also not equally spaced, and this manifests itself in the spectrum of allowed optical transitions, where multiple frequencies will show absorption lines in a far-infrared spectroscopy measurement.

Recher *et al.* [382] study QDs in gapped bilayer graphene under the influence of a magnetic field. They show that the broken inversion symmetry of the gapped system allows bound states to be formed. They plot the dependence of the energy levels on the magnetic field, and show that the valley degeneracy is lifted in this system. The enhanced density of states near the band edge in the gapped system manifests as an increased density of levels in the dot. The trigonal warping term is also important near the band edge, although the authors argue it is less vital in the large magnetic field regime. The authors also describe the regime where the dot levels merge into the bulk Landau levels, and the combination of propagating and decaying modes that this crossover represents. A novel feature of this model is the existence of a bulk Landau level characterized by $n=0$ which persists in the dot. When states bound to the dot cross this level, the dot becomes 'leaky' and electrons may escape from the dot. However, the energy range between

$$E_< = \frac{s\xi U}{l_B^2(\gamma_1^2 + U^2)} \pm \sqrt{\frac{U^2\gamma_1^2}{4(\gamma_1^2 + U^2)} - \frac{t_\perp^2}{l_B^4(t_\perp^2 + V^2)^2}}$$

and $E_> = E_< + U$ (where $l_B$ is the magnetic length and $s = \mathrm{sgn}(B)$) is never crossed by this Landau level, and as such constitutes a region where well-behaved bound states are known to exist.

## 7. Localized states at the edges of graphene nanoribbons

Carbon systems, such as graphite, carbon nanotubes and graphene, are characterized by their $\pi$ electron structure mostly controlled by the sp$^2$ carbon network. Bulk graphene is a zero gap semiconductor whose lattice has hexagonal symmetry with two equivalent sublattices A and B (Section 1.1). The carbon atoms belonging to the two different sublattices form equilateral triangles, therefore each sublattice is invariant under 120° rotation which preserves the $D_{6h}$ symmetry. The band structure of bulk graphene is presented by cone-shaped conduction and valence bands touching at Dirac points (K and K′) in the Brillouin zone. Therefore, at each K-point

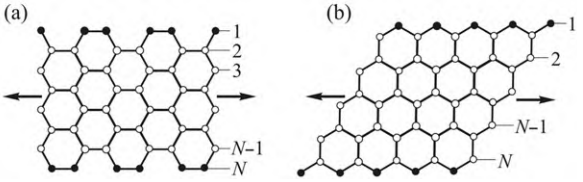

Figure 73. Graphene ribbons confined by (a) armchair and (b) zigzag edges in transverse direction. The arrows show the longitudinal (infinite) direction.

the bands are degenerate and the electronic bands $E(k)$ show linear dispersion near the K points. The Fermi level lies in the plane formed by the K points (Figure 2).

The main difference between bulk graphene and graphene nanoribbons is the presence of edges in nanoribbons. The $\pi$ network of graphene nanoribbons still consists of $sp^2$ bonded carbons, but the carbon atoms at the edges have only two neighbors, thereby developing many sp carbon bonds and unsaturated dangling bonds. Saturation of such dangling bonds through termination by hydrogens decreases the amount of sp hybridization. Disruption of the $sp^2$ carbon network can also be caused by defects and dislocations, which may have less (or more) than three neighboring atoms. As a result, the electronic properties at the edges and at the defect locations are modified in comparison to that of bulk graphene. Most significantly such discontinuities modify the electronic properties of finite nanoscale graphene, which is confined by the edges from all sides. In graphite-like structures there are two basic shapes of the edges – armchair or zigzag (Figure 73). Disruption of the $sp^2$ carbon network at the edges generates localized states. Because the structure, lattice orientation and proportion of the $sp^2$ and sp hybridization of the armchair and zigzag edges are different, their electronic properties differ, particularly in the formation of localized states. The distinction of the electronic properties between the zigzag and armchair edges was initially discussed for graphite and only zigzag edges were predicted to create localized edge states near the Fermi level [387–390].

Graphene nanoribbons – idealized quasi one-dimensional systems – can be built with solely armchair or zigzag edges, i.e. the shape of graphene ribbon can be chosen in such a way that the ribbon in finite directions is confined by either the armchair or the zigzag edges (Figure 73). In this section, we consider the electronic properties of the graphene nanoribbons, both armchair and zigzag, through distribution of the localized electrons at the edges and their spin orientation. Because the localization of the edge states is influenced by many factors, such as size of the nanoribbons, edge geometry and edge termination, their effect on the electronic properties of graphene nanoribbons are included in this section as well.

### 7.1. *Localization of the electron density at the edges*

Armchair and zigzag graphene nanoribbons have attracted considerable attention due to their unique edge properties [391]. Initially, the electronic properties of graphene nanoribbons were investigated via the tight-binding model, also known as

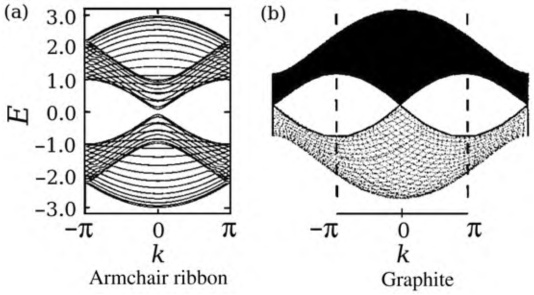

Figure 74. (a) The band structure of an armchair ribbon of width $N$=30 and (b) the band structure of two-dimensional graphite projected onto the armchair axis (Reprinted figure with permission from K. Nakada *et al.*, Physical Review B, 54, 17954, 1996 [391]. Copyright © (1996) by the American Physical Society.).

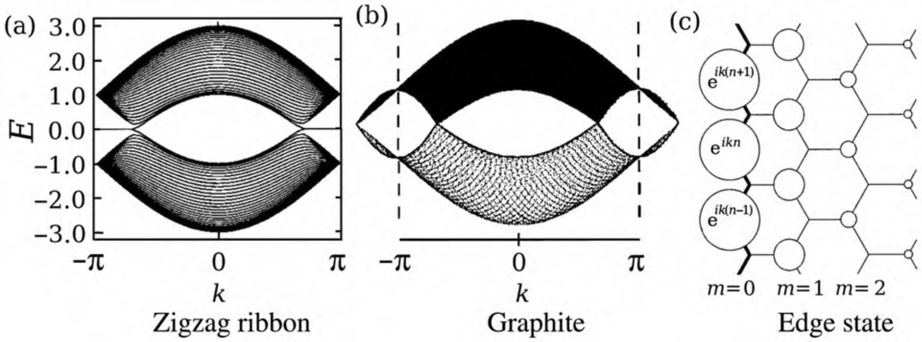

Figure 75. (a) The band structure of a zigzag ribbon of width $N$=30. (b) The band structure of the 2D graphite projected onto the zigzag axis. (c) An analytical solution of wave function for the localized edge state ($k=7\pi/9$) (Reprinted figure with permission from K. Nakada *et al.*, Physical Review B, 54, 17954, 1996 [391]. Copyright © (1996) by the American Physical Society.).

the Hückel approximation [391]. In this model, the transfer integral was set as $t$ for all nearest neighbor interactions. The dangling bonds at the edge sites were terminated by hydrogen to minimize the contribution of the sp-carbon bonds to the electronic properties. The wave vector $k$ was replaced by the translation vector and the energy $E$ by the transfer integral. The obtained band structure of an armchair ribbon of width $N=30$ is displayed in Figure 74 (a). For comparison, the band structure of two-dimensional graphite projected onto the armchair axis is also shown in Figure 74 (b), where the dashed lines are the boundaries of the first Brillouin zone. The band structure of an armchair ribbon is found to be similar to that for two-dimensional graphite: in both cases the conduction and valence bands approach the Dirac points. The main difference is a small direct gap for nanoribbons, whose size was found to be controlled by the nanoribbon width. An increase in $N$ was shown to close the gap.

Similar calculations have been performed for zigzag nanoribbons. The band structure of a zigzag nanoribbon and its comparison with that of 2D graphite

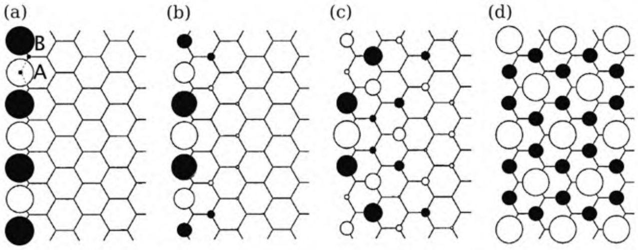

Figure 76. The real part of the wave function obtained from the analytical solution for the semi-infinite graphite. (a) $k = \pi$, (b) $k = 8\pi/9$ (c) $k = 7\pi/9$ (d) $k = 2\pi/3$. Here, the shaded and open circles denote the different sign of the wave functions. A and B denote the two sublattices (Reproduced from M. Fujita *et al.*, Journal of the Physical Society of Japan, 65, 1920 1996 [390]. Copyright © (1996) The Physical Society of Japan).

projected onto the zigzag axis are shown in Figure 75. For graphite, the cone-shaped conduction and valence bands touch at $k \simeq \pm 2\pi/3$ corresponding to the Dirac points, while in graphene after touching these bands remain degenerate. Therefore, the flatness of the conduction and valence bands begins at $k \simeq 2\pi/3$ and extends up to $k = \pi$. The wave functions corresponding to these bands are completely localized on the zigzag edges. The analytical solution for the wave function localized at the zigzag edges, which has been derived within the method of the linear combination of atomic orbitals where the translational symmetry was considered, is presented in Figure 75(c). The charge density at the zigzag edge for each non-nodal site was found to be proportional to $[2\cos(k/2)]^{2m}$, where $m$ is the lattice site ($m = 0$ for zigzag edge). In Figure 75(c), the circle radius was chosen to be proportional to the charge density. It was observed that the charge density diminishes with increasing distance from the edge sites and the damping factor is $-2\cos(k/2)$ per zigzag chain. Due to the translational symmetry considered in the model, the analytical solution implements non-zero charge density only for the sites belonging to one graphene sublattice.

For the zigzag nanoribbon, an analytical solution for the wave functions corresponding to the flat bands within the interval $2\pi/3 \leq | k | \leq \pi$ was also derived in [390]. The alteration of the real part of the wave function with the reduction of wave vector $k$ is presented in Figure 76. The wave function obtained for $k = \pi$ is completely localized on the edges and starts to penetrate into the inner sites for decreasing $k$. The extended state, when the wave function is completely delocalized over the graphene structure, is for $k = 2\pi/3$.

The localized states at the zigzag edges are distinguished by a peak of the density of states near the Fermi level, whose amplitude depends on the size of the ribbon and is found to decrease with increasing nanoribbon size [391] (Figure 77). The peak in the density of states almost disappears with increasing nanoribbon width up to $N = 51$. The structure of the zigzag edge is found to be responsible for the appearance of localized edge states close to the Fermi level.

## 7.2. *Experimental evidence for localized edge states*

The existence of localized states only at zigzag edges, as predicted theoretically, received experimental validation later [392–395]. In the first work, where

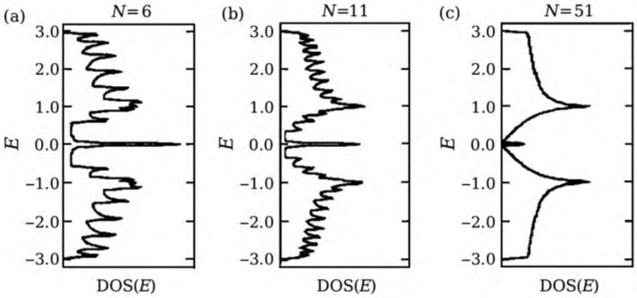

Figure 77. (a) Density of states of the zigzag nanoribbons of different width: (a) $N = 6$, (b) $N = 11$, (c) $N = 51$ (Reprinted figure with permission from K. Nakada *et al.*, Physical Review B, 54, 17954, 1996 [391]. Copyright © (1996) by the American Physical Society.).

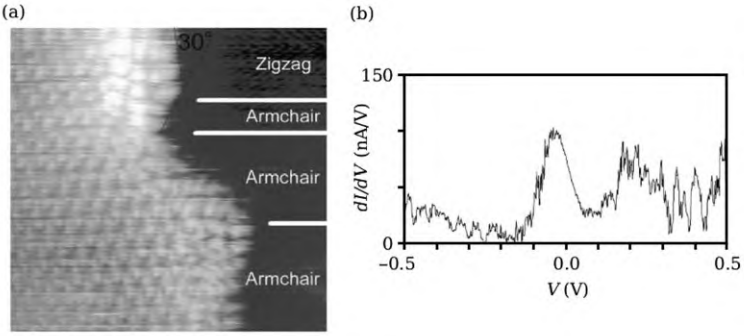

Figure 78. (a) The image of the zigzag and armchair edges ($9 \times 9\,\mathrm{nm}^2$) obtained by scanning tunneling microscopy. The bright points were attributed to the top of the zigzag edges of the monolayer graphite. (b) $dI/dV$ data from scanning tunnelling spectroscopy at the zigzag edges (Reprinted figure with permission from Y. Kobayashi *et al.*, Physical Review B, 71, 193406, 2005 [393]. Copyright © (2005) by the American Physical Society.).

investigation of the edge properties was performed by scanning tunnelling spectroscopy, the peak in the local density of states in the energy range of 90–250 meV above the Fermi level was observed for hydrogenated graphite [392]. The peak has appeared close to a monolayer edge ($\leq 1.5$ nm) while the peak intensity kept growing as the conducting tip approached the edge. Moreover, close to the monolayer edge, bright areas of nearly atomic size were observed on images from the scanning tunnelling microscopy. The brightness indicated the efficiency of the tunnelling current between the conducting tip and the graphite surface. Since the tunnelling current is a function of the local density of states, it was concluded that these bright areas can be generated by localized electrons. The main disadvantage of that experiment was that the nature of the edges was unclear: the type of edges generating bright spots could not be distinguished.

However, in subsequent experiments [393,394] it was clearly shown that localized states occur only at the zigzag edges [Figure 78]. The contrasting bright spots were found to appear at the top part of the zigzag edges. The different edges were distinguished from application of the hexagonal lattice to the images. Moreover, new data were also obtained for formation of the peak in the local density of states on d$I$/d$V$ versus bias voltage curves. In contrast to the first experiment where the peak was shifted by 90–250 meV relative to the zero voltage [392], the latter experiments have shown an appearance of the peak at negative bias voltages in the range of $-100$ to $-20$ meV [394] and in the range of $-30$ meV [393]. It was also confirmed that the intensity of the peak depends on the distance from the edge [394]. Therefore, the peak almost disappears when the distance exceeds 3.5 nm [394] against 1.5 nm in [392]. The intensity and width of the peak were also found to be dependent on the type of graphite [394]. A sharp peak of high intensity was seen for the ZYX exfoliated graphite with maximum amplitude at $\sim-25$ meV, while for the highly oriented pyrolytic graphite the peak was broad with maximum at $\sim-0.40$ meV. In another experiment [396] on graphene sheets employing Raman spectroscopy the blue shift of the G band relative to its position for graphite oxide has been observed and attributed to the alteration of the pattern of the single-double carbon bonds at the zigzag edges of graphene sheets, in particular to the formation of the sp$^3$ carbons [396].

The experimental data therefore clearly confirmed that only the zigzag edges are responsible for the occurrence of localized states in monolayer graphite, thereby validating the theoretical prediction for graphene. However, the experiments have also shown that the peak of the density of states is shifted relative to zero voltage, i.e. indicating a shift of the energy band of the localized states relative to the Fermi level, which was not foreseen in the theoretical studies [391]. It was proposed much later that this shift of the energy bands is a result of doping of graphene through its interaction with the adsorbates in the gaseous environment or with other materials, such as the contacts or the substrate [397,398]. For example, exposure of the graphene sample to $NO_2$ gas was found to shift the Hall resistance and the minimum of the density of states towards higher positive gate voltages with increasing $NO_2$ concentration [397]. Similarly, the shift of the point where the resistance of the graphene monolayer samples reach the maximum relative to zero voltage due to doping by dipolar adsorbates has indeed been observed [398]. The problem of doping by external sources and its influence on the electronic properties of graphene will be considered in Section 8.

## 7.3. *Stabilization of the edge states*

### 7.3.1. *The nearest neighbor interactions*

The flat conduction and valence bands induced by the localized states at the zigzag edges remain degenerate and totally dispersionless for $2\pi/3 < k < \pi$. Therefore, the degenerate bands and high density of states at the Fermi energy possessing a peak in the local density of states suggest an instability of these localized states. Experimental observation of a shift of the peak away from the Fermi level [392–394] is evidence of such an instability. Studies of localized states by first-order perturbation theory for the tight-binding Hamiltonian have demonstrated the role of the nearest neighbor interactions, $\gamma_0$, and the next-nearest neighbor hopping processes, $\gamma_n$, in the stabilization of these edge states [399]. The band structures of graphene obtained with and without contributions from next-nearest neighbor interactions are

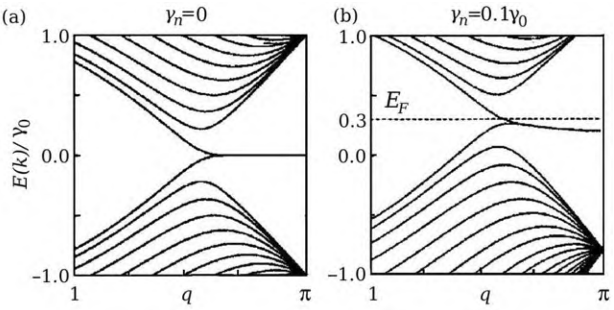

Figure 79. The energy band structure of the zigzag nanoribbon: (a) with nearest neighbor interactions $\gamma_0 = 3.0\,\text{eV}$ and (b) with both nearest neighbour $\gamma_n = 0.1\gamma_0$ and next-nearest neighbor interactions (Reprinted figure with permission from K. Sakaki *et al.*, Applied Physics Letters, 88, 113110, 2006 [399]. Copyright © (2006) American Institute of Physics.).

presented in Figure 79. In the case when the next-nearest neighbor interaction is zero, the Fermi level is located at the zero energy ($E(k)/\gamma_0 = 0$), while the conduction and valence bands are flat after they meet at $q = 2\pi/3$ at the Fermi level, where $q$ is the wave vector. If the next-nearest neighbor interactions $\gamma_n$ are taken into account, the shift of the energies of the whole band structure and the Fermi level occurs. The energy shift of the band structure has been evaluated as $\Delta E \approx \gamma_n(2\cos q + 1)$. The magnitude of $\Delta E$ is maximum when $q = \pi$, thereby generating a stronger stabilization at the edges and larger shift of the bands corresponding to the localized states. If the value of the hopping integral is not zero ($\gamma_n = 0.1\ \gamma_0$ in Figure 79 (b)), the entire band structure including the Fermi level is shifted up on the energy scale $E(k)/\gamma_0$ in such a way that the nearly flat band of the localized states is found to be located below the Fermi level (Figure 79(b)). The localized states at $q = \pi$ exhibit a sharp peak in the local density of states with a maximum at the Fermi level, which is also shifted to negative energy by the stabilization effect. The lowering of the peak amplitude of the local density of states has been seen as one moves away from the edges, and diminishing of the peak when the distance exceeds 2.5 nm is in good agreement with the experimental data (~3.5 nm in [394]).

In the next paper by the same authors, the stabilization of the localized states at the edge has been attributed to the presence of a deformation potential at the edges and the interaction between the magnetic field induced by the localized states and pseudospin polarized nature of these states [400]. The local lattice deformation was considered through the weak next-nearest neighbor interactions at the edges. It was found that the next-nearest neighbor interactions break the particle-hole symmetry in graphene, thereby stabilizing the edge states. Band structure calculations performed for different magnitudes of the deformation stress at the edges have shown that undeformed graphene (zero stress) has a band structure with cone-shaped conduction and valence bands meeting at the K points. For zigzag nanoribbons if the stress at the edges is insignificant, a narrowing of the band gap occurs for $q > 2\pi/3$, while an increase of the stress leads to additional gap narrowing and finally to band closing and flattening of the bands for $q \geq 2\pi/3$. In other theoretical work [401] the deformation of the carbon bonds at the edges was predicted to influence the size of the band gap as well. Based on the results indicating a strong effect of the deformation stress on the electronic properties, it was predicted that not only the stress at the edges, but also the external stress applied to the undeformed graphene, impurities, vacancies and external magnetic field may induce lattice deformation thereby stabilizing the localized states [400].

The edge stress occurs not only at zigzag edges, but also at armchair edges. Investigations of the compressive edge stress at armchair and zigzag edges performed with the density functional theory (DFT) have shown the dependence of the stress value on the type of edges [402]. The nature of the C–C bonds at the armchair and zigzag edges is different. The C–C bond of length $\sim 1.24\,\text{Å}$ at the armchair edges exhibits a higher rate of sp hybridization and higher charge density than that at the zigzag edge of length $\sim 1.37\,\text{Å}$, against the C–C bond of length $\sim 1.42\,\text{Å}$ possessing $sp^2$ hybridization of bulk graphene [403]. As a result, the compressive edge stress at the armchair edges is found to be larger than that at the zigzag edges, while termination of the dangling bonds by hydrogen provides almost stress-free edges [402]. In terms of the edge energy the armchair and zigzag edges are different as well. According to the theoretical [402,403] and experimental investigations [395], the energy of the armchair edge is much lower than that of the zigzag edge. It was also theoretically predicted that a simple reconstruction of the zigzag edge leads to significant lowering of its energy [404] and, therefore, to its structural stabilization. The activation barrier of the applied reconstruction was found to be only 0.6 eV, indicating the metastability of the zigzag edge at room temperature. Therefore, it was concluded that the clean zigzag edges would rarely exist [403] and this can be a way to perform the edge-selective termination of the dangling bonds. Experimental evidence for the formation of stable reczag graphene edges due to reconstruction of the zigzag edges has been reported in [405].

### 7.3.2. *Coulomb interactions*

Coulomb interactions have also been considered for understanding the mechanism of stabilization of the localized states. Simulations performed for graphite ribbons with the Hubbard model using unrestricted Hartree–Fock approximation have shown that magnetic polarization resulting from electron–electron interactions between the spin-polarized states may lead to spontaneous ordering of the spins of the electrons localized at the zigzag edges [390]. Further investigations have shown that a large magnetic moment occurs at zigzag edges even for weak Coulomb repulsion, while no magnetic structure has been found at armchair edges. For the border atoms at the zigzag edges, maximum magnetization was observed, while a move to the inner site of the ribbon reduces the magnitude of the magnetization due to the diminishing density of the localized states. Magnetic ordering of the spin states at the zigzag edge interfaces for a ribbon of width $N = 10$ is presented in Figure 80. The border atoms at the two opposite zigzag edges belong to different sublattices. According to the wave function distribution presented in Figure 76(a), the wave function localized on one edge is nonzero only for the $A$ sublattice, and the increase of the magnetic moment selectively on this sublattice leads to the formation of a local ferrimagnetic spin configuration. The localized state on the opposite zigzag edge belongs to the B sublattice and the spin orientation of the magnetic states localized on the B sublattice is opposite to that on the A sublattice, preserving the total zero

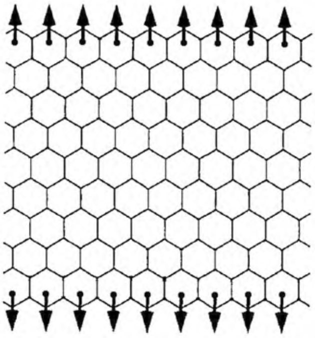

Figure 80. Spin ordering at the edges in the zigzag ribbon for $U/t = 0.1$, where $U$ is the on-site Coulomb repulsion and $t$ is the transfer integral (Reproduced from M. Fujita *et al.*, Journal of the Physical Society of Japan, 65, 1920, 1996 [390]. Copyright © (1996) The Physical Society of Japan.).

magnetization of the graphite ribbon. It was noted that the nanometer-scale size of the graphite fragments is the main requirement for spontaneous spin ordering.

The contribution of Coulomb interactions to the stabilization of the ferromagnetic state has been also considered in later works [406–409]. The results reported in [406] have shown that graphene sheets can have two ferromagnetic phases. One is characterized by the strong magnetization and maximally polarized spin (Nagaoka ferromagnetism), while the other is a weak ferromagnetic state. Moreover, strong Coulomb interactions in conjunction with high electron density at the lattice site (which is higher at the edges) can lead to an antiferromagnetic phase, while weak Coulomb interactions will switch the system to a paramagnetic state. In [407] it was shown that the exchange interactions between Dirac fermions can be the stabilizing factor for the ferromagnetic phase. The transition from the paramagnetic phase to the ferromagnetic one for pure graphene was predicted to occur at low strength of electron–electron interactions, and doping was found to increase the magnitude of the interactions required for the transition. The effect of electron–electron interactions and the doping of graphene lattice on the transition to a ferromagnetic state was also investigated in [409], but the reverse transition from the ferromagnetic to the nonmagnetic state was seen to occur only when large hole doping was applied.

The charge polarization process was also considered as an alternative mechanism for stabilization of the ferromagnetic state for the localized states [410–412]. In the case of the formation of the charge polarized state, the Coulomb interaction between the nearest sites was shown to be responsible for stabilization of this state, which on the opposite zigzag edges is distinguished by the electrical charges characterized by the opposite sign [410]. Therefore, the charge polarized state has a finite electric dipole moment directed from one zigzag edge to the other. The on-site Coulomb interaction has been found to trigger the formation of the spin-polarized state competing with a charge-polarized state. The external electric field due to the coupling with the internal dipole moment leads to stronger stabilization of the charge polarized state, that can make it energetically favorable as compared to the spin-polarized state [410,413]. However, Pisani *et al.* [412] have indicated that according to the first-principles calculations the charge polarized state is highly metastable.

### 7.4. *Spin ordering, symmetry and band gap*

The concept of spontaneous spin polarization of the localized states at zigzag edges has received wide attention. A better understanding of the spin behavior was later provided by many research groups, and is the main subject of the present section, where the influence of spin ordering of the localized states on the magnetism of graphene nanoribbons and on the stabilization of the ground state is considered.

The first-principles calculations were used in [414] to study magnetism in graphene nanoribbons. The spin ordering along the zigzag edges was described by the three states (Figure 81): (i) ferromagnetically ordered spins along each zigzag edge and between the zigzag edges (FM-F), (ii) ferromagnetically ordered spins along each zigzag edge but with opposite spin direction between the zigzag edges (FM-A) and (iii) antiferromagnetically ordered spins along the zigzag edges but with spin alignment between the edges (AF-E). Calculations of the total energy performed with the DFT method based on the local spin-density approximation have shown that FM-A is the lowest energy state characterized by a magnetic moment of $m = 1.28\mu_B$ per edge atom, where $\mu_B$ is the Bohr magneton. The next energetically preferable state is the FM-F state with magnetic moment of $m = 1.19\mu_B$ per edge atom, whose total energy is higher than that of FM-A by ~2.3 meV per edge atom. The total energy of the AF-E state is higher than that for the FM-A state by 81.4 meV per edge atom, while the magnetic moment of the AF-E state is $m = 0.82\mu_B$ per edge atom. The huge difference between the total energies of the FM-A and the AF-E states is the result of destructive interference between the spin-up and spin-down tails of the localized states in the AF-E state. The destructive interference at the inner sites of the graphene nanoribbon is also responsible for the stabilization of the FM-A

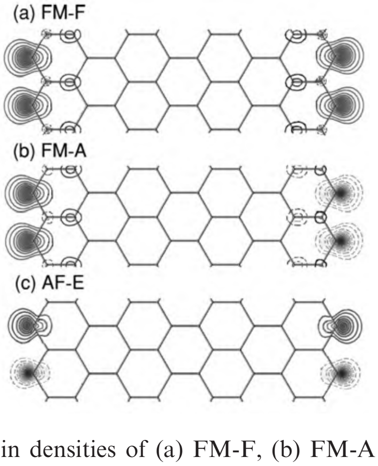

Figure 81. The electronic spin densities of (a) FM-F, (b) FM-A and (c) AF-E states in the graphitic strips. The solid line indicates the spin-up density, and the dashed line is for spin-down density (Reprinted figure with permission from H. Lee *et al.*, Physical Review B, 72, 174431, 2005 [414]. Copyright © (2005) by the American Physical Society.).

in comparison to the FM-F. The energy difference between FM-A and FM-F decreases with increasing nanoribbon width as a result of the reduction of the density of states at the inner sites that suppress the destructive interference. However, it was found [362,412] that the energetic preference of the spin-polarized state over the nonmagnetic state increases with increasing ribbon size. Several reports have confirmed the FM-A state to be the lowest energetic state of graphene [362,412,414–416].

The electronic structure of the FM-A and FM-F states are displayed in Figure 82 [412]. The border atoms at opposite zigzag edges belong to different sublattices. In the spin-polarized state, if the spin ordering between two zigzag edges is ferromagnetic, the sublattice symmetry is preserved and as a result the band gap vanishes for the FM-F state (Figure 82(a)). For the FM-F state the spin-up and spin-down bands cross each other close to the Fermi level without the formation of the electron pair at $k = 2\pi/3a$. For $k \geq 2\pi/3a$, the energy band of the spin-up state is located below the Fermi level, while for the spin-down state, in contrast, the band is located above the Fermi level.

For the FM-A state (see the band diagram in Figure 82(b)), the sublattice symmetry is broken due to the antiferromagnetic ordering of the spin states between the zigzag edges, whose border sites belong to different sublattices. Therefore, over the whole structure the spin-up state is completely localized on the A sublattice, while the spin-down state is localized on the B sublattice, making a singlet pairing between the neighboring sites. The antiparallel spin alignment of the localized states

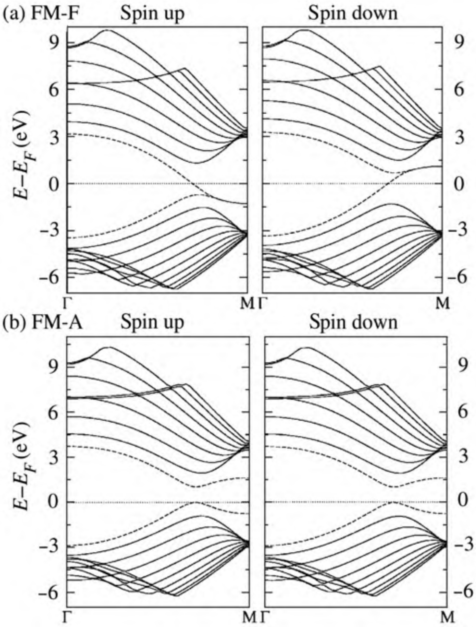

Figure 82. The band structure of the spin-polarized states (a) FM-F and (b) FM-A of the graphene nanoribbons (Reprinted figure with permission from L. Pisani *et al.*, Physical Review B, 75, 064418, 2007 [412]. Copyright © (2007) by the American Physical Society.).

between the opposite zigzag edges breaks the sublattice symmetry because carbon atoms possessing the localized states belong to different sublattices, thereby opening a gap at $k = 2\pi/3a$. An increase in the width of the zigzag ribbon leads to a reduction of the gap following an algebraic decay as $1/N$, i.e. with increasing distance between opposite zigzag edges. For $N \to \infty$ the valence and conduction bands tend to be degenerate, but the spin-polarized edges still would not show the inter-edge magnetic order. The hopping integral $t$ and the on-site Coulomb repulsion $U$ used in earlier works within the Hubbard model have been calculated within the DFT theory [412]. The values within the gradient corrected functional PBE and local-density approximation LSDA are $t$=2.5 eV and $U \sim t$.

Therefore, the lowest energy state of graphene nanoribbons is expected to have ferromagnetic ordering of the localized spin states along the zigzag edge and antiparallel spin orientation between the opposite zigzag edges, thereby breaking the sublattice symmetry and opening a gap. In this state both the band gap and the destructive interference between the spin-up and spin-down tails of the localized states decrease with increasing width of the zigzag nanoribbons. In [416], the antiparallel spin orientation at the opposite zigzag edges was also found to form the states characterized by zero total spin and a lower energy with respect to both the kinetic and interaction energies. However, in [411] the ground state of zigzag nanoribbons of regular rectangular shape was shown to have the high spin state if the many-body configuration interaction within the Hubbard Hamiltonian is taken into account. It was found that the charge polarization rather than spin-polarization is preferable in this case. For the charge polarized state, the spin-up and spin-down states are not localized at the edges but rather mixed through the nanoribbon lattice, while the electron density prefers to accumulate at the edges. As a result, the ground state of the armchair ribbon is a singlet and that of the zigzag ribbon is a high spin state, both showing the insulating behavior. Moreover, doping of graphene by $p$-type or $n$-type charge carriers [417] and oxidation of the edges [418] were found to destroy the magnetism of zigzag nanoribbons.

### 7.5. *Band gap: confinement effect and edge shape*

In addition to spin ordering between the edges, the shape of graphene edges also contributes significantly to the band structure. For localized states, the width of an armchair ribbon was shown to control its band gap [361,391,401,403,419–431]. Initially, the influence of the width on the electronic structure of graphene was reported in [391], where the band structure calculations were performed within the Hubbard model for armchair ribbons (Figure 83). Here the ribbon width dictates whether the band gap is semiconducting or metallic. The insulating band gap has a tendency to decrease with growing structure size due to the decrease of the weight of the edge states in the normalized density of states. However, for zigzag nanoribbons, where the flat band occurs for $2\pi/3 \leq |k| \leq \pi$, the width has not been found to bring any significant changes into its electronic properties.

Investigation of the electronic structure of graphene ribbons performed with the first-principles methods has clearly indicated the role of graphene size on its properties. Several groups [403,419–425,428–430,432] have seen the oscillatory

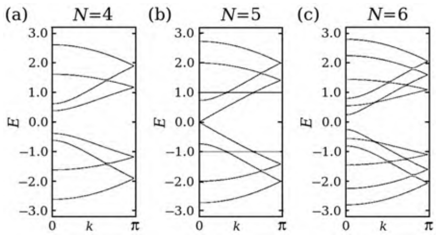

Figure 83. The band diagram of armchair ribbons, whose structure is presented in Figure 73(a), for various widths $N$ (a) $N=4$, (b) $N=5$ and (c) $N=6$. The energy $E$ is scaled by the transfer integral and the wave number $k$ is normalized by the primitive translation vector of the graphene ribbon (Reprinted figure with permission from K. Nakada *et al.*, Physical Review B, 54, 17954, 1996 [391]. Copyright © (1996) by the American Physical Society.).

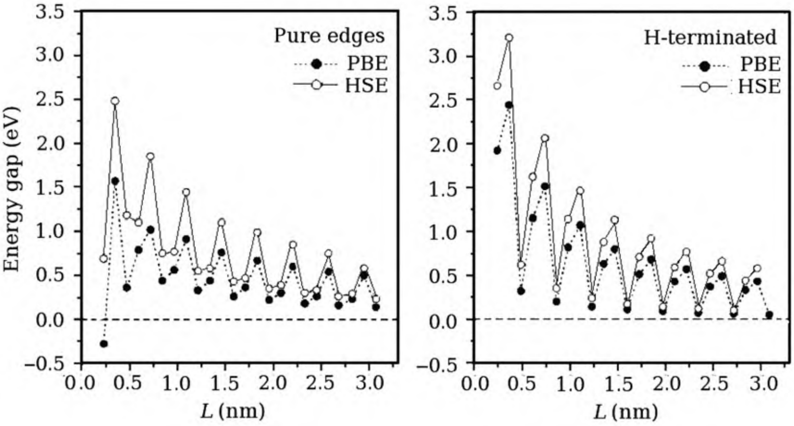

Figure 84. The dependence the size of the band gap on the ribbon width for pristine and hydrogen-terminated armchair ribbons (Reprinted with permission from V. Barone *et al.*, Nano Letters, 6, 2748, 2006 [420]. Copyright © (2006) by the American Chemical Society.).

behavior of the size of the band gap on the width of the armchair nanoribbon. The period of oscillations as $N$ varies is three. The results of DFT calculations performed with the PBE and HSE approximations for nanoribbons with pure edges or edges passivated by hydrogen atoms (to saturate the dangling bonds) are presented in Figure 84. The data were separated in three groups: the points of envelope of the maxima, of the minima and intermediate points. The envelope of the maxima was described as $N=3p+1$, where $p$ is the positive integer number, intermediate points as $N=3p$ and the minima as $N=3p+2$ [419]. The points of the minima were found to belong to the metallic state, while both intermediate and maxima points are characterized as semiconductor states. Hydrogen termination, which takes care of the dangling bonds, changes the obtained dependence so that the intermediate points are shifted closer to the envelope of the maxima in comparison to the pristine edges, where they are located closer to the envelope of the minima. In other work, the shift of the intermediate points away from the envelope of the maxima has been obtained for graphene with hydrogen-terminated edges [433].

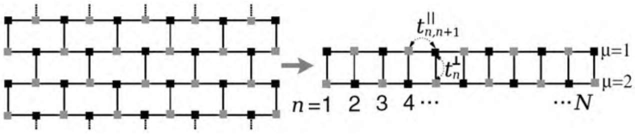

Figure 85. The periodic ladder (left) is topologically equivalent to the armchair ribbon structure in the tight-binding approximation. The condition $k=0$ is a special case when the periodic ladder (left) can be folded into a two-leg ladder (right) (Reprinted figure with permission from Y.-W. Son *et al.*, Physical Review Letters, 97, 216803, 2006 [419]. Copyright © (2006) by the American Physical Society.).

The influence of the edges on the band gap size has been found to remain for ribbon lengths up to few micrometers [435].

The periodicity of the electronic properties of armchair graphene is a result of the nature of the graphene lattice. To explain this phenomena, Son *et al.* [419] proposed to represent graphene by a lattice model describing the armchair nanoribbons within the tight-binding approximation (Figure 85). The Hamiltonian describing the electronic interactions in the longitudinal, $\mu$, and transverse, $n$, directions within the lattice model is

$$\begin{aligned}\mathcal{H}=\sum_{n=1}^{N}\sum_{\mu=1}^{2}\varepsilon_{\mu,n}a^{\dagger}_{\mu,n}a_{\mu,n}-\sum_{n=1}^{N}t^{\perp}_{n}(a^{\dagger}_{1,n}a_{2,n}+h.c.)\\ -\sum_{n=1}^{N-1}\sum_{\mu=1}^{2}t^{\|}_{n,n+1}(a^{\dagger}_{\mu,n}a_{\mu,n+1}+h.c.),\end{aligned}\tag{144}$$

where $\varepsilon_{\mu,n}$ are the site energies, $t^{\|}_{n,n+1}$, $t^{\perp}_{n}$ are the nearest neighbor hopping integrals, $a_{\mu,n}$ is the annihilation operator of $\pi$ electrons on site $\mu, n$. It was assumed that the charge transfer integrals at the borders are $t^{\perp}_{1}=t^{\perp}_{N}\equiv(1+\delta)t$ and the site energies $\varepsilon_{\mu,1}=\varepsilon_{\mu,N}\equiv\varepsilon_0$, while inside the graphene structure $t^{\perp}_{n}=t^{\|}_{n,n+1}\equiv t$ and $\varepsilon_{\mu,n}=0$, regardless of $\mu$. Therefore, the edge effect has been taken into account through the modification of the site energies ($\varepsilon_{\mu,1}$ and $\varepsilon_{\mu,N}$) and charge transfer integrals ($t^{\perp}_{1}$ and $t^{\perp}_{N}$). The model Hamiltonian was solved [419] perturbatively with the energy gaps

$$\begin{aligned}\Delta_{3p}&\simeq\Delta^{0}_{3p}-\frac{8\delta t}{3p+1}\sin^2\frac{p\pi}{3p+1},\\ \Delta_{3p+1}&\simeq\Delta^{0}_{3p+1}+\frac{8\delta t}{3p+2}\sin^2\frac{(p+1)\pi}{3p+2},\\ \Delta_{3p+2}&\simeq\Delta^{0}_{3p+2}+\frac{2|\delta|t}{p+1},\end{aligned}\tag{145}$$

where $\Delta^{0}_{3p}=t[4\cos\frac{p\pi}{3p+1}-2]$, $\Delta^{0}_{3p+1}=t[2-4\cos\frac{(p+1)\pi}{3p+2}]$, $\Delta^{0}_{3p+2}=0$ are the gaps for ideal ribbons terminated at $\delta=\varepsilon_0=0$. The solution suggests that armchair ribbons with lattice deformation at the edges have a nonzero band gap such that $\Delta_{3p+1}>\Delta_{3p}>\Delta_{3p+2}$. However, this dependence was found to work only when the characteristic length of the deformation is less than the ribbon width [425].

The periodicity of the electronic structure of armchair ribbons lies in the change of shape of the armchair edges with increasing $N$. It has been shown that such changes initiate a shift and replacement of the subbands along the energy axis [425].

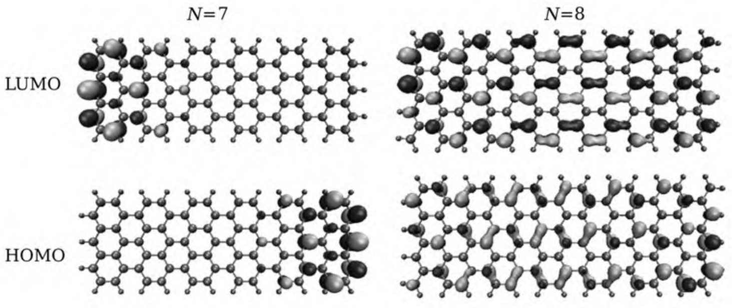

Figure 86. The spatial projection of the LUMO and HOMO molecular orbitals plotted for different zero-dimensional graphene nanoribbon: semiconductor ($N=7$) and metallic ($N=8$) (Reprinted with permission from P. Shamella *et al.*, Applied Physics Letters, 91, 042101, 2007 [423]. Copyright © (2007) by the American Institute of Physics.).

If the subbands are labelled by the quantum number $q$, then the eigenenergy $E_c$ in the center of the first Brillouin zone ($k=0$) is

$$E_c = \pm t\left|2\cos\frac{q\pi}{n+1}+1\right|. \tag{146}$$

For the metallic ribbon ($N=3p+2$), the first conduction or valence band is $q_1=2p+2$, the second one corresponds to $q_2=2p+3$ while the third subband is $q_3=2p+1$. The same analysis for one of the semiconductor ribbons where $N=3p+1$ gives $q_1=2p+1$, $q_2=2p+2$, and $q_3=2p$, while for the second semiconductor ribbon with $N=3p$ we have $q_1=2p+1$, $q_2=2p$, and $q_3=2p+2$ [425]. Therefore, the order of the subbands is changed with the modification of the width of the armchair nanoribbon. Additional confirmation has been obtained in [423,428], where localization of the lowest unoccupied molecular orbital (LUMO) and the highest occupied molecular orbital (HOMO) were found to be a function of the ribbon size. A good example that clearly shows the difference of the electron density distribution of the LUMO and HOMO orbitals between the semiconductor ($N=7$) and the metallic ($N=8$) cases is presented in Figure 86 for zero-dimensional graphene flakes. According to the density distribution, the semiconductor behavior ($N=7$) occurs when the HOMO and LUMO are strongly localized at the opposite zigzag edges. These localized states can be assigned to the $q_1=2p+1$ subbands ($q=5$ if $p=2$) for $N=3p$ and $N=3p+1$ armchair ribbons. For metallic ribbons ($N=3p+2$) assigned to $q_1=2p+2$ subband ($q=6$ if $p=2$) [425], the LUMO and HOMO are delocalized (extended) states (see $N=8$ in Figure 86), i.e. they are distributed over the whole graphene surface. The electron density distribution of the HOMO and LUMO orbitals for a one-dimensional armchair nanoribbon is also different when the system is metallic ($N=3p+2$) or semiconducting ($N=3p+1$ or $N=3p$) [428].

Clearly, the metallic or semiconductor states of graphene result from the ordering of the electronic bands near the Fermi level. For the semiconductor behavior, the HOMO and LUMO are formed by localized states belonging to the subband of $q_1=2p+1$ ($q=5$ if $p=2$), while the delocalized states belonging to subband of $q_1=2p+2$ are shifted deeper into the conduction and valence bands, thereby becoming HOMO-2 and LUMO+2 if $N = 3p$ and HOMO-1 and LUMO+1 if $N = 3p + 1$. Opposite behavior is observed for the metallic ribbon, where the HOMO and LUMO are composed of the delocalized states $q_1 = 2p + 2$, which replaces the localized states by shifting them deeper into the conduction and valence bands. For the metallic behavior, the crossing of the bands near the Fermi level is similar to that of the bulk graphene, where the conduction and valence bands meet at the K points in the Brillouin zone. However, for armchair nanoribbons, the strong confinement effect increases the band gap for the semiconducting states ($N = 3p$, $N = 3p + 1$) and opens a gap for the metallic state ($N = 3p + 2$). It should be mentioned that there is another point of view for the increase of the gap with the reduction of the width of the armchair nanoribbons. In [401] it was shown that the bond deformation which is dominant at the edges is responsible for the appearance of a gap in metallic nanoribbons ($N = 3p + 2$) and its enhancement for nanoribbons in semiconductor states ($N = 3p$, $N = 3p + 1$). In a recent work [436], Rozhkov *et al.* noted that for the metallic state the gap can be closed in nanoribbons of finite size through substitution of the radicals passivating the armchair edges.

The influence of edge passivation on the gap has already been briefly discussed (Figure 84) for armchair ribbons. There are different ways of passivating the carbon atoms at the edges. The passivation by single hydrogen gives $sp^2$ hybridization at the edges, while passivation by two hydrogens leads to $sp^3$ hybridization. The variation of the percentage of the $sp^3$-like bonds has been found to significantly change the electronic properties of the armchair nanoribbon [428]. An increase in the proportion of $sp^3$-like bonds leads to an interplay between the metallic and semiconductor states. Thus the metallic state of the armchair ribbon of width $N = 8$ becomes a semiconductor state for $sp^3$ proportion larger than 20%. The semiconductor state $N = 9$ is found to be metallic if $sp^3$ percentage is $\sim$35%, while the semiconductor state $N = 10$ is switched to the metallic state when the proportion of $sp^3$-like bonds is $> 60\%$. The transition occurs as a result of band reorganization, i.e. the shift of the subbands relative to each other along the energy scale. The electronic properties of armchair nanoribbons are also found to affect the formation energy of the armchair edges [403], a conclusion based on common oscillatory behavior of the formation energy and band gap versus the width, $N$, of armchair ribbons.

Zigzag nanoribbons have been found to possess a direct band gap which also is suppressed with increasing structure size [419,424]. However, the nature of the gap is different from that of armchair nanoribbons (for details, see Section 7.4). The HOMO and LUMO orbitals of the zigzag nanoribbon are formed by the edge states localized at the zigzag edges. The ground state of the zigzag nanoribbon is the FM-A state, characterized by ferromagnetic ordering of the spins of the localized states along each zigzag edge but their antiparallel orientation between the edges. The FM-A state has broken sublattice symmetry, which coupled with the destructive interference between the spin-up and spin-down tails of the localized states at the opposite zigzag edges leads to opening of a gap $\Delta_z^0$ [414]. This gap decreases with increasing width $w_z$ of zigzag ribbons (Figure 87) [414,419,424] due to the vanishing of the confinement effect. The $\Delta_z^1$ band of the edge states close to the zone boundary is found to be highly confined, have dominant edge-state character and is insensitive to the width $w_z$. Therefore, the energy gap $\Delta_z^1$ at the Brillouin zone is virtually independent of the width when $w_z > 12\,\text{Å}$ [419,424].

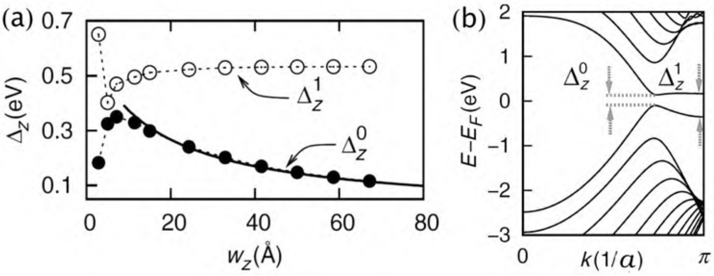

Figure 87. The dependence of the size of the direct band gap $\Delta_z^0$ and energy splitting $\Delta_z^1$ at $ka = \pi$ ($a$ is the unit cell size) on the width $w_z$ of the zigzag nanoribbon (Reprinted figure with permission from Y.-W. Son *et al.*, Physical Review Letters, 97, 216803, 2006 [419]. Copyright © (2006) by the American Chemical Society.).

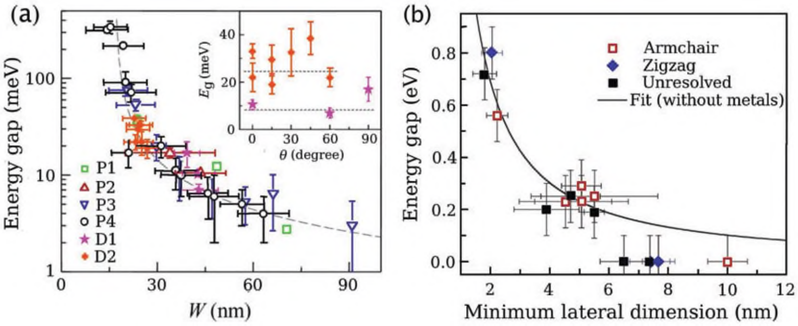

Figure 88. (a) The band gap size ($E_g$) as a function of nanoribbon width for six devices: four (P1–P4) of the parallel type, which contain many parallel ribbons of varying width, and two (D1,D2) devices having ribbons of uniform width and varying orientations described through the relative angle $\theta$ (Reprinted figure with permission from M.Y. Han *et al.*, Physical Review Letters, 98, 206805, 2007 [437]. Copyright © (2007) by the American Physical Society.). (b) The band gap variation ($E_g$) as function of QDs size for the zigzag and armchair systems (Reprinted figure with permission from K.A. Ritter *et al.*, Nature Materials, 8, p. 235, 2009 [441]. Copyright © (2009) Nature Publishing Group.).

Opening of a band gap in graphene induced by the confinement effect has been confirmed experimentally [29,437–440]. The experiment [437] was carried out for graphene nanoribbons fabricated from single sheets of graphene and contacted with the Cr/Au metal electrodes. Two types of devices were designed: one contained many parallel ribbons of varying width (P1–P4) while the second of uniform width and varying orientation described by an angle $\theta$ (D1–D2). The size of the band gap of these devices was found to decrease with increasing nanoribbon width (Figure 88(a)). The band gap was estimated through the dependence of the differential conductance on the gate and bias voltage in the nonlinear response regime. The band gap size was estimated from increasing conductance near the Dirac point with increasing nanoribbon width. Fitting the data gives the dependence of the conductance $G$ on the width $w$ as $G = \sigma(w - w_0)/L$, where $\sigma$ is the sheet conductivity, $(w - w_0)$ is the active width and $L = 2\,\mu\text{m}$ is the uniform length. A fit of the experimental data shows the following dependence of the band gap size on the nanoribbon width: $E_g = \alpha/(w - w^*)$, where $\alpha = 0.2\,\mathrm{eV}\cdot\mathrm{nm}$ and $w^* = 16\,\mathrm{nm}$. The conductance of the nanoribbon is found to be suppressed not only by reduction of the nanoribbon width, but also with a decrease in the temperature $T$. Similar measurements of the size of the band gap in graphene dots was reported in [441] by using scanning tunnelling spectroscopy. The graphene dots were labelled as armchair or zigzag systems by the highest fraction of the edge type presented. The data are shown in Figure 88(b). The confinement effect was found to be present in all the samples, but the zigzag systems were transformed into the metallic state at a smaller lateral dimension than that of the armchair systems. Therefore, the observed results have confirmed the influence of the crystallographic orientation of the edges in nanoscale graphene on its electronic properties and shown the metallic-like behavior of the zigzag nanoribbons.

In summary, for armchair nanoribbons a gap is found to open due to the crucial role of the edge effects which rearrange the subbands in the conduction and valence bands with varying size of nanoribbons. For zigzag nanoribbons, the broken sublattice symmetry resulting from antiferromagnetic spin ordering of the localized states at the zigzag edges also opens a gap. In addition, for both types of graphene nanoribbons, the quantum confinement is found to increase the gap, but an increase of the size of nanoribbons leads to vanishing of the gap.

## 7.6. *Graphene nanoribbons in an electric field*

Graphene is a unique material, where the spin distribution at the zigzag edges creates several metastable states energetically close to each other. The antiferromagnetic state of zigzag nanoribbons for which spins align along the zigzag edges but have opposite orientations between the two opposite zigzag edges, is energetically favorable in comparison to the nonmagnetic state or the ferromagnetic state with the same spin orientation between the zigzag edges [412,414]. Opposite zigzag edges belong to different sublattices, and therefore, in the antiferromagnetic state the spin-up state ($\alpha$-spin state) is completely localized on the A sublattice, while the spin-down state ($\beta$-spin state) is localized on the B sublattice. Moreover, because of the strong localization of the electron density at the zigzag edges, the $\alpha$-and $\beta$-spin states localized on the opposite zigzag edges are spatially separated. An electric field $E_{\mathrm{ext}}$ applied along the armchair edges shifts the energy of the states localized on one zigzag edge downwards and the opposite edge upward, thereby modifying the band gap for different spin states. Therefore, the applied electric field shifts the bands in such a way that if the occupied and unoccupied bands for one spin state move closer in energy, the bands for another spin state will move apart [442]. Modification of the band gap in an applied transverse electric field is presented in Figure 89. For zero electric field (see the left panel in Figure 89), the $\alpha$-and $\beta$-spin states are degenerate in all bands, so the spin degeneracy is not lifted. The applied electric field strongly lifts the bands corresponding to states localized on the opposite zigzag edges apart, thereby increasing the band gap for the $\alpha$-spin state and decreasing for the $\beta$-spin state. Therefore, for a certain electric field that is large enough to close the gap of the $\beta$-spin state, a half-metallic behavior is achieved. The critical electric field required to close the gap for the $\beta$-spin state decreases as the nanoribbon width increases, as the

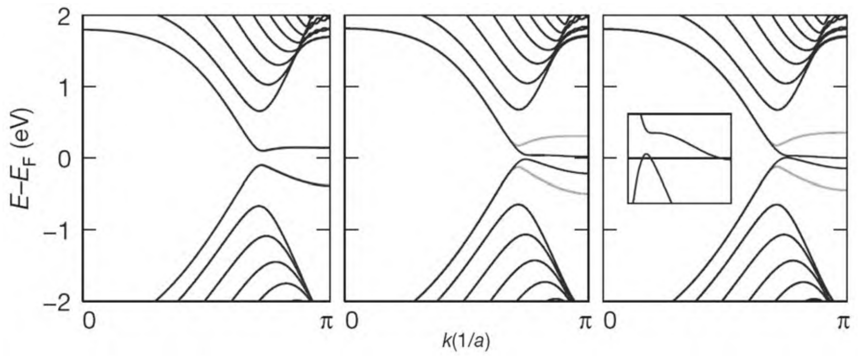

Figure 89. The influence of the transverse electric field on the band structure of zigzag graphene nanoribbons. Left panel: no electric field ($E_{\text{ext}} = 0\,\text{V/Å}$), middle panel: $E_{\text{ext}} = 0.05\,\text{V/Å}$ and the right panel: $E_{\text{ext}} = 0.1\,\text{V/Å}$. The gray color denotes the $\alpha$-spin state, while the black one – $\beta$-spin state. Inset: band structure in the range of $E - E_F < 50\,\text{meV}$ and $0.7\pi \leq ka \leq \pi$, where the horizontal line is $E_F$ (Reprinted figure with permission from Y.-W. Son *et al.*, Nature, 444, p. 347, 2006 [442]. Copyright © with permission from Nature Publishing Group.).

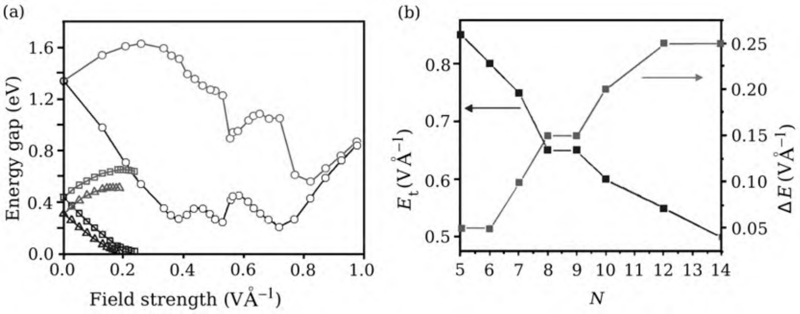

Figure 90. (a) Band gaps for the $\alpha$- spin state (grey line) and the $\beta$-spin state (black line) as a function of the electric field calculated within the DFT methods using three different exchange-correlation functionals: LDA (triangles), BLYP (squares) and B3LYP (circles) (Reprinted figure with permission from E. Rudberg *et al.*, Nano Letters, 7, 2211, 2007 [446]. Copyright © (2007) by the American Chemical Society.). (b) The critical electric field $E_t$ required to obtain the half-metallicity and the range of the electric field strength (from $E_t$ to $E_t + \delta E$) to preserve the half-metallicity as a function of the nanoribbon size ($n$ is the number of the carbon cells along the zigzag edge). The simulation is performed with the B3LYP functional (Reprinted with permission from E.-J. Kan *et al.*, Applied Physics Letters, 91, 243116, 2007 [447]. Copyright © (2007) American Institute of Physics.).

potential difference between two opposite zigzag edges is proportional to the distance between the zigzag edges. For nanoribbons with oxidized zigzag edges, the critical electric field varies with the choice of oxidation scheme [443]. Moreover, the oxidation stabilizes the state with antiferromagnetically ordered spins between the zigzag edges. The possibility to control the gap through breaking of the inversion symmetry by the potential from an external superlattice (e.g. by applying a gate voltage) was also discussed in [444,445]. The band gap size is found to be affected by the strength of the external potential and the lattice constant of the superlattice [444].

Interestingly, the size of the gap estimated by the DFT methods was found to depend on the choice of the exchange-correlation functional [446]. For the B3LYP functional the absence of the half-metallic regime in zigzag graphene nanoribbons was reported even at high electric fields. Results show the closing of the band gap for the $\alpha$- and $\beta$-spin states, as the transverse electric field is applied are presented in Figure 90(a) for three different exchange-correlation functionals: B3LYP, LDA and BLYP. The data obtained within the hybrid B3LYP functional suggest that the condition when the band gap for the $\beta$-spin state vanishes cannot be reached. First of all, at zero electric field the band gaps for the $\alpha$- and $\beta$-spin states are much larger than that obtained within the LDA and BLYP functionals, thereby raising the value of the critical electric field required to close the gap for the $\beta$-spin state. Moreover, at a high electric field (0.8 V/Å) the band gap of the $\beta$-spin state, which is not suppressed to zero, starts to grow again. The band gap for the $\alpha$-spin state also behaves differently at high electric fields than that obtained with the LDA and BLYP functionals. Hence, at a field of 0.3 V/Å, the band gap starts to decrease and for fields higher than 0.8 V/Å, the gap for both spin states has the same size. A study of the influence of the applied electric field on the spin-density distribution has shown that in the middle of the ribbon the spin-density is reduced significantly by the field in comparison to that at the edges.

However, several other theoretical works reported that the non-local exchange correlation should not remove the half-metallicity in zigzag graphene nanoribbons [447,448]. Using a hybrid B3LYP functional, Kan *et al.* [447], found a spin gap asymmetry caused by the applied electric field, where the $\beta$-spin state is gapless. The magnitude of the critical electric field required to transfer the system into a half-metallic state was however larger (about 0.7 V Å$^{-1}$) than that obtained in [442] within the local-density functional approximation (LDA), which is known to underestimate the size of the band gap. The magnitude of the critical electric field $E_t$ decreases with increasing nanoribbon size (Figure 90b). However, in a strong electric field the half-metallicity is found to be destroyed due to the transition to a spin-unpolarized state. Similar results suggesting that at high electric field the system is spin-unpolarized were also reported in [443]. The non-local exchange correlation term (B3LYP functional) was also shown to have negligible impact on the size of the band gap in an electric field [411], but the critical electric field required to achieve half-metallicity was of similar magnitude for different exchange-correlation functionals (about 0.2 V Å$^{-1}$).

Simulations of the zigzag nanoribbon in an electric field reported in [449] with the $\pi$-orbital Hubbard model SCF theory, however, revealed that the gate-induced charge carriers alter the charge distribution, spin configuration and total net spin polarization. For graphene in its antiferromagnetic state, when the localized states of opposite spin are located on the opposite zigzag edges, the gate-induced charge carriers break the charge distribution symmetry around the ribbon center. This leads to coupling of the charge density and spin polarization. Therefore, if the non-colinear regime is allowed within the Hubbard model, the non-colinear spin solution becomes energetically favorable, where spins localized on opposite edges are no longer antiparallel.

For the armchair nanoribbons, the influence of the geometry of nanoribbons on the suppression of the band gap by an electric field and the transition from semiconductor to metallic behavior were investigated within the Peierls approximation [451]. It was found that the magnitude of the critical electric field required to close the band gap for the $\beta$-spin state can fluctuate in the range of 0.06–0.2 V Å$^{-1}$ depending on the geometry of the nanoribbon. In another investigation [452], the transverse electric field applied across armchair nanoribbons was found to dramatically change the electron bands and affect the longitudinal electronic dispersion. Thus the Fermi velocity in metallic nanoribbons is found to be reduced by the field and this leads to an increase in the density of states at the band center. Moreover, the Fermi velocity and the effective mass were found to change sign in an electric field, while the band gap was suppressed by the external field resulting in extra plateaus in the conductance characteristics. The influence of the electric field and the size of graphene on the band gap and the effective mass was also considered in [427]. The magnitude of the effective mass grows with decreasing ribbon width, whereas the sign of the effective mass is reversed in the electric field, similar to the data in [452].

In summary, the external electric field applied to zigzag graphene nanoribbons opens the possibility to induce half-metallicity in the ribbons which has enormous potentials for application in spin-related electronic devices [48,450,453–464].

### 7.7. *Nanoscale graphene*

The band gap of nanoscale graphene with edges of arbitrary shape is found to vary as a function of the edge size and shape [361,420,433,435,465–469]. For graphene nanodots, the band gap deviation induced by the increasing width of the armchair edges was observed [423,466], and was similar to that of graphene nanoribbons. The amplitude of the energy gap oscillation with the length of the edges has been found to be smaller than that for the infinite size ribbons [423,466], while the periodicity of the oscillation was larger, i.e. the number of points between the maxima and minima was near 3, instead of 1 for the nanoribbon. For nanoscale graphene of rectangular shape, the deviation of the band gap with changing width was found to depend on the chirality angle $\phi$ [420,431]. The maximum amplitude of the deviation was achieved for $\phi = 0°$, and this amplitude decreases with increasing $\phi$ [420]. For $\phi = 23.4°$ the band gap is almost zero and independent of the nanoribbon width.

For nanoscale graphene flakes of arbitrary shape, the edges are still characterized by the stronger magnetic moment than the inner sites [470]. However, the applied magnetic field changes the localization of spin density at the edges [361]. In a magnetic field the electron density localized at the edges for the HOMO and LUMO orbitals is shifted closer to the center of graphene dot. Hence for the graphene dot, just as for the nanoribbon, the spin orientation of the localized states at the zigzag edges are associated with the sublattice site. If the zigzag edges belong to two different sublattices then, according to Lieb's theorem [471], the spin-polarized states at different edges exhibit opposite spin orientation [466,469,470,472]. For graphene flakes with mixed edges, it is enough for the defect-free segment of the zigzag edge to be greater than three or four repeat units to have a significant amount of magnetization [470]. The average edge magnetization along all the edges grows with decreasing proportion of the armchair edges and increasing proportion of zigzag edges [470]. Therefore, an obvious way to increase the magnetization of graphene

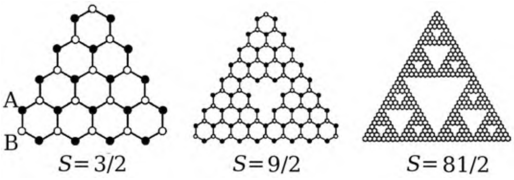

Figure 91. The structures of the nanoscale graphene characterized by the non-zero total spin $S$. The closed and open circles denote the A and B sublattices, respectively (Reprinted with permission from O.V. Yazyev *et al.*, Nano Letters, 8, 766, 2008 [472]. Copyright © (2008) by the American Chemical Society.).

would be to design it with high density of zigzag edges [472–474]. The same rule would apply for structures with mixed edges: the spin-polarized states localized on the border carbon atoms at the zigzag edges will exhibit opposite spin orientation if the carbon atoms belong to different sublattices. Therefore, if graphene has the same amount of zigzag edges in A and B sublattices, the net spin density is zero. Non-zero spin density of nanoscale graphene with high density of zigzag edges can be achieved by increasing the number of zigzag edges belonging to one sublattice (Figure 91) [472]. For triangular structures, sublattice A dominates at the edges over the whole structure resulting in non-zero net spin. Such structures with high spin states can open a new avenue in nanoscale spintronics.

The possibility to create multiple quantum well structures using repeated junctions of armchair graphene nanoribbons was considered in [433,468]. By altering the width and shape of the quantum well, it was shown that the fixed spin state can be confined in the well, and this is a promising direction for engineering the spintronics devices. The transmission coefficient though such devices shows resonant peaks which can be assigned to electronic states localized in the quantum well. Accurate understanding of the dependence of the electronic and magnetic properties of nanoscale graphene on its edge shape is crucial for developing electronic devices based on this system [475–482].

### 7.8. *Bilayer graphene nanoribbons and the effects of edges*

The effects of the arrangements of atoms at the edges of finite-sized graphene flakes are well known in the case of the monolayer [391]. Tight-binding models predict significantly different band gaps depending on the number of atoms across the width of the ribbon (modulo 3), and the magnetic properties of zigzag and armchair edges are also significantly different. This complexity carries over to the bilayer case, and while there is currently no clear picture of the properties of bilayer ribbons and their edges, we shall present the current state of knowledge of this topic.

Recently, it was reported [483] that chemical methods could manufacture graphene nanoribbons with widths ranging from 50 nm to $<10$ nm with possibly well-defined zigzag or armchair edges. Exfoliated graphene was placed in solution, deposited on a substrate, and fashioned into field effect transistors. Figure 1 in [483] shows several nanoribbons which the authors claim are two layers thick – i.e. they are bilayer nanoribbons. Figure 92 shows the current–voltage characteristics for two nanoribbons, and the authors claim that all their ribbons with width $w < 10$ nm

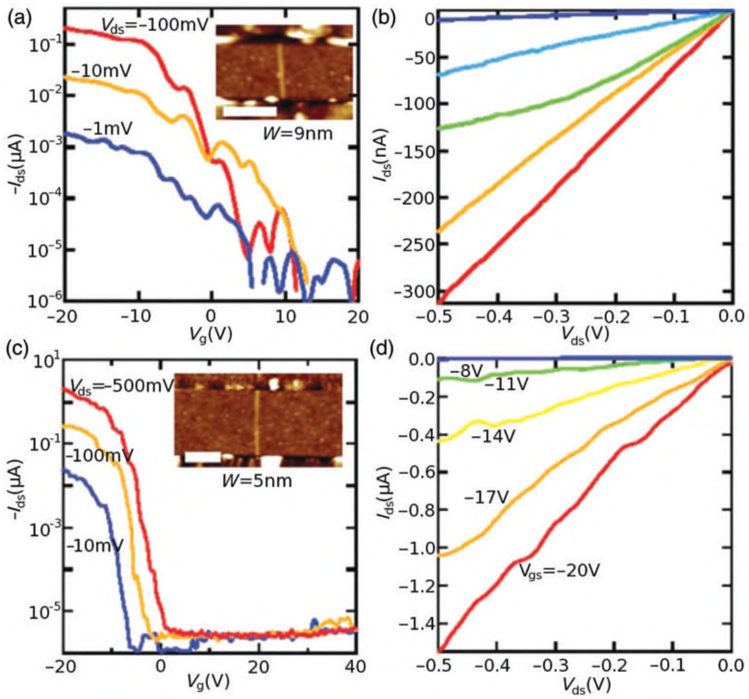

Figure 92. Room-temperature graphene nanoribbon FETs with high on–off ratios. (a) Transfer characteristics (current versus gate voltage) for a $w \approx 9$ nm (thickness ~1.5 nm, ~two layers) and channel length $L \sim 130$ nm GNR with Pd contacts and Si backgate. (Inset) AFM image of this device. Scale bar is 100 nm. (b) Current–voltage curves recorded under various gate voltages for the device in (a). (c) Transfer characteristics for a $w \approx 5$ nm (thickness ~1.5 nm, ~two layers) and channel length $L \sim 210$ nm GNR with Pd contacts. (Inset) The AFM image of this device. Scale bar is 100 nm. (d) Current–voltage characteristics recorded under various gate voltages for the device in (c) (Reprinted figure with permission from X. Li *et al*., Science, 319, p. 1229, 2008 [483]. Copyright © (2008) The American Association for the Advancement of Science.).

had an on-off ratio of better than $10^5$. The band gaps extracted from these transport data fitted the empirical form of $E_g(\text{eV}) = \frac{0.8}{W(\text{nm})}$. However, these band gaps fall between the theoretically predicted values for ribbons with zigzag and armchair edges, and the precise structure of the edges of the flakes is not known.

From a theoretical point of view, the alignment of atoms at the edges of the ribbon are a key factor in the determination of the ribbon's electrical and magnetic properties. As well as the zigzag and armchair terminations (which carry over their definition from the monolayer), there are two alignments of atoms in the layers which must be considered. They are shown in Figure 93 where the commonly-used nomenclature of $\alpha$ and $\beta$ alignments has been adopted. The distinguishing feature of the two alignments is where the dimer bonds are positioned relative to the edge. In the $\beta$ alignment they constitute one part of the last row of atoms, while in the $\alpha$ alignment they do not. Both tight-binding and DFT methods have been used to address the electronic and magnetic properties of finite-sized bilayer graphene. There are some difficulties in the approach of DFT methods, since traditional formulations

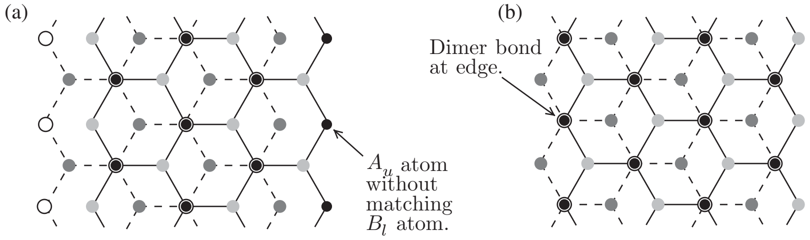

Figure 93. The two orientations of the bilayer ribbon: The $\alpha$ alignment (left), the $\beta$ alignment (right). The essential difference is that the $\beta$ alignment has dimer bonds at the edge, while the $\alpha$ alignment does not.

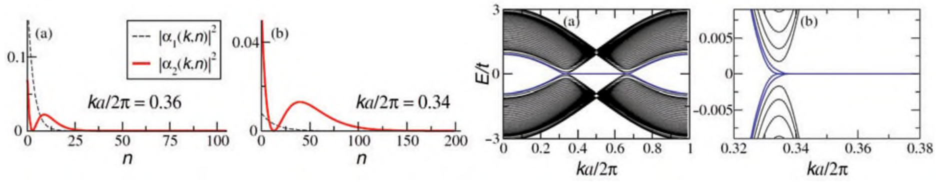

Figure 94. (a) Charge density for bilayer edge states at $ka/2\pi = 0.36$ and (b) $ka/2\pi = 0.34$. (c) Energy spectrum for a bilayer ribbon with zigzag edges: $N = 400$, $\gamma_1 = 0.2\gamma$. (d) Zoom of (c) (Reprinted figure with permission from E.V. Castro *et al.*, Physical Review Letters, 100, 026802, 2008 [486]. Copyright © (2008) by the American Physical Society.).

do not account well for the van der Waals interactions between the layers. Lima [484] accounted for this by adding a nonlocal potential in the Kohn–Sham equations, but otherwise there is some doubt over the accuracy of DFT calculations. For example, Sahu *et al.* [485] find that LDA and GGA make different predictions on the magnetic properties of the lowest energy state in zigzag ribbons in the $\alpha$ alignment.

We shall present a summary of the effects of the finite system size on the band structure, and the possible modes of magnetic ordering at the edges. Most work has so far been done on the $\beta$-aligned zigzag edged system. Castro [486] has shown the existence of two classes of edge state within the tight-binding model: those that are localized in one layer only, and those that have wave function amplitude on both layers. In a semi-infinite system, the edge states exist in the momentum range $2\pi/3 < ka < 4\pi/3$, as in the monolayer case. Figure 94(a) and (b) show two examples of charge density for the edge of a semi-infinite bilayer, i.e. those derived by solving the Schrödinger equation with zero eigenvalue. The penetration depth is of the order of a few tens of lattice sites, $\lambda = -1/\ln|-2\cos(ka/2)|$. The energy spectrum of the nanoribbon is shown in Figure 94(c) and (d) for a ribbon of width $N = 400$, and $\gamma_1 = 0.2t$. The four-fold degeneracy of the edge states (one per class per edge) is clear from (d), and the overall sinusoidal dependence of the energy bands is evident in (c). The lifting of the degeneracy is due to the overlap of the wave functions from the two edges, which occurs where the penetration depth is highest, i.e. at $ka = \pm 2\pi/3$. When an inter layer bias is applied, the degeneracy of the flat bands is lifted. The two 'monolayer' edge states retain their flat dispersion, but split into the conduction and valence bands. The two 'bilayer' edge states gain a dispersion, and cross at $\epsilon = 0$ near the Dirac points. This crossing is justified by treating the inter

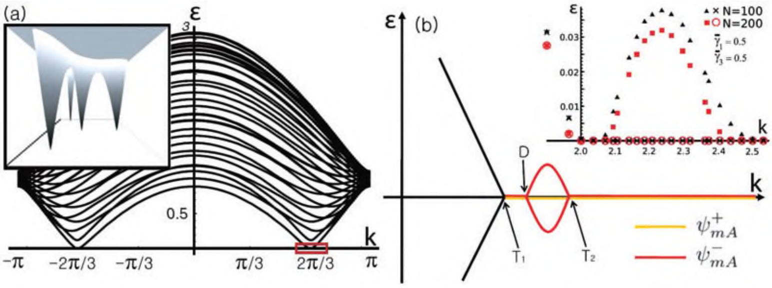

Figure 95. (Colour online) (a) Projected band structure of the 2D graphite bilayer along the direction of the zigzag axis. The boxed region near the Dirac point is magnified in the inset, which shows the trigonal warping. $D$ is the Dirac point at $k = 2\pi/3$ and three $L$ points are the Fermi points of three nearby pockets. (b) A schematic diagram of the zero-energy edge states of a semi-infinite Z-BGNR near the Dirac point within the red box in (a). At $\varepsilon = 0$, the two eigenstates are drawn with different colors. Red (dark gray) for $\psi_-$ and yellow (pale gray) for $_+$. $D$ is the Dirac point while $T_1$, $T_2$ and the two warped bands reflect the effect of trigonal warping of the graphite bilayer. The inset shows the energy dispersion curve obtained by a numerical method for Z-BGNRs with finite widths $N = 100$, 200 (Reprinted figure with permission from J.-W. Rhim *et al.*, Journal of Physics: Condensed Matter, 20, p. 365202, 2008 [487]. Copyright © (2008) IOP Publishing Ltd.).

layer potential as a perturbation to the tight-binding model. Yao *et al.* [445] find the same picture, but emphasize that the dispersive edge states have valley-dependent velocity near the Dirac points, and that the behavior of edge states is determined by the valley-dependent topological charges in the bulk.

Rhim *et al.* [487] introduced the trigonal warping to the analysis of $\beta$-aligned zigzag bilayers (Figure 95). The effect of the Lifshitz transition, and the complex structure of the Fermi surface at low-energy was taken into account, and it was found that the nature of the edge states reflects this complexity. In particular, a forbidden region is introduced for one of the edge states (between $D$ and $T_2$ in Figure 95(b)), a feature unique to zigzag bilayer nanoribbons. The locations of the position of the pockets in the Fermi surface agreed exactly with those calculated for the bulk system [139]. Inclusion of the other next-nearest neighbor inter-layer hopping parameter $\gamma_4$ lifted the electron–hole degeneracy and moves the Fermi points back toward the Dirac point. Also, within the half-filled Hubbard model with the Hartree–Fock approximation, and for realistic values of the Coulomb interaction, ferromagnetic alignment of inter-layer spins is preferred along each edge.

Lima *et al.* [484] reported on the electronic, magnetic and structural properties of both $\alpha$- and $\beta$-aligned ribbons within the DFT framework. They assumed hydrogen passivation, and established that the alignment of the edges is a significant factor for the band structure (see Figure 96(a) and (b)). In the $\beta$ alignment, the state with antiferromagnetic order both along and between the edges was the lowest energy state, although by an amount less than $k_B T$. The $\alpha$-aligned ground state was qualitatively different because there is a strong attractive interaction between the edge atoms of the two layers which produced a geometrical distortion of the lattice. This allowed a gapped, non-magnetic ground state to form, in contrast to other analysis. In fact, the $\alpha$-alignment yielded a lower overall ground state energy than the $\beta$-alignment. The inter-edge interaction can be split into a part which depends

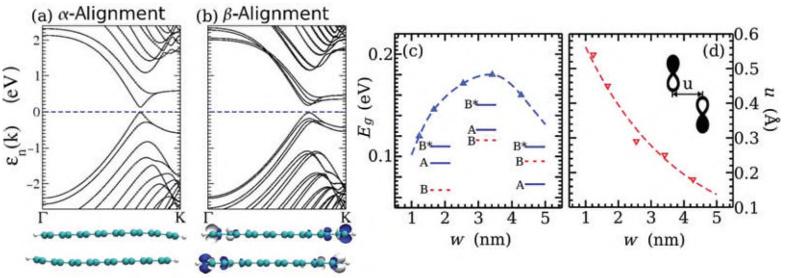

Figure 96. (a) Ground state of fully relaxed bilayer ZGNRs generated by stacking two (7,0) monolayer ZGNRs. Below each band structure the geometry and local magnetization are presented. (i) α-alignment. This state is nonmagnetic and presents a geometric distortion near the edge. (ii) β-alignment. This state shows an antiferromagnetic in-layer and antiferromagnetic inter-layer magnetic order. (b) Dependencies of the (i) energy gap and (ii) the lateral deviation $u = d_{CC} - d$ of the width $w$ (Reprinted figure with permission from M.P. Lima *et al.*, Physical Review B, 79, 153401, 2009 [484]. Copyright © (2009) by the American Physical Society.).

on the ribbon width (and is therefore due to the edge), and a part which is constant (and therefore due to the bulk). Binding energies per unit length fit $E_b(w) = a + bw$, with $b = -2.0$ eV per atom for both alignments. However, $a = -0.26$ eV nm$^{-1}$ for the $\alpha$ alignment, and $a = +0.13$ eV nm$^{-1}$ for the $\beta$-alignment, explaining the overall energy reduction in the former case. The gap which opened in the $\alpha$-aligned case was dependent on the ribbon width, as shown in Figure 96(c). The reason for the peak is the reordering of the electron localization between different sublattices. For narrow ribbons, the top of the valence band is located on the $A$ sublattice, whereas for larger ribbons it is on the $B$ sublattice, as with the Fermi level orbitals in the infinite system.

Sahu *et al.* [485] considered all four types of bilayer ribbon, and showed that the band gaps in armchair ribbons are rather smaller than those in zigzag ribbons using both a tight-binding theory and DFT. They linked the occurrence of edge magnetism to the existence of flat bands, and derived a critical band gap above which applying an interlayer bias will increase the gap, and below which will decrease it. They commented on the sensitivity of the band gap and magnetic ordering to the details of the exchange-correlation potential taken in their DFT.

Finally Lam *et al.* [488] showed DFT calculations of the band structure of $\alpha$-aligned armchair ribbons as a function of the ribbon width, interlayer spacing, and concentration of dopants along the ribbon edges (Figure 97). They found that the optimal interlayer distance is slightly smaller for bilayer ribbons that for the bulk bilayer system. As in the monolayer case, they find a dependence of the band gap on the ribbon width which is periodic in the number of atoms, as shown in Figure 97(a), although the gaps in the bilayer ribbons are systematically smaller than those in the monolayer ribbons. When the optimum interlayer distance is taken, ribbons with $N = 3p+2$ (where $p$ is an integer) are found to have metallic behavior, whereas the cases $N = 3p$ and $N = 3p + 1$ are semiconducting. The authors suggest that this metallic behavior and the consistently smaller gaps are due to the electron–electron interactions between layers at the edges which diminishes the edge effects and helps to restore the bulk (metallic) behavior. If the edges are doped (either with $n$-type or $p$-type dopants, e.g. nitrogen or boron, respectively), the Fermi level is shifted as

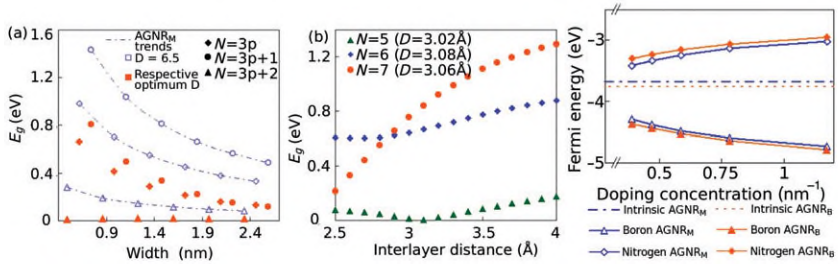

Figure 97. (Colour online) (a) Energy gap as a function of the width of the bilayer AGNR for interlayer distance 0.65nm (hollow points) and the respective optimum inter layer distance $D$ (solid points). Diamond, circle and square points represent the three different families of $N=3p$, $3p+1$, $3p+2$, respectively. Unlike the monolayer ribbons, the family of $N=3p+2$ shows almost zero band gap for any width. The dot-dash lines show the three trends in the monolayer AGNR which coincide with the bilayer trends when the interlayer spacing is large. (b) Dependence of the band gap on $D$ for the bilayer for $N=5,6,7$. The electronic structure depends strongly on its interlayer distance. (c) Fermi level vis-a-vis different boron (triangle) and nitrogen (diamond) doping concentrations for monolayer (blue) and bilayer (red) 7-AGNRs. The dot-dash and dotted lines are the original Fermi level of the undoped mono- and bilayer ribbons, respectively. As doping concentration increases, the band gap of all four cases also decreases (Reprinted with permission from K.-T. Lam *et al*., Applied Physics Letters, 92, 223106, 2008 [488]. Copyright © (2008) American Institute of Physics.).

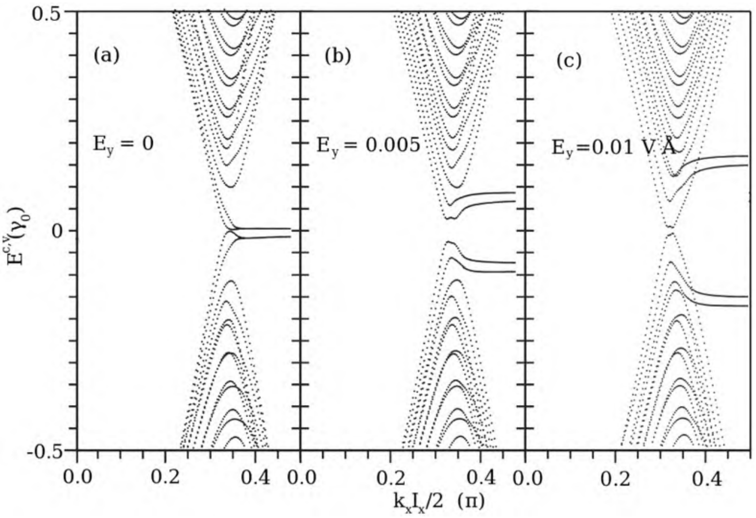

Figure 98. The low-energy electronic structure of $AB$-stacked zigzag GNRs with 40 dimer lines in the $y$ direction, and infinite extent in the $x$ direction. (a) Zero parallel field; (b) parallel field $E_y=0.005$ V Å$^{-1}$; (c) $E_y=0.01$ V Å$^{-1}$ (Reprinted with permission from Y.C. Huang *et al*., Journal of Applied Physics, 104, 103714, 2008 [489]. Copyright © (2008) American Institute of Physics.).

shown in Figure 97(c). The effect of dopants is marginally smaller on the bilayer ribbons than on the equivalent monolayers.

Huang *et al*. [489] showed using exact diagonalization of an explicit tight binding model, that the application of an electric field across the width of the nanoribbon (i.e. parallel to the plane of the ribbon) will also cause a gap to open in the low-energy spectrum. In fact, this field can also cause subband crossings and anticrossings, alter band features and lift the degeneracy of the flat bands, as shown in Figure 98. The application of successively stronger fields moves the flat bands away from the charge-neutrality point, lifts the degeneracy in both the conduction and valence bands, and distorts their shape so that they are no longer flat. The size of the band gap in zigzag nanoribbons is non-monotonic in the strength of the parallel field, $E_y$, since the effect of application of stronger field is two-fold: it moves the partially flat bands away from each other, but the lowest higher energy (nearly parabolic) bands come down in energy. The two types of band cross at approximated $E_y = 0.006\,\mathrm{V\,Å^{-1}}$, and the largest gap is $E_g \approx 0.08\gamma_0 \approx 0.24\,\mathrm{eV}$. The gaps are smaller in armchair ribbons, and there are some values of $E_y$ for which the gap closes completely. The authors also discussed the density of states for zigzag and armchair ribbons.

The properties of bilayer ribbons placed in magnetic fields were investigated by Nemec *et al.* [191], who computed the Hofstadtter butterflies for this material, and Huang *et al.* [197], who not only examined the LLs and magneto-optical absorption of wide bilayer nanoribbons and found many of the same features as exhibited in the bulk system, but also included the second-order interlayer couplings. The existence of bilayer-type edge states in few-layer graphene stacks has also been discussed [490].

## 8. Manipulation of the band gap and magnetic properties of graphene

Despite all the fascinating properties of graphene, such as relativistic massless dispersion and high mobility, the gapless band structure makes its difficult to find a direct application for graphene in field-effect transistors. However, an easy way to avoid a gapless band structure is to decrease its size to the nanoscale, so that the confinement effect induces a gap. The size of the gap is found to fluctuate depending on the geometry of the edge of graphene, which makes it somewhat difficult to manufacture graphene structures with the desired electronic properties because of limitations imposed by current fabrication techniques. However, the problem of the formation of sharp graphene edges with ideal atomic structures [491] has been resolved by unzipping carbon nanotubes to graphene nanoribbons of controllable size [492,493]. This is a significant breakthrough in the fabrication of graphene. These techniques should enhance the interest in manipulation of the electronic properties of graphene nanoribbons by external sources, such as edge modification, adsorption of dopants and introduction of defects into the graphene lattice.

The gapless low-energy band structure is protected by the symmetry of the hexagonal lattice, so any local changes in the lattice or an imbalance of electrons of different spins can break the group or sublattice symmetries and induce a gap. An example of how the hexagonal symmetry [433,434,494,495] can be broken could be done by an external strain applied to the graphene lattice. A symmetrical strain distribution will keep the hexagonal symmetry unchanged and band structure will remain gapless [494]. An asymmetrical strain breaks the translation symmetry of the lattice which opens a gap at the charge-neutrality point, that can be used to tune the size of the gap [434,494]. Such a strain, depending on its strength and direction is found to move the band crossing away from the *K* point [434]. This influence of uniaxial strain on the electronic properties of graphene has been observed experimentally [495,496]. A significant red shift of the 2D and G bands in the Raman spectra, which was attributed to the presence of a gap, has been obtained due to stretching in one direction of the substrate with graphene deposited on top. The *G* band splitting into two subbands as a result of symmetry breaking has indeed been observed [496]. Good reversibility and an upward shift of the Raman peaks when the strain is released was also indicated.

Practical application of the strain induced band gap would primarily be in developing strain sensors. The most useful route to manipulate the electronic properties of graphene would be inducing permanent changes in the graphene lattice, which can break the symmetry and open a gap. The breaking of sublattice symmetry, which can be done by unequal doping of graphene sublattices is one such possibility. Very intensive research is now being undertaken in this direction, such as interaction of the graphene layer with the substrate or adsorbates, the influence of defects and dislocations, doping and functionalizing of the graphene lattice or edges. All these possibilities are dealt with in the present section.

### 8.1. *Interaction of graphene with a substrate*

Experimental [35,140,497–501] and theoretical [383,502–510] studies of epitaxial graphene have shown that the charge exchange between graphene and the substrate directly influences the electronic properties of graphene. It is known that the interaction between two layers of graphene is weak, but for the first layer epitaxially grown on the substrate, the bonding to the substrate can induce structural changes in the graphene lattice. These changes may lead to the formation of a buffer layer, whose electronic properties are different from that of the isolated graphene sheets. This issue has opened a wide discussion in this subfield.

There are two main theoretical models proposed for the description of the interaction between the first graphene layer and the substrate. According to the first model, the graphene layer epitaxially grown on the Si-terminated (0001) or C-terminated $(000\bar{1})$ SiC substrates, forms strong covalent bonds with the substrate [502,503] (Figure 99). The strong bonding occurs because the binding energy between the layers is stronger than the elastic stress at the interfaces [503]. The two dangling

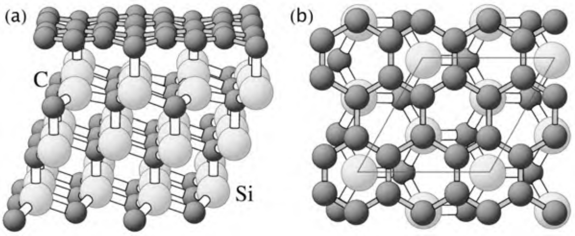

Figure 99. The buffer graphene layer on the SiC (0001) surface (Si-terminated) (a) side view and (b) top view (Reprinted figure with permission from A. Mattausch and O. Pankratov, Physical Review Letters, 99, 076802, 2007 [503]. Copyright © (2007) by the American Physical Society.).

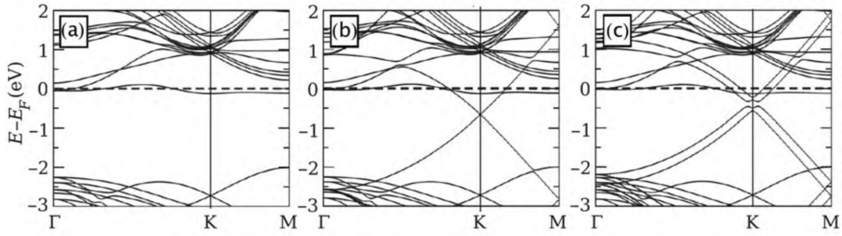

Figure 100. The band structure of epitaxial graphene on the SiC substrate with Si-terminated surface. (a) buffer layer of graphene on the surface, (b) single layer of graphene on the surface, (c) double layer of graphene on the surface (Reprinted figure with permission from F. Varchon *et al.*, Physical Review Letters, 99, 126805, 2007 [502]. Copyright © (2007) by the American Physical Society.).

states of the Si-terminated substrate form covalent bonds to the carbon atoms in graphene, while the third dangling bond is unsaturated, thereby generating half-filled metallic states close to the Fermi level. For the buffer layer on the C-terminated SiC substrate, there are two bands resulting from splitting of the interface state into single occupied and unoccupied states. The crossing of cone-shaped conduction and valence bands of the buffer layer is shifted deeper into the valence band for the Si-terminated case [502,503]. Therefore, the Fermi level of the first undeformed graphene layer on a Si-terminated substrate is located at 0.4 eV above the Dirac point [502], i.e. the graphene is *n*-doped, as was also reported in experimental work [504]. The new conduction band formed by the SiC substrate overlaps with the upper band of the buffer layer thereby making a wide energy gap, as presented in Figure 100(a). For the C-terminated substrate, the Fermi level location corresponds to the Dirac point and the first graphene layer remains undoped. The next layer for both types of substrates exhibits pure graphene properties because of the weak van der Waals interaction with the buffer layer. The electronic structure of this undeformed layer is similar to those for the isolated graphene sheets (Figure 100(b)). In particular, the dispersion of cone-shaped conduction and valence bands is restored. Systems containing two undeformed graphene layers, due to weak interaction between them, shows the properties of bilayer graphene (Figure 100(c)).

The second model assumes a different behavior of the buffer layer. According to the second model, the first graphene layer interacts weakly with the substrate. It was predicted that this model is appropriate for the C-terminated face of the SiC surface, which was experimentally seen to have weaker coupling between the graphene layer and SiC substrate [501] in comparison to the Si-terminated face. This C-terminated face of the SiC surface was later theoretically predicted to exclude formation of the buffer layer between graphene and the substrate [510]. Therefore, in the absence of a buffer layer, the first layer would possess a graphene-like band structure with the cone-shaped conduction and valence bands.

However, according to the experimental data obtained with angle-resolved photo-emission spectroscopy (ARPES), different results for the interaction of the epitaxially grown graphene with SiC substrate have been observed [35]. Formation of a buffer layer has been confirmed and its properties were found to be different from that of graphene, namely the $\sigma$ bands remain similar to that of graphene, while the $\pi$

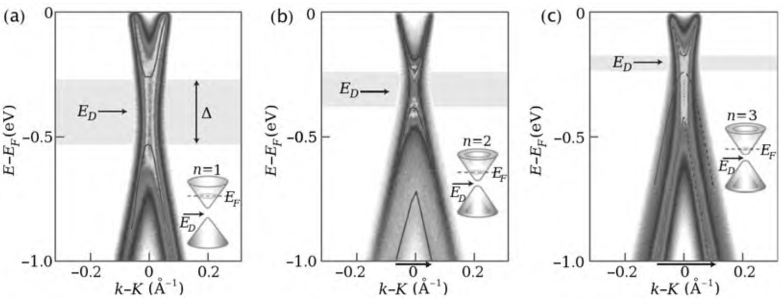

Figure 101. The intensity map obtained with ARPES for (a) single layer of graphene on a 6H-SiC substrate ($\Delta \sim 0.26$ eV), (b) double layer of graphene on a 4H-SiC substrate ($\Delta \sim 0.14$ eV), and (c) triple layer of graphene on a 6H-SiC substrate ($\Delta \sim 0.066$ eV). Here $E_D$ is the energy of the Dirac point (Reprinted figure with permission from S.Y. Zhou *et al.*, Nature Materials, 6, p. 770, 2007 [35]. Copyright © (2007) Nature Publishing Group.).

bands were modified due to hybridization with the dangling bonds from the substrate. The unchanged $\sigma$ bands indicate the presence of a honeycomb lattice in the buffer layer. The interaction of the buffer layer with the next layer was predicted to break the sublattice symmetry structurally and open a gap of $\Delta$ ~0.26 eV [35]. It was observed for the buffer layer that only three Dirac cone replicas out of six were intense and formed a small hexagon around each corner of the Brillouin zone, thereby implying that the six-fold rotational symmetry of graphene was broken by only three-fold. Breaking of the symmetry was seen only near the Dirac points ($E_D$), whereas near the Fermi level the symmetry was preserved. The first undeformed graphene layer was also found to be $n$-type doped and $E_D$ was shifted relative to $E_F$ by ~0.4 eV. Increasing the number of layers resulted in a decrease of the band gap. Experimental data for single, double and triple layers of graphene are presented in Figure 101. For bilayer and trilayer graphene, occurrence of the gap was attributed to the breaking of the sublattice symmetry as a result of AB stacking between the graphene layers. Increasing the number of layers causes a shift of $E_D$ towards $E_F$, so that the $E_D - E_F$ is ~0.3 eV for the double layer and ~0.2 eV for the triple layer. This shift has been attributed to the presence of an electric field formed by the accumulation of charges at the graphene surface, and its reduction with thickness was explained by an increase in distance between the surface layer and the interface. The size of the gap and shift of the Fermi level were found to be independent of the sample preparation and doping of the substrate. Epitaxial graphene thicker than five layers behaves like bulk graphite. Theoretical computations [509] have confirmed that for stacked graphene layers, if the A sublattice is stacked above the B sublattice, the band gap will decrease with increasing number of layers. However, it is expected that the appearance of AB stacking between the buffer and the first graphene layer would be dependent on the type of substrate. For example, according to the experimental data [498], growing graphene on the 4H-SiC sublattice does not provide AB stacked films. Instead, the two graphene sheets are rotated relative to each other, and this produces an electronic structure for multilayer graphene that is similar to an isolated graphene sheet.

There are other points of views relating to the cause of the opening of a band gap in graphene epitaxially grown on the SiC substrate [140,511]. The band gap observed in the experiment [140] was attributed to the breaking of graphene symmetry by the built-in dipole field induced between the depleted SiC substrate and the charge accumulated on the surface of the graphene layer. However in [511], the presence of the Stone–Wales defects in the graphene layer was proposed to be responsible for breaking of the symmetry. There, the gap is found to decrease with increasing graphene thickness, which is in good agreement with experiments [35]. The influence of the Fermi level position on the sample preparation and doping of the substrate also was discussed [499,505]. An independence of the Fermi level position on the doping of the substrate and the substrate type were indicated in experiments performed with Raman spectroscopy [499]. Moreover, it was observed that graphene on an SiC substrate shows a blue shift in the position of the G-peak, which has not been observed for graphene transferred to a $SiO_2$ substrate. However, in theoretical works [505] it was claimed that for graphene on the GaAs substrate, the graphene layer can be doped by doping the GaAs substrate.

The importance of the interaction of graphene with the substrate and its impact on the electronic properties was also considered for other types of substrates. Graphene supported on the $Si/SiO_2$ substrate [497] was found to be doped. As-prepared graphene on the $Si/SiO_2$ substrate has shown to be *p*-doped, but after the samples are exposed in vacuum for 20 h at 200°C they evolve to be *n*-doped. It was proposed that the *p*-doping of the as-prepared samples is a result of its interaction with the gas dissolved in the environment, while the *n*-type behavior in the gas-free environment has been attributed to the intrinsic properties of graphene on an $Si/SiO_2$ substrate. The *n*-doping was explained to be a result of electron donation to graphene from the surface states of $SiO_2$, which are energetically located just below the conduction band edge of graphene. However, it was predicted theoretically that the electronic properties of graphene on an $SiO_2$ substrate can depend on the surface polarity, which is controlled by the substrate termination [506]. It was shown that the O-terminated $SiO_2$ surface provides a strong interaction between the carbon atoms of graphene and the oxygen atoms of the substrate, which can significantly modify the band structure of graphene by removing its cone-shaped bands. If the interaction of the oxygen atoms with one carbon sublattice is stronger than with the other, the appearance of a graphene-like band structure with broken sublattice symmetry and a small gap of 0.13 eV was predicted. Moreover, the strong interaction of the O-terminated substrate with graphene leads to *p*-doping of graphene. The Si-terminated $SiO_2$ surface possessing active dangling bonds has shown weak interaction with *n*-doped graphene. Opening of a gap has also been predicted theoretically in [508]. Thus, the oxygen passivated surface of the $SiO_2$ substrate was found to make covalent bonds to the graphene layer, significantly modifying the electronic properties of graphene by removing the cone-shaped bands (similar to that of graphene on a SiC substrate) and forming a gap. Hydrogen-passivation of the oxygen atoms on the $SiO_2$ substrate removes the covalent bonding between the substrate and the graphene layer and leads to a band structure comparable to that of the isolated graphene sheet. Moreover, the type of doping from the $SiO_2$ substrate in [500] was suggested to depend on the difference between the contact potentials of the graphene layer and the substrate because this difference defines the direction of the dipole orientation generated due to the charge exchange between graphene and the $SiO_2$ substrate.

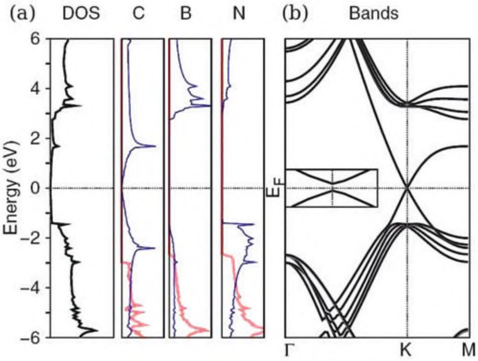

Figure 102. (a) Total density of states for a graphene layer on hexagonal boron nitride substrate with contribution from carbon, boron and nitrogen atoms projected on the *p* states in plane (thick gray line) and out of plane (narrow dark line). (b) Band structure of graphene along the Γ K and KM directions in reciprocal space with band gap of 53 meV, which is magnified in inset (Reprinted figure with permission from G. Giovannetti *et al.*, Physical Review B, 76, 073103, 2007 [383]. Copyright © (2007) by the American Physical Society.).

There are some theoretical predictions for the substrate induced gap in graphene on a boron nitride substrate [383,507]. For graphene on the N-terminated cubic boron-nitride [507], the equivalence between the A and B sublattices of graphene is broken which results in a gap. The effect occurs because the two sublattices are located at different places on the boron-nitride lattice, and therefore have different chemical environments. When the carbon atoms belonging to one sublattice are located on top of the nitrogen atoms, the charge exchange between the dangling bonds of the nitrogen and carbon atoms is significant in comparison to that between the carbon atoms of the other sublattice and the boron atoms. The obtained band gap was ~0.13 eV and the majority and minority spin bands were split. The electronic structure of graphene on a boron nitride substrate was also found to be affected by the termination of the substrate surface. Thus, for the B-terminated cubic boron-nitride the surface states on substrate are energetically located higher than the Fermi level of graphene, thereby having no effect on its properties. Similar results showing opening of a gap were obtained for graphene on a hexagonal boron nitride substrate [383], whose band structure is presented in Figure 102. The opening of a gap is attributed to the inequivalence of the carbon sites belonging to different sublattices due to their location: one carbon atom is placed on top of the boron atom, while the other in the center of the boron-nitride ring. The band structure of graphene on a boron-nitride substrate was found to be similar to that of the isolated graphene sheet, i.e. the appearance of the Dirac cones around the K points has been predicted. However, the dispersion around the Dirac points was quadratic (see inset in Figure 102b). The gap decreases with increasing distance between graphene and the substrate.

When graphene is placed on a metal substrate, the cone-shaped electronic structure of graphene is predicted to be preserved but the Fermi level is shifted relative the Dirac point [512,513]. It was found that the shift can be in either direction giving rise to either *n*-type or *p*-type doping. The shift of the Fermi level $\Delta E_F$ and difference of the workfunctions between the metal-graphene system and the

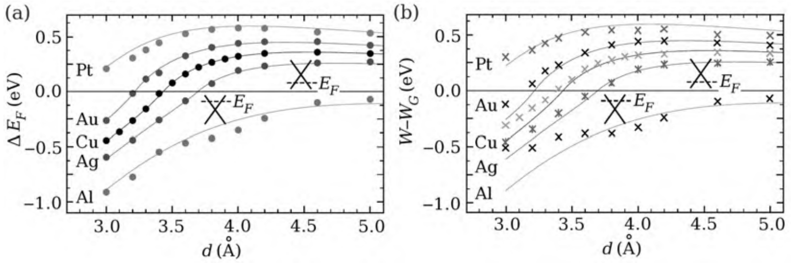

Figure 103. (a) Shift of the Fermi level position ($\Delta E_F$) relative to the Dirac point with increasing distance between graphene and the metal substrate. (b) Estimated difference of the work function between the graphene-metal systems and a pure graphene sheet ($W - W_G$) as a function of the distance between graphene and the metal substrate. The dots and crosses are results obtained from DFT-LDA calculations and solid lines – from phenomenological model (Reprinted figure with permission from P.A. Khomyakov *et al.*, Physical Review B, 79, 195425, 2009 [513]. Copyright © (2009) by the American Physical Society.).

pure graphene sheet ($W - W_G$) as a function of the graphene-metal separation is presented in Figure 103. These results allowed the authors to predict that the charge distribution at the graphene-metal interface depends on both the electron transfer between the metal and graphene (that tends to bring the Fermi level of graphene and the metal to equilibrium), and on the metal-graphene chemical interactions. It was concluded that the shift of the Fermi level position is governed by the magnitude of the charge transfer between the metal and graphene. The switch from *p*- to *n*-type doping occurs as a result of the coincidence of the Fermi level and the Dirac point. The critical value of the metal work function $W(d) = W_G + \Delta_c(d)$ corresponds to this crossover point, where $\Delta_c(d)$ describes the short-range interactions resulting from the overlap of the metal and graphene work functions. Moreover, the presence of the metal-graphene interactions induces the asymmetry of the spin-up and spin-down bands in graphene. For graphene on a Cu(111) substrate [383], the influence of the substrate on the electronic properties was found to be rather weak. It was shown that the inequivalence of the carbon sites belonging to different sublattices is not essential for this substrate, thereby preserving the almost metallic behavior of graphene.

Therefore, we can conclude that the interaction of graphene with the substrate modifies the electronic properties of graphene. The nonequivalent charge exchange between the substrate or the buffer layer and the carbon atoms belonging to different sublattices of graphene, the built-in dipole field induced due to the charge accumulation in the system may break the symmetry of graphene, which results in the formation of a gap. For graphene on a metal substrate the main effect corresponds to doping of graphene as a result of charge exchange between the substrate and graphene.

## 8.2. *Doping of graphene through adsorption*

### 8.2.1. *Adsorption of non-metals on graphene: experimental results*

Most organic molecules interact rather weakly with the surface of pure graphene and because there is no covalent bonding to the surface, the interaction is mostly

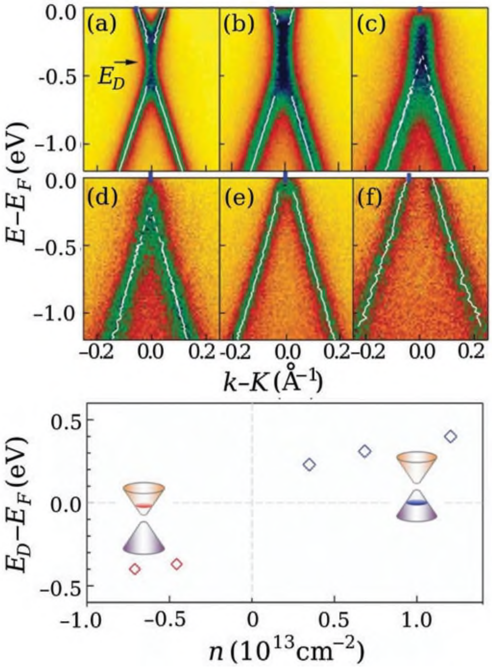

Figure 104. Evolution of the band structure of graphene for increasing concentration of adsorbed $NO_2$ gas molecules on its surface. (a) As-grown sample and (b–f) various doping level of graphene. The lower panel is the plot of the Dirac point energy $E_D$ as a function of carrier concentration (Reprinted figure with permission from S.Y. Zhou *et al.*, Physical Review Letters, 101, 086402, 2008 [515]. Copyright © (2008) by the American Physical Society.).

composed of repulsive interactions and van der Waals interactions [514]. However after exposure to adsorbates, the intra-molecular charge transfer and re-hybridization of the molecular orbitals of graphene due to the interaction with adsorbates lead to a change in the electronic properties. Thus, the conductance of graphene is sensitive to adsorption of gas molecules such as $NO_2$, $H_2O$, $NH_3$ and CO [49]. According to Hall measurements, the $NO_2$ and $H_2O$ behave as acceptors on the graphene surface while $NH_3$ and CO are donors. An increase in the concentration of adsorbed molecules leads to an increase of the induced charge carriers in a single layer of graphene, and step-like changes in its resistance. Moreover, experimental investigation of the adsorption of gas molecules on graphene [515] has shown that adsorption changes the electronic properties of graphene through breaking of its symmetry and doping. A metal–insulator transition has been observed in graphene after exposure to the $NO_2$ gas. This transition was reversible since annealing of the sample or exposure to high proton flux led to closing of the graphene bands. The evolution of the band structure obtained with ARPES as a result of increasing the concentration of $NO_2$ on the graphene surface is presented in Figure 104. The doping by adsorbed molecules shifts the energy bands of graphene. The Dirac points $E_D$ for the as-grown sample is located 0.4 eV below the Fermi level, i.e. the sample is *n*-doped. The adsorption of $NO_2$ results in hole doping. Therefore, an increase in the gas concentration shifts the whole band structure up converting the doping to *p*-type. The Fermi velocity and the electron–phonon coupling have been found to be independent of doping.

The adsorption of aromatic molecules has been studied experimentally with Raman spectroscopy and has been shown to break the symmetry of graphene [516,517]. It was observed that monolayers of graphene sandwiched by aromatic molecules resulted in splitting of the *G*-band [516]. This *G*-band splitting was attributed to breaking of the six-fold symmetry of the graphene sheet and lifting of the two-fold degeneracy of the optical phonon bands at the $\Gamma$ point resulted from the change of the spring constant induced by the adsorption. The adsorption of the aryl group, which was shown to form a bond with the graphene surface [517], has been found to increase significantly the electrical resistance of graphene. It has been proposed that bonding between the adsorbates and the graphene surface changes the $sp^2$ hybridization to $sp^3$, which induces a gap. Additionally, it was experimentally found that the type of doping and its magnitude can be controlled by the type of adsorbed molecules [518,519]. Moreover, the adsorption of dipolar molecules (such as water) has been observed in [398] to provide *p*-type doping of graphene. Doping by dipolar molecules also has been found to induce hysteresis in the field effect behavior of graphene, i.e. a shift of the maximum of the resistance relating to zero voltage arising from the dipolar nature of the adsorbates. Exposure in vacuum was found to reduce the hysteresis effect for some dopants due to the removing of the adsorbed molecules from the graphene surface, but additional heat treatment was seen to be more effective in removing the adsorbed molecules. Moreover, an exposure of graphene samples to $NH_3$ gas converts the *n*-type graphene to *p*-type.

### 8.2.2. *Adsorption of non-metals on graphene: theoretical approaches*

Several theoretical groups have been working extensively on adsorption of different molecules on graphene, which will be discussed below. The interaction between adsorbed organic molecules and the graphene surface is found to be rather low [514]. The long-range electron correlation was found to be responsible for the attraction of the adsorbed molecule to graphene. However in some cases, the adsorbed molecules were found to be able to bond to the graphene surface [520–524].

The very first theoretical paper devoted to the adsorption of organic molecules on the graphene surface was reported in [520] and demonstrated that adsorption can induce magnetism in graphene. The C adatom on the surface of graphene was found to make a bond to two neighboring carbon atoms, which resulted in disturbance of the graphene planarity. The distribution of the four valence electrons of the adatom is shown in Figure 105. There, two electrons participate in bonding with the graphene surface ($sp^2$ hybridization): one forms a dangling $sp^2$ bond and the other one is shared between the $sp^2$ bond and $\pi$ orbital, which is orthogonal to the surface. This $\pi$ orbital does not form a band, therefore remaining localized and spin-polarized. It was shown that the magnetic moment of the adatom is non-zero only for the equilibrium position, where its magnitude is $0.5\mu_B$.

In the graphene lattice, the carbon atoms having four valence electrons donate three of them to form bonds with the nearest carbon atoms, while the fourth electron participates in the formation of the $\pi$ orbitals. Moreover, the fourth electron can participate in interactions with an adsorbate, such as a F, O and N atom, which lack

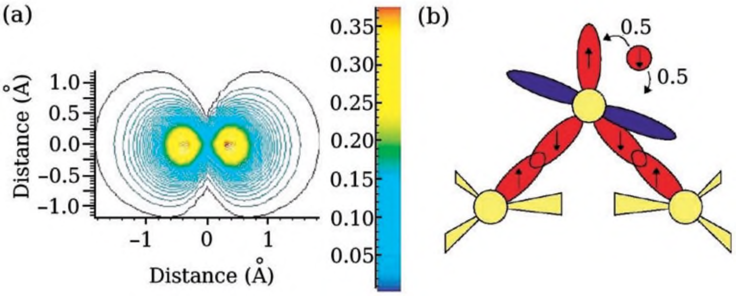

Figure 105. (a) The spin density (e Å$^{-3}$) of an adatom in its equilibrium position on the graphene surface. (b) The bond orbitals through the adatom and two carbon atoms belonging to graphene (Reprinted figure with permission from P.O. Lehtinen *et al.*, Physical Review Letters, 91, 017202, 2003 [520]. Copyright © (2003) by the American Physical Society.).

one, two and three electrons in their outer electron shell, respectively [522]. The F atom adsorbs above the carbon atom with an adsorption energy of −2.01 eV and inter-atomic distance of 1.56 Å. The O atom adsorbs to two carbon atoms with adsorption energy of −2.41 eV and inter-atomic distance of 1.46 Å. The electrons of the F and O atoms are paired and possess no polarization. The adsorption of polarized molecules, such as a N atom which has unpaired electrons, results in a magnetic moment of 0.84 $\mu_B$ per N atom. The N atom adsorbs above the carbon atom with adsorption energy of −0.88 eV and inter-atomic distance of 1.46 Å. The unsaturated electrons of the N atom are spin polarized, inducing polarization of the electrons near the carbon atoms in graphene. Moreover, the N atom is an electron acceptor and its adsorption leads to *p*-type doping of graphene. The orbitals of the N atom generate a peak in the DOS and create a strong acceptor level 0.39 eV below the Dirac point. The partially occupied orbital of the N atom is split by the Hund-like exchange interaction in such a way that the spin-up component is fully occupied and located 2.05 eV below the Dirac point, while the spin-down component is unoccupied and located at 0.39 eV, thereby producing strong acceptor behavior by the N atom. The P atom adsorbed on graphene is also spin-polarized and exhibit a magnetic moment of 0.86 $\mu_B$ [525]. Moreover, the S and P atoms has been found to make chemical bond to the carbon atoms in graphene and for the S atom due to the strong hybridization between S 2p states and C 2p states the band gap of 0.6 eV has been induced.

Theoretical investigations [521] do provide support to the experimental results, where the gap was opened by adsorption [515,516]. In fact, $CrO_3$ adsorbed on graphene was found to act as an acceptor [521]. The alteration of the electronic properties of graphene with $CrO_3$ adsorption for several stable configurations of $CrO_3$ is presented in Figure 106. Orientation of the $CrO_3$ molecule on the graphene surface and its adsorption site are found to affect the efficiency of the charge transfer between graphene and the adsorbate, thereby gradually modifying the properties of graphene. The charge exchange between graphene and the $CrO_3$ molecule was found to lower the Fermi level and the graphene band. Charge transfer of 0.17$\bar{e}$ shifts the Fermi level by 0.69 eV, that of 0.11$\bar{e}$ by 0.64 eV, and 0.20$\bar{e}$ by 0.8 eV, as shown in Figure 106(b–d), respectively. The binding of the $CrO_3$ molecule to graphene (Figure 106b) induces a gap of 0.12 eV at the Dirac point due to the breaking of the

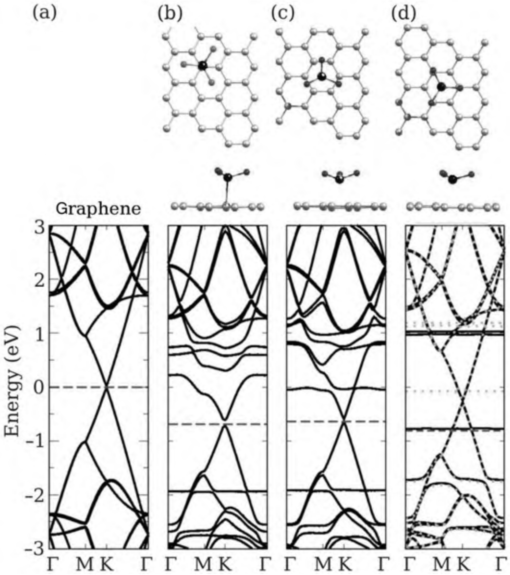

Figure 106. Influence of the adsorption of a $CrO_3$ molecule and its orientation on the graphene surface on the electronic properties of graphene: (a) pristine graphene, (b–d) graphene with adsorbed molecules. The horizontal dashed line is the Fermi level. In (d) the filled and dotted lines corresponds to the majority and minority of the spin levels, respectively (Reprinted with permission from I. Zanella *et al.*, Physical Review B, 77, 073404, 2008 [521]. Copyright © (2008) by the American Physical Society.).

sublattice symmetry. Another confirmation of the influence of the adsorbed molecules on the band gap has been found in [526], where the adsorption of polar molecules, such as $NH_3(CH)_6CO_2$ and $NH_3(CH)_{10}CO_2$ was shown to be able to change the spin symmetric gap to be spin asymmetric. The modification of the gap has been explained by the presence of an electric field induced by the adsorption of polar molecules. It was also shown that induced spin-asymmetry can be controlled by the modification of the dipole moment in the chain through changing the size of the chain formed by the adsorbed molecules.

The interaction of the graphene surface with the adsorbed gas molecules, such as $NO_2$ and $N_2O_4$, is found to lead to paramagnetic or diamagnetic behavior, depending on whether strong doping or no doping occurs, respectively [397]. The diamagnetic $N_2O_4$ has no unpaired electrons, its HOMO is more than 3 eV below the Fermi level of graphene and no charge transfer from $N_2O_4$ to graphene occurs. However, the LUMO of the $N_2O_4$ molecule is localized near the Dirac point and can be populated by the electrons from the graphene flake through thermal excitation, thereby allowing the $N_2O_4$ to act as an acceptor. A paramagnetic adsorbate (such as $NO_2$) on the graphene surface possesses a partially occupied molecular orbital split by the exchange interaction. As a result, its spin-up component is located 1.5 eV below the Dirac point of graphene and is fully occupied, while the spin-down is unoccupied and located 0.4 eV below the Dirac point, thereby producing strong acceptor behavior in the $NO_2$ molecule. It was assumed that for graphene exposed to the $NO_2$ gas, both $NO_2$ and $N_2O_4$ components should participate in charge exchange

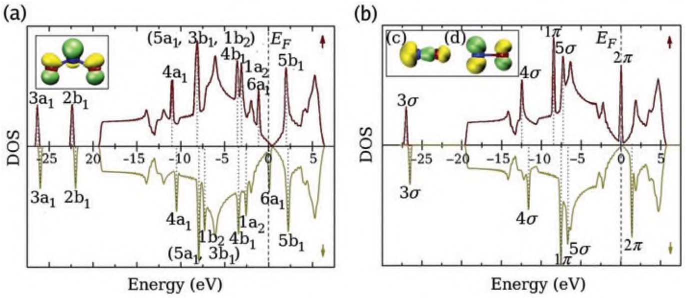

Figure 107. (a) The spin-polarized DOS of $NO_2$ on graphene where the inset is HOMO and LUMO for $NO_2$. (b) The spin-polarized DOS of NO on ghraphene, where insets are (c) the 5$\sigma$ orbital and (d) the HOMO and LUMO (Reprinted figure with permission from O. Leenaerts *et al.*, Physical Review B, 77, 125416, 2008 [527]. Copyright © (2008) by the American Physical Society.).

with the graphene surface, so that several acceptor levels would be induced in the graphene band structure. One is far below the Dirac point, while second is close to it.

However, according to [527,528] not all paramagnetic molecules are strong dopants. The paramagnetic $NO_2$ molecule significantly dopes graphene with holes (as was also seen in [397]). The spin-polarized DOS of the $NO_2$ molecule is presented in Figure 107(a). The LUMO of $NO_2$ ($6a_1,\downarrow$) was found to be located 0.3 eV below the Dirac point, thereby providing large charge transfer from the graphene surface to the $NO_2$ molecule. The HOMO ($6a_1,\uparrow$) is located close to Dirac point and causes the charge transfer in the opposite direction from the $NO_2$ molecule to graphene. The total charge transfer from graphene to the $NO_2$ molecule lies in the range 0.89ē–1.02ē depending on the orientation of the $NO_2$ molecule. The magnetization of such a system is 0.862 $\mu_B$. The NO molecule, which is also paramagnetic, acts as a weak donor, providing a transfer of 0.005ē–0.018ē to graphene. The DOS for a NO molecule on graphene is presented in Figure 107(b). In this system, the half-filled HOMO is degenerate and located only 0.1 eV below the Dirac point of graphene. Therefore, charge transfer from graphene to the NO molecule is insignificant and can be compensated for by orbital mixing which causes charge transfer in the opposite direction. In the same paper [527], adsorption of diamagnetic molecules, such as $NH_3$ (donor) and CO (donor) was found to cause the low charge transfer between graphene and the adsorbate. Similarly, the acceptor behavior of $NO_2$ and donor behavior of $NH_3$ was seen in [529], while CO was found to be a weak acceptor and NO a weak donor. The *p*-doping of graphene by $NO_2$ molecules is also found in [530], where a shift of the graphene bands occurs and the Dirac point is shifted by ~0.2 eV above the Fermi level. Oxygen molecule was also found to be a possible acceptor. In [531], tetracyanoethylene molecule was shown to act as electron acceptor as well, converting graphene to *p*-type. The concentration of the adsorbed tetracyanoethylene molecules has been shown to control the position of the Fermi level relative to the Dirac point. The adsorption of an anion radical of tetracyanoethylene was effective in inducing a spin density in graphene because of the spin splitting and the partially filled $\pi^*$ orbitals of this anion radical.

The effect of interaction of a single water molecule with the graphene surface was found to depend on the orientation of the water molecule [527]. In an energetically favorable position of a water molecule placed on graphene (when one of the hydrogen atom is located closest to the surface, thereby providing efficient electron transfer from graphene to the water) it acts as an acceptor. However, if the oxygen atom is located closest to the surface, the electron transfer is from the oxygen atom to graphene so the molecule acts as a donor. When several water molecules are near the graphene surface, they tend to build a cluster [532,533], where each water molecule uses one of its hydrogen atoms to make a hydrogen bond with the oxygen atom of the neighboring molecule. It was found in [532] such that a water cluster tends to contain as many water molecules as possible, but this cluster has a weak influence on the electronic properties of graphene. The impact of the water adsorbates on the electronic properties of graphene has been found to be more effective when graphene is placed on a defective $SiO_2$ substrate [534] because the dipole moments of adsorbates shift the defect states of the substrate according to position of the conduction band of graphene thereby initiating doping.

Berashevich and Chakraborty [533] showed that adsorption of water molecules on nanoscale graphene, where the edge states and the symmetry of the lattice play the most important roles, and exhibit different effects on its electronic properties than those observed in [532]. Here the water cluster makes a link to the graphene surface through the oxygen atom of a single water molecule. The water link donates an electron to graphene, while most of the water molecules in the cluster act as acceptors. The water cluster, which is linked to the graphene surface somewhere close to the center of the nanoscale graphene, unrolls in the direction of the armchair edges, which are known to have lower energy than the zigzag edges [402,403]. The highest possible symmetry of pristine nanoscale graphene was found to be $D_{2h}$ planar symmetry with an inversion center, which is a metastable state competing with the state with $C_{2v}$ symmetry. The interaction of graphene with water molecules and the charge transfer between them, which is unequal for the two sublattices, leads to the breaking of the $D_{2h}$ symmetry and gives rise to a state with $C_{2v}$ symmetry. The state with $C_{2v}$ symmetry is characterized by ferromagnetic ordering of the spin states along the zigzag edges and antiferromagnetic ordering between the edges. This enhances the gap in nanoscale graphene. The size of the gap is found to depend on the efficiency of the charge transfer between graphene and the adsorbate. Thus, alteration of the number of water molecules in the cluster changes the cluster orientation relative to the graphene surface and therefore the charge exchange between the adsorbate and graphene. This leads to a modification of the band gap (Figure 108a). Moreover, because of the influence of the efficiency of the charge exchange on the band gap, adsorption of different gas molecules on the graphene surface induces band gaps of different sizes, as presented in Figure 108(b) for single $NH_3$, $H_2O$, CO or HF molecules.

Opening of a band gap in monolayer and bilayer graphene has also been demonstrated by adsorption of water molecules on the surface [535]. There, the sublattice symmetry was broken due to the displacement of the carbon atoms (namely the vertical distortion of the graphene lattice) as a result of interaction with the adsorbed molecules. For monolayer graphene, the adsorption of water induces a gap of 18 meV, while ammonia opens a gap of 11 meV. For bilayer graphene (characterized by the parabolic bands near the charge neutrality point) a direct gap

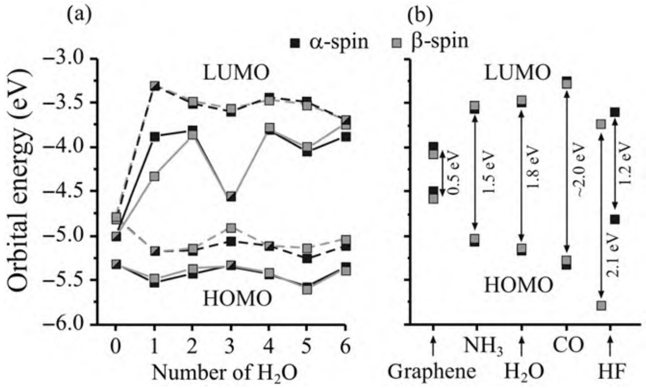

Figure 108. The effect of adsorption of water and gas molecules on the energy of the HOMO and LUMO orbitals of graphene. (a) The band gap for graphene for different numbers of carbon rings along the zigzag edges, $N = 3$ (solid line) and $N = 5$ (dashed line). (b) The alteration of the gap with the adsorption of different molecules on its surface. The pure graphene due to the presence of the confinement effect is characterized by the band gap of 0.5 eV (from [533]).

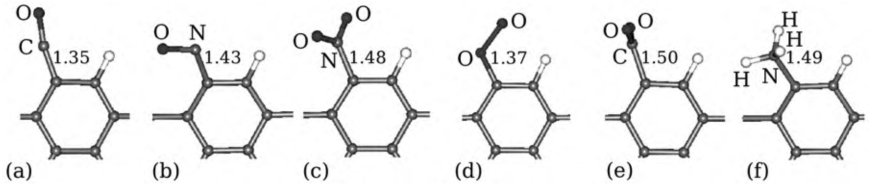

Figure 109. Optimized structures of molecules adsorbed on armchair nanoribbon with single unsaturated dangling bond: (a) CO, (b) NO, (c) $NO_2$, (d) $O_2$, (e) $CO_2$ and (f) $NH_3$ (Reprinted with permission from B. Huang *et al.*, The Journal of Physical Chemistry, C112, 13442, 2008 [523]. Copyright © (2008) by the American Chemical Society.).

of 30 meV was obtained for water adsorption and an indirect gap, located far from the K point, of 42 meV for ammonia.

Adsorption of gas molecules on the surface of a graphene ribbon with armchair-shaped edges, where each armchair edge had a single unsaturated dangling bond while the other dangling bonds are saturated with hydrogen, was studied in [523]. The dangling bonds at the armchair edges are chemically active, and the adsorbed molecules prefer to bond to carbon atoms possessing a dangling bond. The optimized structures of armchair nanoribbons with adsorbed gas molecules are presented in Figure 109. The armchair nanoribbon is naturally in the semiconducting state, but adsorption is found to change its electronic properties. Adsorption of CO and NO molecules leads to the formation of impurity states in the band gap, thereby decreasing its size. For a CO molecule adsorbed on graphene, two half-occupied states are induced, while adsorption of NO induces non-localized, fully-occupied states which are hybridized with states in the valence band. The adsorption of $CO_2$ and $O_2$ molecules leads to *p*-type doping. The band structure of graphene with an adsorbed $O_2$ molecule is presented in Figure 110(a). The impurity states induced by

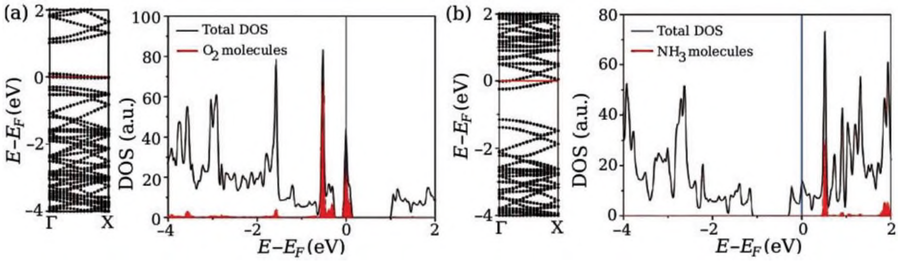

Figure 110. The band structures and DOS of the armchair nanoribbon with adsorbed molecules: (a) $O_2$ and (b) $NH_3$. The Fermi level is set to zero (Reprinted with permission from B. Huang *et al.*, The Journal of Physical Chemistry, C112, 13442, 2008 [523]. Copyright © (2008) by the American Chemical Society.).

these molecules are localized near the valence band. These impurity states are strongly localized and mainly contributed by the adsorbed molecules, therefore suggesting insignificant enhancement of the conductance of graphene in an applied electric field. Adsorption of a $NH_3$ molecule significantly changes the electronic properties of graphene by changing it to an *n*-type semiconductor, whose band structure is presented in Figure 110(b). The transition to an *n*-type semiconductor occurs because of the shift of the Fermi level into the conduction band. Moreover, the states near the Fermi level are found to be created mainly by the carbon atoms, thereby suggesting a significant enhancement of the conductance of graphene in the $NH_3$ gas environment. The *n*-doping of graphene by adsorption of $NH_3$ molecules has received experimental confirmation in [536,537], where the Dirac peak was found to be shifted after exposure to $NH_3$ gas. The possibility of chemical doping of graphene through adsorption was also discussed in [538], where adsorption of organic complexes was found to induce *n*- or *p*-type doping depending on the type of the adsorbates, due to the charge exchange between them and the graphene surface.

Combination of several adsorbed molecules play important roles in the formation of stable configurations of the molecules adsorbed on graphene. When several molecules are adsorbed on the graphene surface, they are found to interact with each other [539]. The interaction strength between two molecules is found to diminish very slowly with increasing distance between them. The sign of the interaction was shown to depend on the location of the adsorbed molecules relative to the sublattice site: two molecules residing on the same sublattice repel each other but they attract when on different sublattices. Another example is adsorption of several hydrogen molecules on a boron-doped structure, which was found to form a H dimer-like structure due to the interaction between hydrogen molecules [540]. Another interesting result is the adsorption of the phenyl group ($C_6H_5$), where the armchair edges have shown higher reactivity than the zigzag edges [541]. The stability of a $C_6H_5$ molecule adsorbed on the graphene surface is found to increase due to the adsorption of a second $C_6H_5$ molecule. The possibility of manipulating the interaction between aromatic compounds and the graphene surface by introducing functional groups was proposed in [542].

Vacancy defects and dopants within the graphene sheet are predicted to attract the adsorbed molecules as well [529,543–548]. In [545], Al-doped graphene sheets

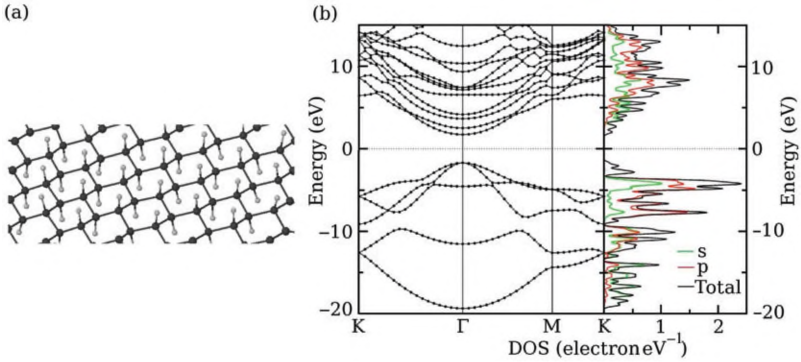

Figure 111. (a) The lattice structure of graphane in the chair conformation. (b) The band structure and DOS of graphane in the chair conformation. The DOS is presented for s and p symmetries (Reprinted figure with permission from J.O. Sofo *et al.*, Physical Review B, 75, 153401, 2007 [549]. Copyright © (2007) by the American Physical Society.).

were shown to have a higher binding energy with $H_2CO$ molecule than for the pristine graphene and occurrence of the orbital hybridization between the $H_2CO$ molecule and the induced Al atom has been reported. Boron-doped graphene is found to have significantly decreased the adsorption energy for hydrogen, due to the electron deficiency [540,546]. Another example of the reduction of the binding energy of the adsorbed molecules is the presence of the Stones–Wales defects or single vacancy defect. The presence of defects initiates the bonding between a SH group and the graphene surface [547], whereas pristine graphene has shown low reactivity against the triol group. Similarly, graphene doped with B, N, Al or S is found to be more reactive in binding with gas molecules whose adsorption was predicted to modify the conductivity of graphene [548]. Moreover, since defects attract the adsorbates, it was found in [544] that the adsorption of $O_2$, $H_2$ or $N_2$ is able to remove adatom defects from graphene.

The main effect of the adsorption of gas and organic molecules on the electronic structure of graphene consists of doping of graphene as a result of charge exchange between the adsorbate and the graphene surface. In cases when an unequal doping of the two sublattices of graphene occurs, the adsorption is found to be capable of breaking the symmetry of the lattice, thereby opening a band gap.

### 8.2.3. *From graphene to graphane*

It was predicted theoretically that adsorption of hydrogen atoms over the whole graphene surface leads to formation of a two-dimensional hydrocarbon – graphane [549]. Graphane, hydrogenated from both sides of the carbon plane has two main conformations: a chair conformation where the carbon atoms belonging to different sublattices are hydrogenated from different sides of the plane, and the boat conformation for which the bonded hydrogen atoms alternate in pairs at the plane sides. The lattice structures of these two conformations are different. In the chair conformation all carbon bonds are of the same length (1.52 Å), while for the boat conformation there are two types of carbon bonds with different lengths, one is

1.52 Å and the other 1.56 Å. The chair conformation is more stable and the difference in the binding energy between two conformations is 0.055 eV per atom. There is not much of a difference in the electronic structure of each conformation, since they both have a direct band gap of 3.5 eV (chair) and 3.7 eV (boat) at the Γ point (within the GW approximation, the size of band gap of the chair conformation is 5.4 eV [550]). The lattice structure, band structure and the density of the states for the chair conformation are presented in Figure 111. The top of the valence band is mainly of *p* symmetry and is doubly degenerate, thereby possessing two different effective masses. Attaching a hydrogen atom to each carbon atom changes the hybridization of the bonds from $sp^2$ to $sp^3$, and leads to opening of a gap as a result of the removal of the conducting $\pi$ bands. However for graphane nanoribbons, the size of the band gap is found to slightly decrease [551] with increasing width of the nanoribbons. Another theoretical investigation [552] predicted that for the chair conformation covering of the graphane surface by hydrogen atoms most likely would not be uniform, in particular the sequence of the up and down H atoms would be broken (frustrated). In the ideal structure of the chair conformation for each side of the graphene lattice, the hydrogen atoms are supposed to bond to carbon atoms belonging to the same sublattice. Therefore, the H frustration forming the uncorrelated H frustrated domains of significant percentage would induce the in-plane dimensional shrinkages into the graphane lattice.

Experimentally it was shown that hydrogenation by the e-beam irradiation of single- and double-layer graphene deposited on the Si wafer coated with $SiO_2$ changes the lattice structure of graphane [553]. The e-beam irradiation of graphene induces the intense D band in the Raman spectra thus indicating the presence of $sp^3$ distortion, and its intensity gradually grows with increasing dose of e-beam irradiation. The following intense laser excitation of the hydrogenated structure reduces the D band intensity. Moreover, it was found that the hydrogenated graphene can be restored by thermal annealing which disorbes the bound hydrogen atoms. It was found that near the room temperature, the hydrogen atoms are more reactive to single-layer graphene than that with a double layer. The effective reactivity of single-layer graphene was explained by distortion, or a degree of freedom in the single layer, not present in a double-layer graphene. The possibility of the reversible hole doping of hydrogenated graphene by oxygen molecules has been indicated.

In a later experiment, opening of a gap with hydrogenation of the graphene surface from one side was reported [280]. Treating the graphene surface with atomic hydrogen, the behavior of graphene changed from the conducting to the insulating state. In fact, the resistivity of graphene is increased by up to 100 times (Figure 112). The characteristics of hydrogenated graphene were stable at room temperature for many days. It was proposed that the deformation of the graphene lattice due to the convex shape of the graphene surface stabilizes the hydrogenated graphene. Further annealing of the sample restores the metallic behavior. However, both the hydrogenated graphene and the restored metallic graphene were *p*-doped, while as-prepared graphene was undoped. The changes in the characteristics of graphene after annealing have been attributed to the presence of induced vacancies. Graphene on $SiO_2$ substrate hydrogenated from one side had the D peak (attributed to the formation of C-H $sp^3$ bonds) half that for hydrogenated free-standing graphene membrane, thereby proving that membrane is hydrogenated from both sides.

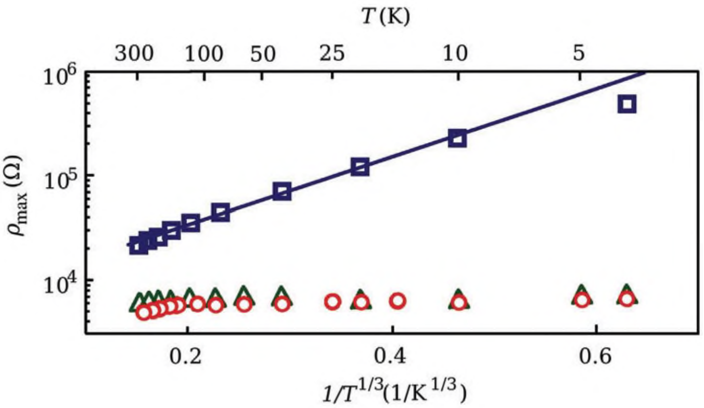

Figure 112. Temperature dependence of the resistivity of pristine graphene (circles), the hydrogenated graphene (squares) and graphene after annealing (triangles). The solid line is a fit obtained from the hopping dependence $\exp[(T_0/T)^{\frac{1}{3}}]$, where $T_0$ is a parameter that depends on gate voltage (Reprinted figure with permission from D.C. Elias *et al.*, Science, 323, p. 610, 2009 [280]. Copyright © (2009) The American Association for Advancement of Science.).

Influence of hydrogenation on the electronic and magnetic properties of graphane has been recently investigated in several theoretical works [554–556]. H-vacancy in the graphane lattice generates a localized state characterized by unpaired spin. Therefore, for several H-vacancy defects their spins can be ferromagnetically or antiferromagnetically ordered. In [554], it was shown that for the graphane sheet hydrogenated from one side the ferromagnetic ordering of the spins of the localized states located on other side of the sheet occurs. The Curie temperature has been estimated to be in a range between 278 and 417 K. The size of the band gap of such sheets is found to be 0.46 eV which is much smaller than that for graphane, hydrogenated from both sides. The possibility to generate the magnetic moment for graphane containing H-vacancy pockets has also been considered in [555]. However, in [556] it was predicted that the ordering of the H-vacancy defects located from one side of the graphane plane depends on its distribution over the plane. It was found that only for the nearest location of the defects significant energy gap between the states characterized by the ferromagnetic and antiferromagnetic ordering is achievable. However, with increasing distance between the defects, the energy difference decreases because the constructive contribution of the spin tails of the localized states located on the same sublattice (considered for the graphene lattice) to the total energy of the system diminishes. Moreover, for graphane containing many vacancy defects on one side of the plane significant distortion of its lattice is noticed and contribution of this distortion into the total energy is found to be destructive for the energy difference between the states with ferro- and antiferromagnetic spin ordering. For the H-vacancy defects distributed between two sides of the graphane plane but located close to each other, the antiferromagnetic ordering of their spins is found to be energetically preferable as a result of the location of the localized states on different sublattices. The influence of the degree of hydrogenation on the electronic properties also has been considered in [556]. Hydrogenation of the edges of the graphane sheet therefore plays an important role in defining the size of the gap. The gap is found to increase from 3.04 to 7.51 eV when hybridization of the edges is changed from $sp^2$ to $sp^3$ type, which is performed by hydrogenation of the edge carbon atoms by one or two hydrogen atoms, respectively. The fluctuation of the size of the gap also takes place with changing the concentration of the H-vacancy defects and their distribution between the sides of the plane.

The interplay of pure graphene and hydrogenated graphene due to the different size of their gaps has been shown to be a way to create periodic multi-quantum systems [557] that has the potential for application in nanoelectronic devices. The possibility of tuning the gap by functionalization of the entire graphene surface has been also discussed elsewhere [558,559]. It was shown that the gap can be changed between 0.64 and 3 eV by using various functional groups. For example, bonding of lithium atoms to graphene has been shown to disrupt the planarity of the graphene lattice and gives rise to the metallic behavior in graphene [560]. Another way to manipulate the size of the bandgap in graphane is via the elastic strain [561]. The stiffness of graphane is less (27%) than that of graphene due to the modification of its lattice (hybridization and planarity) induced by bonding of the carbon atoms with the hydrogen atoms. The strain ($\epsilon$) applied in the elastic range significantly modifies the gap. For example, for a strain ranging from 0.0 to ~0.13 the gap grows from 5.5 to 6.5 eV (in the $G_0W_0$ approximation), but for higher values of strain the gap decreases. For $\epsilon > 0.3$ it drops down to 2.0 eV.

### 8.2.4. *Adsorption of metal atoms on graphene: experimental results*

The adsorption of metal atoms on the graphene surface has been extensively studied by several experimental groups [140,255,504,562–564]. In investigations [564] involving ARPES, the adsorption of Na atoms was found to change the band structure of graphene (degradation of the linear $\pi$ band and developing new parabolic band), while in others [140,255,504] the adsorption of the adatoms induced doping of graphene. The adsorption of potassium on the surface of bilayer graphene grown on a SiC substrate was considered elsewhere [140]. It was declared that the symmetry of bilayer graphene in an as-prepared sample was broken due to the dipole field created between the depleted SiC and the charge accumulated on the surface of the top layer. The adsorption initiated electron exchange between the lone valence electron in potassium and the surface layer of graphene, thereby altering the concentration of the accumulated charge on the surface. This led to modification of the induced dipole field, which controls the size of the gap through the symmetry breaking process. The alteration of the band structure of bilayer graphene by potassium adsorption is presented in Figure 113. Low concentration of potassium on the graphene surface results in a band gap while increasing its concentration leads to reduction of the gap and finally closing of the gap. When the contribution of doping from the adsorbates exceeds the impact from the built-in dipole field, the gap is reopened. Therefore, when the number of electrons per unit cell transferred from potassium to graphene is $0.0125\bar{e}$, the built-in dipole field of the sample is neutralized, which closes the gap. Extra doping induces a field in the direction opposite to the built-in dipole field. Therefore, if charge transfer of $0.0125\bar{e}$ is considered to be non-doped because of suppression of the intrinsic dipole field

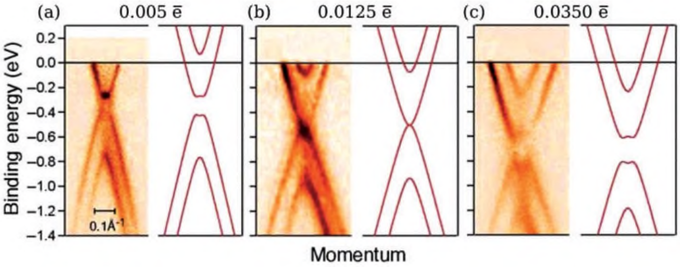

Figure 113. Alteration of the band structure of bilayer graphene by the potassium adsorption. The left picture in each panel are the experimental results, the right are the theoretical estimations obtained from tight-binding calculations. The number of electrons per unit cell transferred from a lone pair of a valence electron of potassium to the graphene surface is indicated at the top of the panels (Reprinted figure with permission from T. Ohta *et al.*, Science, 313, p. 951, 2006 [140]. Copyright © (2006) The American Association for the Advancement of Science.).

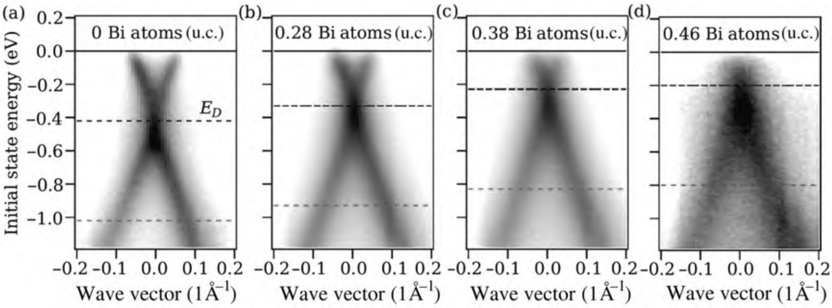

Figure 114. The experimentally obtained band structure of the epitaxial graphene on the SiC substrate doped by the adsorbed Bi atoms. Light and dark areas correspond to the low and high photoelectron current, respectively (Reprinted with permission from I. Gierz *et al.*, Nano Letters, 8, 4603, 2008 [504]. Copyright © (2008) by the American Chemical Society).

(see the crossing of the conduction and valence band of graphene in the middle panel in Figure 113), then relative to this case graphene in the left panel is *p*-doped, while that in the right panel is *n*-doped. Therefore, the built-in dipole field is acting as an external electric field which shifts the bands relative to the Fermi level and allows one to regulate the doping of graphene. Similar experiments have been performed for a single graphene layer on a *n*-type 6H-SiC substrate [255], and *n*-type doping by potassium adsorption has been obtained: the doping shifted the bands to higher binding energy. Moreover, the bands were found to be strongly renormalized near the Dirac point and the Fermi level, due to contributions from electron–electron, electron–phonon and electron–plasmon couplings.

The doping of epitaxial graphene on SiC substrate through adsorption of Bi and Sb alkali atoms has been performed experimentally in [504]. The evolution of the band structure of graphene due to its *p*-doping by alkali atoms is presented in Figure 114. Epitaxially grown graphene on a SiC substrate is naturally *n*-doped and its Dirac point is shifted into the valence band by ~420 meV, as shown in

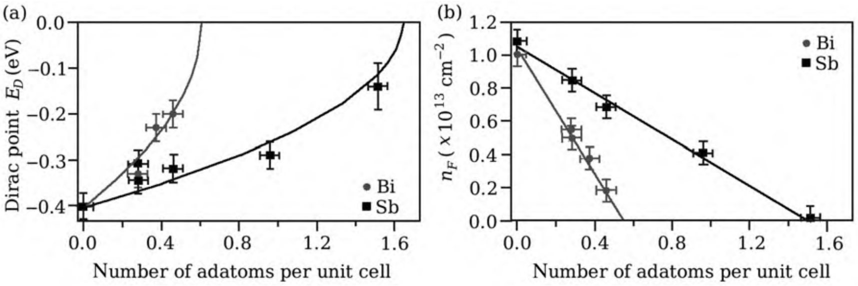

Figure 115. The alteration of (a) the position of the Dirac point $E_D$ and (b) the free charge density $n_F$ due to doping of graphene by the Bi and Sb atoms. Solid line – theoretical estimation is from $E_D = -\sqrt{\pi}\hbar\upsilon_F\sqrt{N_0 - N_h}$, where the Fermi velocity $\hbar\upsilon_F = 6.73$ eVÅ was defined experimentally, $N_0$ and $N_h$ are the numbers of the electrons in the conduction bands and the holes doped into graphene, respectively. The concentration of the free charge carriers were found as $n_F = (k_F)^2\pi$, where $k_F$ is the Fermi wave vector (Reprinted with permission from I. Gierz *et al.*, Nano Letters, 8, 4603, 2008 [504]. Copyright © (2008) by the American Chemical Society.).

Figure 114(a). The linear dispersion of the conduction and valence bands close to the Dirac point has been indicated. The doping shifts the Dirac point toward the Fermi level, which corresponds to *p*-type doping, while the linear dispersion of the bands remains unchanged. The shift of the Dirac point and the change of the free carrier density ($n_F$) as a function of the number of adatoms on the graphene surface is presented in Figure 115. It was observed that the Dirac point approaches the Fermi level and the free charge carrier density is reduced with increasing adatom coverage. For an element with higher electron affinity such as a gold, *p*-type doping was also obtained and for two gold atoms per graphene the shift of the Dirac point in comparison to pristine graphene was found to be 520 meV. The bands of graphene doped by gold are narrower than when doped by Bi or Sb.

In an experiment [565] where graphene was in contact with In, a shift of −400 meV of the Fermi level relative to the Dirac point, i.e. *n*-type doping, has been observed. The doping was also assigned to the charge transfer between the In contact and graphene. The shift of the Dirac point due to the increased coverage by adsorbed atoms such as Ti, Fe and Pt, was also seen in [566]. There, the adsorption of Ti atoms in the low coverage regime has shown a significant shift of the minimum in the gate-dependent conductivity towards negative gate voltage indicating the *n*-type doping of graphene. The shift induced by Ti adatoms was larger than that induced by Fe and Pt adatoms. The ineffective *n*-type doping of graphene by Pt atoms instead of the expected *p*-type doping predicted from the large difference of the work functions of Pt and graphene led to the conclusion that in addition to the work function difference, the interfacial dipole plays a crucial role in doping. Doping of the graphene layer and the asymmetric behavior of its spins induced by the metal adsorption have also been found in theoretical works [567–569]. Spin asymmetry has been attributed to the Coulomb potential [570], which can break the particle–hole symmetry under specific conditions.

The adsorption of Au and Pt atoms and their behavior on the graphene surface have been investigated in another experiment [562]. It was observed that metal atoms

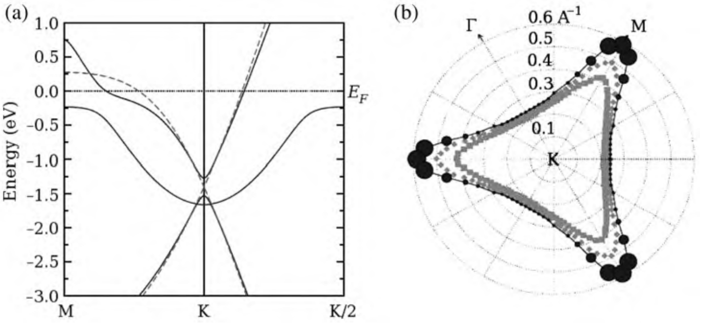

Figure 116. (a) The band diagram of the $CaC_6$ monolayer (solid line) plotted in the Brillouin zone of graphene (dashed line). (b) The influence of doping on the Fermi surface of the $CaC_6$ monolayer. Circles are the theoretical data from [576], where circle size is proportional to the electron–phonon coupling magnitude. Square and diamonds are the experimental results obtained in [577]. (Reprinted figure with permission from M. Calandra and F. Mauri, Physical Review B, 76, 161406, 2007 [576]. Copyright © (2007) by the American Chemical Society.)

tend to replace carbon atoms and can reside on single or multiple vacancies. Due to the attractive interaction between the metal atoms, they migrate to form clusters characterized by an unstable structure. It was also concluded based on magnitude of the activation energy for the in-plane migration (around 2.5 eV) that Au and Pt atoms can make covalent bonds with the carbon atoms. In another experiment [563], the effective dispersion of the gold nanoparticles on the graphene surface in the solution of gold and graphene has been obtained. Theoretically, it was shown that the gold–gold interaction is much stronger than the gold–carbon interactions [571,572], which explains why the formation of gold clusters occurs. The enhancement of the stability of the Pt and Au clusters on the graphene surface by induction of a carbon vacancy has been reported in a theoretical work [573]. Moreover, the unique influence of adsorption of the $Au_nPt_n$ clusters on the size of the band gap has been obtained theoretically in [574]. The cluster composition has been found to define whether graphene shows semiconductor or metallic behavior. In fact, Au, AuPt and $Au_3Pt_3$ on the graphene surface provide charge transfer from graphene to the clusters generating a metallic band structure. For Au on graphene, the spin-up and spin-down bands overlap exactly, producing a gapless band structure, while for AuPt and $Au_3Pt_3$ clusters the spin degeneracy is lifted and half-metallicity occurs. The Pt and $Au_2Pt_2$ clusters act as charge donors and induce a semiconductor band gap. In another theoretical work [575], adsorption of the $Au_{38}$ nanoparticles has also been seen to make charge exchange with the graphene surface. Moreover, adsorption modified the electronic structure of originally gapless graphene causing mini-gaps and the formation of new Dirac points. For a moderate coverage of the graphene surface by the nanoparticles ($\approx 0.2\,\text{nm}^{-2}$), the periodic deformation of the graphene lattice and consequence opening of the gap of the few tens of meV was also observed.

### 8.2.5. *Adsorption of metal atoms on graphene: theoretical approaches*

Alteration of the electronic structure of graphene due to adsorption of metals has been extensively studied theoretically as well. The deposition of a Ca atom on the surface of pristine graphene with formation of the $CaC_6$ stoichiometry was considered in [576]. There, the interaction between the Ca atom and graphene modified the electronic properties of graphene by inducing an impurity band and opening a gap (Figure 116). The induced Ca band was significantly hybridized with the $\pi^*$ states of the carbon atoms which resulted in nonlinearity of this $\pi^*$ band. An increase in the charge transfer from the Ca atom to graphene has been shown to influence the band structure (Figure 116b).

When metal atoms are adsorbed on the graphene surface, the dependence of the charge transfer between the adsorbate and graphene on the work function shift [568] is similar to that for graphene on a metallic substrate [512,513]. It was found that metal atoms of groups I–III are strongly bounded to the graphene surface when they are localized above the center of a graphene hexagon [568]. The distortion of the graphene surface and the subsequent alteration of the electronic structure of graphene induced by the adsorption of metal atoms of this group is minimal, whereas both the charge transfer and the work-function shift are found to be significant. Titanium and iron atoms make covalent bonds with the graphene surface, and their formation is found to depend on the position of the atoms relative to the graphene cells, which is consistent with other investigations [578]. The strongest binding is still obtained when these atoms are positioned in the middle of the graphene hexagon [568]. Due to the covalent bonding, strong hybridization of the electronic structures of Ti and Fe metals on the graphene surface is observed. Pd, Au and Sn atoms on graphene have been found to induce significant distortion into the graphene lattice and predicted to change the $sp^2$ hybridization to more covalently reactive $sp^3$ type. Moreover, the diffusion of these atoms along the hexagonal bond network is possible, and for Au and Sn atoms the diffusion barrier was very small. In [579], it was found that for graphene-metal contacts, metals such as Sc, Ca, Co, Ni and Ti, which have the 3d orbitals located around the Fermi level, can make a strong chemical bond to graphene. The chemical contact of Li and K atoms with graphene may occur via ionic bonding, while Au and Cu are expected to interact weakly with graphene. Therefore, the strength of the chemical interactions defines the width and height of the potential barrier at the metal–graphene interface thereby controlling the transport properties of contacts and the conductivity is predicted to be highest for the Ti–graphene contact for which the chemical interactions are strongest.

For a Cu atom on the graphene surface, the most stable configuration was found to be when the Cu atom was placed directly above a carbon atom, while for a Cu dimer it was when the dimer was above a carbon bond and perpendicular to the graphene surface [580]. Moreover, the electronic structure of graphene was different depending on whether a single Cu atom or a dimer had been adsorbed onto the graphene surface. A single Cu atom has been found to induce a magnetic moment into the adsorbate–graphene system due to the unsaturated s-electrons of Cu atom. For adsorption of transition metal atoms such as Fe and Ti, the most stable configuration is above the center of a graphene hexagon [581]. The Fe atoms are found to preferentially form a cluster, while Ti atoms cover the graphene surface uniformly. Moreover, increase of the concentration of the transition metals on the graphene surface was found to change the binding energy of the adsorbate. However in experimental work [566], the tendency to form a cluster have been seen for several transition metals, such as Ti, Fe and Pt. The possibility to initiate the transition of a semiconducting armchair ribbon into a metal characterized by ferromagnetic properties and a large magnetic moment has been obtained with adsorption of Mg and B atoms [582].

Clustered coverage is favorable over homogeneous distribution for Zr atoms on the graphene surface [583], because the Zr–Zr bond is stronger than that of Zn–C. The Zr atoms formed bonds to graphene and their binding energy was found to depend on the Zr/C coverage ratio. Moreover, the study indicated that Zr and $Zr_3$ clusters on graphene undergo diffusion at room temperature, and that the diffusion barrier for the $Zr_3$ cluster is lower than for a single Zr atom. It was proposed that this diffusion is responsible for clustering of the Zr atoms. It was shown that the charge transfer from Zr atoms to graphene decreases as the Zr/C coverage ration increases and saturates at Zr/C ration ~0.375. Moreover, the Zr/graphene system was spin-polarized and it was concluded that for all configurations of the Zr atoms on the graphene surface the spin-polarization is provided by 4d orbitals of zirconium. The magnitude of the local spin polarization was around $2\mu_B$.

According to theoretical investigations performed in [584], the binding of alkali and alkaline-earth metal atoms above the center of the graphene hexagon was also found to be energetically favorable than that directly above the carbon atoms. The adsorption energy was found to be affected by the ionization energy, the radius of the metal ions, and the amount of charge transfer between the adsorbates and the graphene surface. Thus, adsorption was found to be possible if the difference between the change of the electrostatic energy after the charge transfer between the adsorbates

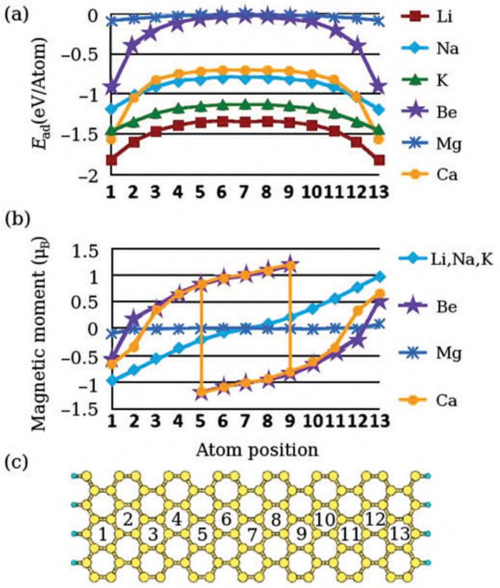

Figure 117. (a) The adsorption energy $E_{ad}$ of the metal atoms as a function of their position on the surface of the zigzag nanoribbons in (c). (b) The magnetic moment induced by the adsorption of metal at various graphene sites numerated in (c) (Reprinted figure with permission from S.-M. Choi and S.-H. Jhi, Physical Review Letters, 101, 266105, 2008 [584]. Copyright © (2008) by the American Physical Society.).

and graphene was larger than the difference between the metal ionization energy and the work function of graphene. For metals which did not meet this condition, such as Be and Mg, the adsorption onto the graphene surface is not possible because the binding energy is zero. The adsorption energy is also found to vary depending on the lattice site, i.e. the position of the adsorbates in respect to the zigzag edges of graphene, as presented in Figure 117(a). The strongest binding is obtained for the edges of the zigzag nanoribbons because the electrostatic interactions between positively charged metal atoms and the zigzag edges are strongest in this case. Even for a Be atom, which cannot be adsorbed in the center of the graphene sheet, the binding energy is nonzero at a zigzag edge. Transfer of an electron from the metal atom to graphene creates a non-zero magnetic moment and its magnitude also depends on the lattice site (Figure 117b). If Li, Na or K atoms are adsorbed at the edges, the charge transfer from the metal to graphene results in a net magnetic moment of $-\mu_B$ because the donated electron occupies a single spin state localized on this edge. Therefore, in the case of Li, Na, K adsorbed at the center of the graphene structure, the transferred electron occupies both spin states equally thereby inducing no change in the magnetic moment of graphene. Other metal atoms placed close to the edges, such as Ca and Be atoms, can donate about $1.33\bar{e}$ which will occupy one spin state fully and the other partially, thereby generating the net magnetic moment of about $-0.66\mu_B$. At the center of the graphene structure, these metals can donate about $1.0\bar{e}$, equally distributed between both spin states, thereby leaving one electron on the metal atom, which is responsible for a net magnetic moment $\mu_B$ of the graphene–metal system. Moving the metal atom from one edge to the other, flips the spin orientation of the electrons in the metal atom due to their interaction with a certain spin state at the zigzag edge, creating hysteresis. The variation of the adsorption energy and the magnetic moment for different metals has been shown to be useful for developing spin-valve devices, where the position of the adsorbed metal on the graphene surface and magnetic moment induced by adsorption can be controlled by an external electric field. The dependence of the adsorption energy, net magnetic moment, and the electronic structure of the graphene–metal systems on the location of the adsorbed molecule have been also investigated in [585] for a Ni atom adsorbed on the graphene surface. It was also found that at the zigzag edges the Ni atom forms more stable configuration than that in the middle of the ribbon.

A systematic first-principles study of metal atoms adsorbed on pristine graphene and graphene with a defect, such as a single vacancy (SV) or a double vacancy (DV), was reported in [586]. For metal atoms adsorbed on pristine graphene, the binding energy is 0.2–1.5 eV and the barrier for migration of the metals along the surface is in the range of 0.2–0.8 eV. Therefore at room temperature, the adsorbed atom would rather migrate along the graphene surface and the magnetic moment induced by the adsorption would be unstable, making it difficult to use adsorption for manufacturing a graphene-based Kondo system. The introduction of a vacancy in the graphene lattice significantly improves the metal adsorption, changing the binding energy up to $\sim -7$ eV, which would prevent the adsorbed atom from moving away from the vacancy. The calculated results of the magnetic moment and the binding energy of a metal atom adsorbed on graphene containing single and double vacancies are presented in Figure 118. For most metals, the bonding with the graphene surface is strong thereby creating a hybridized state. This induces a small dispersion into the

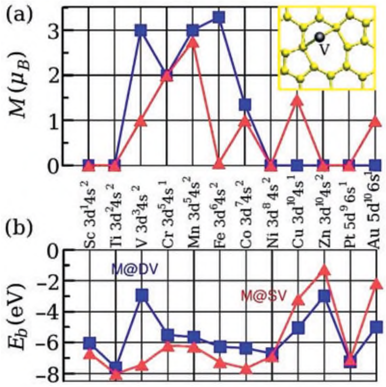

Figure 118. (a) The magnetic moment of the graphene sheet with the adsorbed metal atoms and (b) the binding energies of the metals. For both cases, squares corresponds to the case of graphene containing a single vacancy (SV), white triangle – to a double vacancy (DV). The M@SV and M@DV denote the metal-graphene system with SV and DV, respectively (Reprinted figure with permission from A.V. Krasheninnikov *et al.*, Physical Review Letters, 102, 126807, 2009 [586]. Copyright © (2009) by the American Physical Society.).

bands, which appears close to the Fermi energy and below. The M@DV complexes (metal–graphene system with the double vacancy) are found to be magnetic for all transition metals from V to Co. The larger 'hole' created by a double vacancy was suggested to cause the weaker interaction of the impurity atom with the ligand bonds leading to the higher spin state. In [587] it was also shown that adsorption of metals and small metallic structures can initiate the formation of mono- and bivacancies in the graphene lattice, thereby changing its electronic structure. The formation energy for these vacancies are found to be reduced due to the presence of the transition metal impurities, while a gold impurity almost did not affect the characteristics of the vacancies.

The effect of interaction of the adsorbed metal ions with the zigzag edges terminated by fluorine has been used in [588] to control the migration of the Li ions along the graphene surface. It was shown that at room temperature (~300 K) Li ions would migrate along the graphene surface without approaching the edges because of the repulsive interaction with the positive charge of the C–F carbon bond, whereas at higher temperature the Li ion can move freely near the edge region. The possibility to control the magnetic moment of the graphene with adsorbed metal atoms by the electric field has been discussed in [589]. There it was shown that an applied electric field can induce a shift of the chemical potential, thereby moving the magnetic field created by the adsorbates in the vertical direction.

### 8.3. *Lattice defects*

The interest in defects in the graphene lattice as a source of magnetization was triggered by an experimental work [590] where proton irradiation with energy 2.25 MeV was found to induce magnetism in highly oriented pyrolytic graphite

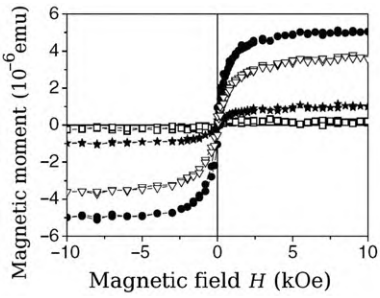

Figure 119. The magnetic moment of the pyrolytic graphite after first irradiation step (□), second (∗), third (●) and fourth (▽) (Reprinted figure with permission from P. Esquinazi *et al.*, Physical Review Letters, 91, 227201, 2003 [590]. Copyright © (2003) by the American Physical Society.).

samples. The magnetic moment of the pyrolytic graphite on a Si substrate has been measured, and the results obtained after subtraction of the substrate contribution are displayed in Figure 119. Because irradiation has been performed in several steps, a clear increase of the magnetic moment within the ferromagnetic loop with each step of the irradiation was observed (Figure 119). The authors came to the conclusion that the appearance of the magnetism after proton irradiation is related to magnetic ordering which is stable at room temperature, and not to the contribution from magnetic impurities. In another experiment [591], the electron-beam irradiation resulted in the appearance of a strong disorder band in the Raman spectrum of the single graphene layer. This was attributed to the damage to the graphene lattice caused by the radiation. Room-temperature ferromagnetism of graphene sheets has also been obtained [592]. There, the magnetization is believed to be induced by defects generated in the annealing process, because for samples of graphene oxide with induced magnetic impurities no ferromagnetism has been observed. An increase of the annealing temperature for some samples caused the enhancement of magnetization. The influence of the sample preparation on the presence of the charged impurities even if no doping has been applied has been noticed in [593], where the impurity concentration has been defined from the shift of the $G$-peak in the Raman spectra. It was shown that irradiation can also influence the charge transfer characteristics [565], which is proposed to be the result of a decrease in the Fermi velocity and modification of the hopping integral after irradiation.

The experimentally achieved ferro- or ferrimagnetism in graphite (explained by generation of defects in the graphite lattice) has stimulated an extensive investigation of the influence of defects on the magnetic properties of graphene. In [594,595], several mechanisms explaining the appearance of magnetism in carbon systems were proposed: under-coordinated atoms, itinerant ferromagnetism and negatively curved $sp^2$ bonded nano regions in the carbon lattice. However, defects are considered to be the most likely cause of magnetism. There are several types of defects responsible for the magnetic phenomena, vacancies and atoms on the graphene edges possessing dangling bonds (either passivated or free). The localized electronic states induced by these defects contribute to the density of states at the Fermi level and can induce magnetism.

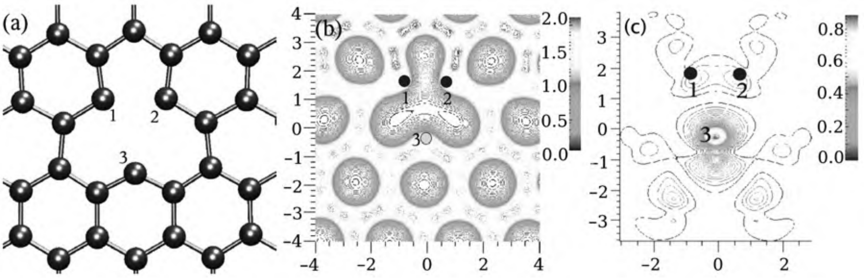

Figure 120. (a) Atomic structure of a single vacancy in graphene, which undergoes a Jahn–Teller distortion. The weak covalent C–C bond of length 2.02 Å is formed between atoms 1 and 2. (b) the charge density distribution (e Å$^{-3}$). (c) the spin density distribution (e Å$^{-3}$) (Reprinted with permission from Y. Ma *et al.*, New Journal of Physics, 6, p. 68, 2004 [595]. Copyright © (2004) IOP Publishing Ltd.).

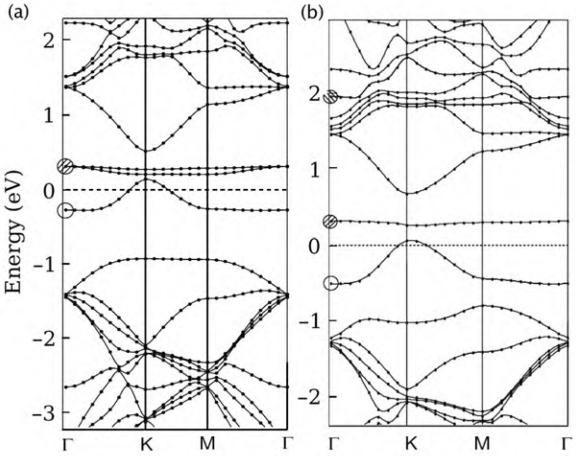

Figure 121. The band structure of graphene containing single vacancy of different symmetries: (a) the vacancy having the $D_{3h}$ symmetry of the honeycomb network, (b) the vacancy of $C_s$ symmetry. The band structures are obtained with DFT-LDA calculations. The Fermi level is set to zero. The shaded circles denote the $\sigma$ band, while open circles correspond to the $\pi$ band (Reprinted figure with permission from H. Amara *et al.*, Physical Review B, 76, 115423, 2007 [597]. Copyright © (2007) by the American Physical Society).

### 8.3.1. *Vacancy defects*

Spin-polarized calculations of the electronic structure were applied to investigate the effect of a single vacancy on the electronic properties of graphene [594,595]. The atomic structure of a single vacancy, its charge and spin density are presented in Figure 120. The carbon atoms surrounding the vacancy have sp$^2$ dangling bonds, but the formation of a pentagon leads to the saturation of two of these bonds, while the remaining unsaturated dangling bond will induce a magnetic moment of 1.04 $\mu_B$. However, the energy difference between a spin-polarized state and a non-polarized state was found to be only about 0.1 eV, suggesting an instability of magnetism of a single carbon vacancy which can be destroyed by interlayer interactions or finite temperature. However, it was also shown that the single vacancy defect can have two conformations: the vacancy having the $D_{3h}$ symmetry of the honeycomb network and the vacancy of $C_s$ symmetry which undergoes a Jahn–Teller distortion [596,597]. In the case of the vacancy of $C_s$ symmetry, the positions of the carbon atoms are distorted, namely two atoms near the vacancy move closer to each other and the third atom is displaced out of plane [597], and the presence of such vacancies significantly affects the electronic properties. The band structures of a graphene sheet containing the $D_{3h}$ or $C_s$ vacancies are presented in Figure 121. First of all, the presence of a vacancy and the magnetic ordering of the states localized on the vacancy break the symmetry of the graphene $\pi$-orbital system, which leads to opening of a gap. The gap between the $\pi$ bands is larger for the vacancy with $C_s$ symmetry than that with higher $D_{3h}$ symmetry. Second, the vacancies induce extra bands near the Fermi level, which are flat $\sigma$ bands associated with the defect states localized on the carbon atoms around the vacancy. For the vacancy of $D_{3h}$ symmetry, there are two symmetric $\sigma$ bands which are slightly separated and one antisymmetric $\pi$ band (Figure 121a). For the vacancy of $C_s$ symmetry, the $\pi$ bands are shifted upward with respect to the position of the Fermi level and, because of broken planar symmetry, one $\sigma$ band is moved deeper into the valence band. The study of a single vacancy with molecular dynamics methods [598] has shown that an electron trapped at the vacancy is stable at low temperature, while increasing the temperature up to 300 K leads to the structural changes of the graphene lattice that can allow the trapped electron to escape.

Therefore, even a single vacancy can induce magnetization into the graphene system through the formation of the spin-polarized localized state [328,594,595,597–604]. However, the presence of several vacancies in the graphene lattice can completely change the magnetization phenomena due to the correlation of the positions of the vacancies [601,605–610]. The presence of a single vacancy breaks both the lattice and sublattice symmetries and opens a gap. Two identical vacancies on different sublattices can restore the sublattice symmetry, thus suppressing the gap [605]. However, two identical vacancies located on the same sublattice results in a larger band gap. Therefore, the sublattice imbalance induced by the distribution of the vacancies over an initially balanced graphene lattice defines the magnetic properties of graphene lattice with defects [474,606].

Considering the spin properties of the defects, it was established that the defects according to Lieb's theorem [471] can interact ferromagnetically or antiferromagnetically depending on the sublattice imbalance. As a result, the total spin of the system will be defined by these local magnetic interactions. It was also found that at a certain defect density, the local magnetization can disappear [606,607]. These results suggesting disappearance of magnetization are in good agreement with the experimental data, where the suppression of magnetization has been observed after four steps of irradiation [590] (Figure 119). In [608], the total magnetization was reduced not only by increasing the vacancy density but also by decreasing the distance between vacancies. The dependence of the magnetization on the distance between the vacancies is a result of the bonding and antibonding interaction of the defect states. Thus, for the vacancies located on different sublattices, the energy splitting decreases with increasing distance between the vacancies [609]. More extensive investigation of the density of vacancies and the sublattice imbalance has

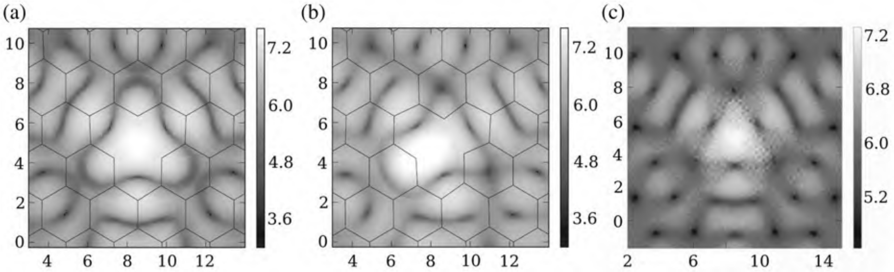

Figure 122. The scanning tunneling microscopy images of the single vacancy in graphene computed with positive tip potential of 0.2 V. (a) The non-reconstructed $D_{3h}$ vacancy, (b) the reconstructed $C_s$ vacancy, (c) average of the three equivalent $C_s$ structure rotated by $\pm 2\pi/3$ (Reprinted figure with permission from H. Amara *et al.*, Physical Review B, 76, 115423, 2007 [597]. Copyright © (2007) by the American Physical Society.).

been performed in [609] with the help of a combination of the Hubbard model and first-principles methods. For vacancies which are equally distributed over the two sublattices, the magnetic moments on these sublattices are characterized by the opposite spin orientation and therefore they have magnetization of the opposite sign. This leads to a compensation effect in the total magnetization. It was concluded that a finite total magnetic moment can only be achieved in the case of the domination of the vacancies arranged on the same sublattice. In another study [601] the dependence of the gap on the concentration of uncompensated vacancies was reported. In the case when the electron–hole symmetry is preserved, the high dilution of the vacancies has been found to result in flattening of the DOS around the band center, while breaking of the electron–hole symmetry leads to broadening of the DOS peak at the Fermi level.

Lattice defects induce a significant alteration of the local electronic properties due to the scattering and interference of the electron waves at these defects. There are many experimental works devoted to the investigation of scanning tunnelling microscopy (STM) images of the defects as each type of defect is supposed to have its own signature [611–616]. For different types of defects the STM images have also been generated with first-principles methods [596,597,599,617]. The STM images of a single vacancy with different symmetries ($D_{3h}$ and $C_s$) are presented in Figure 122. For a $D_{3h}$ vacancy, the trigonal symmetry of the image at the center of the vacancy is observed, which is the result of the localization of the electron density at the three dangling bonds. The $C_s$ vacancy is not characterized by the three-fold symmetry. The rotation of the pentagon by $\pm 2\pi/3$ for a $C_s$ vacancy was found to restore the trigonal symmetry of the graphene lattice.

### 8.3.2. *Vacancy defects saturated by hydrogen*

The single vacancy is also interesting for understanding how it interacts with the adsorbed molecules. The interaction of helium atoms with a single vacancy induces a magnetic moment of about $\mu_B$ per vacancy, while interaction with an ideal graphite lattice was found to be weak, demonstrating no magnetic signal [594]. A similar situation is obtained for the interaction of adsorbed hydrogen with a single vacancy.

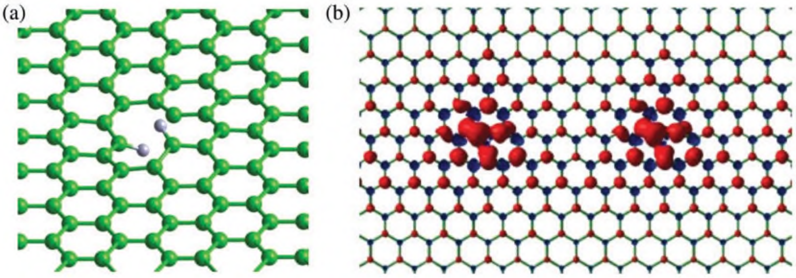

Figure 123. (a) The graphene sheet with the vacancy defect saturated by hydrogen atoms above and below the graphene plane. (b) The spin density distribution for the graphene sheet containing two identical vacancy defects saturated by hydrogens which are placed at a distance of 20 Å (Reprinted figure with permission from L. Pisani *et al.*, New Journal of Physics, 10, p. 033002, 2008 [618]. Copyright © (2008) IOP Publishing Ltd).

However, if one dangling bond of the vacancy is saturated by hydrogen, that leads to a metastable state, and a magnetic moment of $2.3\,\mu_B$ is obtained. There is another stable magnetic configuration for a single vacancy saturated by hydrogens: if a single hydrogen atom interacts with a vacancy which is already saturated by another hydrogen, the stable configuration with two hydrogen atoms placed above and below of the graphene sheet is formed (Figure 123a). The magnetic moment of this configuration was found to be $1.2\,\mu_B$ in [594] and about $2.0\,\mu_B$ in [618]. There are two unpaired electrons on this defect [618], one of them occurs due to the breaking of the $\sigma$ bond, whereas the other electron is the result of breaking of the three $\pi$ bonds between the vacancy and the neighboring carbon atoms, which leads to the appearance of 1/3 of an unpaired electron on each atom. Because the three carbon atoms neighboring a vacancy belong to one sublattice, these unpaired electrons have the same spin orientation, therefore producing a spin-polarized electron localization, as shown in Figure 123(b). In the case of two vacancies embedded into a graphene sheet, the magnetic moment of the system will increase if the defects appear on the same sublattice as a result of the ferromagnetic coupling between their localized spin moments. Therefore, coupling between the defects possesses magnetic ordering at high temperature. The presence of these defects in the graphene lattice has also been found to break the sublattice symmetry thereby opening a gap of 0.51 eV for the majority spin band and of 0.55 eV for the minority. The calculated energy bands for the majority and minority spin states are presented in Figure 124 for two defects separated by distance $L$ of 20 Å. It was also found that the opening of the gap is not related to the spin–orbit coupling and the gap size was shown to change with increasing distance between defects according to the scale $L^{-2}$.

### 8.3.3. *Divacancy defects*

The divacancy defect [597], which is formed when two neighboring vacancies coalesce, significantly changes the electronic and magnetic properties of the graphene flake. There are $\pi$ bands which are located around the Fermi level, while $\sigma$ bands induced by the vacancies are not located near the Fermi level but move deeper into the conduction and valence bands. The transition from the spin degenerate case of

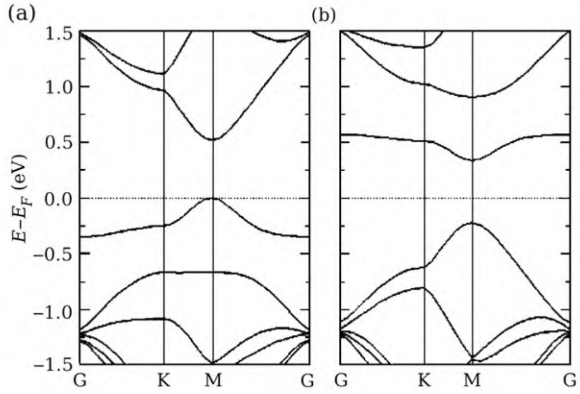

Figure 124. The band diagram for (a) majority and (b) minority spin states of the ferromagnetic state in graphene containing two vacancy defects saturated by hydrogens and separated by 20 Å (Reprinted figure with permission from L. Pisani *et al.*, New Journal of Physics, 10, p. 033002, 2008 [618]. Copyright © (2008) IOP Publishing Ltd).

pure graphene to highly spin-polarized state has been found in [619] due to the presence of a divacancy defect. In [620] the transition of graphene with armchair edges from a semiconductor to a metal was predicted to occur due to the presence of divacancies distributed over the graphene lattice with a constant period. Moreover, the presence of a divacancy defect was found to lead to strong interaction between graphene and the adsorbed molecules [621]. Thus, the adsorption of CO and $N_2$ molecules on graphene containing a divacancy defect led to a metallic behavior. Moreover, the adsorbed molecules were found to dissociate in the vicinity of a divacancy defect and take the place of the missing carbon atoms. For example, $N_2$ molecules play the role of a substitutional impurity for the missing carbon atom in graphene. The adsorption of a gold atom on the graphene sheet containing vacancy defects leads to the in-plane bonding of the gold atom [622]. The diffusion barrier for a gold atom on the graphene surface was found to decrease with increasing size of the vacancy. In addition to the divacancy, other type of vacancies with several carbon atoms missing have been investigated elsewhere [602,606,620,623] and spin-polarized states have also been generated from them. Jeong *et al.* [624] have seen the stabilization of some defects in the presence of pentagon and three pentagon vacancies.

### 8.3.4. *Crystallographic and chemisorption defects*

Attention has also been paid to crystallographic defects [605,625]. For a semiconducting graphene nanoribbon, the Stone–Wales defects have been found to induce a defect band at 0.6 eV above the Fermi level [625]. It was shown that adsorption of a COOH group is capable of significantly shifting this defect band closer to the Fermi level [625]. An increase in the number of Stone–Wales defects with adsorbed COOH groups can lead to the transition of the graphene sample from a semiconductor to a *p*-type metal. For metallic graphene, the presence of a single Stone–Wales defect shifts the Dirac point maintaining the two-fold degeneracy, but removing the degeneracy at the K point, which results in a gap of 27.8 meV, while for three defects a gap is 80.3 meV [605]. Therefore for low density of the Stone–Wales defects, the size of the gap increases almost linearly with increasing defect concentration. The dynamic stability of the Stone–Wales defects has been found to be rather low in a planar graphene sheet [626], while similar crystallographic defects, such as pentagon–heptagon pairs, were dynamically stable. Random arrangement of the crystallographic defects, which are shown to form linearly stable configurations, has been seen to provide the formation of meta-crystal structure of graphene [627].

Chemisorption defects on the graphene surface, such as a carbon adatom or a hydrogen adatom, have been studied in [594,597,599,628]. The presence of vacancy defects has already been mentioned to initiate the formation of the chemisorption defects due to the attraction of the adatoms by vacancy defects [627]. It was found in [599] that hydrogen chemisorption defects induce a magnetic moment of $\mu_B$ per defect, and defect bands. The band maximum for the majority spin is located below the Fermi level, while in the minority spin case, it is above the Fermi level. The magnetic moment of the hydrogen chemisorption defects is independent of the distance between the two defects and the system remains spin-polarized in a wide range of defect concentration. However, the magnetic moment of the system depends on the distribution of the defects over the graphene sublattices where ferromagnetic coupling between defects give rise to an increase in the magnetic moment. Thus, the ferromagnetic ordering of the defects occurs when two defects are localized on the same sublattice as a result of non-oscillating behavior of the magnetization of the $p_z$ orbital of the carbon atom and indirect coupling between defects.

In [603], the magnetic moment induced by the presence of an adatom, such as C, B, N, is found to be independent of the defect concentration, while the alteration of the band gap has been indicated. Moreover in the same work, the defects such as substitutional atoms and vacancy defects have been found to break symmetry of the graphene lattice and induce the magnetic quasi-localized states for which the magnetic moment is defined by the density of defects. For a carbon adatom incorporated into the graphene sheet [597], the flat bands of the localized states occur in the vicinity of the defect, which is similar to that obtained for the single vacancy defect (Figure 121a). The saturation of the carbon adatom by hydrogen [594] induces a magnetic moment of $0.9\,\mu_B$ resulting from the C–H group. The conductance of graphene has been found to be modified by the presence of the carbon adatom [628], for example, the conductance dip was dependent on the location of the defect relative to the edges and the severity of the defect. In general, the conductance of graphene is found to decrease in the presence of defects [628,629]. Moreover, the presence of a defect is found to affect the transport length scale in graphene [630], which is shown to fluctuate significantly as the topology of the edge irregularities are changed.

### 8.3.5. *Substitutional doping of graphene*

Another interesting topic is doping of graphene by impurities. It was observed experimentally that graphene is converted from *p*-type (pristine graphene) to *n*-type by substitutional doping of N atoms [631]. The investigation of doped graphene with first-principles methods [632] has also shown a transition of the armchair

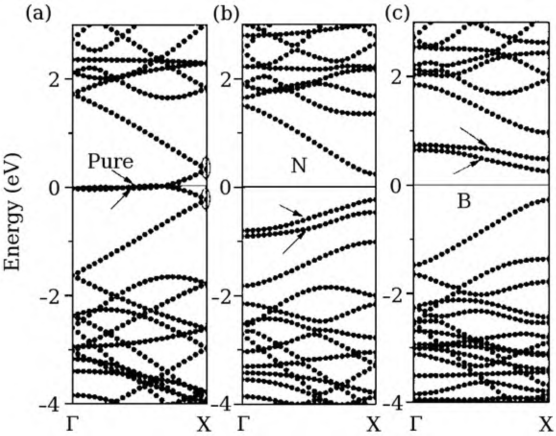

Figure 125. (a) The band diagram of pure graphene. (b) The band diagram of graphene doped by N. (c) The band diagram of graphene doped by B (Reprinted with permission from B. Huang *et al.*, Applied Physics Letters, 91, 253122, 2007 [632]. Copyright © (2007) American Institute of Physics.).

nanoribbon from metallic to semiconducting behavior due to doping. The degradation of the electronic properties with doping is shown in Figure 125. Pristine graphene was observed to be metallic, whereas the substitutional doping by either N atoms or B atoms opens a gap. The substitution of a carbon atom by N (N-doping), induces a impurity level below the Fermi level (*p*-type semiconductor), while B-doping induces a impurity level above the Fermi energy, thereby leading to *n*-type semiconductor behavior of graphene in addition to the opening of a gap. The band gap is also modulated by the doping concentration. For low doping concentration, the band gap increases as the concentration of dopants grows, then achieves a maximum at concentration of $0.1365\,\text{Å}^{-1}$ and starts to decrease with further increase of the doping. Substitutional doping is found to be energetically more favorable at the interfaces of the zigzag edges.

A transition of graphene from metallic to semiconducting type has been found elsewhere [633] as result of substitutional N-doping. There, by controlling a chemical composition of $C_xN_y$ graphene, the band gap was modulated in the range of 3–5 eV. The $C_xN_y$ graphene layers were created under the conditions that chemical valences of four for C atoms and of three for N atoms were satisfied. This was achieved by generating a single vacancy of a C atom in a periodic manner. The optimization process has shown that some of the conformations were stable and had no confining compressional stress, but some conformations were found to spontaneously adopt buckled geometries. In the case when the carbon atom is substituted by a B atom, the transformation of graphene to the metallic type has also been reported [634]. Moreover, substitution of carbon atoms by B or N atoms was found to change the magnetism of the graphene nanoribbon [635]. There, the magnetic phase of graphene, i.e. the spin alignment between two opposite zigzag edges, has been controlled by the charge injection. The switching of the antiparallel spin orientation of the localized states between zigzag edges to the parallel one thereby modifying the size of gap was obtained. The presence of an impurity band induced by the substitutional doping has also been observed in [601]. There, the impurity band had a split structure and was completely detached from the main band. For small impurity concentration, the change of the electronic structure consists of a rigid shift of the Dirac point. In the case when the impurities are located close to each other, the interference and hybridization effects leading to re-splitting of the low-energy resonance were observed.

The occurrence of an impurity-induced resonance near the Dirac point was observed in the local density of states as a result of the substitutional doping of two carbon atoms in graphene [636]. The existence of two nonequivalent Dirac points in the Brillouin zone has been proposed to cause this resonance effect. The embedding of the magnetic impurity into graphene has been shown to result in exchange splitting of the resonance in the two spin channels. The contribution of the exchange scattering is found to enhance the polarization of the impurity state. Moreover, the role of the substitutional impurity on the transport properties of graphene has been considered in [637]. The presence of impurities such as B or N was found to result in resonant backscattering, the efficiency of which was strongly dependent on the symmetry of the graphene sample, the edges and the location of the impurities within the graphene lattice. The possibility to convert the armchair nanoribbon in the semiconducting state to a metal by embedding a boron cluster was discussed in [638,639]. Another interesting result was reported in [640], where a method of substitutional doping of the graphene sheet by a B atom without an activation barrier was proposed. The barrierless doping was obtained due to selective exposing of each side of graphene sheet to different elements, such as nitrogen and boron.

## 8.4. *Functionalization of the edges*

The edges play a crucial role in the establishment of the electronic properties of nanoscale graphene. For example, structural changes of the edges [404,641,642], such as bond reconstruction, edge passivation and even edge aromaticity often lead to a change of the $\pi$ network composition at the edges (percentage of sp, sp$^2$ and sp$^3$ bonds [428]), thereby modifying the electronic properties of graphene. In [641] the change of the electronic structure of a graphene nanoribbon activated by the edge modification as a function of the hydrogen content of the environment was investigated with first-principles methods. The simulations were performed for zigzag and armchair edges of stable and unstable configurations, the structures and electronic properties of which are presented in Figure 126(a) and (b), respectively. The results show that alteration of the edges changes the band structure by shifting the band crossing along the $k$-axis and along the energy axis or by modifying the size of the band gap. Therefore, the main conclusion here is that edge reorganization is a prospective way of manipulating the electronic properties of graphene (including size of the band gap) due to the significant contribution of the edges into the electronic properties of graphene. The edge structure can also be changed by saturation of the dangling bonds at the edges through its bonding with chemical groups (edge functionalization [643]) which may be another way to obtain the desired properties, such as spin polarization, spin gap asymmetry and controllable size of the band gap. There are two ways to functionalize graphene which have been extensively

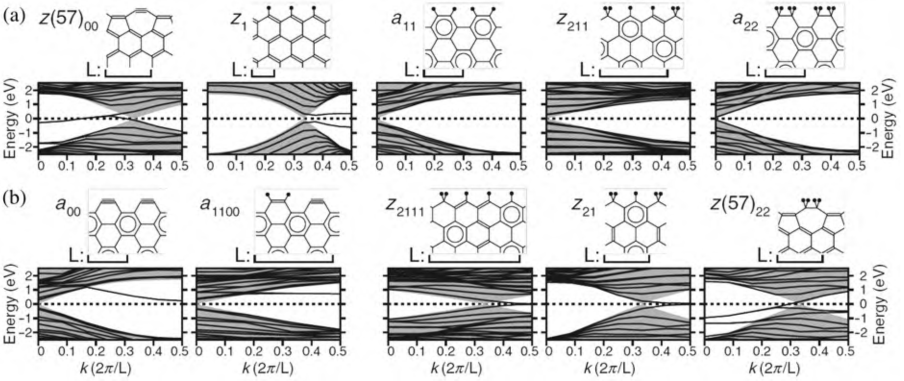

Figure 126. The configuration of zigzag (*z*) and armchair (*a*) edges of graphene and the corresponding band structure. The filled circles are hydrogen atoms. The structures are periodic along the edge with periodicity *L*. The gray area shows the bands allowed in 'bulk' graphene. (a) Most stable edge configuration, (b) other stable edge modifications. Here *z* denotes the zigzag edges, while *a* denotes the armchair edge (Reprinted figure with permission from T. Wassmann *et al*., Physical Review Letters, 101, 096402, 2008 [641]. Copyright © (2008) by the American Physical Society).

investigated – identical modification of two opposite edges or modification of a single edge. Because the zigzag edges are known to possess localized states, they have attracted considerable attention from the researchers. A wide range of chemical groups have been used for functionalizing the graphene edges: from simple chemical groups, such as $NH_2$, $NO_2$, O to massive molecules such as short branched alkanes [644]. Below, we consider the influence of the edge functionalization by different chemical groups on the electronic properties of graphene.

The lowest energy state of a graphene nanoribbon is known to have opposite spin ordering between the zigzag edges [362,412,414–416], i.e. when a spin-up state is localized on one sublattice, and a spin-down state is localized on the other, thereby opening a gap. The energetic bands of this state are most often spin degenerate, but can be slightly non-degenerate providing similar band structures for both spin states where the spin gap symmetry is preserved. A similar picture is observed when the two opposite zigzag edges are identically functionalized by the same groups [645–648]. Thus, for edges terminated with hydrogen or hydroxyl groups, the system is spin polarized in equilibrium and doubly degenerate [645], while using OH or NH functional groups gives a spin-unpolarized system. Almost degenerate spin states are found for graphene with zigzag edges terminated by $NH_2$ groups at each second carbon atom [646]. Moreover, by changing the type of the functional groups the size of a gap, spin ordering along the zigzag edges and distribution of the molecular orbitals over the graphene structure can be manipulated [648]. The simulation of the size of the band gap when both zigzag edges are functionalized by the same chemical groups are presented in Figure 127. According to the presented data, the oxidation of the graphene edges can decrease the band gap to almost half that of mono-hydrogenated zigzag edges. However, functionalization of both zigzag edges does not lift the degeneracy.

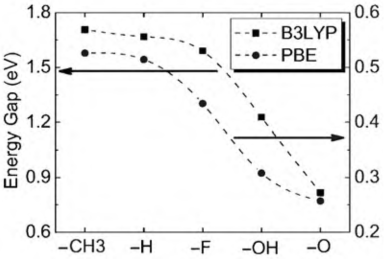

Figure 127. The band gap of the nanoscale graphene with the zigzag edges functionalized by the same chemical groups. The simulations are performed with PBE and B3LYP functionals (Reprinted figure with permission from H. Zheng and W. Duley, Physical Review B, 78, 045421, 2008 [648]. Copyright © (2008) by the American Physical Society.).

Modification of opposite zigzag edges by different chemical groups, which stabilizes a state with ferromagnetic ordering between the opposite edges, can induce an asymmetry in the potentials between these edges. This leads to an energy shift of the orbitals localized on the edges, thereby lifting the spin degeneracy of the electronic states localized on the opposite zigzag edges. Therefore, functionalization of a single zigzag edge is the way to generate a fully spin-polarized state in graphene, which can also be characterized by the spin gap asymmetry. For example, bearded ribbons where one zigzag edge is pure and has dangling bonds whereas the other edge has an additional carbon bond saturating each dangling bond have been found to have a gap [643]. But the most common case is when functionalization of the zigzag edge is performed by termination of the dangling bonds by some atoms which are not carbon. It was shown in [649] with first-principles methods that for graphene with one mono-hydrogenated zigzag edge and one di-hydrogenated edge, spontaneous magnetization occurs. The electronic structure of such a graphene system is fully spin-polarized and has a flat band near the Fermi level composed of the localized edge states. The flat band of the spin-up states is located below the Fermi level, while for the spin-down states it is just above the Fermi level. The achieved splitting between spin-up and spin-down states was 0.5–0.6 eV, while the gap was ~0.2 eV. The magnetic moment of such a structure was not zero and the total spin equaled one half of the number of unit cells. The functionalization of a single edge by fluorine atoms or oxygen atoms when a second edge is monohydrogenated has been considered in [650]. The band structures of fluorinated and oxidized graphene are similar to each other and distinguished by the presence of flat bands, which appear near the Fermi level and are spin-polarized only around the K point. However, the spin-up and spin-down states are slightly separated from each other in energy, thereby possessing a weak spin gap asymmetry.

The methylene-substituted graphene structure, where every carbon atom or every second carbon atom at a single zigzag edge is bound to a methylene group, did not show a strong magnetic behavior. Cervantes-Sodi *et al.* [646,647] considered different functional groups terminating the dangling bonds at a single zigzag edge to induce the spin-polarization in graphene. The simulation results of the spin density of the states performed with first-principles method are shown in Figure 128. There the edge functionalization significantly modifies the electronic structure of the graphene

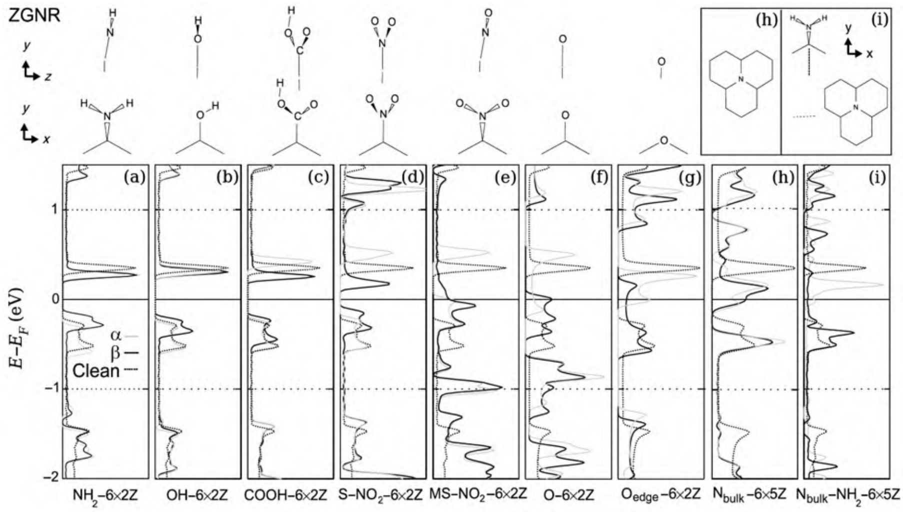

Figure 128. The spin density of the states for graphene with a single zigzag edge functionalized by the chemical groups. The spin density distribution for $\alpha$- and $\beta$-spin states is presented in comparison to those for pure (clean) graphene (Reprinted figure with permission from F. Cervantes-Sodi *et al.*, Physical Review B, 77, 165427, 2008 [646]. Copyright © (2008) by the American Physical Society.).

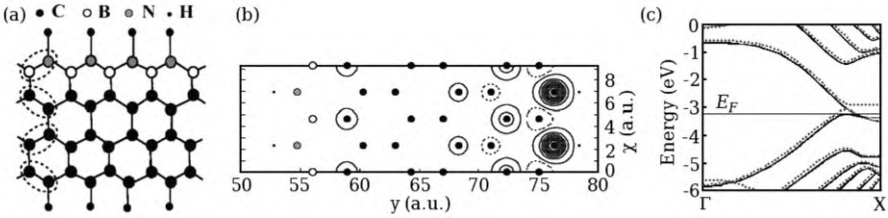

Figure 129. The structure and electronic properties of graphene where the border carbon atoms at one zigzag edge are substituted by the B or N atoms. (a) The structure of the graphene ribbon, (b) The spin-density distribution for the state where spin separation between sublattices does not occur. (c) The energy band structure for a ferrimagnetic state. Solid and dashed lines represent the spin-up and spin-down states (Reprinted figure with permission from J. Nakamura *et al.*, Physical Review B, 72, 205429, 2005 [415]. Copyright © (2005) by the American Physical Society.).

ribbon, particularly lifting the spin degeneracy. In some cases, a significant spin gap asymmetry is achieved producing half-metallic behavior at zero electric field (see the S–$NO_2$–6 × 2Z structure). However, functionalization of the armchair edges has been shown to slightly lift the spin degeneracy [646] and induce impurity bands. Similar results, showing that if two opposite zigzag edges are functionalized by two different types of chemical groups, a gap asymmetry of the $\alpha$- and $\beta$-spin channels can be obtained, was also presented [418,651,652]. Thus, if one zigzag edge is terminated by OH groups and the opposite one by Cl atoms, zero band gap for one spin state and semiconductor gap for the other spin state are observed, thereby giving half-metallicity [651].

Another way to generate asymmetry of the potentials between two opposite zigzag edges is by substitution of the carbon atoms at the edges. Substitution of carbon atoms at a single zigzag edge by the B and N atoms [415], as presented in Figure 129(a), leads to occupation of the A and B sublattices by both spins, thereby providing the ferromagnetic spin ordering of the localized states between the zigzag edges and $n_{\uparrow} - n_{\downarrow} = 0.29$ per unit cell. The spin density distribution and band diagram for this state are presented in Figure 129(b) and (c), respectively. The spin ordering occurs due to the imbalance of the majority and minority spins at the zigzag edge, where substitution of the carbon atoms is performed. The obtained band structure corresponds to a metallic system. The lattice dissimilarity between the opposite zigzag edges generates asymmetry of the potentials between the opposite zigzag edges. The nanoribbons must be wider than a certain minimum value before spontaneous spin polarization may occur.

In [653], Berashevich and Chakraborty reported that for nanoscale graphene the highest symmetry is $D_{2h}$ for which the sublattice symmetry is preserved and a gap can occur only due to the confinement effect. For the $D_{2h}$ symmetry the HOMO and LUMO orbitals are localized at the zigzag edges but their electron density is equally distributed over both edges. Termination of a single zigzag edge by hydrogen or substitutional doping of the carbon atoms along a single zigzag edge by a dopant, such as nitrogen, breaks the sublattice symmetry thereby lowering the $D_{2h}$ symmetry to the $C_{2v}$ symmetry with a mirror plane of symmetry perpendicular to the zigzag edges. For the $C_{2v}$ symmetry, the HOMO and LUMO orbitals are characterized by the $\alpha$- and $\beta$-spin states localized on the opposite zigzag edges. For pure graphene in a state with the $C_{2v}$ symmetry, where symmetry breaking is induced by the spin distribution between the zigzag edges, the band gaps for two different spins $\Delta_\alpha$ and $\Delta_\beta$ are almost identical. Thus, for graphene with four carbon rings along the zigzag edge and five along the armchair edge, these band gaps are found to be of the order of $\sim$1.5 eV. The hydrogenation of a single zigzag edge leads to saturation of the dangling $\sigma$ bonds at the terminated edge but does not significantly change the energy of the $\mathrm{HOMO}_\alpha$ and $\mathrm{LUMO}_\beta$ states localized at the terminated edge. The resulting non-degeneracy of the $\alpha$- and $\beta$-spin states is not large, and the gap of the $\alpha$-spin state ($\Delta_\alpha = 1.8$ eV) is almost identical to that of the $\beta$-spin state ($\Delta_\beta = 2.1$ eV). However, hydrogen termination along a single zigzag edge increases the gap from $\sim$1.5 eV for pure graphene in state of $C_{2v}$ symmetry to $\sim$1.9 eV due to major breaking of the sublattice symmetry. The substitutional doping by nitrogen along a single zigzag edge shifts down the orbital energies of the $\mathrm{HOMO}_\alpha$ and $\mathrm{LUMO}_\beta$ states localized at the doped edge and results in a strong electron non-degeneracy for these orbitals. Slight enhancement of the gap occurs for the $\alpha$-spin state up to $\Delta_\alpha = 2.2$ eV, but there is a significant decrease of the gap for the $\beta$-spin state down to $\Delta_\beta = 0.8$ eV. The achieved size of the band gap for $\alpha$- and $\beta$-spin states corresponds to the half-semiconducting behavior. However, increasing the size of the graphene sample results in a decrease of both the $\Delta_\alpha$ and $\Delta_\beta$ gaps due to diminishing confinement effect. When the number of carbon rings along the zigzag edges is six and seven along the armchair edges, the gap for the $\alpha$-spin state is already suppressed to 1.13 eV while for the $\beta$-spin state it is 0.19 eV, which corresponds to the half-metallic behavior.

The state with ferromagnetic spin ordering between the zigzag edges when one edge is doped by boron was obtained in [448]. Metallic behavior for the majority spin channel and insulating behavior for the minority spin channel was observed in this case. An applied electric field was found to have no influence on this behavior, i.e. the magnitude of the gap remains the same for a wide range of the field strengths as a result of identical influence of the transverse electric field on both spin channels. In [654] it was shown that for substitution of one or several carbon atoms at the zigzag edges, the system becomes fully spin-polarized with a opening of band gap near the Fermi level, thereby switching from metallic to semiconducting behavior. The opposite was found in another case [646], where initially semiconducting graphene was converted to the metallic state by substitution of carbon atoms at both zigzag and armchair edges. Moreover, the substitution of the carbon atoms at a single zigzag edge by O (Figure 128g) and in the center of the ribbon by N (Figure 128h) has induced impurity states in the band gap of the zigzag nanoribbons, consequently providing the semiconductor-metal transition. Additionally, it was found [655] that the substitutional doping of a single carbon atom at the zigzag edge by an O, B or N atom can inject a hole or electron into graphene depending on the impurity type. Therefore, such substitution induces a localized impurity state close to the Fermi level. Because the induced impurity level affects the $\pi/\pi^*$ levels of graphene, alteration of the transport properties of graphene occurs. For the armchair nanoribbon [646], the substitution of carbon atoms on the armchair edges by B and N was found to induce localized states which appear deep inside the valence and conduction bands. This actually could discourage manipulation of the electronic properties of the armchair nanoribbons.

In the system with a line of atomic substitutions in the middle of the graphene sheet, both metal–semiconductor and semiconductor–metal transitions have been observed [656]. The impurity line breaks the translation symmetry normal to the edges, and provides a modification of the electronic properties. For a zigzag nanoribbon, the impurity line induced along the armchair edges splits the graphene sheet into two stacked nanoribbons and therefore its electronic properties are significantly modified. If the graphene structure cannot be divided equally then the achieved electronic structure is a superposition of two bands of the nanoribbons of different sizes. For armchair nanoribbons a similar impurity line has been placed along the zigzag edge [656]. Depending on the nanoribbon geometry, there were three types of energy band structures: two semiconductor and one metallic. The single impurity line has been found to convert the semiconducting armchair nanoribbon to a metallic one and the metallic to semiconducting ribbon. Replacing the middle carbon chain by a boron-nitride, nanoribbon was also investigated [657]. It was found that depending on the number of replaced chains the properties of the graphene ribbon can be modified. The system with two chains replaced by a B–N system, shows a spin gap asymmetry, where one spin channel is semiconducting with a gap of 0.5 eV (whose size is similar to that of pure graphene), while the gap in the second spin channel is significantly reduced in comparison to the case of pure graphene. The replacement of four chains leads to the appearance of one conducting channel and an increase of the band gap for the second spin channel, whereas replacement of six chains shows a decrease in the gap for both spin channels. However, such a replacement breaks the particle symmetry, thus mixing spin states along the edges and therefore the whole lattice is characterized by no dominance of spin states at any sites.

As we have shown above, the main advantage of functionalization of the edges of a graphene ribbon is the possibility to achieve a half-metallic behavior of graphene without applying an external electric field. This has enormous potential for application in developing spin-selective devices based on graphene systems [48,450,453–464].

## Acknowledgements

This work was supported by the Canada Research Chairs program and the NSERC Discovery Grant, both awarded to T. Chakraborty. The work of K. Ziegler was supported by the Deutsche Forschungsgemeinschaft. T. Chakraborty would like to thank Dr. Xuefeng Wang for valuable discussions and help in preparing the section on plasmons in graphene. We thank Professor Peter Fulde for his support. We also thank Jean-Noel Fuchs, Mark Goerbig, Peter Maksym, Sergei Sharapov for reading the early version of the manuscript and offering valuable comments to improve the article. Finally, we wish to thank numereous colleagues who offered valuable suggestions based on the preprint version (abridged): arXiv:1003.0391, posted online.

## Notes

1. Structures with up to 10 carbon layers are known as few-layer graphenes, while structures with 10–100 layers are known as thin graphite films [1].
2. The experimental study of very thin graphite is older than Geim and Novoselov's 'initial' discovery in 2004. For example, [19,20], both discuss the possible fabrication of graphene.
3. *Nanoculture – Implications of the New Technoscience*, edited by N. Katherine Hayles (Intellect Books, 2004)
4. This assumption does not adequately produce the band structure near the center of the Brillouin zone where the $\sigma$ bands have the lowest energy. See, for example, [140] for the experimental evidence of the $\sigma$ bands, and [13] for a description of the tight-binding $\sigma$ bands in monolayer graphene. However, the low-energy and transport properties of bilayer graphene are determined by the $\pi$ bands, so we limit ourselves only to their discussion.
5. Both mono- and bilayer graphene spontaneously form corrugations, or ripples, which are a significant mechanism for the stable formation of the two-dimensional crystal, and which may add to the disorder in the system (Section 5).
6. There is a certain confusion in the literature over the labelling of Landau levels in bilayer graphene since two common notations exist. In the two-band model, it is convenient to label using $\mathfrak{n} \in \{\ldots, -3, -2, 0, 1, +2, +3, \ldots\}$, while in the four-band model, the notation $n \in \{\ldots, -2, -1, -0, +0, +1, +2, \ldots\}$ is usually used. In this section we shall use the notations as defined in this endnote, so that $\mathfrak{n}$ refers to the 'two-band' labels, while $n$ denotes 'four-band' labels.
7. The parameter $\beta$ phenomenologically describes the small splitting between the $\mathfrak{n} = 0$ and $\mathfrak{n} = 1$ levels caused by effects like those parametrized by $\Delta$ and $t'$. The notation $\mathfrak{n}$ is defined in endnote 6.
8. As a result of the multiplication of the model Slater determinant wave function $\varphi$ by the correlation factor $F$, the multiparticle state $F\varphi$ will most likely have projections on states outside of the bands, in particular on states with energies lower than the bottom of the valence band. This is clearly unphysical and has to be rectified by requiring that projections of $F\varphi$ on the states with momenta larger than a cut-off momentum, must

vanish. This cut-off momentum is determined, for example by requiring it to yield the correct number of allowed valence band states. Another constraint which is perhaps necessary is to impose explicitly the normalization of $g(r)$, i.e.

$$\int \mathrm{d}r[g(r) - 1] = -1$$

(P. Pietiläinen, private communication).

9. The spin–orbit coupling strength in graphene can be small [249]. However, the results presented in this section are valid for similar gap size in the energy band.
10. For $|\mu| \gg |\omega|$ the expression in Equation (71) is linear in $\mu$. However, the conductivity vanishes when we take the DC limit at fixed scattering rate.
11. The SCBA has been criticized by several authors as being not applicable to Dirac fermions [311,312,319,320]. This is based on the fact that certain terms of the perturbative series are neglected in the SCBA. The above analysis sheds a different light on this issue, namely that the SCBA is only the result of a special scalar form of the solution of the more general matrix saddle-point equation. This implies that the average one-particle Green's function, including the density of states, requires the full solution of the matrix equation (81). On the other hand, for the scattering rate $\eta$ the scalar equation (80) (i.e. the SCBA) is justified as a reasonable approximation even for Dirac fermions.

## References

[1] A.K. Geim and K.S. Novoselov, Nat. Mater. 6 (2007), p. 183.
[2] M.J. Allen, V.C. Tung, and R.B. Kaner, Chem. Rev. 110 (2010), p. 132.
[3] T. Ando, Physica E 40 (2007), p. 213.
[4] V.P. Gusynin, S.G. Sharapov, and J.P. Carbotte, Int. J. Mod. Phys. B 21 (2007), p. 4611.
[5] N.M.R. Peres, J. Physica Condens. Matter 21 (2009), p. 323201.
[6] Eur. Phys. J. Spec. Top. 148 (2007), pp. 1–181; Solid State Commun. 143 (2007), pp. 1–125; Solid State Commun. 149 (2009), pp. 1039–1160.
[7] A.K. Geim and A.H. MacDonald, Phys. Today 60 (2007), p. 35; A.K. Geim and P. Kim, Sci. Am. 298 (2008), p. 90.
[8] T. Chakraborty, *Quantum Dots*, Elsevier, Amsterdam, 1999.
[9] T. Chakraborty, Comments Condens. Matter Phys. 16 (1992), p. 35.
[10] P.R. Wallace, Phys. Rev. 71 (1947), p. 622; J.C. Slonczewski and P.R. Weiss, Phys. Rev. 109 (1958), p. 272.
[11] J.W. McClure, Phys. Rev. 104 (1956), p. 666.
[12] R.R. Haering and P.R. Wallace, J. Phys. Chem. Solids 3 (1957), p. 253; H. Sato, J. Phys. Soc. Japan 14 (1959), p. 609.
[13] R. Saito, G. Dresselhaus, and M.S. Dresselhaus, *Physical Properties of Carbon Nanotubes*, Imperial College Press, London, 1998.
[14] S. Reich, C. Thomsen, and J. Maultzsch, *Carbon Nanotubes*, Wiley-VCH, Weinheim, 2004.
[15] T. Ando, in *Nano-Physics and Bio-Electronics: A New Odyssey*, Chap. 1, T. Chakraborty, F. Peeters, and U. Sivan, eds., Elsevier, Amsterdam, 2002.
[16] T. Ando, T. Nakanishi, and R. Saito, J. Phys. Soc. Japan 67 (1998), p. 2857.
[17] K.S. Novoselov, A.K. Geim, S.V. Morozov, D. Jiang, M.I. Katsnelson, I.V. Grigorieva, S.V. Dubonos, and A.A. Firsov, Nature 438 (2005), pp. 197–200.
[18] A. Grüneis, C. Attaccalite, A. Rubio, D.V. Vyalikh, S.L. Molodtsov, J. Fink, R. Follath, W. Eberhardt, B. Büchner, and T. Pichler, Phys. Rev. B 80 (2009), p. 075431.
[19] X. Lu, M. Yu, H. Huang, and R.S. Ruoff, Nanotechnology 10 (1999), p. 269.

[20] R.B. Little, J. Cluster Sci. 14 (2003), p. 135.
[21] K.S. Novoselov, A.K. Geim, S.V. Morozov, D. Jiang, Y. Zhang, S.V. Dubonos, I.V. Grigorieva, and A.A. Firosov, Science 306 (2004), p. 666.
[22] K.S. Novoselov, D. Jiang, F. Schedin, T.J. Booth, V.V. Khotkevich, S.V. Morozov, and A.K. Geim, PNAS 102 (2005), p. 10451.
[23] A.C. Ferrari, J.C. Meyer, V. Scardaci, C. Casiraghi, M. Lazzeri, F. Mauri, S. Piscanec, D. Jiang, K.S. Novoselov, S. Roth, and A.K. Geim, Phys. Rev. Lett. 97 (2006), p. 187401.
[24] J.C. Meyer, A.K. Geim, M.I. Katsnelson, K.S. Novoselov, T.J. Booth, and S. Roth, Nature 446 (2007), p. 60.
[25] K.I. Bolotin, K.J. Sikes, Z. Jiang, M. Klima, G. Fudenberg, J. Hone, P. Kim, and H.L. Stormer, Sol. State Commun. 146 (2008), p. 351.
[26] X. Du, I. Skachko, A. Barker, and E.Y. Andrei, Nat. Nanotechnol. 3 (2008), p. 491.
[27] S.V. Morozov, K.S. Novoselov, M.I. Katsnelson, F. Schedin, D.C. Elias, J.A. Jaszczak, and A.K. Geim, Phys. Rev. Lett. 100 (2008), p. 016602.
[28] C. Berger, Z. Song, T. Li, X. Li, A.Y. Ogbazghi, R. Feng, Z. Dai, A.N. Marchenkov, E.H. Conrad, P.N. First, and W.A. de Heer, J. Phys. Chem. B 108 (2004), p. 19912.
[29] C. Berger, Z. Song, X. Li, X. Wu, N. Brown, C. Naud, D. Mayou, T. Li, J. Hass, A.N. Marchenkov, E.H. Conrad, P.N. First, and W.A. de Heer, Science 312 (2006), p. 397.
[30] J. Hass, W.A. de Heer, and E.H. Conrad, J. Phys.: Condens. Matter 20 (2008), p. 323202.
[31] W.A. de Heer, C. Berger, X. Wu, P.N. First, E.H. Conrad, X. Li, T. Li, M. Sprinkle, J. Hass, M.L. Sadowski, M. Potemski, and G. Martinez, Solid State Commun. 143 (2007), p. 92.
[32] F. Varchon, R. Feng, J. Hass, X. Li, B. Ngoc Nguyen, C. Naud, P. Mallet, J.-Y. Veuillen, C. Berger, E.H. Conrad, and L. Magaud, Phys. Rev. Lett. 99 (2007), p. 126805.
[33] Th. Seyller, A. Bostwick, K.V. Emtsev, K. Horn, L. Ley, J.L. McChesney, T. Ohta, J.D. Riley, E. Rotenberg, and F. Speck, Phys. Status Solidi b 245 (2008), p. 1436.
[34] M.L. Sadowski, G. Martinez, M. Potemski, C. Berger, and W.A. de Heer, Phys. Rev. Lett. 97 (2006), p. 266405.
[35] S.Y. Zhou, G.-H. Gweon, A.V. Fedorov, P.N. First, W.A. de Heer, D.-H. Lee, F. Guinea, A.H. Castro Neto, and A. Lanzara, Nat. Materi. 6 (2007), p. 770.
[36] A. Bostwick, T. Ohta, Th. Seyller, K. Horn, and E. Rotenberg, Nat. Phys. 3 (2007), p. 36.
[37] A.N. Obraztsov, E.A. Obraztsova, A.V. Tyurnina, and A.A. Zolotukhin, Carbon 45 (2007), p. 2017.
[38] A. Reina, X. Jia, J. Ho, D. Nezich, H. Son, V. Bulovic, M.S. Dresselhaus, and J. Kong, Nano Lett. 9 (2009), p. 30.
[39] K.S. Kim, Y. Zhao, H. Jang, S.Y. Lee, J.M. Kim, K.S. Kim, J.-H. Ahn, P. Kim, J.-Y. Choi, and B.H. Hong, Nature 457 (2009), p. 706.
[40] Q. Yu, J. Lian, S. Siriponglert, H. Li, Y.P. Chen, and S.-S. Pei, Appl. Phys. Lett. 93 (2008), p. 113103.
[41] J. Coraux, A.T. N'Diaye, C. Busse, and T. Michely, Nano Lett. 8 (2008), p. 565.
[42] X. Li, W. Cai, J. An, S. Kim, J. Nah, D. Yang, R. Piner, A. Velamakanni, I. Jung, E. Tutuc, S.K. Banerjee, L. Colombo, and R.S. Ruoff, Science 324 (2009), p. 1312.
[43] M.C. Lemme, Solid State Phenom. 156–158 (2010), pp. 499–509.
[44] Y.-M. Lin, K.A. Jenkins, A. Valdes-Farcia, J.P. Small, D.B. Farmer, and P. Avouris, Nano Lett. 9 (2009), p. 422.
[45] I. Meric, N. Baklitskaya, P. Kim, and K.L. Shepard, *Electron Devices Meeting*, 2008. (IEDM 2008), IEEE International, San Francisco, 2008.

[46] J.S. Moon, D. Curtis, M. Hu, D. Wong, C. McGuire, P.M. Campbell, G. Jernigan, J.L. Tedesco, B. VanMil, R. Myers-Ward, C. Eddy, and D.K. Gaskill, IEEE Electron Dev. Lett. 30 (2009), p. 650.

[47] C. Stampfer, E. Schurtenberger, F. Molitor, J. Güttinger, T. Ihn, and K. Ensslin, Nano Lett. 8 (2008), pp. 2378–2383.

[48] N. Tombros, C. Jozsa, M. Popinciuc, H.T. Jonkman, and B.J. van Wees, Nature 448 (2007), p. 571.

[49] F. Schedin, A.K. Geim, S.V. Morozov, E.W. Hill, P. Blake, M.I. Katsnelson, and K.S. Novoselov, Nat. Mater. 6 (2007), p. 652.

[50] J.S. Bunch, S.S. Verbridge, J.S. Alden, A.M. van der Zande, J.M. Parpia, H.G. Craighead, and P.L. McEuen, Nano Lett. 8 (2008), p. 2458.

[51] E. Stolyarova, D. Dtolyarov, K. Bolotin, S. Ryu, L. Liu, K.T. Rim, M. Kilma, M. Hybertsen, I. Pogorelsky, I. Pavlishin, K. Kusche, J. Hone, P. Kim, H. Stormer, V. Yakimenko, and G. Flynn, Nano Lett. 9 (2009), p. 332.

[52] B. Standley, W. Bao, H. Zhang, J. Bruck, and C.N. Lau, Marc Bockrath Nano Lett. 8 (2008), p. 3345.

[53] X. Wang, L. Zhi, and K. Müllen, Nano Lett. 8 (2008), p. 323.

[54] P. Blake, P.D. Brimicombe, R.R. Nair, T.J. Booth, D. Jiang, F. Schedin, L.A. Ponomarenko, S.V. Morozov, H.F. Gleeson, E.W. Hill, A.K. Geim, and K.S. Novoselov, Nano Lett. 8 (2008), p. 1704.

[55] M. Gibertini, A. Singha, V. Pellegrini, M. Polini, G. Vignale, A. Pinczuk, L.N. Pfeiffer, and K.W. West, Phys. Rev. B 79 (2009), p. 241406.

[56] B.A. Bernevig, T.L. Hughes, S.-C. Zhang, H.-D. Chen, and C. Wu, Int. J. Mod. Phys. B 20 (2006), p. 3257.

[57] J.H. Ho, Y.H. Lai, Y.H. Chiu, and M.F. Lin, Physica E 40 (2008), pp. 1722–1725.

[58] Y. Zheng and T. Ando, Phys. Rev. B 65 (2002), p. 245420.

[59] J. Alicea and M.P.A. Fisher, Phys. Rev. B 74 (2006), p. 075422.

[60] D.A. Abanin, P.A. Lee, and L.S. Levitov, Phys. Rev. Lett. 98 (2007), p. 156801.

[61] V. Lukose, R. Shankar, and G. Baskaran, Phys. Rev. Lett. 98 (2007), p. 116802.

[62] R.S. Deacon, K.-C. Chuang, R.J. Nicholas, K.S. Novoselov, and A.K. Geim, Phys. Rev. B 76 (2007), p. 081406(R).

[63] Z. Jiang, E.A. Henriksen, L.C. Tung, Y.-J. Wang, M.E. Schwartz, M.Y. Han, P. Kim, and H.L. Stormer, Phys. Rev. Lett. 98 (2007), p. 197403.

[64] D.L. Miller, K.D. Kubista, G.M. Rutter, M. Ruan, W.A. de Heer, P.N. First, and J.A. Stroscio, Science 324 (2009), pp. 924–927.

[65] G. Li, A. Luican, and E.Y. Andrei, Phys. Rev. Lett. 102 (2009), p. 176804.

[66] G. Li and E.Y. Andrei, Nat. Phys. 3 (2007), pp. 623–627.

[67] W. Kohn, Phys. Rev. 123 (1961), p. 1242.

[68] P. Plochocka, C. Faugeras, M. Orlita, M.L. Sadowski, G. Martinez, M. Potemski, M.O. Goerbig, J.-N. Fuchs, C. Berger, and W.A. de Heer, Phys. Rev. Lett. 100 (2008), p. 087401.

[69] C.P. Chang, C.L. Lu, F.L. Shyu, R.B. Chen, Y.K. Fang, and M.F. Lin, Carbon 42 (2004), p. 2975.

[70] T. Nakajima and H. Aoki, Physica E 40 (2008), p. 1354.

[71] I.A. Luk'yanchuk and A.M. Bratkovsky, Phys. Rev. Lett. 100 (2008), p. 176404.

[72] T. Chakraborty and P. Pietiläinen, *The Quantum Hall Effects*, 2nd ed., Springer, Heidelberg, New York, 1995.

[73] T. Chakraborty, Adv. Phys. 49 (2000), p. 959.

[74] V.P. Gusynin and S.G. Sharapov, Phys. Rev. Lett. 95 (2005), p. 146801.

[75] P.M. Ostrovsky, I.V. Gornyi, and A.D. Mirlin, Phys. Rev. B 77 (2008), p. 195430.

[76] H. Aoki and T. Ando, Solid State Commun. 38 (1981), p. 1079.

[77] R.E. Pringe, Phys. Rev. B 23 (1981), p. 4802.
[78] D.J. Thouless, J. Phys. C 14 (1981), p. 3475.
[79] D.J. Thouless and M. Kohmoto, Phys. Rev. Lett. 49 (1982), p. 41.
[80] V.P. Gusynin and S.G. Sharapov, Phys. Rev. B 73 (2006), p. 245411.
[81] N.M.R. Peres, F. Guinea, and A.H. Castro Neto, Phys. Rev. B 73 (2006), p. 125411.
[82] B. Dóra and P. Thalmeier, Phys. Rev. B 76 (2007), p. 035402.
[83] S. Masubuchi, K. Suga, M. Ono, K. Kindo, S. Takeyama, and T. Machida, J. Phys. Soc. Japan 77 (2008), p. 113707.
[84] K.S. Novoselov, Z. Jiang, Y. Zhang, S.V. Morozov, H.L. Stormer, U. Zeitler, J.C. Maan, G.S. Boebinger, P. Kim, and A.K. Geim, Science 315 (2007), p. 1379.
[85] Y. Zhang, Y.-W. Tan, H.L. Stormer, and P. Kim, Nature 438 (2005), pp. 201–204.
[86] X. Wu, Y. Hu, M. Ruan, N.K. Madiomanana, J. Hankinson, M. Sprinkle, C. Berger, and W.A. de Heer, Appl. Phys. Lett. 95 (2009), p. 223108.
[87] T. Shen, J.J. Gu, M. Xu, Y.Q. Wu, M.L. Bolen, M.A. Capano, L.W. Engel, and P.D. Ye, Appl. Phys. Lett. 95 (2009), p. 172105.
[88] Z. Jiang, Y. Zhang, Y.-W. Tan, H.L. Stormer, and P. Kim, Solid State Commun. 143 (2007), pp. 14–19.
[89] A.J.M. Giesbers, U. Zeitler, M.I. Katsnelson, L.A. Ponomarenko, T.M. Mohiuddin, and J.C. Maan, Phys. Rev. Lett. 99 (2007), p. 206803.
[90] A.J.M. Giesbers, U. Zeitler, M.I. Katsnelson, L.A. Ponomarenko, T.M.G. Mohiuddin, and J.C. Maan, Physica E 40 (2008), pp. 1089–1091.
[91] Z. Jiang, Y. Zhang, H.L. Stormer, and P. Kim, Phys. Rev. Lett. 99 (2007), p. 106802.
[92] Y. Zhang, Z. Jiang, J.P. Small, M.S. Purewal, Y.-W. Tan, M. Fazlollahi, J.D. Chudow, J.A. Jaszczak, H.L. Stormer, and P. Kim, Phys. Rev. Lett. 96 (2006), p. 136806.
[93] J.G. Checkelsky, L. Li, and N.P. Ong, Phys. Rev. Lett. 100 (2008), p. 206801.
[94] J.G. Checkelsky, L. Li, and N.P. Ong, Phys. Rev. B 79 (2009), p. 115434.
[95] X. Du, I. Skachko, F. Duerr, A. Luican, and E.Y. Andrei, Nature 462 (2009), p. 192.
[96] K.I. Bolotin, F. Ghahari, M.D. Shulman, H.L. Stormer, and P. Kim, Nature 462 (2009), p. 196.
[97] A.J.M. Giesbers, L.A. Ponomarenko, K.S. Novoselov, A.K. Geim, M.I. Katsnelson, J.C. Maan, and U. Zeitler, Phys. Rev. B 80 (2009), p. 201403.
[98] K. Nomura and A.H. MacDonald, Phys. Rev. Lett. 96 (2006), p. 256602.
[99] D.N. Sheng, L. Sheng, and Z.Y. Weng, Phys. Rev. B 73 (2006), p. 233406.
[100] V.P. Gusynin, V.A. Miransky, S.G. Sharapov, and I.A. Shovkovy, Phys. Rev. B 74 (2006), p. 195429.
[101] M.O. Goerbig, R. Moessner, and B. Douçot, Phys. Rev. B 74 (2006), p. 161407(R).
[102] K. Yang, S. Das Sarma, and A.H. MacDonald, Phys. Rev. B 74 (2006), p. 075423.
[103] J. Alicea and M.P.A. Fisher, Solid. State. Commun. 143 (2007), pp. 504–509.
[104] D.A. Abanin, P.A. Lee, and L.S. Levitov, Sol. State. Commun. 143 (2007), pp. 77–85.
[105] M. Koshino and T. Ando, Phys. Rev. B 75 (2007), p. 033412.
[106] L. Sheng, D.N. Sheng, F.D.M. Haldane, and L. Balents, Phys. Rev. Lett. 99 (2007), p. 196802.
[107] K. Yang, Solid State Commun. 143 (2007), pp. 27–32.
[108] E.V. Gorbar, V.P. Gusynin, and V.A. Miransky, Low Temp. Phys. 34 (2008), p. 790.
[109] V.P. Gusynin, V.A. Miransky, S.G. Sharapov, and I.A. Shovkovy, Phys. Rev. B 77 (2008), p. 205409.
[110] A.L.C. Pereira and P.A. Schulz, Phys. Rev. B 77 (2008), p. 075416.
[111] V.P. Gusynin, V.A. Miransky, S.G. Sharapov, and I.A. Shovkovy, Low Temp. Phys. 34 (2008), p. 778.
[112] T. Kawarabayashi, Y. Hatsugai, and H. Aoki, Phys. Rev. Lett. 103 (2009), p. 156804.
[113] T. Chakraborty and P. Pietiläinen, Eur. Phys. Lett. 80 (2007), p. 37007.

[114] I.F. Herbut, Phys. Rev. B 75 (2007), p. 165411.
[115] J.-N. Fuchs and P. Lederer, Phys. Rev. Lett. 98 (2007), p. 016803.
[116] N.A. Viet, H. Ajiki, and T. Ando, J. Phys. Soc. Japan 63 (1994), p. 3036.
[117] H. Ajiki and T. Ando, J. Phys. Soc. Japan 64 (1995), p. 260.
[118] H. Ajiki and T. Ando, J. Phys. Soc. Japan 65 (1996), p. 2976.
[119] H. Ajiki and T. Ando, Phys. B 227 (1996), p. 342.
[120] M. Arikawa, Y. Hatsugai, and H. Aoki, Phys. Rev. B 78 (2008), p. 205401.
[121] S. Park and H.-S. Sim, Phys. Rev. B 77 (2008), p. 075433.
[122] L. Brey and H.A. Fertig, Phys. Rev. B 73 (2006), p. 195408.
[123] D.A. Abanin, P.A. Lee, and L.S. Levitov, Phys. Rev. Lett. 96 (2006), p. 176803.
[124] A.H. Castro Neto, F. Guinea, and N.M.R. Peres, Phys. Rev. B 73 (2006), p. 205408.
[125] H.A. Fertig and L. Brey, Solid State Commun. 143 (2007), pp. 86–91.
[126] D.A. Abanin, K.S. Novoselov, U. Zeitler, P.A. Lee, A.K. Geim, and L.S. Levitov, Phys. Rev. Lett. 98 (2007), p. 196806.
[127] D.-K. Ki, S. Jo, and H.-J. Lee, Appl. Phys. Lett. 94 (2009), p. 162113.
[128] E. Shimshoni, H.A. Fertig, and G.V. Pai, Phys. Rev. Lett. 102 (2009), p. 206408.
[129] V.M. Apalkov and T. Chakraborty, Phys. Rev. Lett. 97 (2006), p. 126801.
[130] V. Apalkov, X.-F. Wang, and T. Chakraborty, Int. J. Mod. Phys. B 21 (2007), pp. 1165–1179.
[131] M.O. Goerbig and N. Regnault, Phys. Rev. B 75 (2007), p. 241405.
[132] C. Toke, P.E. Lammert, V.H. Crespi, and J.K. Jain, Phys. Rev. B 74 (2006), p. 235417.
[133] Z. Papic, M.O. Goerbig, and N. Regnault, Solid State Commun. 149 (2009), p. 1056.
[134] F.D.M. Haldane, Phys. Rev. Lett. 51 (1983), p. 605.
[135] N. Shibata and K. Nomura, J. Phys. Soc. Japan 78 (2009), p. 104708.
[136] C.-H. Zhang and Y.N. Joglekar, Phys. Rev. B 75 (2007), p. 245414.
[137] R.B. Laughlin, Phys. Rev. Lett. 50 (1983), p. 1395.
[138] D.A. Abanin, I. Skachko, X. Du, E.Y. Andrei, and L.S. Levitov, Phys. Rev. B 81 (2010), p. 115410.
[139] E. McCann and V.I. Falko, Phys. Rev. Lett. 96 (2006), p. 086805.
[140] T. Ohta, A. Bostwick, T. Seyller, K. Horn, and E. Rotenberg, Science 313 (2006), p. 951.
[141] K.S. Novoselov, E. McCann, S.V. Morozov, V.I. Falko, M.I. Katsnelson, U. Zeitler, D. Jiang, F. Schedin, and A.K. Geim, Nat. Phys. 2 (2006), p. 177.
[142] P. Blake, E.W. Hill, A.H. Castro Neto, K.S. Novoselov, D. Jiang, R. Yang, T.J. Booth, and A.K. Geim, Appl. Phys. Lett. 91 (2007), p. 063124.
[143] D.S.L. Abergel, A. Russell, and V.I. Falko, Appl. Phys. Lett. 91 (2007), p. 063125.
[144] S. Roddaro, P. Pingue, V. Piazza, V. Pellegrini, and F. Beltram, Nano Lett. 7 (2007), p. 2707.
[145] C. Casiraghi, A. Hartschuh, E. Lidorikis, H. Qian, H. Harutyunyan, T. Gokus, K.S. Novoselov, and A.C. Ferrari, Nano Lett. 7 (2007), p. 2711.
[146] R.R. Nair, P. Blake, A.N. Grigorenko, K.S. Novoselov, T.J. Booth, T. Stauber, N.M.R. Peres, and A.K. Geim, Science 320 (2008), p. 1308.
[147] A.B. Kuzmenko, E. van Heumen, D. van der Marel, P. Lerch, P. Blake, K.S. Novoselov, and A.K. Geim, Phys. Rev. B 79 (2009), p. 115441.
[148] F. Wang, Y. Zhang, C. Tian, C. Girit, A. Zettl, M. Crommie, and Y.R. Shen, Science 320 (2008), p. 206.
[149] E.J. Nicol and J.P. Carbotte, Phys. Rev. B 77 (2008), p. 155409.
[150] L. Benfatto, S.G. Sharapov, and J.P. Carbotte, Phys. Rev. B 77 (2008), p. 125422.
[151] D.S.L. Abergel and V.I. Falko, Phys. Rev. B 75 (2007), p. 155430.
[152] Z.H. Ni, H.M. Wang, J. Kasim, H.M. Fan, T. Yu, Y.H. Wu, Y.P. Feng, and Z.X. Shen, Nano Lett. 7 (2007), p. 2758.

[153] P.E. Gaskell, H.S. Skulason, C. Rodenchuk, and T. Szkopek, Appl. Phys. Lett. 94 (2009), p. 143101.

[154] E.D. Palik, *Handbook of Optical Constants of Solids*, Elsevier, New York, 1998.

[155] G.E. Jellison, J.D. Hunn, and H.N. Lee, Phys. Rev. B 76 (2007), p. 085125.

[156] E.A. Obraztsova, A.V. Osadchy, E.D. Obraztsova, S. Lefrant, and I.V. Yaminsky, Phys. Status Solidi b 245 (2008), p. 2055.

[157] J.H. Warner, M.H. Rümmeli, T. Gemming, B. Büchner, and G.A.D. Briggs, Nano Lett. 9 (2009), p. 102.

[158] E. Sutter, D.P. Acharya, J.T. Sadowski, and P. Sutter, Appl. Phys. Lett. 94 (2009), p. 133101.

[159] D. Graf, F. Molitor, K. Ensslin, C. Stampfer, A. Jungen, C. Hierold, and L. Wirtz, Nano Lett. 7 (2007), p. 238.

[160] P. Poncharal, A. Ayari, T. Michel, and J.-L. Sauvajol, Phys. Rev. B 78 (2008), p. 113407.

[161] Z. Ni, Y. Wang, T. Yu, Y. You, and Z. Shen, Phys. Rev. B 77 (2008), p. 235403.

[162] J.M. Lopes dos Santos, N.M.R. Peres, and A.H. Castro Neto, Phys. Rev. Lett. 99 (2007), p. 256802.

[163] T. Ohta, A. Bostwick, J.L. McChesney, T. Seyller, K. Horn, and E. Rotenberg, Phys. Rev. Lett. 98 (2007), p. 206802.

[164] A.B. Kuzmenko, I. Crassee, D. van der Marel, P. Blake, and K.S. Novoselov, Phys. Rev. B 80 (2009), p. 165406.

[165] L.M. Zhang, Z.Q. Li, D.N. Basov, M.M. Fogler, Z. Hao, and M.C. Martin, Phys. Rev. B 78 (2008), p. 235408.

[166] L.M. Malard, J. Nilsson, D.C. Elias, J.C. Brant, F. Plentz, E.S. Alves, A.H. Castro Neto, and M.A. Pimenta, Phys. Rev. B 76 (2007), p. 201401(R).

[167] L.M. Malard, J. Nilsson, D.L. Mafra, D.C. Elias, J.C. Brant, F. Plentz, E.S. Alves, A.H. Castro Neto, and M.A. Pimenta, Phys. Status Solidi b 245 (2008), p. 2060.

[168] H. Min, B. Sahu, S.K. Banerjee, and A.H. MacDonald, Phys. Rev. B 75 (2007), p. 155115.

[169] P. Gava, M. Lazzeri, A. Marco Saitta, and F. Mauri, Phys. Rev. B 79 (2009), p. 165431.

[170] M. Mucha-Kruczyński, O. Tsyplyatyev, A. Grishin, E. McCann, V.I. Falko, A. Bostwick, and E. Rotenberg, Phys. Rev. B 77 (2008), p. 195403.

[171] Z.F. Wang, Q. Li, H. Su, X. Wang, Q.W. Shi, J. Chen, J. Yang, and J.G. Hou, Phys. Rev. B 75 (2007), p. 085424.

[172] M.I. Katsnelson and M.F. Prokhorova, Phys. Rev. B 77 (2008), p. 205424.

[173] J.C. Meyer, A.K. Geim, M.I. Katsnelson, K.S. Novoselov, D. Obergfell, S. Roth, C. Girit, and A. Zettl, Solid State Commun. 143 (2007), p. 101.

[174] S.Y. Zhou, G.-H. Gweon, J. Graf, A.V. Fedorov, C.D. Spataru, R.D. Diehl, Y. Kopelevich, D.-H. Lee, Steven G. Louie, and A. Lanzara, Nat. Phys. 2 (2006), p. 595.

[175] M. Mucha-Kruczyński, D.S.L. Abergel, E. McCann, and V.I. Falko, J. Phys.: Condens. Matter 21 (2009), p. 344206.

[176] K. Kechedzhi, V.I. Falko, E. McCann, and B.L. Altshuler, Phys. Rev. Lett. 98 (2007), p. 176806.

[177] R.V. Gorbachev, F.V. Tikhonenko, A.S. Mayorov, D.W. Horsell, and A.K. Savchenko, Phys. Rev. Lett. 98 (2007), p. 176805.

[178] E. McCann, Phys. Rev. B 74 (2006), p. 161403.

[179] A. Bostwick, T. Ohta, J.L. McChesney, K.V. Emtsev, T. Seyller, K. Horn, and E. Rotenberg, New J. Phys. 9 (2007), p. 385.

[180] F. Guinea, A.H. Castro Neto, and N.M.R. Peres, Phys. Rev. B 73 (2006), p. 245426.

[181] E.V. Castro, K.S. Novoselov, S.V. Morozov, N.M.R. Peres, J.M.B. Lopes dos Santos, J. Nilsson, F. Guinea, A.K. Geim, and A.H. Castro Neto, Phys. Rev. Lett. 99 (2007), p. 216802.

[182] V.M. Pereira, R.M. Ribeiro, N.M.R. Peres, and A.H. Castro Neto, Phys. Rev. B 79 (2009), p. 045421.

[183] K.F. Mak, C.H. Lui, J. Shan, and T.F. Heinz, Phys. Rev. Lett. 102 (2009), p. 256405.

[184] Y. Zhang, T.-T. Tang, C. Girit, Z. Hao, M.C. Martin, A. Zettl, M.F. Crommie, Y.R. Shen, and F. Wang, Nature 459 (2009), p. 820.

[185] J.B. Oostinga, H.B. Heersche, X. Liu, A.F. Morpurgo, and L.M.K. Vandersypen, Nat. Mater. 7 (2008), p. 151.

[186] M. Aoki and H. Amawashi, Solid State Commun. 142 (2007), p. 123.

[187] G. Fiori and G. Iannaccone, IEEE Electron Dev. Lett. 30 (2009), p. 261.

[188] J.-R. Huang, J.-Y. Lin, B.-H. Chen, and M.-H. Tsai, Phys. Status Solidi b 245 (2007), p. 136.

[189] E.K. Yu, D.A. Stewart, and S. Tiwari, Phys. Rev. B 77 (2008), p. 195406.

[190] J. Milton Pereira Jr, F.M. Peeters, and P. Vasilopoulos, Phys. Rev. B 76 (2007), p. 115419.

[191] N. Nemec and G. Cuniberti, Phys. Rev. B 75 (2007), p. 201404.

[192] M. Nakamura, L. Hirasawa, and K.-I. Imura, Phys. Rev. B 78 (2008), p. 033403.

[193] Y.H. Lai, J.H. Ho, C.P. Chang, and M.F. Lin, Phys. Rev. B 77 (2008), p. 085426.

[194] E.A. Henriksen, Z. Jiang, L.-C. Tung, M.E. Schwartz, M. Takita, Y.-J. Wang, P. Kim, and H.L. Stormer, Phys. Rev. Lett. 100 (2008), p. 087403.

[195] D.S.L. Abergel and T. Chakraborty, Phys. Rev. Lett. 102 (2009), p. 056807.

[196] M. Mucha-Kruczyński, E. McCann, and V.I. Falko, Solid State Commun. 149 (2009), p. 1111.

[197] Y.C. Huang, C.P. Chang, and M.F. Lin, Phys. Rev. B 78 (2008), p. 115422.

[198] S. Viola Kusminskiy, D.K. Campbell, and A.H. Castro Neto, Eur. Phys. Lett. 85 (2009), p. 58005.

[199] M. Ezawa, J. Phys. Soc. Japan 76 (2007), p. 094701.

[200] M. Ezawa, Physica E 40 (2007), p. 269.

[201] T. Misumi and K. Shizuya, Phys. Rev. B 77 (2008), p. 195423.

[202] Y. Barlas, R. Côté, K. Nomura, and A.H. MacDonald, Phys. Rev. Lett. 101 (2008), p. 097601.

[203] K. Shizuya, Phys. Rev. B 79 (2009), p. 165402.

[204] T. Ando, J. Phys. Soc. Japan 76 (2007), p. 104711.

[205] B.E. Feldman, J. Martin, and A. Yacoby, Nat. Phys. 5 (2009), p. 889.

[206] Y. Zhao, P. Cadden-Zimansky, Z. Jiang, and P. Kim, Phys. Rev. Lett. 104 (2010), p. 066801.

[207] J. Nilsson, A.H. Castro Neto, N.M.R. Peres, and F. Guinea, Phys. Rev. B 73 (2006), p. 214418.

[208] E.H. Hwang and S. Das Sarma, Phys. Rev. Lett. 101 (2008), p. 156802.

[209] T. Stauber, N.M.R. Peres, F. Guinea, and A.H. Castro Neto, Phys. Rev. B 75 (2007), p. 115425.

[210] E.V. Castro, N.M.R. Peres, T. Stauber, and N.A.P. Silva, Phys. Rev. Lett. 100 (2008), p. 186803.

[211] S. Viola Kusminskiy, J. Nilsson, D.K. Campbell, and A.H. Castro Neto, Phys. Rev. Lett. 100 (2008), p. 106805.

[212] E.H. Hwang, B.Y.-K. Hu, and S. Das Sarma, Phys. Rev. Lett. 99 (2007), p. 226801.

[213] J. Martin, N. Akerman, G. Ulbricht, T. Lohmann, J.H. Smet, K. von Klitzing, and A. Yacoby, Nat. Phys. 4 (2008), p. 144.

[214] S.K. Saha, U.V. Waghmare, H.R. Krishnamurthy, and A.K. Sood, Phys. Rev. B 78 (2008), p. 165421.

[215] J.-A. Yan, W.Y. Ruan, and M.Y. Chou, Phys. Rev. B 77 (2008), p. 125401.

[216] S. Piscanec, M. Lazzari, F. Mauri, A.C. Ferrari, and J. Robertson, Phys. Rev. Lett. 93 (2004), p. 185503.

[217] J. Yan, E.A. Henriksen, P. Kim, and A. Pinczuk, Phys. Rev. Lett. 101 (2008), p. 136804.

[218] L.M. Malard, D.C. Elias, E.S. Alves, and M.A. Pimenta, Phys. Rev. Lett. 101 (2008), p. 257401.

[219] L.M. Malard, M.H.D. Guimarães, D.L. Mafra, M.S.C. Mazzoni, and A. Jorio, Phys. Rev. B 79 (2009), p. 125426.

[220] A.H. Castro Neto and F. Guinea, Phys. Rev. B 75 (2007), p. 045404.

[221] A. Das, B. Chakraborty, S. Piscanec, S. Pisana, A.K. Sood, and A.C. Ferrari, Phys. Rev. B 79 (2009), p. 155417.

[222] T. Ando and M. Koshino, J. Phys. Soc. Japan 78 (2009), p. 034709.

[223] I. Martin, Ya.M. Blanter, and A.F. Morpurgo, Phys. Rev. Lett. 100 (2008), p. 036804.

[224] D.S.L. Abergel and T. Chakraborty, Appl. Phys. Lett. 95 (2009), p. 062107.

[225] P. San-Jose, E. Prada, E. McCann, and H. Schomerus, Phys. Rev. Lett. 102 (2009), p. 247204.

[226] H. Min, G. Borghi, M. Polini, and A.H. MacDonald, Phys. Rev. B 77 (2008), p. 041407.

[227] D.S.L. Abergel, P. Pietiläinen, and T. Chakraborty, Phys. Rev. B 80 (2009), p. 081408(R).

[228] D. Pines and P. Nozieres, *The Theory of Quantum Liquids*, Vol. 1, Benjamin, New York, 1966.

[229] G.D. Mahan, *Many Particle Physics*, 3rd ed., Kluwer/Plenum, New York, 2000.

[230] J.P. Eisenstein, L.N. Pfeiffer, and K.W. West, Phys. Rev. Lett. 68 (1992), p. 674; Phys. Rev. B 50 (1994), p. 1760; I.S. Millard, N.K. Patel, C.L. Foden, E.H. Linfield, M.Y. Simmons, D.A. Ritchie, and M. Pepper, *ibid.* B 55 (1997), p. 6715; E.A. Galaktionov, G.D. Allison, M.M. Fogler, A.K. Savchenko, S.S. Safonov, M.Y. Simmons, and D.A. Ritchie, Physica E 34 (2006), p. 240; S.I. Dorozhkin, J.H. Smet, K. von Klitzing, V. Umansky, W. Wegscheider, R.J. Haug, and K. Ploog, *ibid.* 12 (2002), p. 97.

[231] Y. Barlas, T. Pereg-Barnea, M. Polini, R. Asgari, and A.H. MacDonald, Phys. Rev. Lett. 98 (2007), p. 236601.

[232] D.E. Sheehy and J. Schmalian, Phys. Rev. Lett. 99 (2007), p. 226803.

[233] There are many effects predicted in the literature that are directly attributed to the presence of Coulomb interactions in monolayer graphene. See, for example, J. Gonzalez, F. Guinea, and M.A.H. Vozmediano, Phys. Rev. B 63 (2001), p. 134421; E.G. Mishchenko, Phys. Rev. Lett. 98 (2007), p. 216801; I.F. Herbut, V. Juricic, and O. Vafek, Phys. Rev. Lett. 100 (2008), p. 046403; M. Polini, R. Asgari, G. Borghi, Y. Barlas, T. Pereg-Barnea, and A.H. MacDonald, Phys. Rev. B 77 (2008), p. 081411.

[234] M.W.C. Dharma-wardana, Phys. Rev. B 75 (2007), p. 075427.

[235] B. Tanatar and D.M. Ceperley, Phys. Rev. B 39 (1989), p. 5005.

[236] H.P. Dahal, Y.N. Joglekar, K.S. Bedell, and A.V. Balatsky, Phys. Rev. B 74 (2006), p. 233405.

[237] F.A. Stevens Jr and M.A. Pokrant, Phys. Rev. A 8 (1973), p. 990.

[238] X.F. Wang and T. Chakraborty, Phys. Rev. B 75 (2007), p. 033408.

[239] X.F. Wang and T. Chakraborty, Phys. Rev. B 75 (2007), p. 041404(R).

[240] B. Wunsch, T. Stauber, F. Sols, and F. Guinea, New J. Phys. 8 (2006), p. 318.

[241] E.H. Hwang and S. Das Sarma, Phys. Rev. B 75 (2007), p. 205418.

[242] A. Qaiumzadeh and R. Asgari, Phys. Rev. B 79 (2009), p. 075414.

[243] P.K. Pyatkovskiy, J. Phys.: Condens. Matter 21 (2009), p. 025506.

[244] M. Polini, R. Asgari, G. Borghi, Y. Barlas, T. Pereg-Barnea, and A.H. MacDonald, Phys. Rev. B 77 (2008), p. 081411(R).

[245] Y. Barlas and K. Yang, Phys. Rev. B 80 (2009), p. 161408(R).

[246] A. Hill, S.A. Mikhailov, and K. Ziegler, Eur. Phys. Lett. 87 (2009), p. 27005.

[247] C.L. Kane and E.J. Mele, Phys. Rev. Lett. 95 (2005), p. 226801.

[248] N.A. Sinitsyn, J.E. Hill, H. Min, J. Sinava, and A.H. Mac Donald, Phys. Rev. Lett. 97 (2006), p. 106804.

[249] H. Min, J.E. Hill, N.A. Sinitsyn, B.R. Sahu, L. Kleinman, and A.H. MacDonald, Phys. Rev. B 74 (2006), p. 165310.

[250] B. Vinter, Phys. Rev. B 15 (1977), p. 3947.

[251] X.F. Wang, Phys. Rev. B 72 (2005), p. 85317.

[252] N.M.R. Peres, F. Guinea, and A.H. Castro Neto, Phys. Rev. B 72 (2005), p. 174406.

[253] D.P. DiVincenzo and E.J. Mele, Phys. Rev. B 29 (1984), p. 1685.

[254] A. Bostwick, T. Ohta, J.L. McChesney, T. Seyller, K. Horn, and E. Rotenberg, Solid State Commun. 143 (2007), p. 63.

[255] A. Bostwick, T. Ohta, J.L. McChesney, T. Seyller, K. Horn, and E. Rotenberg, Eur. Phys. J. Spec. Top. 148 (2007), p. 5.

[256] A. Qaiumzadeha, N. Arabchi, and R. Asgari, Solid State Commun. 147 (2008), p. 172.

[257] D.V. Khveshchenko, Phys. Rev. B 74 (2006), p. 161402(R).

[258] O. Vafek, Phys. Rev. Lett. 97 (2006), p. 266406.

[259] Y.H. Chiu, J.H. Ho, C.P. Chang, D.S. Chuu, and M.F. Lin, Phys. Rev. B 78 (2008), p. 245411.

[260] F. Rana, IEEE Trans. Nanotechnol. 7 (2008), p. 91.

[261] A.R. Wright, G.X. Wang, W. Xu, Z. Zeng, and C. Zhang , Microelectron. J. 40 (2009), p. 857.

[262] M. Koshino and T. Ando, Phys. Rev. B 73 (2006), p. 245403.

[263] M Tahir and K Sabeeh, J. Phys.: Condens. Matter 20 (2008), p. 425202.

[264] M. Tahir and K. Sabeeh, Phys. Rev. B 76 (2007), p. 195416.

[265] O.L. Berman, G. Gumbs, and Y.E. Lozovik, Phys. Rev. B 78 (2008), p. 085401.

[266] S. Adam and S. Das Sarma, Phys. Rev. B 77 (2008), p. 115436.

[267] J. Nilsson, A.H. Castro Neto, F. Guinea, and N.M.R. Peres, Phys. Rev. B 78 (2008), p. 045405.

[268] X.-F. Wang and T. Chakraborty, Phys. Rev. B 81 (2010), p. 081402 (R).

[269] T. Oka and H. Aoki, Phys. Rev. B 79 (2009), p. 081406(R). See also the associated Erratum: T. Oka and H. Aoki, Phys. Rev. B 79 (2009), p. 169901(E).

[270] M.V. Fistul and K.B. Efetov, Phys. Rev. Lett. 98 (2007), p. 256803.

[271] S.E. Shafranjuk, J. Phys.: Condens. Matter 21 (2009), p. 015301.

[272] F.J. López-Rodríguez and G.G. Nuamis, Phys. Rev. B 78 (2008), p. 201406(R).

[273] A.R. Wright, J.C. Cao, and C. Zhang, Phys. Rev. Lett. 103 (2009), p. 207401.

[274] K. Nomura and A.H. MacDonald, Phys. Rev. Lett. 98 (2007), p. 076602.

[275] P.A. Lee, Phys. Rev. Lett. 71 (1993), p. 1887.

[276] N.M.R. Peres, F. Guinea, and A.H. Castro Neto, Phys. Rev. B 73 (2006), p. 125411.

[277] Y.-W. Tan, Y. Zhang, K. Bolotin, Y. Zhao, S. Adam, E.H. Hwang, S. Das Sarma, H.L. Stormer, and P. Kim, Phys. Rev. Lett. 99 (2007), p. 246803.

[278] J.H. Chen, C. Jang, S. Adam, M.S. Fuhrer, E.D. Williams, and M. Ishigami, Nat. Phys. 4 (2008), p. 377.

[279] R. Danneau, F. Wu, M.F. Craciun, S. Russo, M.Y. Tomi, J. Salmilehto, A.F. Morpurgo, and P.J. Hakonen, J. Low Temp. Phys. 153 (2008), p. 374.

[280] D.C. Elias, R.R. Nair, T.M.G. Mohiuddin, S.V. Morozov, P. Blake, M.P. Halsall, A.C. Ferrari, D.W. Boukhvalov, M.I. Katsnelson, A.K. Geim, and K.S. Novoselov, Science 323 (2009), p. 610.

[281] I.F. Herbut, V. Juricic, and O. Vafek, Phys. Rev. Lett. 100 (2008), p. 046403.

[282] E.G. Mishchenko, Europhys. Lett. 83 (2008), p. 17005.

[283] D.E. Sheehy and J. Schmalian, Phys. Rev. B 80 (2009), p. 193411.

[284] Z.Q. Li, E.A. Henriksen, Z. Jiang, Z. Hao, M.C. Martin, P. Kim, H.L. Stormer, and D.N. Basov, Nat. Phys. 4 (2008), p. 532.

[285] J. Yan, Y. Zhang, P. Kim, and A. Pinczuk, Phys. Rev. Lett. 98 (2007), p. 166802.

[286] T.M.G. Mohiuddin, A. Lombardo, R.R. Nair, A. Bonetti, G. Savini, R. Jalil, N. Bonini, D.M. Basko, C. Galiotis, N. Marzari, K.S. Novoselov, A.K. Geim, and A.C. Ferrari, Phys. Rev. B 79 (2009), p. 205433.

[287] Y. Zhang, V.W. Brar, F. Wang, C. Girit, Y. Yayon, M. Panlasigui, A. Zettl, and M.F. Crommie, Nat. Phys. 4 (2008), p. 627.

[288] A. Bostwick, J.L. McChesney, K.V. Emtsev, T. Seyller, K. Horn, S.D. Kevan, and E. Rotenberg, Phys. Rev. Lett. 103 (2009), p. 056404.

[289] A.H. Castro Neto, F. Guinea, N.M.R. Peres, K.S. Novoselov, and A.K. Geim, Rev. Mod. Phys. 81 (2009), p. 109.

[290] S.V. Morozov, K.S. Novoselov, M.I. Katsnelson, F. Schedin, L.A. Ponemereanteo, D. Jiany, and A.K. Gein, Phys. Rev. Lett. 97 (2006), p. 016801.

[291] E. McCann, K. Keehedzhi, V.I. Falko, H. Suzuura, T. Ando, and B.L. Altshuler, Phys. Rev. Lett. 97 (2006), p. 146805.

[292] H. Suzuura and T. Ando, *Anti-localization in a graphene sheet without spin-orbit interaction*, in *Physics of Semiconductors 2002*, A.R. Long and J.H. Davies, eds., Institute of Physics Publishing, Bristol, 2003, p. D226.

[293] B. Dóra and K. Ziegler, New J. Phys. 11 (2009), p. 095006.

[294] M.I. Katsnelson, Eur. Phys. J. B 51 (2006), p. 157.

[295] K. Ziegler, Phys. Rev. Lett. 97 (2006), p. 266802.

[296] K. Ziegler, Phys. Rev. B 78 (2008), p. 125401.

[297] J.Z. Bernád, U. Zülicke and K. Ziegler, Physica E42 (2010), p. 755.

[298] A.W.W. Ludwig, M.P.A. Fisher, R. Shankar, and G. Grinstein, Phys. Rev. B 50 (1994), p. 7526.

[299] E. Fradkin, Phys. Rev. B 33 (1986), p. 3263.

[300] K. Ziegler, Phys. Rev. Lett. 80 (1998), p. 3113.

[301] K. Ziegler, Phys. Rev. B 75 (2007), p. 233407.

[302] J.Z. Bernad, M. Jaaskelainen, U. Zuelicke, Phys. Rev. B 81 (2010), p. 073403.

[303] V.P. Gusynin, S.G. Sharapov, and J.P. Carbotte, Phys. Rev. Lett. 98 (2007), p. 157402.

[304] S.A. Mikhailov and K. Ziegler, Phys. Rev. Lett. 99 (2007), p. 016803.

[305] V.P. Gusynin, S.G. Sharapov, and J.P. Carbotte, New J. Phys. 11 (2009), p. 095013.

[306] J. Cserti, Phys. Rev. B. 75 (2007), p. 033405.

[307] H. Suzuura and T. Ando, Phys. Rev. Lett. 89 (2002), p. 266603.

[308] D.V. Khveshchenko, Phys. Rev. Lett. 97 (2006), p. 036802.

[309] N.H. Shon and T. Ando, J. Phys. Soc. Japan 67 (1998), p. 2421.

[310] V.S. Dotsenko and VI.S. Dotsenko, J. Phys. C 15 (1982), p. 495.

[311] I.L. Aleiner and K.B. Efetov, Phys. Rev. Lett. 97 (2006), p. 236801.

[312] M.S. Foster and I.L. Aleiner, Phys. Rev. B 77 (2008), p. 195413.

[313] A. Altland, Phys. Rev. Lett. 97 (2006), p. 236802.

[314] M. Boquet, D. Serban, and M.R. Zirnbauer, Nucl. Phys. B 578 (2000), p. 628.

[315] J.S. Langer and T. Neal, Phys. Rev. Lett. 16 (1966), p. 984.

[316] R. Oppermann and F. Wegner, Z. Phys. B 34 (1979), p. 327.

[317] P. Fulde, *Electron Correlations in Molecules and Solids*, Springer, Berlin, 1995.

[318] K. Ziegler, Phys. Rev. Lett. 102 (2009), p. 126802; Phys. Rev. B 79 (2009), p. 195424.

[319] A.A. Nersesyan, A.M. Tsvelik, and F. Wegner, Phys. Rev. Lett. 72 (1994), p. 2628.

[320] D.V. Khveshchenko, Europhys. Lett. 82 (2008), p. 57008.

[321] S.-J. Xiong and Y. Xiong, Phys. Rev. B 76 (2007), p. 214204.

[322] Y.-Y. Zhang, J. Hu, B.A. Bernevig, X.R. Wang, X.C. Xie, and W.M. Liu, Phys. Rev. Lett. 102 (2009), p. 106401.

[323] J.H. Bardarson, J. Tworzydlo, P.W. Brouwer, and C.W.J. Beenakker, Phys. Rev. Lett. 99 (2007), p. 106801.

[324] C.H. Lewenkopf, E.R. Mucciolo, and A.H. Castro Neto, Phys. Rev. B 77 (2008), p. 081410(R).

[325] J.H. Bardarson, M.V. Medvedyeva, J. Tworzydlo, A.R. Akhmerov, and C.W.J. Beenakker, Phys. Rev. B 81 (2010), p. 121414(R).

[326] H. Schomerus, Phys. Rev. B 76 (2007), p. 045433.

[327] E.J. Duplock, M. Scheffler, and P.J.D. Lindan, Phys. Rev. Lett. 92 (2004), p. 225502.

[328] V.M. Pereira, F. Guinea, J.M.B. Lopes dos Santos, N.M.R. Peres, and A.H. Castro Neto, Phys. Rev. Lett. 96 (2006), p. 036801.

[329] T. Stauber, N.M.R. Peres, and F. Guinea, Phys. Rev. B 76 (2007), p. 205423.

[330] F. Guinea, M.I. Katsnelson, and M.A.H. Vozmediano, Phys. Rev. B 77 (2008), p. 075422.

[331] V.V. Cheianov, V.I. Falko, B.L. Altshuler, and I.L. Aleiner, Phys. Rev. Lett. 99 (2007), p. 176801.

[332] K. Ziegler, A. Sinner, arXiv:1002.3734.

[333] S. Cho and M.P.A. Fisher, Phys. Rev. B 55 (1997), p. 1025.

[334] J.T. Chalker, N. Read, V. Kagalovsky, B. Herovitz, Y. Avishai, and A.W.W. Ludwig, Phys. Rev. B 65 (2001), p. 012506.

[335] M.V. Medvedyeva, J. Tworzydlo, and C.W.J. Beenakker, arxiv:1004.1111.

[336] D.V. Khveshchenko, Phys. Rev. Lett. 87 (2001), p. 206401.

[337] E.V. Gorbar, V.P. Gusynin, V.A. Miransky, and I.A. Shovkovy, Phys. Rev. B 66 (2002), p. 045108.

[338] J.E. Drut and T.A. Lähde, Phys. Rev. Lett. 102 (2009), p. 026802.

[339] M.R. Buitelaar, A. Bachtold, T. Nussbaumer, M. Iqbal, and C. Schönenberger, Phys. Rev. Lett. 88 (2002), p. 156801; D.H. Cobden and J. Nygřard, *ibid.* 89 (2002), p. 046803; S. Moriyama, T. Fuse, M. Suzuki, Y. Aoyagi, and K. Ishibashi, *ibid.* 94 (2005), p. 186806; S.-H. Ke, H.U. Baranger, and W. Yang, *ibid.* 91 (2003), p. 116803.

[340] K. Ishibashi, S. Moriyama, D. Tsuya, and T. Fuse, J. Vac. Sci. Technol. A 24 (2006), p. 1349.

[341] O. Klein, Z. Phys. 53 (1929), p. 157.

[342] M.I. Katsnelson, Mater. Today 10 (2007), p. 20.

[343] A. Calogeracos and N. Dombey, Contemp. Phys. 40 (1999), p. 313.

[344] N. Stander, B. Huard, and D. Goldhaber-Gordon, Phys. Rev. Lett. 102 (2009), p. 026807.

[345] A.F. Young and P. Kim, Nat. Phys. 5 (2009), pp. 222–226.

[346] R. Giachetti and E. Sorace, Phys. Rev. Lett. 101 (2008), p. 190401.

[347] L.A. Ponomarenko, F. Schedin, M.I. Katsnelson, R. Yang, E.W. Hill, K.S. Novoselov, and A.K. Geim, Science 320 (2008), p. 356.

[348] S. Schnez, F. Molitor, C. Stampfer, J. Güttinger, I. Shorubalko, T. Ihn, and K. Ensslin, Appl. Phys. Lett. 94 (2009), p. 012107.

[349] J. Güttinger, C. Stampfer, S. Hellmüller, F. Molitor, T. Ihn, and K. Ensslin, Appl. Phys. Lett. 93 (2008), p. 212102.

[350] H.-Y. Chen, V. Apalkov, and T. Chakraborty, Phys. Rev. Lett. 98 (2007), p. 186803.

[351] P.G. Silvestrov and K.B. Efetov, Phys. Rev. Lett. 98 (2007), p. 016802.

[352] A. De Martino, L. Dell'Anna, and R. Egger, Phys. Rev. Lett. 98 (2007), p. 066802.

[353] L. Dell'Anna and A. De Martino, Phys. Rev. B 79 (2009), p. 045420.

[354] W. Hausler and R. Egger, Phys. Rev. B 80 (2009), p. 161402.

[355] M.V. Berry and R.J. Mondragon, Proc. R. Soc. A 412 (1987), p. 53.

[356] J. Wurm, A. Rycerz, I. Adagideli, M. Wimmer, K. Richter, and H.U. Baranger, Phys. Rev. Lett. 102 (2009), p. 056806.
[357] F. Libisch, C. Stampfer, and J. Burgdörfer, Phys. Rev. B 79 (2009), p. 115423.
[358] T. Yamamoto, T. Noguchi, and K. Watanabe, Phys. Rev. B 74 (2006), p. 121409(R).
[359] M. Ezawa, Phys. Rev. B. 76 (2007), p. 245415.
[360] J. Fernandez-Rossier and J.J. Palacios, Phys. Rev. Lett. 99 (2007), p. 177204.
[361] Z.Z. Zhang, K. Chang, and F.M. Peeters, Phys. Rev. B 77 (2008), p. 235411.
[362] D. Jiang, B.G. Sumpter, and S. Dai, J. Chem. Phys. 127 (2007), p. 124703.
[363] C. Tang, W. Yan, Y. Zheng, G. Li, and L. Li, Nanotechnology 19 (2008), p. 435401.
[364] E. McCann and V.I. Falko, J. Phys.: Condens. Matter 16 (2004), p. 2371.
[365] A.R. Akhmerov and C.W.J. Beenakker, Phys. Rev. B 77 (2008), p. 085423.
[366] P. Potasz, A.D. Guclu, and P. Hawrylak, Phys. Rev. B 81 (2010), p. 033403.
[367] A.V. Rozhkov and F. Nori, Phys. Rev. B 81 (2010), p. 155401.
[368] B. Wunsch, T. Stauber, and F. Guinea, Phys. Rev. B 77 (2008), p. 035316.
[369] I. Romanovsky, C. Yannouleas, and U. Landman, Phys. Rev. B 79 (2009), p. 075311.
[370] Y. Aharonov and D. Bohm, Phys. Rev. 115 (1959), p. 485.
[371] S. Russo, J.B. Oostinga, D. Wehenkel, H.B. Heersche, S.S. Sobhani, L.M.K. Vandersypen, and A.F. Morpurgo, Phys. Rev. B 77 (2008), p. 085413.
[372] P. Recher, B. Trauzettel, A. Rycerz, Y.M. Blanter, C.W.J. Beenakker, and A.F. Morpurgo, Phys. Rev. B 76 (2007), p. 235404.
[373] D.S.L. Abergel, V.M. Apalkov, and T. Chakraborty, Phys. Rev. B 78 (2008), p. 193405.
[374] D.A. Bahamon, A.L.C. Pereira, and P.A. Schulz, Phys. Rev. B 79 (2009), p. 125414.
[375] E. Rossi, J.H. Bardarson, P.W. Brouwer, and S. Das Sarma, Phys. Rev. B 81 (2010), p. 121408(R).
[376] A. Matulis and F.M. Peeters, Phys. Rev. B 77 (2008), p. 115423.
[377] P. Hewageegana and V. Apalkov, Phys. Rev. B 79 (2009), p. 115418.
[378] P. Hewageegana and V. Apalkov, Phys. Rev. B 77 (2008), p. 245426.
[379] G. Gamow, Z. Phys. 51 (1928), p. 204.
[380] G. Giavaras, P.A. Maksym, and M. Roy, J. Phys.: Condens. Matter 21 (2009), p. 102201.
[381] J. Sucher, Phys. Rev. 107 (1957), p. 1448; 109 (1958), p. 1010; Phys. Rev. A 22 (1980), p. 348; Int. J. Quantum Chem. 25 (1984), p. 3.
[382] P. Recher, J. Nilsson, G. Burkard, and B. Trauzettel, Phys. Rev. B 79 (2009), p. 085407.
[383] G. Giovannetti, P.A. Khomyakov, G. Brocks, P.J. Kelly, and J. van der Brink, Phys. Rev. B 76 (2007), p. 073103.
[384] J.M. Pereira Jr, F.M. Peeters, and P. Vasilopoulos, Phys. Rev. B 75 (2007), p. 125433.
[385] S. Schnez, K. Ensslin, M. Sigrist, and T. Ihn, Phys. Rev. B 78 (2008), p. 195427.
[386] J. Milton Pereira Jr, P. Vasilopoulos, and F.M. Peeters, Nano Lett. 7 (2007), p. 946.
[387] S.E. Stein and R.L. Brown, J. Am. Chem. Soc. 109 (1987), p. 3721.
[388] K. Tanaka, S. Yamashita, H. Yamabe, and T. Yamabe, Synth. Met. 17 (1987), p. 143.
[389] M. Fujita, M. Yoshida, and K. Nakada, Fuller. Sci. Technol. 4 (1996), p. 565.
[390] M. Fujita, K. Wakabayashi, K. Nakada, and K. Kusakabe, J. Phys. Soc. Japan 65 (1996), p. 1920.
[391] K. Nakada, M. Fujita, G. Dresselhaus, and M.S. Dresselhaus, Phys. Rev. B 54 (1996), p. 17954.
[392] Z. Klusek, Z. Waqar, E.A. Denisov, T.N. Kompaniets, I.V. Makarenko, N. Titkov, and A.S. Bhatti, Appl. Surf. Sci. 161 (2000), p. 508.
[393] Y. Kobayashi, K. Fukui, T. Enoki, K. Kusakabe, and Y. Kaburagi, Phys. Rev. B 71 (2005), p. 193406.

[394] Y. Niimi, T. Matsui, H. Kambara, K. Tagami, M. Tsukada, and H. Fukuyama, Phys. Rev. B 73 (2006), p. 085421.
[395] Y. Kobayashi, K. Fukui, T. Enoki, and K. Kusakabe, Phys. Rev. B 73 (2006), p. 125415.
[396] K.N. Kudin, B. Ozbas, H.C. Schniepp, R.K. Prud'homme, I.A. Aksay, and R. Car, Nano Lett. 8 (2008), p. 36.
[397] T.O. Wehling, K.S. Novoselov, S.V. Morozov, E.E. Vdovin, M.I. Katsnelson, A.K. Geim, and A.I. Lichtenstein, Nano Lett. 8 (2008), p. 173.
[398] T. Lohmann, K. von Klitzing, and J.H. Smet, Nano Lett. 9 (2009), p. 1973.
[399] K. Sakaki, S. Murakami, and R. Saito, Appl. Phys. Lett. 88 (2006), p. 113110.
[400] K. Sakaki, S. Murakami, and R. Saito, J. Phys. Soc. Japan 75 (2006), p. 074713.
[401] M. Fujita, M. Igami, and K. Nakada, J. Phys. Soc. 66 (1997), p. 1864.
[402] S. Jun, Phys. Rev. B 78 (2008), p. 073405.
[403] S. Okada, Phys. Rev. B 77 (2008), p. 041408(R).
[404] P. Koskinen, S. Malola, and H. Hákkinen, Phys. Rev. Lett 101 (2008), p. 115502.
[405] P. Koskinen, S. Malola, and H. Hákkinen, Phys. Rev. B 80 (2009), p. 073401.
[406] N.M.R. Peres, M.A.N. Araújo, and D. Bozi, Phys. Rev. B 70 (2004), p. 195122.
[407] N.M.R. Peres, F. Guinea, and A.H. Castro Neto, Phys. Rev. B 72 (2005), p. 174406.
[408] K. Sasaki and R. Saito, J. Phys. Soc. Japan 77 (2008), p. 054703.
[409] H.-H. Lin, T. Hikihara, H.-T. Jeng, B.-L. Huang, C.-Y. Mou, and X. Hu, Phys. Rev. B 79 (2009), p. 035405.
[410] A. Yamashiro, Y. Shimoi, K. Harigaya, and K. Wakabayashi, Phys. Rev. B 68 (2003), p. 193410.
[411] S. Dutta, S.L. Lakshmi, and S.K. Pati, Phys. Rev. B 77 (2008), p. 073412.
[412] L. Pisani, J.A. Chan, B. Montanari, and N.M. Harrison, Phys. Rev. B 75 (2007), p. 064418.
[413] A. Yamashiro, Y. Shimoi, K. Harigaya, and K. Wakabayashi, Physica E 22 (2004), p. 668.
[414] H. Lee, Y.-W. Son, N. Park, S. Han, and J. Yu, Phys. Rev. B 72 (2005), p. 174431.
[415] J. Nakamura, T. Nitta, and A. Natori, Phys. Rev. B 72 (2005), p. 205429.
[416] J. Jung, T. Pereg-Barnea, and A.H. MacDonald, Phys. Rev. Lett. 102 (2009), p. 227205.
[417] F. Wu, E. Kan, H. Xiang, S.-H. Wei, M.-H. Whangbo, and J. Yang, Appl. Phys. Lett. 94 (2009), p. 223105.
[418] D.W. Boukhvalov and M.I. Katsnelson, Nano Lett. 8 (2008), p. 4373.
[419] Y.-W. Son, M.L. Cohen, and S.G. Louie, Phys. Rev. Lett 97 (2006), p. 216803.
[420] V. Barone, O. Hod, and G.E. Scuseria, Nano Lett. 6 (2006), p. 2748.
[421] M. Ezawa, Phys. Rev. B 73 (2006), p. 045432.
[422] L. Brey and H.A. Fertig, Phys. Rev. B 73 (2006), p. 235411.
[423] P. Shemella, Y. Zhang, M. Mailman, P.M. Ajayan, and S.K. Nayak, Appl. Phys. Lett. 91 (2007), p. 042101.
[424] L. Yang, C.-H. Park, Y.-W. Son, M.L. Cohen, and S.G. Louie, Phys. Rev. Lett 99 (2007), p. 186801.
[425] H. Zheng, Z.F. Wang, T. Luo, and Q.W. Shi, J. Chen, Phys. Rev. B 75 (2007), p. 165414.
[426] K. Kudin, ACS Nano 2 (2008), p. 516.
[427] H. Raza and E.C. Kan, Phys. Rev. B 77 (2008), p. 245434.
[428] Y.H. Lu, R.Q. Wu, L. Shen, M. Yang, Z.D. Sha, Y.Q. Cai, P.M. He, and Y.P. Feng, Appl. Phys. Lett. 94 (2009), p. 122111.
[429] X.W. Zhang and G.W. Yang, J. Phys. Chem. C. 113 (2009), p. 4662.
[430] A.K. Singh and B.I. Yakobson, Nano Lett. 9 (2009), p. 1540.
[431] F. Tseng, D. Unluer, K. Holcomb, M.R. Stan, and A.W. Ghosh, Appl. Phys. Lett. 94 (2009), p. 223112.
[432] Q. Yan, B. Huang, J. Yu, F. Zheng, J. Zang, J. Wu, B.-L. Gu, F. Liu, and W. Duan, Nano Lett. 7 (2007), p. 1469.

[433] H. Sevinçli, M. Topsakal, and S. Ciraci, Phys. Rev. B 78 (2008), p. 245402.
[434] M. Mohr, K. Papagelis, J. Maultzsch, and C. Thomsen, Phys. Rev. B 80 (2009), p. 205410.
[435] O. Hod, J.E. Peralta, and G.E. Scuseria, Phys. Rev. B 76 (2007), p. 233401.
[436] A.V. Rozhkov, S. Savel'ev, and F. Nori, Phys. Rev. B 79 (2009), p. 125420.
[437] M.Y. Han, B. Özyilmaz, Y. Zhang, and P. Kim, Phys. Rev. Lett. 98 (2007), p. 206805.
[438] M.Y. Han, B. Özyilmaz, Y. Zhang, R. Jarillo-Herero, and P. Kim, Phys. Status Solidi b 244 (2007), p. 4134.
[439] L. Tapasztó, G. Dobrik, P. Lambin, and L.P. Biró, Nat. Nanotechnol. 3 (2008), p. 397.
[440] F. Molitor, C. Stampfer, J. Güttinger, A. Jacobsen, T. Ihn, and K. Ensslin, Semicond. Sci. Technol. 25 (2010), p. 034002.
[441] K.A. Ritter and J.W. Lyding, Nat. Mater. 8 (2009), p. 235.
[442] Y.-W. Son, M.L. Cohen, and S.G. Louie, Nature 444 (2006), p. 347.
[443] O. Hod, V. Barone, J.E. Peralta, and G.E. Scuseria, Nano Lett. 7 (2007), p. 2295.
[444] R.P. Tiwari and D. Stroud, Phys. Rev. B 79 (2009), p. 205435.
[445] W. Yao, S.A. Yang, and Q. Niu, Phys. Rev. Lett. 102 (2009), p. 096801.
[446] E. Rudberg, P. Salek, and Y. Luo, Nano Lett. 7 (2007), p. 2211.
[447] E.-J. Kan, Z. Li, J. Yang, and J.G. Hou, Appl. Phys. Lett. 91 (2007), p. 243116.
[448] D. Dutta and S.K. Pati, J. Phys. Chem. B 112 (2008), p. 1333.
[449] J. Jung and A.H. MacDonald, Phys. Rev. B 79 (2009), p. 235433.
[450] S. Cho, Y.-F. Chen, and M.S. Fuhrer, Appl. Phys. Lett. 91 (2007), p. 123105.
[451] C. Ritter, S.S. Makler, and A. Latgé, Phys. Rev. B 77 (2008), p. 195443.
[452] D.S. Novikov, Phys. Rev. Lett. 99 (2007), p. 056802.
[453] V.M. Karpan, G. Giovannetti, P.A. Khomyakov, M. Talanana, A.A. Starikov, M. Zwierzycki, J. van der Brink, G. Brocks, and P.J. Kelly, Phys. Rev. Lett. 99 (2007), p. 176602.
[454] D. Gunlycke, D.A. Areshkin, J. Li, J.W. Mintmire, and C.T. White, Nano Lett. 7 (2007), p. 3608.
[455] W.Y. Kim and K.S. Kim, Nat. Nanotechnol. 3 (2008), p. 408.
[456] J. Guo, D. Gunlycke, and C.T. White, Appl. Phys. Lett. 92 (2008), p. 163109.
[457] T. Yokoyama, Phys. Rev. B 77 (2008), p. 073413.
[458] O.V. Yazyev and M.I. Katsnelson, Phys. Rev. Lett. 100 (2008), p. 047209.
[459] S. Hong, Y. Yoon, and J. Guo, Appl. Phys. Lett. 92 (2008), p. 083107.
[460] C. Józsa, M. Popinciuc, N. Tombros, H.T. Jonkman, and B.J. van Wees, Phys. Rev. Lett. 100 (2008), p. 236603.
[461] M. Ezawa, Eur. Phys. J. B 67 (2009), p. 543.
[462] J. Guo and Y. Ouyang, Appl. Phys. Lett. 94 (2009), p. 243104.
[463] F. Muñoz-Rojas, J. Fernández-Rossier, and J.J. Palacios, Phys. Rev. Lett. 102 (2009), p. 136810.
[464] W. Han, W.H. Wang, K. Pi, K.M. McCreary, W. Bao, Y. Li, F. Miao, C.N. Lau, and R.K. Kawakami, Phys. Rev. Lett. 102 (2009), p. 137205.
[465] Z. Xu, Q.-S. Zheng, and G. Chen, Appl. Phys. Lett. 90 (2007), p. 233115.
[466] O. Hod, V. Barone, and G.E. Scuseria, Phys. Rev. B 77 (2008), p. 035411.
[467] S. Banerjee and D. Bhattacharyya, Comput. Mater. Sci. 44 (2008), p. 41.
[468] M. Topsakal, H. Sevinçli, and S. Ciraci, Appl. Phys. Lett. 92 (2008), p. 173118.
[469] X. Wu and X.C. Zeng, Nano Res. 1 (2008), p. 40.
[470] S. Bhowmick and V.B. Shenoy, J. Chem. Phys. 128 (2008), p. 244717.
[471] E.H. Lieb, Phys. Rev. Lett. 62 (1989), p. 1201.
[472] O.V. Yazyev, W.L. Wang, S. Meng, and E. Kaxiras, Nano Lett. 8 (2008), p. 766.
[473] W.L. Wang, S. Meng, and E. Kaxiras, Nano Lett. 8 (2008), p. 241.

[474] M. Vanević, V.M. Stojanović, and M. Kindermann, Phys. Rev. B 80 (2009), p. 045410.

[475] B. Wang, J. Wang, and H. Guo, Phys. Rev. B 79 (2009), p. 165417.

[476] Z. Li, H. Qian, J. Wu, B.-L. Gu, and W. Duan, Phys. Rev. Lett. 100 (2008), p. 206802.

[477] F. Muñoz-Rojas, D. Jacob, J. Fernández-Rossier, and J.J. Palacios, Phys. Rev. B 74 (2006), p. 195417.

[478] M. Wimmer, İ. Adagideli, S. Berber, D. Tománek, and K. Richter, Rev. Lett. 100 (2008), p. 177207.

[479] L.A. Agapito and H.-P. Cheng, J. Phys. Chem. C 111 (2007), p. 14266.

[480] L. Rosales, M. Pacheco, Z. Barticevic, A. Latgé, and P.A. Orellana, Nanotechnology 20 (2009), p. 095705.

[481] H. Li, L. Wang, and Y. Zheng, J. Appl. Phys. 105 (2009), p. 013703.

[482] Y.P. Chen, Y.E. Xie, L.Z. Sun, and J. Zhong, Appl. Phys. Lett. 93 (2008), p. 092104.

[483] X. Li, X. Wang, L. Zhang, S. Lee, and H. Dai, Science 319 (2008), p. 1229.

[484] M.P. Lima, A. Fazzio, and Antônio J.R. da Silva, Phys. Rev. B 79 (2009), p. 153401.

[485] B. Sahu, H. Min, A.H. MacDonald, and S.K. Banerjee, Phys. Rev. B 78 (2008), p. 045404.

[486] E.V. Castro, N.M.R. Peres, J.M.B. Lopes dos Santos, A.H. Castro Neto, and F. Guinea, Phys. Rev. Lett. 100 (2008), p. 026802.

[487] J.-W. Rhim and K. Moon, J. Phys.: Condens. Matter 20 (2008), p. 365202.

[488] K.-T. Lam and G. Liang, Appl. Phys. Lett. 92 (2008), p. 223106.

[489] Y.C. Huang, C.P. Chang, and M.F. Lin, J. Appl. Phys. 104 (2008), p. 103714.

[490] E.V. Castro, N.M.R. Peres, and J.M.B. Lopes dos Santos, Eur. Phys. Lett. 84 (2008), p. 17001.

[491] X. Jian, M. Hofmann, V. Meunier, B.G. Sumpter, J. Campos-Delgado, J.M. Romo-Herrera, H. Son, Y.-P. Hsieh, A. Reina, J. Kong, M. Terrones, and M.S. Dresselhaus, Science 323 (2009), p. 1701.

[492] L. Jiao, L. Zhang, X. Wang, G. Diankov, and H. Dai, Nature 458 (2009), p. 877.

[493] D.V. Kosynkin, A.L. Higginbotham, A. Sinitskii, J.R. Lomeda, A. Dimiev, B.K. Price, and J.M. Tour, Nature 458 (2009), p. 872.

[494] G. Gui, J. Li, and J. Zhong, Phys. Rev. B 78 (2008), p. 075435.

[495] Z.H. Ni, T. Yu, Y.H. Lu, Y.Y. Wang, Y.P. Feng, and Z.X. Shen, ACS Nano 2 (2008), p. 2301.

[496] M. Huang, H. Yan, C. Chen, D. Song, T.F. Heinz, and J. Hone, PNAS 106 (2009), p. 7304.

[497] H.E. Romero, N. Shen, P. Joshi, H.R. Guitierrez, S.A. Tadigadapa, J.O. Sofo, and P.C. Eklund, ACS Nano 2 (2008), p. 2037.

[498] J. Hass, F. Varchon, J.E. Millán-Otoya, M. Sprinkle, N. Sharma, W.A. de Heer, C. Berger, P.N. First, L. Magaud, and E.H. Conrad, Phys. Rev. Lett. 100 (2008), p. 125504.

[499] D.S. Lee, C. Riedl, B. Krauss, K. von Klitzing, U. Starke, and J.H. Smet, Nano Lett. 8 (2008), p. 4320.

[500] Y. Shi, X. Dong, P. Chen, J. Wang, and L.-J. Li, Phys. Rev. B 79 (2009), p. 115402.

[501] F. Hiebel, P. Mallet, F. Varchon, L. Magaud, and J.-Y. Veuillen, Phys. Rev. B 78 (2008), p. 153412.

[502] F. Varchon, R. Feng, J. Hass, X. Li, B.N. Nguyen, C. Naud, P. Mallet, J.-Y. Veuillen, C. Berger, E.H. Conrad, and L. Magaud, Phys. Rev. Lett. 99 (2007), p. 126805.

[503] A. Mattausch and O. Pankratov, Phys. Rev. Lett. 99 (2007), p. 076802.

[504] I. Gierz, C. Riedl, U. Starke, C.R. Ast, and K. Kern, Nano Lett. 8 (2008), p. 4603.

[505] T.A.G. Eberlein, R. Jones, J.P. Goss, and P.R. Briddon, Phys. Rev. B 78 (2008), p. 045403.

[506] Y.-J. Kang, J. Kang, and K.J. Chang, Phys. Rev. B 78 (2008), p. 115404.

[507] Y.H. Lu, P.M. He, and Y.P. Feng, J. Phys. Chem. C 112 (2008), p. 12683.

[508] P. Shemella and S.K. Nayak, Appl. Phys. Lett. 94 (2009), p. 032101.

[509] M.M. Li, J. Zhang, F.J. Li, F.X. Zhu, M. Zhang, and X.F. Zhao, Phys. Status Solidi c. 6 (2009), p. S90.

[510] L. Magaud, F. Hiebel, F. Varchon, P. Mallet, and J.-Y. Veuillen, Phys. Rev. B 79 (2009), p. 161405(R).

[511] X. Peng and R. Ahuja, Nano Lett. 8 (2008), p. 4464.

[512] G. Giovannetti, P.A. Khomyakov, G. Brocks, V.M. Karpan, J. van den Brink, and P.J. Kelly, Phys. Rev. Lett. 101 (2008), p. 026803.

[513] P.A. Khomyakov, G. Giovannetti, P.C. Rusu, G. Brocks, J. van den Brink, and P.J. Kelly, Phys. Rev. B 79 (2009), p. 195425.

[514] F. Ortmann, W.G. Schmidt, and F. Bechstedt, Phys. Rev. Lett. 95 (2005), p. 186101.

[515] S.Y. Zhou, D.A. Siegel, A.V. Fedorov, and A. Lanzara, Phys. Rev. Lett. 101 (2008), p. 086402.

[516] X. Dong, Y. Shi, Y. Zhao, D. Chen, J. Ye, Y. Yao, F. Gao, Z. Ni, T. Yu, Z. Shen, Y. Huang, P. Chen, and L.-J. Li, Phys. Rev. Lett. 102 (2009), p. 135501.

[517] E. Bekyarova, M.E. Itkis, P. Ramesh, C. Berger, M. Sprinkle, W.A. de Heer, and R.C. Haddon, J. Am. Chem. Soc. 131 (2009), p. 1336.

[518] X. Dong, D. Fu, W. Fang, Y. Shi, P. Chen, and L.-J. Li, Small 5 (2009), p. 1422.

[519] R. Voggu, B. Das, C.S. Rout, and C.N.R. Rao, J. Phys.: Condens. Matter 20 (2008), p. 472204.

[520] P.O. Lehtinen, A.S. Foster, A. Ayuela, A. Krasheninnikov, K. Nordlund, and R.M. Nieminen, Phys. Rev. Lett. 91 (2003), p. 017202.

[521] I. Zanella, S. Guerini, S.B. Fagan, J. Mendes Filho, and A.G. Souza Filho, Phys. Rev. B 77 (2008), p. 073404.

[522] M. Wu, E.-Z. Liu, and J.Z. Jiang, Appl. Phys. Lett. 93 (2008), p. 082504.

[523] B. Huang, Z. Li, Z. Liu, G. Zhou, S. Hao, J. Wu, B.-L. Gu, and W. Duan, J. Phys. Chem. C 112 (2008), p. 13442.

[524] E.R. Margine, M.-L. Bocquet, and X. Blase, Nano Lett. 8 (2008), p. 3315.

[525] Y.G. Zhou, X.T. Zu, F. Gao, H.F. Lv, and H.Y. Xiao, Appl. Phys. Lett. 95 (2009), p. 123119.

[526] S.D. Dalosto and Z.H. Levine, J. Phys. Chem. C 112 (2008), p. 8196.

[527] O. Leenaerts, B. Partoens, and F.M. Peeters, Phys. Rev. B 77 (2008), p. 125416.

[528] O. Leenaerts, B. Partoens, and F.M. Peeters, Appl. Phys. Lett. 92 (2008), p. 243125.

[529] Y.-H. Zhang, Y.-B. Chen, K.-G. Zhou, C.-H. Liu, J. Zeng, H.-L. Zhang, and Y. Peng, Nanotechnology 20 (2009), p. 185504.

[530] S.J. Sque, R. Jones, and P.R. Briddon, Phys. Status Solidi a 204 (2007), p. 3078.

[531] Y.H. Lu, W. Chen, Y.P. Feng, and P.M. He, J. Phys. Chem. B 113 (2009), p. 2.

[532] O. Leenaerts, B. Partoens, and F.M. Peeters, Phys. Rev. B 79 (2009), p. 235440.

[533] J. Berashevich and T. Chakraborty, Phys. Rev. B 80 (2009), p. 033404.

[534] T.O. Wehling, A.I. Lichtenstein, and M.I. Katsnelson, Appl. Phys. Lett. 93 (2008), p. 202110.

[535] R.M. Ribeiro, N.M.R. Peres, J. Coutinho, and P.R. Briddon, Phys. Rev. B 78 (2008), p. 075442.

[536] X. Wang, X. Li, L. Zhang, Y. Yoon, P.K. Weber, H. Wang, J. Guo, and H. Dai, Science 324 (2009), p. 768.

[537] H.E. Romero, P. Joshi, A.K. Gupta, H.R. Gutierrez, M.W. Cole, S.A. Tadigadapa, and P.C. Eklund, Nanotechnology 20 (2009), p. 245501.

[538] A.K. Manna and S.K. Pati, Chem. Asian J. 4 (2009), p. 855.
[539] A.V. Shytov, D.A. Abanin, and L.S. Levitov, Phys. Rev. Lett. 103 (2009), p. 016806.
[540] R.H. Miwa, T.B. Martins, and A. Fazzio, Nanotechnology 19 (2008), p. 155708.
[541] D. Jiang, B.G. Sumpter, and S. Dai, J. Phys. Chem. B 110 (2006), p. 23628.
[542] A. Rochefort and J.D. Wuest, Langmuir 25 (2009), p. 210.
[543] P. Cabrera-Sanfelix, J. Phys. Chem. A 113 (2009), p. 493.
[544] L. Tsetseris and S.T. Pantelides, J. Phys. Chem. B 113 (2009), p. 941.
[545] M. Chi and Y.-P. Zhao, Comput. Mater. Sci. 46 (2009), p. 1085.
[546] Y.G. Zhou, X.T. Zu, F. Gao, J.L. Nie, and H.Y. Xiao, J. Appl. Phys. 105 (2009), p. 014309.
[547] P.A. Denis, J. Phys. Chem. C 113 (2009), p. 5612.
[548] J. Dai, J. Yuan, and P. Giannozzi, Appl. Phys. Lett. 95 (2009), p. 232105.
[549] J.O. Sofo, A.S. Chaudhari, and G.D. Barber, Phys. Rev. B 75 (2007), p. 153401.
[550] S. Lebégue, M. Klintenberg, O. Eriksson, and M.I. Katsnelson, Phys. Rev. B 79 (2009), p. 245117.
[551] U. Li, Z. Zhou, P. Shen, and Z. Chen, J. Phys. Chem. C 113 (2009), p. 15043.
[552] M.Z.S. Flores, P.A.S. Autreto, S.B. Legoas, and D.S. Galvao, Nanotechnology 20 (2009), p. 465704.
[553] S. Ryu, M.Y. Han, J. Maultzsch, T.F. Heinz, P. Kim, M.L. Steigerwald, and L.E. Brus, Nano Lett. 8 (2008), p. 4597.
[554] J. Zhou, Q. Wang, Q. Sun, X.S. Chen, Y. Kawazoe, and P. Jena, Nano Lett. 9 (2009), p. 3867.
[555] H. Şahin, C. Ataca, and S. Ciraci, Appl. Phys. Lett. 95 (2009), p. 222510.
[556] J. Berashevich and T. Chakraborty, arxiv: 1001.0919v1.
[557] L.A. Chernozatonski, P.B. Sorokin, and J.W. Brüning, Appl. Phys. Lett. 91 (2007), p. 183103.
[558] D.W. Boukhvalov, M.I. Katsnelson, and A.I. Lichtenstein, Phys. Rev. B 77 (2008), p. 035427.
[559] D.W. Boukhvalov and M.I. Katsnelson, Phys. Rev. B 78 (2008), p. 085413.
[560] C.-K. Yang, Appl. Phys. Lett. 94 (2009), p. 163115.
[561] M. Topsakal, S. Cahangirov, and S. Ciraci, Appl. Phys. Lett. 96 (2010), p. 091912.
[562] Y. Gan, L. Sun, and F. Banhart, Small 4 (2008), p. 587.
[563] R. Muszynski, B. Seger, and P.V. Kamat, J. Phys. Chem. C 112 (2008), p. 5263.
[564] C.G. Hwang, S.Y. Shin, S.-M. Choi, N.D. Kim, S.H. Uhm, H.S. Kim, C.C. Hwang, D.Y. Noh, S.-H. Jhi, and J.W. Chung, Phys. Rev. B 79 (2009), p. 115439.
[565] L. Tapasztó, G. Dobrik, P. Nemes-Incze, G. Vertesy, Ph. Lambin, and L.P. Biró, Phys. Rev. B 78 (2008), p. 233407.
[566] K. Pi, K.M. McCreary, W. Bao, W. Han, Y.F. Chiang, Y. Li, S.-W. Tsai, C.N. Lau, and R.K. Kawakami, Phys. Rev. B 80 (2009), p. 075406.
[567] Y. Mao, J. Yuan, and J. Zhong, J. Phys.: Condens. Matter 20 (2008), p. 115209.
[568] K.T. Chan, J.B. Neaton, and M.L. Cohen, Phys. Rev. B 77 (2008), p. 235430.
[569] B. Uchoa, C.-Y. Lin, and A.H. Castro Neto, Phys. Rev. B 77 (2008), p. 035420.
[570] A.H. Castro Neto, V.N. Kotov, J. Nilsson, V.M. Pereira, N.M.R. Peres, and B. Uchoa, Solid State Commun. 149 (2009), p. 1094.
[571] R. Varns and P. Strange, J. Phys.: Condens. Matter 20 (2008), p. 225005.
[572] G.M. Wang, J.J. BelBruno, S.D. Kenny, and R. Smith, Phys. Rev. B 69 (2004), p. 195412.
[573] Y. Okamoto, Chem. Phys. Lett. 420 (2006), p. 382.
[574] O.Ü. Aktürk and M. Tomak, Phys. Rev. B 80 (2009), p. 085417.
[575] S.S. Carara, R.J.C. Batista, and H. Chacham, Phys. Rev. B 80 (2009), p. 115435.
[576] M. Calandra and F. Mauri, Phys. Rev. B 76 (2007), p. 161406(R).

[577] J.L. McChesney, A. Bostwick, T. Ohta, K.V. Emtsev, T. Seyller, K. Horn and E. Rotenberg, arXiv:0705.3264.
[578] M.I. Rojas and E.P.M. Leiva, Phys. Rev. B 76 (2007), p. 155415.
[579] Q. Ran, M. Gao, X. Guan, Y. Wang, and Z. Yu, Appl. Phys. Lett. 94 (2009), p. 103511.
[580] M. Wu, E.-Z. Liu, M.Y. Ge, and J.Z. Jiang, Appl. Phys. Lett. 94 (2009), p. 102505.
[581] I. Zanella, S.B. Fagan, R. Mota, and A. Fazzio, J. Phys. Chem. C 112 (2008), p. 9163.
[582] N. Gorjizadeh, A.A. Farajian, K. Esfarjani, and Y. Kawazoe, Phys. Rev. B 78 (2008), p. 155427.
[583] Y. Sanchez-Paisal, D. Sanchez-Portal, and A. Ayuela, Phys. Rev. B 80 (2009), p. 045428.
[584] S.-M. Choi and S.-H. Jhi, Phys. Rev. Lett. 101 (2008), p. 266105.
[585] V.A. Rigo, T.B. Martins, A.J.R. da Silva, A. Fazzio, and R.H. Miwa, Phys. Rev. B 79 (2009), p. 075435.
[586] A.V. Krasheninnikov, P.O. Lehtinen, A.S. Foster, P. Pyykkö, and R.M. Nieminen, Phys. Rev. Lett. 102 (2009), p. 126807.
[587] D.W. Boukhvalov and M.I. Katsnelson, Appl. Phys. Lett. 95 (2009), p. 023109.
[588] H. Tachikawa, J. Phys. Chem. C 112 (2008), p. 10193.
[589] B. Uchoa, V.N. Kotov, N.M.R. Peres, and A.H. Castro Neto, Phys. Rev. Lett. 101 (2008), p. 026805.
[590] P. Esquinazi, D. Spemann, R. Höhne, A. Setzer, K.-H. Han, and T. Butz, Phys. Rev. Lett. 91 (2003), p. 227201.
[591] D. Teweldebrhan and A.A. Balandin, Appl. Phys. Lett. 94 (2009), p. 013101.
[592] Y. Wang, Y. Huang, Y. Song, X. Zhang, Y. Ma, J. Liang, and Y. Chen, Nano Lett. 9 (2009), p. 220.
[593] C. Casiraghi, S. Pisana, K.S. Novoselov, A.K. Geim, and A.C. Ferrari, Appl. Phys. Lett. 91 (2007), p. 233108.
[594] P.O. Lehtinen, A.S. Foster, Y. Ma, A.V. Krasheninnikov, and R.M. Neiminen, Phys. Rev. Lett 93 (2004), p. 187202.
[595] Y. Ma, P.O. Lehtinen, A.S. Foster, and R.M. Neiminen, New J. Phys. 6 (2004), p. 68.
[596] A.A. El-Barbary, R.H. Telling, C.P. Ewels, M.I. Heggie, and P.R. Briddon, Phys. Rev. B 68 (2003), p. 144107.
[597] H. Amara, S. Latil, V. Meunier, Ph. Lambin, and J.-C. Charlier, Phys. Rev. B 76 (2007), p. 115423.
[598] H. Tachikawa and H. Kawabata, J. Phys. Chem. C 113 (2009), p. 7603.
[599] O.V. Yazyev and L. Helm, Phys. Rev. B 75 (2007), p. 125408.
[600] G. Forte, A. Grassi, G.M. Lombardo, A.L. Magna, G.G.N. Angilella, R. Pucci, and R. Vilardi, Phys. Lett. A 372 (2008), p. 6168.
[601] V.M. Pereira, J.M.B. Lopes dos Santos, and A.H. Castro Neto, Phys. Rev. B 77 (2008), p. 115109.
[602] M.P. López-Sancho, F. de Juan, and M.A.H. Vozmediano, Phys. Rev. B 79 (2009), p. 075413.
[603] R. Singh and P. Kroll, J. Phys.: Condens. Matter 21 (2009), p. 196002.
[604] H. Kumazaki and D.S. Hirashima, J. Phys. Soc. Japan 76 (2007), p. 064713.
[605] J. Kang, J. Bang, B. Ryu, and K.J. Chang, Phys. Rev. B 77 (2008), p. 115453.
[606] J.J. Palacios, J. Fernández-Rossier, and L. Brey, Phys. Rev. B 77 (2008), p. 195428.
[607] B. Huang, F. Liu, J. Wu, B.-L. Gu, and W. Duan, Phys. Rev. B 77 (2008), p. 153411.
[608] Y. Zhang, S. Talapatra, S. Kar, R. Vajtai, S.K. Nayak, and P.M. Ajayan, Phys. Rev. Lett. 99 (2007), p. 107201.
[609] O.V. Yazyev, Phys. Rev. Lett. 101 (2008), p. 037203.
[610] B.-L. Huang and C.-Y. Mou, Eur. Phys. Lett. 88 (2009), p. 68005.
[611] J.R. Hahn and H. Kang, Phys. Rev. B 60 (1999), p. 6007.

[612] P. Ruffieux, O. Gröning, P. Schwaller, L. Schlapbach, and P. Gröning, Phys. Rev. Lett. 84 (2000), p. 4910.

[613] P. Ruffieux, M. Melle-Franco, O. Gröning, M. Bielmann, F. Zerbetto, and P. Gröning, Phys. Rev. B 71 (2005), p. 153403.

[614] G.M. Rutter, J.N. Crain, N.P. Guisinger, T. Li, P.N. First, and J.A. Stroscio, Science 317 (2007), p. 219.

[615] P. Mallet, F. Varchon, C. Naud, L. Magaud, C. Berger, and J.-Y. Veuillen, Phys. Rev. B 76 (2007), p. 041403(R).

[616] C. Bena, Phys. Rev. Lett. 100 (2008), p. 076601.

[617] Y. Ferro and A. Allouche, Phys. Rev. B 75 (2007), p. 155438.

[618] L. Pisani, B. Montanari, and N.M. Harrison, New J. Phys. 10 (2008), p. 033002.

[619] R.Y. Oeiras, F.M. Araújio-Moreira, and E.Z. da Silva, Phys. Rev. B 80 (2009), p. 073405.

[620] M. Topsakal, E. Aktürk, H. Sevinçli, and S. Ciraci, Phys. Rev. B 78 (2008), p. 235435.

[621] B. Sanyal, O. Eriksson, U. Jansson, and H. Grennberg, Phys. Rev. B 79 (2009), p. 113409.

[622] S. Malola, H. Häkkinen, and P. Koskinen, Appl. Phys. Lett. 94 (2009), p. 043106.

[623] M.A.H. Vozmediano, M.P. López-Sancho, T. Stauber, and F. Guinea, Phys. Rev. B 72 (2005), p. 155121.

[624] B.W. Jeong, J. Ihm, and G.-D. Lee, Phys. Rev. B 78 (2008), p. 165403.

[625] F. OuYang, B. Huang, Z. Li, J. Xiao, H. Wang, and H. Xu, J. Phys. Chem. C 112 (2008), p. 12003.

[626] A. Carpio, L.L. Bonilla, F. de Juan, and M.A.H. Vozmediano, New J. Phys. 10 (2008), p. 053021.

[627] M.T. Lusk and L.D. Carr, Phys. Rev. Lett. 100 (2008), p. 175503.

[628] J.Y. Yan, P. Zhang, B. Sun, H.-Z. Lu, Z. Wang, S. Duan, and X.-G. Zhao, Phys. Rev. B 79 (2009), p. 115403.

[629] N. Gorjizadeh, A.A. Farajian, and Y. Kawazoe, Nanotechnology 20 (2009), p. 015201.

[630] A. Cresti and S. Roche, Phys. Rev. B 79 (2009), p. 223404.

[631] D. Wei, Y. Liu, Y. Wang, H. Zhang, L. Huang, and G. Yu, Nano Lett. 9 (2009), p. 1752.

[632] B. Huang, Q. Yan, G. Zhou, J. Wu., B.-L. Gu, W. Duan, and F. Liu, Appl. Phys. Lett. 91 (2007), p. 253122.

[633] M. Deifallah, P.F. McMillan, and F. Corà, J. Phys. Chem. C 112 (2008), p. 5447.

[634] O.Ü. Aktürk and M. Tomak, Appl. Phys. Lett. 96 (2010), p. 081914.

[635] K. Sawada, F. Ishii, M. Saito, S. Okada, and T. Kawai, Nano Lett. 9 (2009), p. 269.

[636] T.O. Wehling, A.V. Balatsky, M.I. Katsnelson, A.I. Lichtenstein, K. Scharnberg, and R. Wiesendanger, Phys. Rev. B 75 (2007), p. 125425.

[637] B. Biel, X. Blase, F. Triozon, and S. Roche, Phys. Rev. Lett. 102 (2009), p. 096803.

[638] A. Quandt, C. Özdogan, J. Kunstmann, and H. Fehske, Nanotechnology 19 (2008), p. 335707.

[639] A. Quandt, C. Özdogan, J. Kunstmann, and H. Fehske, Phys. Status Solidi b 245 (2008), p. 2077.

[640] R.B. Pontes, A. Fazzio, and G.M. Dalpian, Phys. Rev. B 79 (2009), p. 033412.

[641] T. Wassmann, A.P. Seitsonen, A.M. Saitta, M. Lazzeri, and F. Mauri, Phys. Rev. Lett. 101 (2008), p. 096402.

[642] H. Xu, T. Heinzel, and I.V. Zozoulenko, Phys. Rev. B 80 (2009), p. 045308.

[643] K. Wakabayashi and M. Sigrist, Phys. Rev. Lett. 84 (2000), p. 3390.

[644] D. Konatham and A. Striolo, Nano Lett. 8 (2008), p. 4630.

[645] D. Gunlycke, J. Li, J.W. Mintmire, and C.T. White, Appl. Phys. Lett. 91 (2007), p. 112108.

[646] F. Cervantes-Sodi, G. Csányi, S. Piscanec, and A.C. Ferrari, Phys. Rev. B 77 (2008), p. 165427.
[647] F. Cervantes-Sodi, G. Csányi, S. Piscanec, and A.C. Ferrari, Phys. Status Solidi b 245 (2008), p. 2068.
[648] H. Zheng and W. Duley, Phys. Rev. B 78 (2008), p. 045421.
[649] K. Kusakabe and M. Maruyama, Phys. Rev. B 67 (2003), p. 092406.
[650] M. Maruyama and K. Kusakabe, J. Phys. Soc. Japan 73 (2004), p. 656.
[651] M. Wu, X. Wu, Y. Gao, and X.C. Zeng, Appl. Phys. Lett. 94 (2009), p. 223111.
[652] E.-J. Kan, Z. Li, J. Yang, and J.G. Hou, J. Am. Chem. Soc. 130 (2008), p. 4224.
[653] J. Berashevich and T. Chakraborty, Phys. Rev. B 80 (2009), p. 115430.
[654] T.B. Martins, R.H. Miwa, A.J.R. da Silva, and A. Fazzio, Phys. Rev. Lett. 98 (2007), p. 196803.
[655] T.B. Martins, A.J.R. da Silva, R.H. Miwa, and A. Fazzio, Nano Lett. 8 (2008), p. 2293.
[656] R.N. Costa Filho, G.A. Farias, and F.M. Peeters, Phys. Rev. B 76 (2007), p. 193409.
[657] S. Dutta, A.K. Manna, and S.K. Pati, Phys. Rev. Lett. 102 (2009), p. 096601.